# STUDIES OF ANODE SUPPORTED SOLID OXIDE FUEL CELLS (SOFCS) BASED ON LA- AND CA-DOPED $SrTiO_3$

**Lanying Lu**

**A Thesis Submitted for the Degree of PhD**
**at the**
**University of St Andrews**

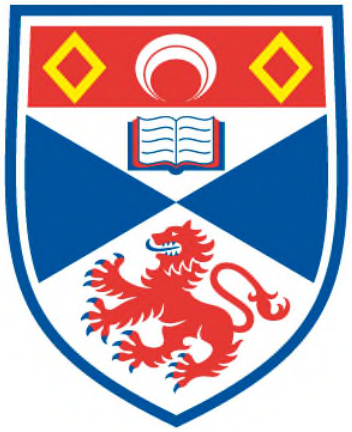

**2015**

# Studies of Anode Supported Solid Oxide Fuel Cells (SOFCs) Based on La- and Ca-Doped $SrTiO_3$

Lanying Lu

University of
St Andrews

This thesis is submitted in partial fulfilment for the degree of PhD
at the
University of St Andrews

Submitted January 2015

# Declarations

I, Lanying Lu, hereby certify that this thesis, which is approximately 52,000 words in length, has been written by me, and that it is the record of work carried out by me, or principally by myself in collaboration with others as acknowledged, and that it has not been submitted in any previous application for a higher degree.

I was admitted as a research student in October 2011 and as a candidate for the degree of Doctor of Philosophy in October 2014; the higher study for which this is a record was carried out in the University of St Andrews between 2011 and 2014.

Date …… signature of candidate ……

I hereby certify that the candidate has fulfilled the conditions of the Resolution and Regulations appropriate for the degree of Doctor of Philosophy in the University of St Andrews and that the candidate is qualified to submit this thesis in application for that degree.

Date …… signature of supervisor……

Date …… signature of supervisor ……

In submitting this thesis to the University of St Andrews I understand that I am giving permission for it to be made available for use in accordance with the regulations of the University Library for the time being in force, subject to any copyright vested in the work not being affected thereby. I also understand that the title and the abstract will be published, and that a copy of the work may be made and supplied to any bona fide library or research worker, that my thesis will be electronically accessible for personal or research use unless exempt by award of an embargo as requested below, and that the library has the right to migrate my thesis into new electronic forms as required to ensure continued access to the thesis. I have obtained any third-party copyright permissions that may be required in order to allow such access and migration, or have requested the appropriate embargo below.

The following is an agreed request by candidate and supervisors regarding the publication of this thesis:

Access to printed copy but embargo on electronic copy for a period of 2 years on the following ground:

Publication would preclude future publication.

Date …… signature of candidate ……

Date …… signature of supervisor ……

Date …… signature of supervisor ……

# Acknowledgements

First and foremost, I would like to sincerely thank my supervisors, Prof. John Irvine and Dr. Mark Cassidy, for giving me the opportunity to work as a PhD student in the research filed of solid oxide fuel cells. My knowledge and experience on solid oxide fuel cells were quite minimal before I started this project, but they have been always patient to me and responded to my queries associated with the laboratory work and data analysis very promptly. Their support, trust and profound knowledge are definitely the most essential factors for the completion of my thesis. Without their involvement, I would never be capable of finishing my thesis.

I would like to thank all the members of the JTSI group for the help with testing instruments and result discussion during my three years in St Andrews. In particular, I want to show my deep gratitude to Dr. Maarten Verbraeken for teaching me the slurry preparation and tape casting technique, Dr. David Miller for the TEM and EDX analysis on my samples and Dr. Mark Cassidy for the kind help on screen printing technique. I also acknowledge Mrs. Julie Nairn and Dr. Paul Conner who helped me a lot in the lab, Mrs Sylvia Williamson who taught me to operate TGA and dilatometer, and Mr. Ross Blackley for the demonstration of SEM equipments.

My deepest gratitude goes to Mr. Alan Davidson in Napier University, Edinburgh for his supervision and guidance on the work about Ni-YSZ anode fabrication using the electroless Ni-YSZ co-deposition process. Special thanks to Dr Callum Wilson, Dr. Neil Shearer and Mr. Dong Wang for the lab-related work and discussion.

My thanks also to MCS company, Edinburgh that collaborated with my research. Mr. Stewart McCracken, Dr. Andrew Gibson and Dr. Stephen Mee have helped me to slot my samples for FIB preparation even when the cutting system was extremely busy and spared their time for my manuscript correction.

I would like to grant my special thanks to my family for all the help and support throughout my study. Although being far away, my parents have encouraged me to pursue my PhD study all the time. To my husband, Dr. Chengsheng Ni, who always stood by me even at the bad times and gave me his best suggestions about my experimental analysis. Without their intrinsic love and inspiration, I would not be able to conquer the difficulties I have encountered for the completion of my thesis.

The last but not the least, I would like to express my gratitude to the Fuel Cells and Hydrogen Joint Technology Initiative and Energy Technology Partnership (ETP) for funding that supports me throughout my PhD journey.

# Abstract

Solid oxide fuel cells (SOFCs) have attracted much interest as the most efficient electrochemical device to directly convert chemical energy to usable electrical energy. The porous Ni-YSZ anode known as the state-of-the-art cermet anode material is found to show serious degradation when using hydrocarbon as fuel due to carbon deposition, sulphur poisoning, and nickel sintering. In order to overcome these problems, doped strontium titanate has been investigated as a potential anode material due to its high electronic conductivity and stability in reducing atmosphere. In this work, A-site deficient strontium titanate co-doped with lanthanum and calcium, $La_{0.2}Sr_{0.25}Ca_{0.45}TiO_3$ ($LSCT_{A-}$), was examined.

Flat multilayer ceramics have been produced using the aqueous tape casting technique by controlling the sintering behaviour of $LSCT_{A-}$, resulting in a 450μm thick porous $LSCT_{A-}$ scaffold with a well adhered 40μm dense YSZ electrolyte. Impregnation of $CeO_2$ and Ni results in a maximum power density of $0.96Wcm^{-2}$ at $800^oC$, higher than those of without impregnation ($0.124Wcm^{-2}$) and with impregnation of Ni alone ($0.37Wcm^{-2}$). The addition of catalysts into $LSCT_{A-}$ anode significantly reduces the polarization resistance of the cells, suggesting an insufficient electrocatalytic activity of the $LSCT_{A-}$ backbone for hydrogen oxidation, but $LSCT_{A-}$ can provide the electronic conductivity required for anode.

Later, the cells with the configuration of $LSCT_{A-}$/YSZ/LSCF-YSZ were prepared by the organic tape casting and impregnation techniques with only 300-μm thick anode as support. The effects of metallic catalysts in the anode supports on the initial performance and stability in humidified hydrogen were discussed. The nickel and iron impregnated $LSCT_{A-}$ cell exhibits a maximum powder density of $272mW/cm^2$ at $700^oC$, much larger than $43mW/cm^2$ for the cell without impregnation and $112mW/cm^2$ for the cell with nickel impregnation. Simultaneously, the bimetal Ni-Fe impregnates have significantly reduced the degradation rates in humidified hydrogen (3% $H_2O$) at $700^oC$. The enhancement from impregnation of the bi-metal can possibly be the result of the presence of ionic conducting Wustite $Fe_{1-x}O$ that resides underneath the Ni-Fe metallic particles and better microstructure.

Third, in order to improve the ionic conductivity of the anode support and increase the effective TPBs, ionic conducting ceria was impregnated into the $LSCT_{A-}$ anode, along with the metallic catalysts. The $CeO_2$-$LSCT_{A-}$ cell shows a poor performance upon operation in hydrogen atmosphere containing 3% $H_2O$; and with addition of metallic catalysts, the cell performance increases drastically by almost three-fold. However, the infiltrated Ni particles on the top of ceria layer cause the deposition of carbon filament leading to cell cracking when exposure to humidified methane (3% $H_2O$). No such behaviour was observed on the $CeO_2$-NiFe impregnated anode. The microstructure images of the impregnated anodes at different times during stability testing demonstrate that the grain growth of catalysts, the interaction between the anode backbone and infiltrates, and the spalling of the agglomerated catalysts are the main reasons for the performance degradation.

Fourth, the YSZ-$LSCT_{A-}$ composites including the YSZ contents of 5-80wt.% were investigated to determine the percolation threshold concentration of YSZ to achieve electronic and ionic conducting pathways when using the composite as SOFC anode backbone. The microstructure and dilatometric curves show that when the YSZ content is below 30%, the milled sample has a lower shrinkage than the unmilled one due to the blocking effect from the well distributed YSZ grains within $LSCT_{A-}$ bulk. However, at the YSZ above 30% where two phases start to form the individual and interconnected bulk, the composites without ball milling process show a lower densification. The impact of YSZ concentration and ball milling process on the electrical properties of the composites reveals that the percolation threshold concentration is not only dependant on the actual concentration, but also related to the local arrangement of two phases.

In Napier University, the electroless nickel-ceramic co-depositon process was investigated as a manufacturing technique for the anodes of planar SOFCs, which entails reduced costs and reduced high-temperature induced defects, compared with conventional fabrication techniques. The Ni-YSZ anodes prepared by the electroless co-deposition technique without the addition of surfactant adhere well to the YSZ electrolyte before and after testing at 800$^{o}$C in humidified hydrogen. Ni-YSZ anodes co-deposited with pore-forming starch showed twice the maximum power density compared with those without the starch. It has therefore been demonstrated that a

porous Ni-YSZ cermet structure was successfully manufactured by means of an electroless plating technique incorporating pore formers followed by firing at 450$^{o}$C in air. Although the use of surfactant (CTAB) increases the plating thickness, it induces the formation of a Ni-rich layer on the electrolyte/anode interface, leading to the delamination of anode most likely due to the mismatched TECs with the adjacent YSZ electrolyte.

# Abbreviations

| | |
|---|---|
| 8YSZ | 8mol.% yttria doped zirconia |
| AFC | alkaline fuel cell |
| ASR | area specific resistance |
| BET | brunauer–emmett–teller |
| BSE | backscattered electron |
| BZCYYb | $BaZr_{0.1}Ce_{0.7}Y_{0.1}Yb_{0.1}O_{3-\delta}$ |
| CPE | constant phase element |
| CTAB | cetyltrimethyl ammonium bromide |
| DBP | di-n-butyl phthalate |
| EDS | energy dispersive x-ray spectroscopy |
| EIS | electrochemical impedance spectroscopy |
| EMF | electromotive force |
| EN | electroless nickel |
| FEG | field emission gun |
| FIB | focused ion beam |
| GDC/CGO | gadolinia-doped ceria |
| HF | high frequency |
| I-P | current-power |
| I-V | current-voltage |
| LF | low frequency |
| LSBT | $La_{0.4}Sr_{0.6-x}Ba_xTiO_3$ ($0<x\leq0.2$) |
| LSC | strontium-doped lanthanum cobalt |
| LSCF | lanthanum strontium cobalt ferrite |
| $LSCT_{A-}$ | A-site deficient lanthanum strontium calcium titanate |
| LSCX | $La_{0.75}Sr_{0.25}Cr_{0.5}X_{0.5}O_{3-\delta}$ (X=Co, Fe, Ti, Mn) |
| LSF | strontium-doped lanthanum ferrite |
| LSGM | lanthanum strontium gallium magnesium oxide |
| LSM | strontium-doped lanthanum manganite |
| LST | lanthanum-doped $SrTiO_3$ |
| LSTC | La and Cr co-doped $SrTiO_3$ |
| LSTCo | Co-doping in B site on LST |
| LSTM | Mn-doping in B site on LST |
| LVDT | linear variable displacement transducer |
| MCFC | molten carbonate fuel cell |
| MIEC | mixed ionic and electronic conductor |
| OCV | open circuit voltage |
| PAFC | phosphoric acid fuel cell |
| PEG | poly(ethylene glycol) |
| PEMFC | polymer electrolyte membrane fuel cell |
| PSA | particle size analysis |

| | |
|---|---|
| PVA | polyvinyl alcohol |
| PVB | polyvinyl butyral |
| redox | reduction-oxidation |
| RT | room temperature |
| ScSZ | scandia stabilized zirconia |
| SDC | samaria-doped ceria |
| SEM | scanning electron microscopy |
| SOFC | solid oxide fuel cell |
| SSA | specific surface area |
| SSC | $Sm_{0.5}Sr_{0.5}CoO_3$ |
| STF | iron-doped $SrTiO_3$ |
| STN | niobium–doped $SrTiO_3$ |
| STO | strontium titanium oxide |
| TEC | thermal expansion coefficient |
| TEM | transmission electron microscopy |
| TGA | thermal gravimetric analysis |
| TPB | triple phase boundary |
| XRD | x-ray diffraction |
| YST | yttrium-doped $SrTiO_3$ |
| YSTCo | Co-doping in B site on YST |
| YSZ | yttria-stabilized zirconia |

# Contents

# Chapter 1. Introduction

## 1.1 Fuel cell technology

### 1.1.1 Definition

Fuel cells are energy conversion devices that transfer the chemical energy directly into electricity through the chemical reaction between a fuel and an oxidant. Across the different types of fuel cells, a typical fuel cell is composed of three basic elements: anode (fuel electrode), electrolyte and cathode (air electrode), as shown in Figure 1.1. The fuel (such as hydrogen or methanol) is fed into the anode and oxidized liberating electrons to the external circuit; the oxidant (usually air or oxygen) is reduced on the cathode in combination with electrons from the external circuit. The ions produced during reduction or oxidation transport from one electrode to the other through electrolyte that is an ionic conductor but electronic insulator. The electrolyte also serves as a barrier for gaseous diffusion. The electrons flowing through the external circuit from the anode side to the cathode side generate the electricity on the load. Theoretically, a fuel cell system produces electricity continuously as long as the fuel and oxidant are introduced into the chambers, but the malfunction of each component can cause the degradation of performance, limiting the practical application.

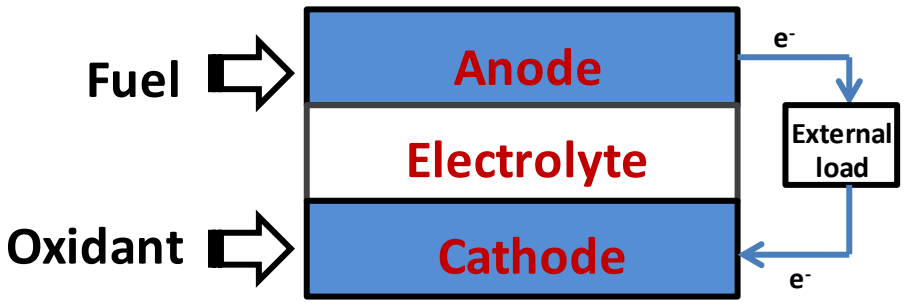


Figure 1.1 Schematic of a fuel cell: an electrolyte is sandwiched by an anode and a cathode

### 1.1.2 History

The concept of fuel cells has been efficiently demonstrated by Humphry Davy dating from the early nineteenth century [1]. The first hydrogen fuel cell was successfully invented by William Grove in 1839 [2], generally referred as the start of fuel cell history. He discovered a small amount of current flowing between the two platinum electrodes immersed into the sulphuric acid as a result of the chemical reaction of hydrogen and oxygen produced from electrolysis reaction of water [3].

Until the early $20^{th}$ century, much effort had been devoted to the optimization of the original fuel cells. However, the development of fuel cell technology has been limited by the electrode materials and manufacturing methods. In 1959, Francis Bacon successfully prepared a 5KW stationary fuel cell using alkaline solution as electrolyte and metallic nickel as electrodes, unveiling a prosperous era for development of fuel cells. Since the early 1960s, significant advances in fuel cell technology have been achieved: they have been used for space vehicles [4], submarines [5] and power suppliers for commercial and industrial locations.

Nowadays, with concerns over energy shortage and environmental contamination caused by combustion of fossil fuel, much work has aimed at the development and optimization of more efficient and cleaner fuel cell system. In despite of the fact that fuel cell has been developed for over 170 years, there are still some issues in respect to process techniques, material selection and stability needed to be addressed to prompt the practical application.

### 1.1.3 Classification of fuel cells

According to the different types of electrolytes used in the cells, fuel cells are classified into 5 major kinds: polymer electrolyte membrane fuel cells (PEMFCs), alkaline fuel cells (AFCs), phosphoric acid fuel cells (PAFCs), molten carbonate fuel cells (MCFCs) and solid oxide fuel cells (SOFCs). Generally, the operating temperature is dependent on the type of electrolyte materials. The first three kinds of fuel cells are usually operated at the low temperature, while the other two types are employed at high temperature above $500^{o}C$. The comparison of working temperatures,

fuels, electrolyte materials and conducting mechanism among all kinds of fuel cells are listed in the Table 1.1 [6].

Table 1.1 Comparison of different types of fuel cells [6]

| Type | Operating Temperature ($^oC$) | Fuel | Electrolyte | Mobile Ion |
|---|---|---|---|---|
| Polymer electrolyte membrance fuel cell (PEMFC) | 70-110 | $H_2$, $CH_3OH$ | Polymers | $(H_2O)_nH^+$ |
| Alkaline fuel cell (AFC) | 100-250 | $H_2$ | Aqueous K(OH) | $OH^-$ |
| Phosphoric acid fuel cell (PAFC) | 150-250 | $H_2$ | $H_3PO_4$ (liquid) | $H^+$ |
| Molten carbonate fuel cell (MCFC) | 500-700 | Hydrocarbon, $H_2$, CO | $(Na, K)_2CO_3$ (liquid) | $CO_3^{2-}$ |
| Solid oxide fuel cell (SOFC) | 700-1000 | Hydrocarbon, $H_2$, CO | $(Zr, Y)O_{3-\delta}$ | $O^{2-}$ |

Despite of the similar operating principle, significant differences lie in design, application, efficiency and cost due to varied electrolytes and temperature of operation. PEMFCs employ solid electrolytes at the low temperature, which reduces the corrosion and electrolyte management problems; however, they are subjected to poisoning by the trace contaminants in fuel. Moreover, the need for the high cost platinum catalyst is another limiting factor for the practical application of PEMFCs. AFCs as the most mature fuel-cell technologies offer high electrical efficiencies under non-precious metal catalysts, but suffer from the problem of low resistance to poisoning by carbon dioxides and liquid electrolyte management. PAFCs are tolerant to the impurities in hydrogen, such as CO, while the cathodic reaction is slow and requires the use of the platinum catalyst. In addition, the highly corrosive nature of phosphoric acid requires the use of expensive materials. Because MCFCs are used at relatively high temperature, no expensive electro-catalysts are required, and both CO and certain hydrocarbon can be used as fuels. The challenge for MCFCs stems mainly from the mobile and corrosive electrolyte and high operating temperature, promoting

material problems and causing the performance degradation upon operation. SOFCs are composed of solid components, which alleviate the corrosion problems in the cell. The high operating temperature for SOFCs allows using low-cost electro-catalysts and varied fuels, but it places severe constraints on material selection and manufacturing processes. And the long-term reliability of the materials under operating conditions is also of the greatest concern.

The application of solid electrolyte precludes the need for corrosive liquid, prompting the development of PEMFCs and SOFCs. The SOFC is more demanding than the PEMFC from the standpoint of materials and has been developed for its potential application arising from the flexibility of fuel from hydrogen to hydrocarbon then further to CO, higher energy conversion efficiency operated at high temperature and less emission of pollutants, compared to the conventional internal combustion engines and other types of fuel cells.

### 1.1.4 Advantages

One of the most attractive properties of fuel cells is their extremely high energy-conversion efficiency which is superior to those conventional internal combustion engines. Because the fuel cells convert the chemical energy directly into the electrical energy without thermal energy conversion as intermediate steps, the conversion efficiency is not confined by the Carnot cycle. Theoretically, the efficiency of fuel cells is expected to be 40–60% when converting fuel to electricity [7]. If the heat from the fuel cell system can be captured and utilized, the overall system efficiencies could be up to 80–85% [7]. For hydrogen fuelled fuel cells, the only product is water. Fuel cells can eliminate CO emission in exhaust gases by converting into $CO_2$ at high operating temperature. Besides those advantages, fuel cells offer some additional benefits, such as, quite operation, long life expectancy, and flexible size construction.

## 1.2 Basics of solid oxide fuel cells

### 1.2.1 Principles of operation

SOFCs with hydrogen as fuel and oxygen as oxidant have been studied extensively. The operating principles of a typical SOFC are shown in Figure 1.2 using hydrogen and oxygen as fuel and oxidant respectively. The anode and cathode must be porous, to allow fuel and oxidant to access the corresponding triple phase boundaries (TPB) where gaseous species, ions and electrons meet and the chemical reaction occurs upon catalyst surfaces [8]. On the cathode side, $O_2$ is absorbed and combines with electrons to form $O^{2-}$, which can migrate through the ion conducting electrolyte to the anode side. On the anode side, supplied $H_2$ reacts with $O^{2-}$ to produce $H_2O$ and release electrons. Consequently, electrical power is generated as the result of the electrons passing through the external circuit from the anode to cathode.

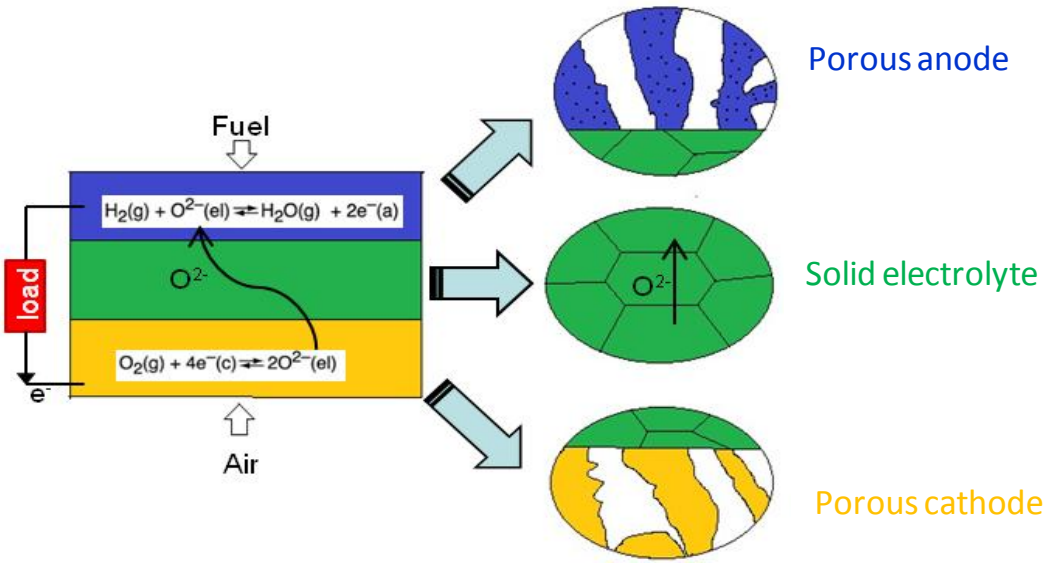


Figure 1.2 Operating principle of a basic SOFC using $H_2$ as fuel and $O_2$ as oxidant. The abbreviations g, el, a and c in the reaction equations refer to gas, electrolyte, anode and cathode, respectively.

### 1.2.2 Thermodynamic principles of SOFCs

In a typical SOFC device, oxidant is reduced at the cathode side and fuel is oxidised at the anode side. If hydrogen and oxygen are used as fuel and oxidant in SOFC, the overall reaction in the fuel cell is given as

$$H_{2\,(anode)} + 1/2O_{2\,(cathode)} = H_2O_{\,(anode)} \qquad \text{(Equation 1.1)}$$

where the subscripts anode and cathode refer to the states at the anode and cathode, respectively.

The reaction of oxygen and hydrogen occurs on the cathode and anode, respectively, according to Equations (1.2) and (1.3):

$$O_{2\,(cathode)} + 4e^- = 2O^{2-}_{\,(electrolyte)} \qquad \text{(Equation 1.2)}$$

$$H_{2\,(anode)} + O^{2-}_{(electrolyte)} = H_2O_{\,(anode)} + 2e^- \qquad \text{(Equation 1.3)}$$

where the subscript electrolyte represents the oxygen ions transporting through the electrolyte.

The equilibrium voltage, $E$, is given by the Nernst equation:

$$E = E^0 + \frac{RT}{4F}\ln \mathrm{P}(\mathrm{O}_{2\ \mathrm{cathode}}) + \frac{RT}{2F}\ln \frac{\mathrm{P}(\mathrm{H}_{2\ \mathrm{anode}})}{\mathrm{P}(\mathrm{H_2O}_{\ \mathrm{anode}})} \qquad \text{(Equation 1.4)}$$

Where $R$ is the gas constant, $F$ the Faraday's constant, $T$ the temperature, and $\mathrm{P}(\mathrm{O}_{2\ \mathrm{cathode}})$, $\mathrm{P}(\mathrm{H}_{2\ \mathrm{anode}})$ and $\mathrm{P}(\mathrm{H_2O}_{\ \mathrm{anode}})$ the partial pressure of cathodic oxygen, anodic hydrogen and water vapour, respectively. $E^0$ is the equilibrium voltage at the standard state for oxidation of $H_2$, which can be established by

$$E^0 = -\frac{\Delta G^0}{4F} = -\frac{\Delta H^0 - T\Delta S^0}{4F} \qquad \text{(Equation 1.5)}$$

where $\Delta G^0$ represents the standard Gibbs energy change of reaction of hydrogen with oxygen to produce water, $\Delta H^0$ is the standard enthalpy change and $\Delta S^0$ is the standard entropy. However, the actual cell voltage $E_c$ under current load is less than the theoretical Nernst value or electromotive force (EMF) due to the irreversible losses

associated with ohmic losses, mass transport and the kinetics of electrode reactions, as depicted in Figure 1.3 [9].

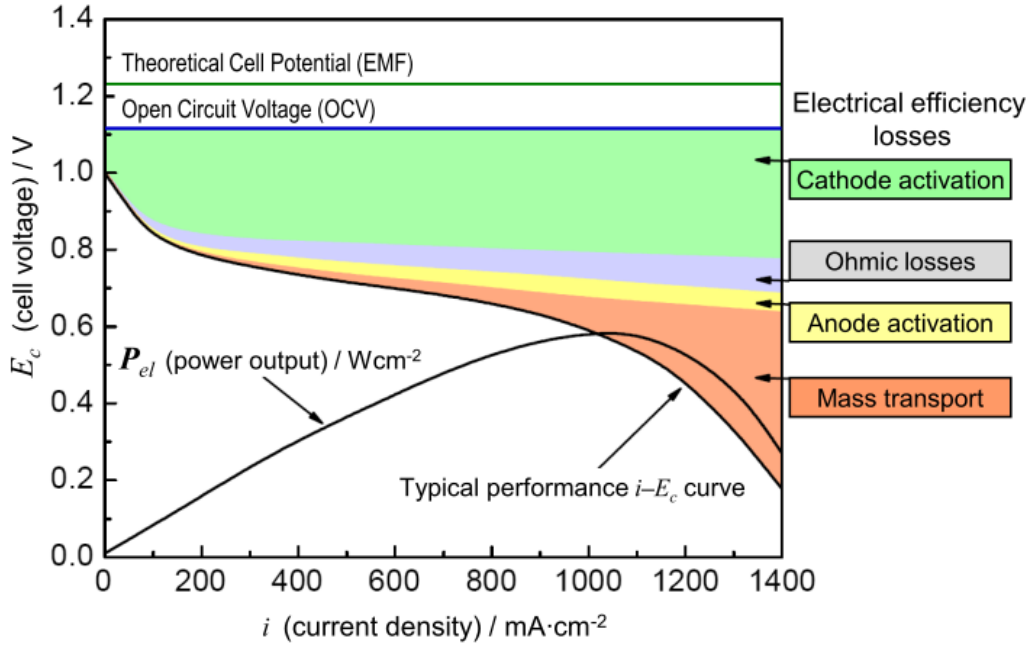


Figure 1.3 Schematic of a current-voltage curve with marked regions of the different contribution of polarization losses. Image is taken from reference [9].

The maximum thermodynamic efficiency, $\varepsilon$, can be obtained only when the Gibbs free energy of the cell reaction, $\Delta G$, is totally converted into electrical energy, therein expressed by the following equation:

$$\varepsilon = \frac{\Delta G}{\Delta H} \qquad \text{(Equation 1.6)}$$

where $\Delta H$ is the enthalpy changes for the combustion of fuel. In practise, $\Delta G$ is consumed not only to achieve the cell reaction but also to produce heat and water vapour above 100$^{o}$C, resulting in a significant energy losses compared to the maximum efficiency.

### 1.2.3 Configuration and evolution of SOFCs

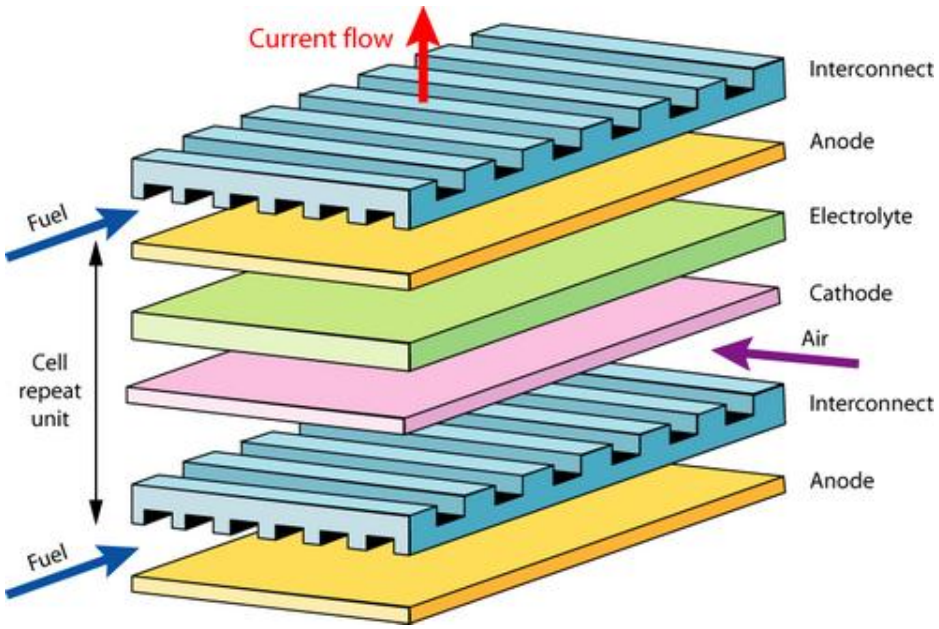


Figure 1.4 Planar design of SOFCs. Image is taken from reference [10].

In general, there are two types of SOFC designs: planar and tubular. In a planar cell, each component is made into flat plates and all components are assembled into a stack by connecting the interconnect plates of two adjacent cells, shown in Figure 1.4. In this system, the interconnect plates form gas flow channels for fuel and oxidant and serve as bipolar gas separators contacting the anode and the cathode of adjoining cells [11].

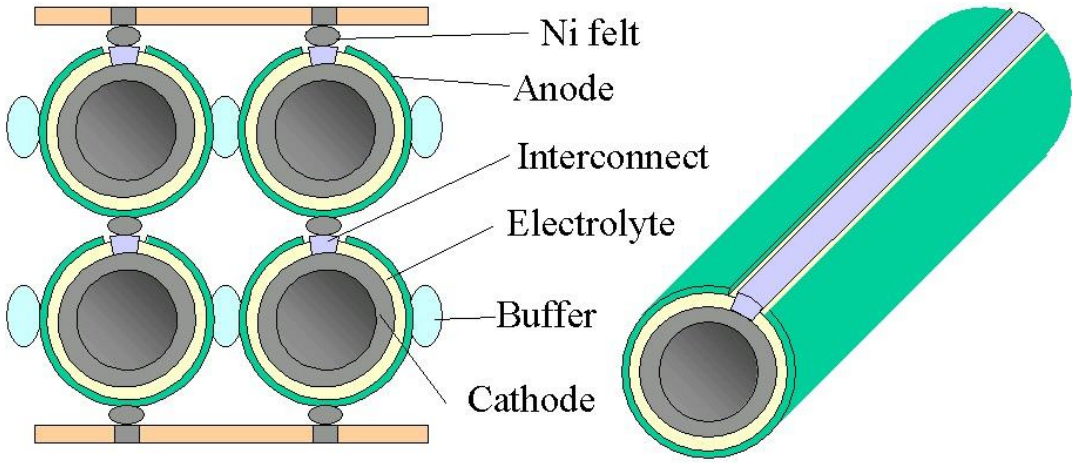


Figure 1.5 Tubular design of SOFCs. Image is taken from reference [12].

Another important type of SOFC configuration is tubular. As illustrated in Figure 1.5, outside of one electrode is electrolyte and another electrode in order. Generally, one electrode is fabricated into a long tube by extrusion and sintering, and then the other components are deposited as a thin layer on the electrode tube. The main advantage of this type of SOFC configuration is the elimination of gas-tight seal problem and mechanical strength. However, the cell internal resistance and gas diffusion are the limiting factors of this design [13].

The development of SOFCs can be divided into three stages according to operating temperature. The earlier SOFCs were based on electrolyte-supported fuel cells, which contain a thick yttria-stabilized zirconia (YSZ) layer as electrolyte, operated at high temperature up to 1000$^{o}$C [14]. The next generation involves an electrode-supported fuel cell operating at intermediate temperature (600-800$^{o}$C), and is the most widely studied at present. The benefits of lowering the operating temperature can be summarized in the following ways: 1) increasing the choice of materials, such as using metallic interconnect; 2) the lower constraints imposed by the cell components and seals; 3) improved stability and durability [15,16]. Moreover, an anode-supported fuel cell is preferred due to the higher diffusivity of hydrogen than that of oxygen through the electrodes with a similar porosity at intermediate temperatures [17,18], which will decrease the diffusion losses of the whole fuel cell. The third generation tends to be metal-supported cells, which provide significant advantages over conventional ceramic cells including low material cost, ruggedness, and tolerance to rapid thermal cycling and redox cycling [19]. They are believed to achieve a good performance at lower temperature around 500-600$^{o}$C as an alternative to the anode- and electrolyte-supported cells [20~22].

## 1.3 Electrolyte materials for SOFCs

The electrolyte in SOFCs serves as a separator between the fuel and the oxidant and an ionic conductor from the cathode to the anode. In terms of its function, the electrolyte should satisfy several needs, including efficient ionic conductivity, negligible electronic conductivity and good chemical stability over a broad range of oxygen partial pressure and temperature.

Currently, 8mol.% yttria-stabilized zirconia (YSZ) known as fluorite structure is widely used as SOFC electrolyte due to excellent ionic conduction at 1000°C and chemical stability under redox condition. The dopant of the yttria serves two roles [23]: it stabilizes the high temperature cubic phase in zirconia and also generates oxygen vacancies through the following defect reaction, as written in Kroger-Vink notation:

$$Y_2O_3 \xrightarrow{ZrO_2} 2Y'_{Zr} + 3O^{\times}_{O} + V^{\bullet\bullet}_{O} \qquad \text{(Equation 1.7)}$$

The high ionic conductivity is attributed to the produced oxygen ion vacancies, which are created by doping with $Y_2O_3$. It has been reported that the highest conductivity levels can be achieved by doping yttria in $ZrO_2$ at the range of 8-11mol.% [24]. The further addition could increase the association of the oxygen vacancies into complex defects of low mobility, and therefore decrease the ionic conductivity. The ohmic resistance from the thick YSZ electrolyte will cause a significant decrease of power density at intermediate temperature due to the insufficient ionic conductivity. In addition, chemical reaction between YSZ electrolytes with the cathode materials to produce insulating phases is generally of greatest concern [25]; for example, the most commonly used cathode material, $La_{1-x}Sr_xMnO_3$ (LSM), in a combination with YSZ electrolyte, can react with YSZ to produce the electronically insulating phases at high temperature. In terms of the strontium content in the A-site stoichiometric LSM, the LSM/YSZ ratio and the temperature, two zirconate phases, i.e., the pyrochlore $La_2Zr_2O_7$ and the perovskite $SrZrO_3$, would form at the interface between LSM and YSZ [26~32].

To decrease the resistance from the YSZ electrolyte, two methods can be employed: either decreasing the thickness of YSZ electrolyte or using new materials exhibiting a high ionic conductivity at lower temperature, such as Gd-doped ceria (GDC/CGO) [33] and lanthanum strontium gallium magnesium oxide ($La_{1-x}Sr_xGa_{1-y}Mg_yO_{3-\delta}$, referred to as LSGM) [34]. Based on the conductivity data in Figure 1.6, LSGM and GDC are preferable for being operated at the intermediate temperature. In addition, GDC has a better chemical stability with high-performance cathode materials, such as $La_{1-x}Sr_xCoO_3$ [35~37], compared with YSZ. However, GDC electrolyte when exposed to reducing conditions at high temperature, exhibits electronic conductivity

and therefore provides a short-circuit pathway [38], which reduces the efficiency of SOFCs [39]. Furthermore, lattice expansion from the chemical state change between $Ce^{4+}$ and $Ce^{3+}$ in the reducing atmosphere can cause cracks and delamination [40], resulting in cell degradation.

The conductivity of LSGM is comparable to GDC and much higher than YSZ. LSGM does not have an easily reducible ion, like $Ce^{4+}$, and thus is superior to GDC for use in the reducing conditions [25]. However, it has been found difficult to synthesize a pure phase electrolyte material of LSGM, and the cathode and anode materials suitable for LSGM need further development.

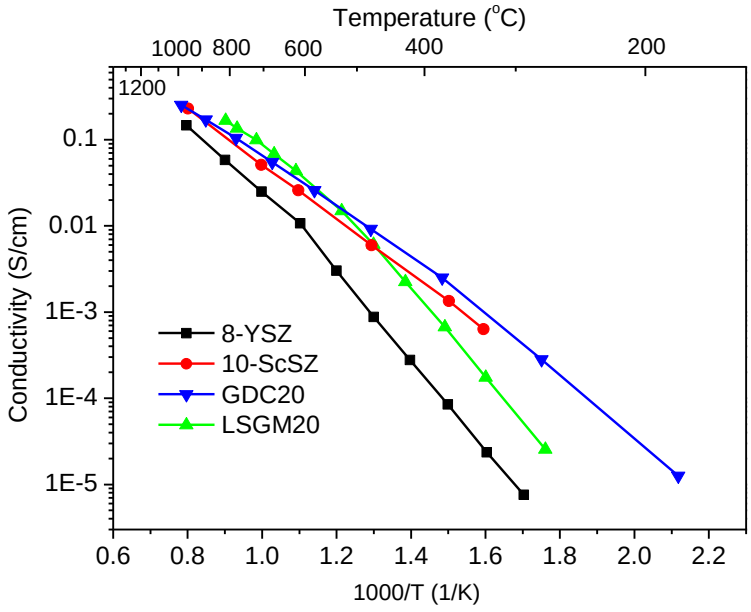


Figure 1.6 Comparison of the conductivity data for various ionic conductors: 8-YSZ (8mol.% $Y_2O_3$ doped $ZrO_2$) [41], 10-ScSZ (10mol.% $Sc_2O_3$ doped $ZrO_2$)[42], GDC20 ($Gd_{0.2}Ce_{0.8}O_{1.9}$) [42] and LSGM20 ($La_{0.2}Sr_{0.8}Ga_{0.85}Mg_{0.15}O_{3-\delta}$) [43]

Scandia stabilised zirconia (ScSZ) also gives a high conductivity in intermediate temperature, as shown in Figure 1.6. This can be attributed to a smaller mismatch in size between $Sc^{3+}$ and $Zr^{4+}$, as compared to that between $Y^{3+}$ and $Zr^{4+}$, decreasing energy for defect association and thus increasing conductivity [44]. However, ScSZ was not widely used as the SOFC electrolyte material because of its phase transition and conductivity degradation under operating temperature of SOFCs. Therefore, in

order to decrease the ohmic loss, a thin film of YSZ electrolyte, typically 40-60μm in thickness, was employed in this study.

## 1.4 Cathode materials for SOFCs

The cathodes for SOFCs as the sites for oxygen reduction need to meet the following requirements [45]: 1) high electronic conductivity (preferably more than 100S/cm under oxidizing condition); 2) matched thermal expansion coefficients (TECs) with electrolyte materials; 3) good chemical compatibility with other cell components; 4) sufficient porosity for the gaseous species to diffuse to triple phase boundaries (TPBs); 5) good stability in oxidizing condition; 6) high catalytic activity for oxygen reduction.

Strontium-doped lanthanum manganite (LSM) has been known as the most commonly used cathode material, where substitution of lower valent strontium for lanthanum enables to increase the content of $Mn^{4+}$ in oxidizing atmospheres and therefore enhances the electronic conductivity. However, the Sr dopant does not increase the oxygen vacancies, which can be explained by the following equation:

$$SrO + Mn_{Mn}^{\times} \xrightarrow{LaMnO_3} Sr_{La}^{'} + Mn_{Mn}^{\bullet} + O_O^{\times} \qquad \text{(Equation 1.8)}$$

This reaction increases the electron-hole concentration and therefore improves the electrical conductivity under oxidizing atmosphere; however, this reaction also suggests that LSM lacks sufficient oxygen ionic conductivity. So the reduction of oxygen in LSM is restricted to the interface between the electrolyte and the LSM cathode, where oxygen, electrolyte and cathode are in intimate contact. The limitation of reaction sites has a great impact on the cell performance when using single phase LSM as cathode.

The addition of ionic conductor, such as YSZ, to LSM cathodes has been reported to show a better performance than those composed of single phase LSM, since the TPBs for reduction of oxygen have been extended into the composite cathode three-dimensionally [46~49]. In general, the LSM-YSZ composite is prepared by screen-printing onto the YSZ electrolyte with the inks that contain the LSM, YSZ and pore formers, followed by a calcination step to sinter the cathode onto the electrolyte [50].

The calcination temperature should be high enough to yield good LSM particle percolation but not so high as to cause substantial particle coarsening and densification [51]. Choi et al. [52] reported that the optimal firing temperature for the LSM-YSZ composite was 1100$^{o}$C, when the composite offers the optimum cathodic performance by compromising the interfacial resistance and the TPB sites. In addition, infiltration of the nanoparticles of LSM into the porous YSZ backbone has been demonstrated as an effective method to produce the connected electronic and ionic transporting networks for SOFC cathodes [50,53~56].

Another way to improve the cathode performance is to replace LSM with mixed ionic electronic conductors (MIECs), such as strontium-doped $LaCoO_3$ (LSC) [35,57,58], $LaFeO_3$ (LSF) [59~61] and $LaCo_yFe_{1-y}O_3$ (LSCF) [62~64]. They show high electronic and ionic conductivity at intermediate temperature as well as electrocatalytic activity for the reduction of oxygen, therefore reducing the polarization losses. LSCF series show an intermediate performance between LSC and LSF. Their electronic conductivity, ionic conductivity and also the thermal expansion coefficients (TECs) are listed in Table 1.2.

Table 1.2 Comparison of the electronic and ionic conductivity (S/cm) at 800$^{o}$C in air, and TECs ($10^{-6}K^{-1}$) of LSC, LSF and LSCF

| | Typical composition | Electronic conductivity | Ionic conductivity | TEC |
|---|---|---|---|---|
| LSC | $La_{0.6}Sr_{0.4}CoO_{3-\delta}$ | Over 1000 [65] | 0.22 [66] | 25.0 [67] |
| LSF | $La_{0.6}Sr_{0.4}FeO_{3-\delta}$ | 128 [67] | $5.6\times10^{-3}$ [67] | 13.4±0.4 [68] |
| LSCF | $La_{0.6}Sr_{0.4}Co_{0.2}Fe_{0.8}O_{3-\delta}$ | Around 300 [69] | $8\times10^{-3}$ [67] | 13.2 [70] |

LSC is an attractive cathode material for intermediate temperature SOFCs (below 800$^{o}$C) because of the higher electronic and oxygen ionic conductivity, and higher catalytic activity for oxygen incorporation reaction than LSM [71]. However, the mismatch of thermal expansion coefficients (TECs) between LSC and the typical SOFC electrolytes, such as YSZ and doped ceria (11-12$\times10^{-6}K^{-1}$) could result in

cracking and delamination of cell components due to the stress developed during fabrication and operation [72]. Moreover, a highly reactivity between YSZ electrolyte and LSC cathode forming insulting phases, such as $La_2Zr_2O_7$ and $SrZrO_3$, is another drawback hindering its development [61,73] when using YSZ as electrolytes. In order to minimize the mismatch of TECs between the LSC and electrolyte materials, the efforts have been made by incorporating LSC into ceria-based cathode backbone to form a composite cathode [71,74] on ceria-based or LSGM electrolytes.

Despite the lower electronic and ionic conductivity than LSC, LSF exhibits a closely matched TEC with commonly used electrolyte materials [68], such as YSZ and GDC, and no detrimental reaction occurs between LSF and YSZ [75] under sintering conditions.

In order to achieve a desirable electrochemical performance, along with chemical and mechanical compatibility with electrolyte materials such as YSZ and GDC, the combination of LSC and LSF was proposed by incorporating strontium in the A site and cobalt in the B site on the perovskite $LaFeO_3$, known as $La_{1-x}Sr_xCo_yFe_{1-y}O_3$ (LSCF). Previous research [76~79] has shown that the properties, such as ionic and electronic conductivity, TEC and reactivity with the YSZ electrolyte are related with the composition, namely the content of Sr and Co. The electrical and ionic conductivities increased with increasing Sr and/or Co content, and they show the highest value for the composition $La_{0.2}Sr_{0.8}Co_{0.8}Fe_{0.2}O_3$. However, the increasing Sr and Co content causes an increase in thermal expansion $>26\times10^{-6}K^{-1}$, which is not compatible with the commonly used electrolytes. Therefore the composition with $0.2<x<0.4$ and $y<0.5$ seem to be more attractive as cathode material for SOFCs. Moreover, in order to prevent the undesired chemical reactions between LSCF cathode and YSZ electrolyte, two effective methods have been investigated: to employ GDC as an interlayer [63,64] or prepare the cathode at the low temperature [80,81]. It has been reported that no impurity phase is observed when LSCF is formed on the YSZ skeleton after firing at $800^oC$ [81].

## 1.5 Anode materials for SOFCs

### 1.5.1 Requirements for anode

Based on the operation principle and laminated structure, an anode material must meet some requirements to function efficiently [82]:

1) High electronic conductivity. The electrons produced from oxidation of fuel on the triple phase boundaries (TPBs) on the anode, where electrons, oxygen ions and fuel meet together and react, need to be transported to the external circuit. The thicker the anode layer is, the longer distance electrons travel through the anode to current collector and therein the higher electronic conductivity the anode requires.

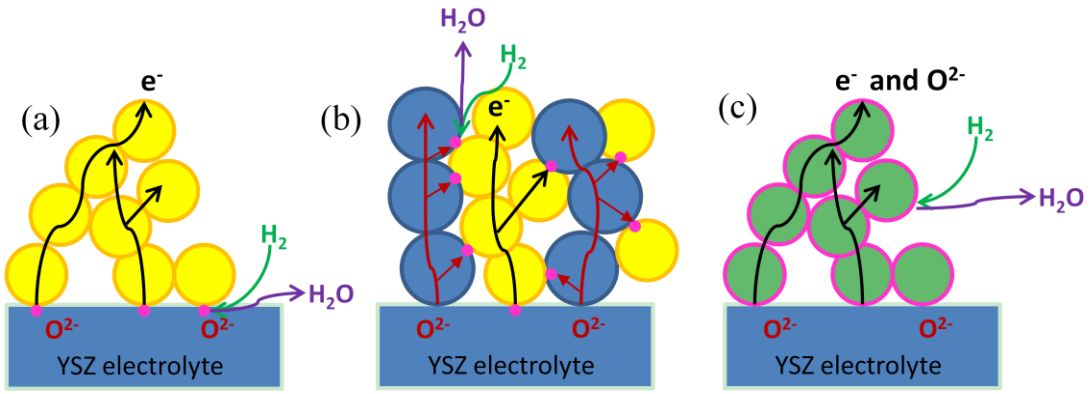


Figure 1.7 Schematic of the sites where the electrochemical reaction occurs for different types of anode: (a) metal, (b) Ni-YSZ cermet and (c) MIEC. The yellow, blue and green spheres represent Ni, YSZ and MIEC particles, respectively. The pink areas indicate TPBs where the oxidation of fuel takes place.

2) High oxygen ionic conductivity. Three types of materials have been employed as anode for SOFCs: metal (such as Pt and Ni), Ni-YSZ cermet and mixed ionic and electronic conductor (MIEC, such as Gd-doped ceria). Take metal anode as example, as shown in Figure 1.7(a), the electrochemical reaction only takes place at the interface of electrolyte/anode (1-D). For the Ni-YSZ as anode, the TPBs spread out over the Ni/YSZ particle interface within the bulk anode (in Figure 1.7(b)). When MIEC being used as anode, the electrochemical reaction is more likely to occur at the surface area of anode particles (2-D) as the fuel reaches, shown in Figure 1.7(c). It is

clear that the sites where the electrochemical reaction occurs are increased significantly by applying mixed ionic electronic conductor as anode.

3) High catalytic activity for the oxidation reaction of the fuel. The oxidation of hydrogen and hydrocarbon on the anode begins with a chemisorption and dissociation, then followed by a reaction of the products from the dissociation with $O^{2-}$ from the electrolyte [83]. The catalyst plays an important role in facilitating these reactions to occur.

4) Chemical stability. The anode is required to be chemically stable not only in the reducing and oxidizing atmospheres, but also with the electrolyte and current collector in contact with anode.

5) Thermal compatibility with the contacting components. The thermal expansion of the anode must match that of the electrolyte and current collector during heating stage and reduction-oxidation (redox) cycles. Otherwise, the delamination and cracking of the cell components can be induced by the mismatch, resulting in failure for operation of the fuel cell.

6) Porosity. Because the gaseous species must transport to the TPBs of the anode and meet the electron and oxygen ions, the anode need to retain a porous structure during operation to allow the fuel into and the products out of the anode.

### 1.5.2 Ni-YSZ cermet anodes

For SOFCs based on YSZ electrolyte, Ni(O)-YSZ cermets are the-state-of-the-art materials for anode [84,85]. In this composite, YSZ phase acts as a supporting matrix for metal phase, ensuring a uniform dispersion of nickel particles and inhibiting coarsening of nickel [86]; the Ni phase provides the electronic conducting pathways and catalytic activity for hydrogen oxidation.

Because the TECs of Ni metal and NiO are $16.9\times10^{-6}$ and $14.2\times10^{-6}/^{o}C$ [87], respectively, much larger than that of YSZ ($10.9\times10^{-6}/^{o}C$) [88], which has potential to cause mechanical stresses on the cells, especially upon thermal cycles, lowering Ni content will effectively decrease thermal expansion of anode and make it more

compatible with YSZ electrolyte. However, the conductivity would be decreased with increasing loading of YSZ [89]. A lot of work has been undertaken for optimization of the ratio between Ni and YSZ [84,86,90]. Based on the conductivity and TEC of Ni-YSZ pellets with different content of Ni (vol.%) [86] listed in Table 1.3, nickel-YSZ cermets with 30-50vol.% Ni are more attractive anode materials.

Table 1.3 Electrical conductivity (S/cm) at 900°C and TEC ($\times 10^{-6} K^{-1}$) of Ni-YSZ containing 15-50vol.% Ni [86]

| Ni content (vol.%) | Conductivity | TEC (room temperature-900°C) |
|---|---|---|
| 15 | 0.103 | 10.40 |
| 30 | 40.00 | 11.64 |
| 50 | 989.00 | 13.20 |

Typically, the porosity in the Ni(O)-YSZ anode is achieved by the reduction of NiO under reducing atmosphere; however, the transition of Ni/NiO upon reduction and redox cycles tends to cause bulk expansion of the cermet structure [91,92], breaking the electrolyte and weakening the mechanical strength of the cell [93]. Therefore, it is necessary to control the Ni/YSZ ratio and distribution in terms of electrochemical and mechanical properties.

Long-term operation at intermediate (500-800°C) or high temperature (>900°C) is necessary for SOFC application. The microstructural change is considered as the dominant factor for the degradation of Ni-YSZ cermet anodes, reflected mainly by the agglomeration and particle coarsening of the metallic Ni [94]. This could result in the reduction of triple phase boundary (TPB) and electrical conductivity by loss of nickel percolation, and subsequently, causing a significant increase in the electrode polarization resistance for the oxidation reaction of fuels [95]. Simwonis et al. [94] studied the relationship between the electrical conductivity and nickel particle size of Ni-YSZ samples in reducing atmosphere. They found an increase of 26% in average nickel particle size and a decrease up to 33.3% in electrical conductivity for Ni-YSZ anode after being exposed in 4% $H_2$/3% $H_2O$/Ar at 1000°C for 4000h. Performance degradation test was also carried out on Ni-YSZ anode supported cells at 850°C with

air and humidified $H_2$ (3% $H_2O$) as oxidant and fuel, respectively [96]. The results show that both the cell voltage decay and the Ni growth appear to reach a plateau after about 800h operation, presenting a strong relationship between degradation and the coarsening of Ni particles occurring in the anode.

When using hydrocarbon fuels, more disadvantages can be found on Ni-YSZ anodes, such as low tolerance to sulphur poisoning [97] and carbon deposition [98,99], besides the redox instability and nickel coarsening mentioned above. Sulfur is a common compound in conventional and low-cost hydrocarbon fuels. Upon reforming, sulfur compounds are converted into hydrogen sulphide ($H_2S$), which inhibits the rapid catalysis of nickel-YSZ anode, leading to a drastic drop of cell performance and lifetime [100]. One hypothesis has been generally acknowledged that the sulfur poisoning is caused by the strong adsorption of the elemental sulphur on Ni surface, which blocks the active sites for oxidation of fuel and degrades the cell performance [90,100~103].

Carbon is another harmful species that can deposit on the metal surface and block the reaction sites at the triple phase boundary (TPB), increasing the mass transport resistance and reducing the cell performance [104,105]. Buccheri et al. [106] conducted the cell testing in dry methane at 750$^oC$ on electrolyte- and anode-supported Ni-YSZ/YSZ/Pt cells: a remarkable degradation is observed for both cells possibly due to carbon damaging the anode and blocking pores. The Ni-YSZ supported cells have shown a rapid degradation from 1.0V to zero in dry methane at 100mA/$cm^2$ within 10h operation due to coking [107]. However, the carbon deposition might be oxidized at high current density due to sufficient oxygen supply from ionic conductor, presented as reversible carbon deposition [99].

### 1.5.3 Modified Ni-YSZ based anodes

Two approaches have been proposed to solve the problems of Ni-YSZ cermet anode stated above [108]: one is to replace Ni by other catalytic materials and the other is to modify the existing structure by alloying Ni with less active elements or decorating Ni surface with lower surface energy oxides.

Since Cu is known to be a poor catalyst for C-C bond breaking and formation, Cu has been considered as an alternative to Ni for SOFC anode. Although Cu-YSZ cermets were found to be stable in hydrocarbon environments, they exhibited low performance for direct oxidation of hydrocarbon [109,110]. The Cu-YSZ anode performance can be significantly improved by addition of ceria due to its catalytic property and ionic conductivity [111]; however, agglomeration and growth of Cu particles is still the dominant factor for performance degradation in hydrogen [112].

The partial substitution of Ni with other metals is believed to be an alternative to reduce coarsening of the metallic particles and also achieve good performance. Ringued é et al. [113~115] have successfully prepared homogeneous mixture of nanocrystalline powders of (Ni, Co)-YSZ, (Ni, Cu)-YSZ and (Ni, Fe)-YSZ by combustion synthesis from mixtures of molten nitrates and urea. After reduction at 973K, the Cu-Ni mixtures in the porous YSZ scaffold formed single-phase alloys [116] and showed an excellent tolerance for carbon formation in dry methane at 1073K [117]. Especially, Cu (80%)–Ni (20%) cermet showed a significant increase in power density with time during operation in dry methane for 500h due to enhanced electronic conductivity in the anode [117]. The same behaviour has been observed in Cu electroplated Ni-YSZ cermet anode: Cu-Ni-YSZ anode supported single cell shows a slightly lower performance but a more enhanced durability in methane than those of Ni-YSZ anode supported single cell [118]. Compared with Ni-SDC ($Ce_{0.8}Sm_{0.2}O_{1.9}$) anodes, tri-metal alloys $Fe_{0.25}Co_{0.25}Ni_{0.5}$-SDC ($Ce_{0.8}Sm_{0.2}O_{1.9}$) anodes show a higher power density and a lower polarization resistance [119]. So far, the improved electrochemical performance has been attributed to the alloy formation and surface reconstruction effects of the binary/ternary electrocatalysts.

The surface modification on the Ni-YSZ surface with low-energy oxides, such as $Nb_2O_5$ and $CeO_2$, can effectively improve the sulphur tolerance on the anode [120~122]. A thin layer of the ceria or $Nb_2O_5$ nanoparticles on the Ni-YSZ anode surface can react with $H_2S$ as a sulphur sorbent to form oxysulfide, which prohibits the absorption of sulphur by nickel to form the harmful phase $Ni_3S_2$. Compared with the bare Ni-YSZ anode, the modified Ni-YSZ anode demonstrates a more stable performance over 500 hours when exposed to the sulphur-containing $H_2$ fuel [123].

### 1.5.4 $SrTiO_3$ (STO)-based perovskite anodes

Since the drawbacks of Ni-YSZ cermet anodes restrict the development and application for SOFCs, some alternative anode materials have been extensively studied and reported. One of the most promising anode materials is titanate perovskite with general formula $ABO_3$ because of the multiple oxidation states of titanium ($Ti^{4+}/Ti^{3+}$) providing a high electronic conductivity under reducing conditions. Of the available titanates, strontium titanium oxide, $SrTiO_3$ (STO) has been extensively reported in the early literatures. As illustrated in Figure 1.8, the Sr atoms occupy the body centres and $TiO_6$ octahedra take all the corners of every cube, which gives the Sr atom 12-fold oxygen coordination and the Ti atom 6-fold oxygen coordination. In 1953, the conductivity of strontium titanate was first reported revealing a very strong dependence of the material's electrical properties on its state of reduction [124]. However, even in reducing conditions, pure STO shows a very low electronic conductivity, which has prevented its applications as anode material for SOFC.

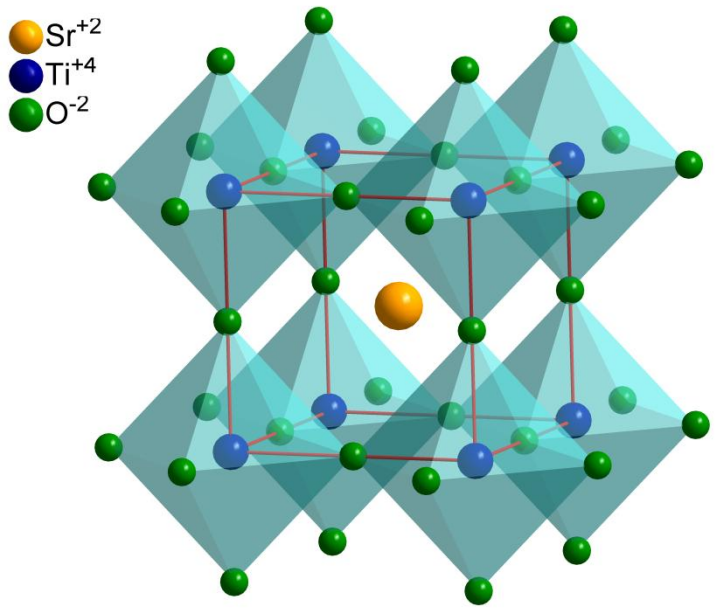


Figure 1.8 The cubic structure of $SrTiO_3$

### 1.5.4.1 A-site doped $SrTiO_3$

Strontium titanate can be converted into a highly semiconducting material by doping with higher valent cation on the Sr site [125~127]. Promising results have been achieved with lanthanum strontium titanate (LST). In order to maintain the electro-neutrality the substitution of $Sr^{2+}$ with $La^{3+}$ can be compensated by introducing the extra oxygen beyond the $ABO_3$ stoichiometry under oxidizing conditions, defined as 'oxygen excess' as in the formula $La_xSr_{1-x}TiO_{3+x/2}$ or creating A-site vacancies, as in $La_xSr_{1-3x/2}TiO_3$, named 'A-site deficient' [128]. The high conductivity in reducing conditions for A-site deficient sample can be explained by the following equations:

$$Sr_{Sr}^{X} + O_O^X \leftrightarrow V_{Sr}^{''} + V_O^{\bullet\bullet} + SrO \qquad \text{(Equation 1.9)}$$

$$O_O^X \leftrightarrow V_O^{\bullet\bullet} + 2e' + \frac{1}{2}O_2 \qquad \text{(Equation 1.10)}$$

The large value of $V_{Sr}^{''}$ reduces the number of intrinsic Schottky defects pushing Equation (1.9) towards left and hence reducing $V_O^{\bullet\bullet}$. Equation (1.10) would shift right to oppose the change, facilitating the removal of lattice oxygen and the associated generation of free electrons [129]. In this case, the substitution of $La^{3+}$ and the subsequent increase of A-site deficiency greatly promote the formation of free electrons. It has been found that A-site deficient strontium titanate have higher conductivity than the corresponding stoichiometric sample in reducing condition [130~132]. Reduced composition of A-site deficient La-doped $SrTiO_3$ have shown conductivities as high as 100S/cm at 800$^oC$ in 4% $H_2$/Ar [133]. Moreover, A-site deficient samples have been found to show a close thermal expansion coefficient with YSZ electrolyte, high chemical stability under oxidizing and reducing atmosphere, and low tendency to react with zirconia electrolytes forming $SrZrO_3$ [134,135 ]. Considering these properties, A-site deficient doped strontium titanate reduced at high temperature is more likely to be considered as a good anode candidate.

It is clear that A-site lanthanum doping significantly improves the electronic conductivity but is coupled with a low ionic conductivity and a poor catalytic activity towards the oxidation of fuels, which limits its performance as anode. This can be

illustrated by the poor performance for the cells using LST as anode [136~138]. In order to achieve a good combination of ionic and electronic conductivity, the cells with LST and YSZ as anode matrix phase was investigated for the potential use as anode for SOFCs [139~141].

Moreover, the catalytic activity for hydrogen oxidation can be optimized significantly by the incorporation of various transition metals, as well as ceria to porous ceramic anodes. The use of nickel has been found to improve the cell performance significantly, with an almost five times increase in the maximum powder density observed in an LST-GDC anode at 800$^o$C in 97% $H_2$+3% $H_2O$[142]. When $CeO_2$ and Ni were used as impregnates, a remarkable improvement of the anode performance was observed compared with the anode using pure lanthanum strontium calcium titanate ($LSCT_{A-}$) or impregnated with ceria only at 900$^o$C in pure hydrogen with 1% $H_2O$ [143,144]. The amount of catalyst incorporation into a porous anode can also have an important effect on the fuel cell performance. The cermet of 10wt.% Ni/YST-YSZ showed the minimal polarization resistance among nickel concentrations ranging from 5 to 50wt.% and stable cell performance even after five consecutive redox cycles operated at 1000$^o$C in humidified hydrogen (0.6% $H_2O$) [145]. Sun and Fan et al. [136,146] have also found that the addition of ceria/GDC can significantly improve the anode structure, and thus fuel cell performance. A-site deficient $Y_{0.07}Sr_{0.895}TiO_{3-\delta}$ (YST) with infiltration of 3wt.% NiO exhibited a cell performance of over 1.0Acm$^{-2}$ at 0.7V and 800$^o$C in dry hydrogen, which already reached the practical application level [147]. Recently, the nano-scale electrocatalytic active particles exsoluted from the doped LST matrix is regarded to be an effective way to promote the anode performance dramatically and prevent the sintering and agglomeration of nanoparticles under redox cycles and operation at high temperature [148~153].

While nickel is found to show the highest catalytic activity for oxidation of hydrogen, other metals are also found to present sufficient catalytic activity and good resistance against sulphur poisoning especially combined with ceria or gadolinia-doped ceria (GDC). Savaniu et al. [154~157] have studied $La_{0.2}Sr_{0.7}TiO_3$ anode impregnated with 20mol.% GDC and copper, demonstrating that power densities in excess of 0.5Wcm$^{-2}$ can be achieved at 750$^o$C using humidified hydrogen (3% $H_2O$) as fuel. Kurokawa et

al. [158] have reported that the ceria- and Ru-infiltrated YST-YSZ anode showed a high sulphur tolerance in 10-40ppm $H_2S$ and drastically decreased the polarization resistance from 2.9Ωcm$^{-2}$ for the non-infiltrated cell to 0.5Ωcm$^{-2}$ at 800$^{o}$C in 3% humidified hydrogen. The combination of ceria and Pd has been demonstrated as an effective catalyst to improve the cell performance on LSTM ($La_{0.4}Sr_{0.6}Ti_{0.8}Mn_{0.2}O_3$) [159,160] and LST-YSZ [161] anode. Samaria-doped ceria (SDC) is also discovered to be more effective in both electrical conductivity and electrocatalytic activity towards the oxidation of fuels than YSZ, resulting in a relatively higher performance of 140mWcm$^{-2}$ for Ni/YST-SDC compared with that of Ni/YST-YSZ (115mWcm$^{-2}$) in 1000$^{o}$C using humidified $H_2$ (3% $H_2O$) as fuel [162].

### 1.5.4.2 B-site doped $SrTiO_3$

Many efforts have also been devoted to enhancing the electronic conductivities of $SrTiO_3$ materials by the replacement of Nb in B site. The substitution of pentavalent $Nb^{5+}$ for the host cation $Ti^{4+}$ has been reported to drastically enhance the electronic conductivity by an increased electronic compensation due to the formation of $Ti^{3+}$ and $Nb^{4+}$ [ 163 , 164 ]. Blennow et al. [ 165 ] studied Nb-doped $SrTiO_3$, (STN, $Sr_{0.94}Ti_{0.9}Nb_{0.1}O_{3-\delta}$) as a SOFC anode material in terms of electrochemical properties and redox stability, showing a promising redox stability feature. However, the ionic conductivity of STN pre-reduced at 980$^{o}$C was insufficient as an anode when compared with the composite electrode of YSZ and STN. As expected, the electrochemical performance of the anode was greatly improved with increasing Ni-CGO loadings, and showed a strong dependence on the structural parameters of the electrode (porosity, pore size etc.) [166]. Similarly, Ni-CGO infiltrated STN:FeCr composite anode showed a comparable performance and promising durability properties; 0.7A/cm$^2$ was recorded under 0.6V at 650$^{o}$C in 4% humidified hydrogen for the button cell with active surface area of 0.5cm$^2$ [167]. Ramos et al. [168] reported a preliminary comparison of the impact of catalyst M: Ni, Pd, Ru on the impedance and stability of M/GDC co-infiltrated STN/YSZ SOFC anodes. They found that the total polarization resistance ($R_p$) decreased in the order Ni/GDC >> Pd/CGO > Ru/CGO and Ru/CGO stayed reproducibly around 20mΩcm$^2$ over 200h at 850$^{o}$C, 50% $H_2O/H_2$, while Ni/CGO degraded by a factor of 3 in an equivalent period.

An alternative approach has been proposed by partially substituting the reducible lower-valence transition metal cations for the $Ti^{4+}$ cations, which may not only improve the electronic conductivity, but also introduce oxygen vacancies that lead to significant ionic conductivity [169]. Rothschild et al. [170] studied the electronic structure, defect chemistry, and transport properties of mixed ionic electronic conducting $SrTi_{1-x}Fe_xO_{3-y}$ (STF): STF exhibited mixed ionic and electronic conductivity at elevated temperatures, with a predominant transformation from p-type conductor at high oxygen partial pressure (cathode condition) to n-type conductor at low oxygen partial pressure (anode condition). The test of an LSGM electrolyte-supported cell with $SrTi_{1-x}Fe_xO_{3-y}$ (x=0, 0.4 and 0.7) mixed with GDC as anode, $La_{0.4}Ce_{0.6}O_2$ as barrier layer and LSCF as cathode indicates that the Fe-containing anodes yielded much lower total cell resistance and higher performance than $SrTiO_3$ [169]. A maximum power density of $337mW/cm^2$ can be achieved for the $SrTi_{0.3}Fe_{0.7}O_{3-\delta}$-GDC anode cell with thick LSGM electrolyte (0.6mm) at $800^oC$ in ~3% $H_2O$/97% $H_2$.

### 1.5.4.3 A- and B-site co-doped $SrTiO_3$

In recent years, (La)$SrTiO_3$-based oxides doped with various transition metal elements (Cr, Co, Mn, Ni, Mg etc.) on the B site have also been developed in order to optimize the electronic and/or ionic conductivity. It is generally acknowledged that donor doping in the Sr site tends to increase the electrical conductivity, while acceptor doping in the Ti site has the possibility to improve the ionic conductivity [127,130]. In addition, B-site transition metal may provide the catalytic activity to promote the fuel-oxidation processes.

Danilovic et al. [ 171 ] have investigated a series of perovskite oxides $La_{0.75}Sr_{0.25}Cr_{0.5}X_{0.5}O_{3-\delta}$ (LSCX, X=Co, Fe, Ti, Mn) as solid oxide fuel cell electrocatalysts. The Ti-containing composition showed the minimum fuel cell performance in methane and hydrogen due to the lowest catalytic conversion for fuels from Ti among all the doped transition metals, while all the compositions provided the sufficient electronic conductivity in reducing atmosphere. In addition, it was found that the cell performance can be considerably improved by the addition of GDC,

at least due to the additional ionic conductivity imparted by the mixed conductor GDC.

It has been known that the general trend of catalytic activity for the transition metals is found to be in the order Co > Mn > Cr on the oxidation-reduction process [127,172]. The effect of Co doping in YST (YSTCo) on the electrical and ionic conductivity has been studied [173]. It was well noted that the addition of Co in LST or YST improves remarkably the ionic conductivity and catalytic activity for fuel oxidation of A-site doped $SrTiO_3$, making it a potential candidate for SOFC anode. The electrical conductivities of YSTCo samples decrease with Co-doping amount, while the ionic conductivities increase up to 4mol.% Co doped in B site. At 800$^o$C in 5% $H_2$-Ar atmosphere, 4mol.% Co-containing composite exhibited a total electrical conductivity of 20S/cm and an ionic conductivity of $1.6\times10^{-3}$S/cm. Yoo et al. [172] have found that 1-2mol.% Co doping in LST (LSTCo) reduced significantly the polarization resistance and improved the stability under operation. An encouraging performance of 250mW/cm$^2$ at 800$^o$C using 97% $H_2$ + 3% $H_2O$ as fuel was achieved for Ni-impregnated LSTCo-GDC anode on LSGM electrolyte-supported cell. Similar results have also been found by Cui et al. [153]; they reported that after pre-reduction at 900$^o$C in reducing condition, both LST and LSTCo were active for the oxidation of hydrogen, and the Co substitution significantly improved the cell performance (230mW/cm$^2$ for LSTCo vs 90mW/cm$^2$ for LST at 900$^o$C in pure hydrogen).

The substitution of Mn on the Ti site for LST (LSTM) can also improve its catalytic activity and stabilize the perovskite lattice by Mn valence (+4, +3, +2) change with the oxygen partial pressure [ 174 ~ 176 ]. While possessing adequate electronic conductivity, LSTM presents a very low ionic conductivity that is insufficient to obtain a reasonable TPB length as a functional SOFC anode [177]. Therefore, it is necessary to use a composite of LSTM and YSZ in anode application. Although a higher performance of LSTM-YSZ than LST-YSZ anode at 800$^o$C was achieved [140], the addition of $CeO_2$ could decrease significantly the polarization values of LSTM-YSZ anode because of the catalytic activity as well as the extended TPBs with LSTM by creating more electronic percolation paths [159,160].

The pure phase La and Cr co-doped $SrTiO_3$ (LSTC, $La_{0.3}Sr_{0.55}Ti_{1-x}Cr_xO_{3-\delta}$) was synthesized using citric acid-nitrate process with a chromium dopant up to 20mol.% [178]. But the electronic conductivity of $La_{0.3}Sr_{0.55}Ti_{0.8}Cr_{0.2}O_{3-\delta}$ pellet need to be further improved if LSTC is considered as an anode material. Du et al. [137] studied the electrical conductivity and redox stability of $La_{0.3}Sr_{0.7}Ti_{1-x}Cr_xO_{3-\delta}$ synthesized by conventional solid-state reaction method and then sintered in 5% $H_2$/Ar at 1500$^o$C for 10h. It was found that the total electrical conductivity decreased with Cr doping level (230S/cm for LST vs 53S/cm for x = 0.2 composition at 800$^o$C in 5% $H_2$-Ar), which can be attributed to the reduction in the concentration of charge carrier from the direct substitution of $Cr^{3+}$ for $Ti^{3+}$.

## 1.6 Direct oxidation of hydrocarbon

The direct utilisation of hydrocarbon fuels is one of the most attractive advantages for SOFCs, because the use of natural gas could save the investment on infrastructure for $H_2$. Upon operation, the oxygen anions migrate through the ionic conducting electrolytes from the cathode to the anode where the direct oxidation of fuels occurs. For example, alkane, $C_nH_{2n+2}$ is used as fuel with the reaction as follows:

$$C_nH_{2n+2} + (3n+1)O^{2-} \rightarrow nCO_2 + (n+1)H_2O + (6n+2)e^- \quad \text{(Equation 1.11)}$$

The reduction of oxygen takes place at the cathode side with the electrons supplied by the external circuit from the anode in terms of the following reaction:

$$O_2(g) + 4e^- \rightarrow 2O^{2-} \quad \text{(Equation 1.12)}$$

The total reaction is known as:

$$C_nH_{2n+2} + \frac{(3n+1)}{2}O_2(g) \rightarrow nCO_2 + (n+1)H_2O \quad \text{(Equation 1.13)}$$

According to the overall reaction, the relationship between partial pressures and the equilibrium cell potential can be written as:

$$E = E^0 + \frac{RT}{2(3n+1)F} \times \ln \frac{P(C_nH_{2n+2anode})P(O_{2cathode})^{(3n+1)/2}}{P(CO_{2anode})^n P(H_2O_{anode})^{n+1}} \quad \text{(Equation 1.14)}$$

This equation is applied only when the alkane is completely oxidized into water and carbon dioxide without the formation of other intermediate products. The standard cell potential, $E^0$, for hydrocarbon is higher than that for hydrogen; for example, at 700°C, the standard potentials for oxidation of hydrogen, methane and n-butane are 1.01, 1.05 and 1.13V, respectively [179].

The primary issue for direct utilization of hydrocarbon is the formation of carbon originating from thermal cracking reaction of hydrocarbon under the catalytic activity of nickel, as shown below

$$C_nH_{2n+2} \xrightarrow{\text{catalyst}} nC + (n+1)H_2 \quad \text{(Equation 1.15)}$$

In humidified hydrocarbon, steam reforming reaction also happens:

$$C_nH_{2n+2} + nH_2O \rightarrow nCO + (2n+1)H_2 \quad \text{(Equation 1.16)}$$

Under Fe or Co catalyst, CO decomposition could provide another resource for carbon deposition:

$$2CO \xrightarrow{\text{catalyst}} C + CO_2 \quad \text{(Equation 1.17)}$$

As a result, the mechanical strength will be deteriorated leading to the fracture of the cell and the clogging of the fuel channels due to the formation of filamentous carbon [180]. In the highly humidified fuels, the equation (1.17) can be inhibited by the water-gas-shift reaction:

$$CO + H_2O \xrightarrow{\text{catalyst}} H_2 + CO_2 \quad \text{(Equation 1.18)}$$

Because the carbon formation is influenced by the gas composition, carbon free region for hydrocarbon fuels can be given based on the thermodynamic calculation as a function of steam to carbon ($H_2O/C$) ratio. In general, the higher $H_2O/C$ ratio reduces the carbon deposition. However, the kinetics is more responsible for the carbon deposition than thermodynamics under the catalytic activity of nickel.

Filament formation of carbon on Ni occurs because carbon deposition takes place more rapidly than carbon removal by steam, even if thermodynamic calculations show that carbon will not be stable at equilibrium [181]. Typically, there are two methods to prevent SOFC from carbon coking. The first one is to apply highly humidified hydrocarbon as fuels and the second one to explore the alternative anode that does not catalyze the carbon formation.

## 1.7 Infiltration/impregnation method

The conventional method to fabricate the composite electrodes, such as Ni(O)-YSZ for anode and LSM-YSZ for cathode, involves the high-temperature co-sintering for anode/electrolyte/cathode structure to ensure the percolation of every phase. The sintering condition could affect the microstructure of electrodes, the intimacy between electrode and electrolyte and the reactivity within different composites [182]. In general, a high sintering temperature of 1300$^{o}$C or higher is commonly required to obtain a fully dense and airtight YSZ electrolyte [183]. However, this high sintering temperature can cause several problems involving the undesirable reactions to produce insulating particulates [184,185], warping and delamination due to the different densification among components, and the growth of particles that results in the decrease of TPBs and cell performance.

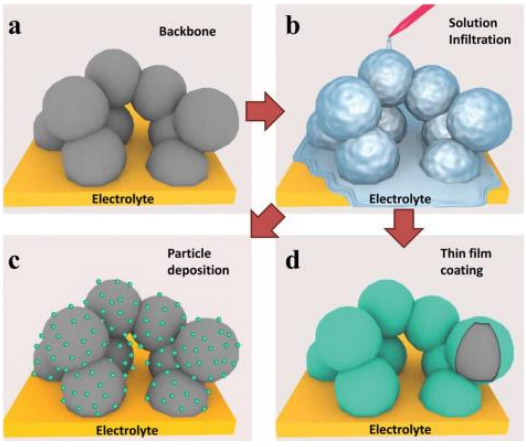


Figure 1.9 Schematics of a typical infiltration process: (a) an as-fired electrode backbone; (b) a process of solution drops entering into the electrode backbone; two typical morphologies of infiltrated electrode after thermal treatment: c) particle deposition and d) thin film coating. Images are taken from reference [186].

In recent years, infiltration/impregnation methods have been widely employed in fabrication of SOFC electrodes and found to be an effective way to solve a number of problems induced by high-temperature sintering, as mentioned above. As illustrated in Figure 1.9, a typical infiltration process involves the following three steps [186]: 1) preparation of porous electrode backbone (Figure 1.9(a)), which has been fired at elevated temperature to ensure a good adhesion of electrode and electrolyte, an excellent connectivity for effective conduction of oxygen ions and electrons, and good structure stability under operation; 2) infiltration of catalyst in the anode or electronic conductors in the cathode (Figure 1.9(b)). A liquid solution, which contains metal salt precursors along with dispersant and surfactant, is dropped into the pre-sintered backbone. 3) After thermal treatment, two different morphologies of infiltrated materials can be observed: discrete particles and thin film coating, as shown in Figure 1.9(c) and (d), respectively.

The infiltration approach has shown many advantages when compared with the conventional fabrication method. First, since the catalyst or conductive phase is additive to the pores of the as-sintered scaffold, it is much easier to fabricate an engineered backbone with desirable structures using mature manufacturing and processing techniques [186]. This leads to the formation of the percolation of conductive phase and offers a possibility to optimize the microstructure of the electrode. Second, infiltration and subsequential low firing temperature enables easier control of composition and particle sizes of catalyst [187], and avoids the formation of undesirable secondary phase between the backbone and catalyst at high temperature. Third, finely dispersed and nano-sized catalyst is more active than the composite ceramics [188], because the structure of infiltrated composite is not random. Finally, the large TEC of infiltrated composite, such as NiO/Ni or perovskite, would not harm the integrity of the whole cell.

## 1.8 Objective of the work

In the present work, an A-site deficient lanthanum- and calcium- co-doped strontium titanate $La_{0.2}Sr_{0.25}Ca_{0.45}TiO_3$ ($LSCT_{A-}$) which has been found to exhibit sufficient electronic conductivity in fuel electrode environments, excellent redox stability, and

promising performance [143,189] is used as an anode support for button fuel cells. In order to improve the performance of $LSCT_{A-}$ anode, precursors including Ni or Ni-Fe bimetallic phases as well as $CeO_2$ were impregnated into porous $LSCT_{A-}$ scaffolds to improve the catalytic activity for the oxidation of hydrogen.

In order to cater the development of intermediate temperature SOFCs, results are presented showing the fuel cell performance obtained on $LSCT_{A-}$ anode-supported button fuel cells with thin electrolytes. To investigate effects on the performance and optimise this, varied catalyst impregnated anodes are studied.

The infiltration of metal oxides can be used to enhance the catalysis of perovskite anode; however, the stability of impregnated nanoparticles in porous scaffold under SOFC operating conditions is becoming a concern. Most studies of stability testing have been focused on cathode materials [59,190,191], suggesting that the degradation can be attributed to the growth and densification of impregnated coatings on the scaffold surface, leading to the decrease in the effective electrochemical reaction sites and therefore the significant reduction of performance. Similarly, for the titanate perovskite anode, a strong degradation was also observed and has been mainly attributed to the increase of polarization resistance [192,193]. In this work, we present some stability studies on $LSCT_{A-}$ anode-supported fuel cells with Ni or Ni-Fe as well as ceria infiltrated into the anode, and try to understand the mechanism for the degradation via the high-resolution scanning electron microscopy (SEM) on the cross-section of the the ion beam etched samples. The Focused Ion Beam (FIB) technique was utilised for cross-section preparation to reveal the interface between the catalyst and titanate, because it is very difficult to distinguish the interaction between impregnates and scaffolds on the surface morphology that occurs in the sub-micron scale underneath the surface of the scaffold particles.

In summary, the main objective of this work is to study and develop a high-performance anode via infiltrating nano-catalysts into pre-establishes $LSCT_{A-}$ anode backbone for intermediate-temperature SOFCs. High power density and reliability are critical for SOFC application in the future. So the targeted properties of the infiltrated cells in our work are as follows: (1) a current density reaches $1.0A/cm^2$ for a cell voltage equal to 0.7V at $800^oC$ in humidified hydrogen (3% $H_2O$); (2) a relatively

stable stage under a given voltage/current density should be achieved in the operation condition.

The electroless nickel-ceramic co-depositon process was investigated as an alternative manufacturing technique for the anodes of planar solid oxide fuel cells (SOFCs). The effects of the added pore formers (starch) and surfactant (CTAB) in the plating solution on the anode microstructure and electrochemical performance were discussed in order to evaluate the practicability of electroless co-deposition technique for preparation of the electrodes.

# Chapter 2. Experimental techniques

## 2.1 Cell fabrication techniques

### 2.1.1 Tape casting

Tape casting is a well-established technique used for the mass production of large-area ceramic substrates and multi-layered structures [194]. This technique allows fabrication of wide variety of controlled morphologies, such as highly porous electrodes and fully dense electrolytes [195~199]. The method involves three steps: milling, casting and drying, as shown in Figure 2.1. The slurry preparation involves two milling stages. At the first stage, the appropriate amount of ceramic powder and pore formers are mixed and ball milled at a fast rate with addition of solvent and dispersant. This milling process is able to break the agglomerate particles and ensures a properly dispersed ceramic in the mixture. At the second stage, binder, plasticizer and defoamer are added, followed by ball-milling and de-airing process, in order to obtain the homogeneous and bubble-free slurry.

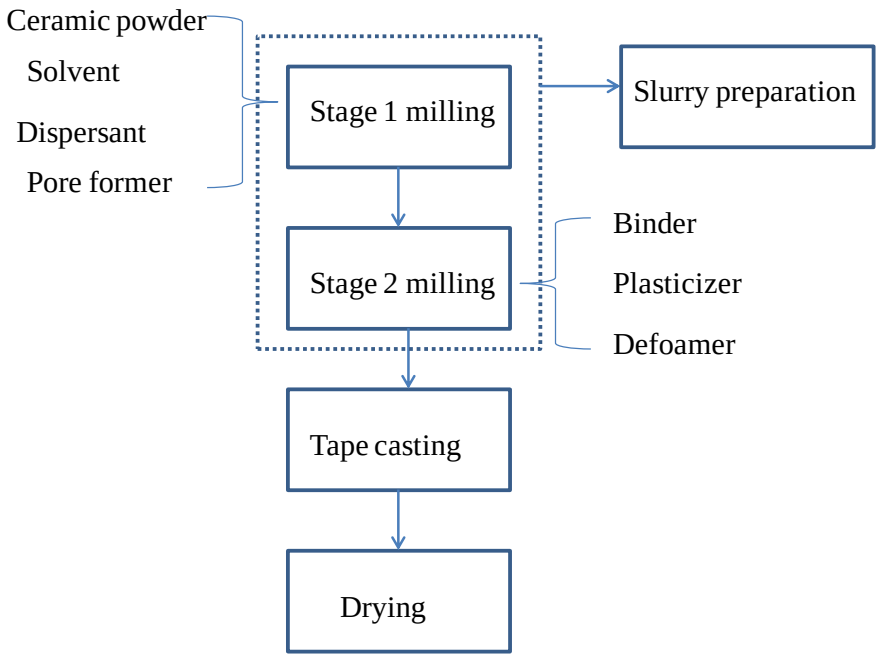


Figure 2.1 Flow chart for the fabrication of a green tape

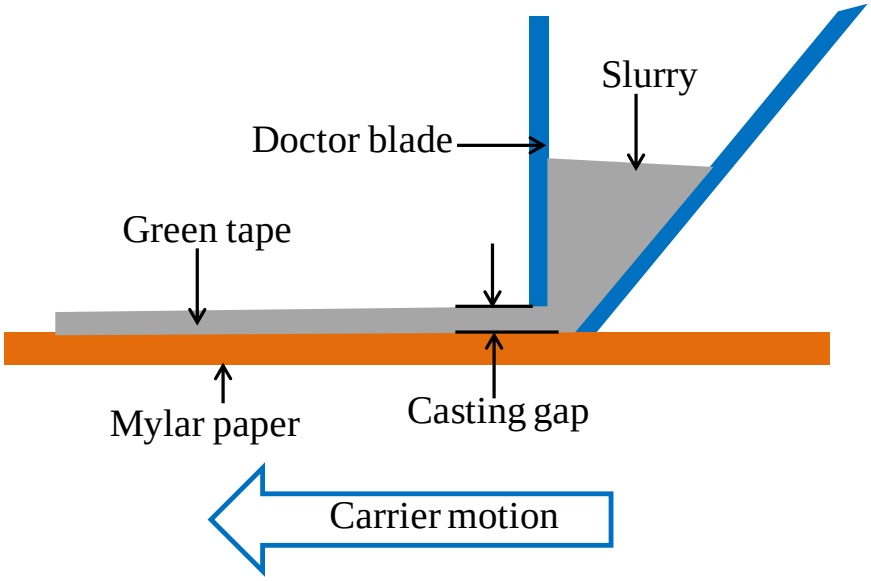


Figure 2.2 Schematic of the tape-casting set-up

The slurry is then cast on a Mylar$^{TM}$ carrier film upon a carrier moving at a controlled speed. Figure 2.2 illustrates the basic principles of the tape casting process. The wet thickness of the green tape is defined by the gap between the doctor blade and the Mylar$^{TM}$ film, which can be adjusted by the micrometer on the doctor blade. The cast tape is then kept in the drying chamber to allow the solvents to evaporate from the surface, leaving a dry tape on the carrier surface. After drying, the different green tapes are cut into appropriate size and laminated into a multi-layer structure by uniaxial pressing and passing through a hot laminator with the temperature around 80$^{o}$C. The laminated tapes then are placed on the zirconia plates and sintered at high temperature, typically above 1300$^{o}$C.

In order to reduce the required lamination steps in forming multi layer structures and also increase the adhesion between different layers, the slurry can be cast on the top of a previously dried green tape with a different formulation, namely a co-casting process. Typically, the electrode slurry is cast on the dense electrolyte green tape after drying [198~201].

Tape casting can be divided into two forms, in terms of the selected solvent and the subsequential additives: non-aqueous (organic-based) tape casting and aqueous (water-based) tape casting. Organic-based solvents can ensure a dispersion of the ceramic powder without hydration reaction and dissolution of organic components.

Although the solvents are more volatile and irritating, strong, uniform green tapes are easy to achieve [194]. However, the enormous environmental and safety concerns associated with organic solvents, such as toxicity, volatility and inflammability, have stimulated interests in developing aqueous tape casting [202]. It is difficult to obtain flat fuel cells with thin gastight electrolytes using aqueous tape casting because of the slow drying rate of the tape that causes the precipitation of different components, high crack sensitivity and poor wetting of the slip owing to the high surface tension of water [197,203]. In this work crack-free and flat anode-supported fuel cells were fabricated using aqueous (in Chapter 3) and non-aqueous (in Chapter 4) tape casting techniques by adjusting the slurry formula and sintering profiles.

### 2.1.2 Screen printing

Screen printing is another low-cost technique that has been widely used in manufacturing the SOFC layers because of its efficient and reproducible manner. The quality of the printed layer is associated with the preparation of the ink. The ceramic powder with or without pore formers depending on the function of the formed layers, is first dispersed into acetone with a small amount of dispersant using rotary ball milling. After addition of vehicle, the mixture is kept agitated until the acetone is evaporated to yield the final ink.

In this work, the LSM-YSZ composite cathode was screen printed on the dense YSZ electrolyte (in Chapter 7). LSM/YSZ ink was prepared by weighting an exact amount of YSZ and LSM powder (50:50 in weight; the total mass of powder was 10 grams) and mixing with 0.2 gram of KD-1 dispersant in the plastic bottle. 20 zirconia balls with 1cm in diameter were also placed into the bottle. Acetone was then poured into the bottle until it covered all the powder and balls. The bottle was placed on a roller ball milling machine for 16h at a rotation speed of 160rpm. This milling step could increase the surface area of powder and improve the homogeneity of mixture. After ball milling, the mixture was moved into a beaker. The organic vehicle consisting of 5wt.% polyvinyl butyral (PVB) and 95wt.% terpineol was weighted out and poured into the beaker. The mass ratio of ceramic powder and vehicle was 30:70. The beaker was covered by a pierced parafilm and placed on a magnetic stirrer at room temperature to evaporate the acetone slowly to form the LSM-YSZ ink.

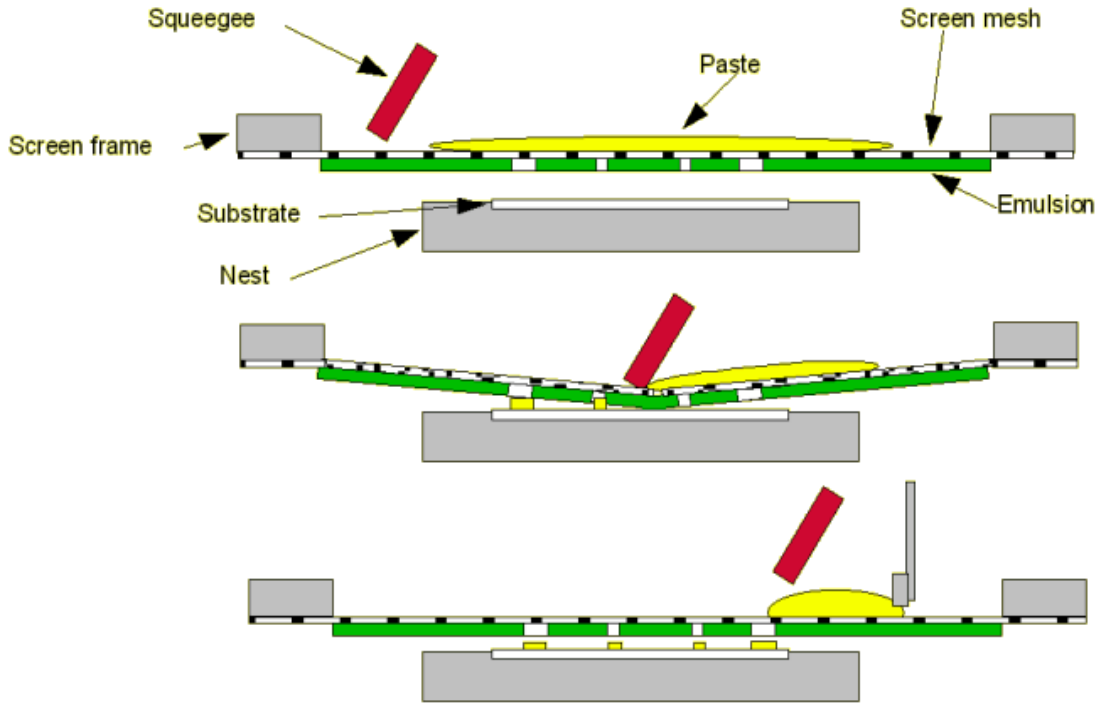


Figure 2.3 The basic principle of screen printing process. Images are taken from reference [204].

Figure 2.3 illustrates the basic operating principle for the screen printing process. At the first step, the screen made of an open weave mesh (in this case stainless steel) is set up on the top of the substrate and fastened by the peripheral frames. Meanwhile, the gap between the screen and substrate, namely printing gap (generally 1-2mm) is adjusted to ensure the contact of the mesh and substrate under a controlled pressure from the squeegee during the printing stroke. Then the prepared ink is put on the top of the screen. As the squeegee moves across the screen, a downward pressure is exerted, which brings the mesh into contact with the substrate. This downward force along with the forward motion of the squeegee and the angle this makes with the screen force the ink through the mesh and onto the substrate. Behind the squeegee, the tension within the mesh will pull the mesh away from the substrate immediately leaving the ink deposited on the substrate surface. After every printing, the sample needs to be dried in an oven.

In this work, the screen printing process was carried out on DEK 248 semi-automatic screen printer with an installed computer to control the printing program and ensure the reproducible property of the printed layers. The LSM-YSZ cathode ink was

printed on dense YSZ electrolyte, which has been sintered at 1350$^{o}$C for 2h in air. The printing process need to be repeated for several times to obtain a desired thickness for each cathode. After each printing, the sample was placed in an oven with a temperature of 80$^{o}$C to allow the printed coating fully dry. Then the resulting sample was firing at 1050$^{o}$C for 1h in air with a heating and cooling ramp of 3$^{o}$C/min.

### 2.1.3 Infiltration/impregnation

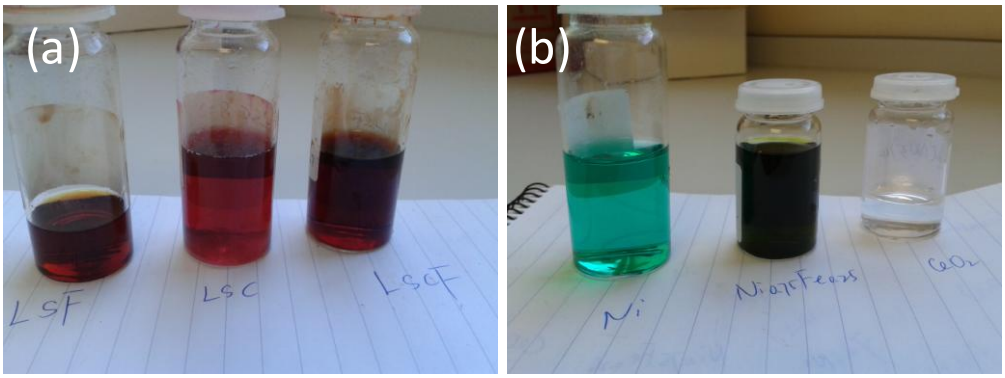


Figure 2.4 Picture of metal nitrate solutions for wet impregnation in the (a) cathode side and (b) anode side

The porous YSZ cathode and $LSCT_{A-}$ anode scaffolds have been fabricated by tape casting and sintering approaches. Although YSZ can provide the ionic conductivity required for the cathode, the lacking electronic conductivity and catalytic activity for oxygen reduction would result in a poor performance, limiting the SOFC application. Three kinds of aqueous solution were prepared by mixing the metal nitrates at an exact ratio according to the formed compositions with critic acid and dissolving into deionised water. The precursor solutions used for impregnation containing $La_{0.8}Sr_{0.2}FeO_3$ (LSF), $La_{0.8}Sr_{0.2}CoO_3$ (LSC) and $La_{0.8}Sr_{0.2}Co_{0.2}Fe_{0.8}O_3$ (LSCF) were made from $La(NO_3)_2$•$6H_2O$ (Aldrich Chemistry, 99.99%), $Sr(NO_3)_2$ (Aldrich, ≥99%), $Co(NO_3)_2$•$6H_2O$ (Sigma-Aldrich, ACS reagent, ≥98%) and $(Fe(NO_3)_3$•$9H_2O$ (Fisher Scientific, Analytical agent grade), as shown in Figure 2.4(a). Citric acid was also added into the solution at a molar ratio of 1:1 for total metal ions: citric acid and the total concentration of metallic ions were 1mol/L. The aqueous solution was placed on the stirrer to accelerate the dissolution and dispersion process of nitrates. The impregnation approach was performed by dropping a small amount of solution on the

top of the porous electrode, which diffused into the pores by a capillary force. After every impregnation, the samples were placed in the furnace and fired at 450$^oC$ for 30 minutes to decompose nitrate. Multiple cycles of impregnation and calcination at 450$^oC$ were used until the desired loading of impregnates of oxides was reached. For aqueous tape casted cells, LSF and LSC were impregnated into the YSZ scaffold successively to get a final loading of 15wt.% LSF and 5wt.% LSC (see section 3.2). For organic tape casted cells, 25wt.% LSCF were obtained after multi-impregnation process and firing at 450$^oC$ (Chapter 4 and 5). The weight ratio of the impregnated oxides is relative to the total weight of the YSZ cathode scaffold and the impregnated oxides in this study.

In order to increase the effective reaction sites and improve the electro-catalytic activity in the anode, Ni or Ni-Fe bimetal, as well as ceria was introduced into the anode scaffold by wet impregnation technique. The nitrate precursor solutions including $CeO_2$ and Ni were prepared by dissolving $Ce(NO_3)_3.6H_2O$ (Sigma-Aldrich) and $Ni(NO_3)_2.6H_2O$ (Newburyport, MA USA) into deionised water, respectively. The precursor solution containing $Ni_{0.75}Fe_{0.25}$ were made by mixing $Ni(NO_3)_2.6H_2O$ (Newburyport, MA USA) and $Fe(NO_3)_3•9H_2O$ (Fisher Scientific, Analytical agent grade) at a molar ratio of 3:1 for Ni: Fe in deionised water, as shown in Figure 2.4(b). Citric acid was subsequently added into the Ni-Fe nitrate solution at a molar ratio of 1:1 for total metal ions: citric acid. The total concentration of metallic ions were 1mol/L. The solutions dropped onto the surface of porous $LSCT_{A-}$ anode would diffuse along the pores into the $LSCT_{A-}$ scaffold by a capillary force. The impregnation steps were repeated to obtain a desired loading. After each impregnation, the samples were fired at 450$^oC$ for 30 minutes to decompose the nitrate. In our experiment, the final loadings of catalysts were 6wt.% $CeO_2$, 3wt.% Ni and 3wt.% Ni-Fe bimetal. The weight ratio of $CeO_2$ or metal catalyst in the anode is relative to the total weight of the $LSCT_{A-}$ anode scaffold and the impregnated catalysts in this study.

## 2.2 Material characterization

### 2.2.1 X-Ray Diffraction (XRD)

X-Ray Diffraction (XRD) is an analytical technique used for identifying the structure of a crystalline material and determining the information of unit cell dimensions [205]. It can provide the reproducible patterns and does not destroy the sample itself.

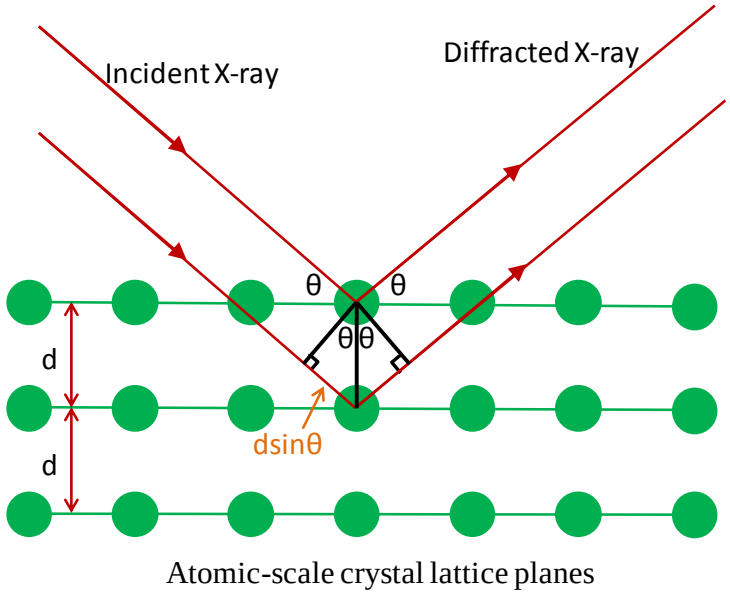


Figure 2.5 Illustration of Bragg diffraction

A crystal lattice can be considered as a unique arrangement of atoms in three dimensions. These atoms are arranged on a series of parallel planes and the spacing between the adjacent planes is noted as d.

When two parallel incident X-rays with identical wavelength, λ, approach interplanar crystal atoms, the X-ray reaching the top layer has less distance than the X-ray reaching the lower layer. Likewise, the X-ray diffracted from the top layer has travelled less distance than the X-ray scattered from the lower surface, as illustrated in Figure 2.5. The total distance can be noted as $2dsin\theta$, depending on the interplanar spacing, $d$ and the angle of incident rays, $\theta$. When the distance is equal to a multiple of the wavelength, the reflected waves are in phase where the reflected rays with the maximum intensity occur. The equation can be expressed as:

$$2d\sin\theta = n\lambda \qquad \text{(Equation 2.1)}$$

where *n* is an integer. The equation is known as Bragg's Law.

X-ray diffraction (XRD) data on $LSCT_{A-}$ powder calcined at different temperatures and reduced at 1000°C were obtained using a John PANalytical X-ray diffractometer with $CuK_{\alpha 1}$ radiation ($\lambda$ = 1.54056Å) in the range $2\theta$ = 20-100°. The XRD patterns were analysed using the X'Pert HighScore Plus and STOE WinXPOW softwares to determine the crystal structure and the lattice cell parameters. The cell parameters were also refined with Fullprof software.

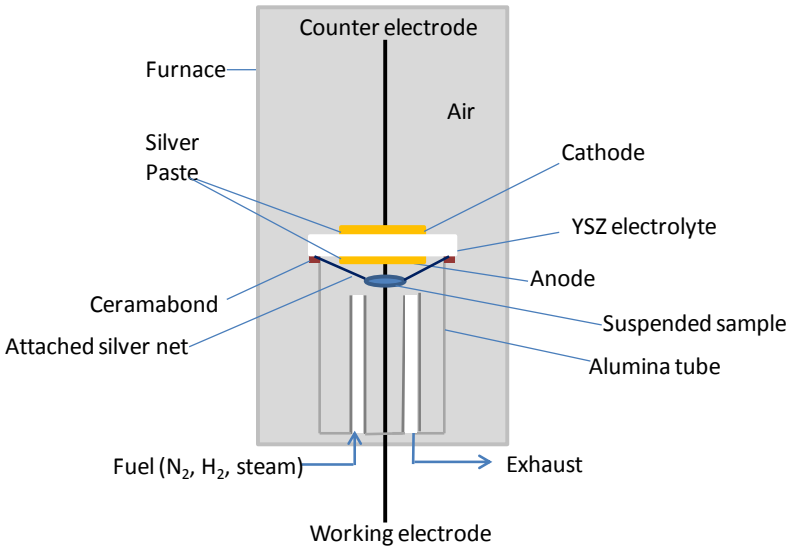


Figure 2.6 Schematic of metallic catalysts reduced at the simulated fuel cell operation condition

The XRD experiments were also performed on Ni and Ni-Fe catalysts after the different thermal treatments using a John PANalytical X-ray diffractometer with $CuK_{\alpha 1}$ radiation ($\lambda$ = 1.54056Å) in the range $2\theta$ = 20-100°. In order to identify the phase of the impregnated materials, $Ni(NO_3)_2.6H_2O$ and $Fe(NO_3)_3.9H_2O$ were dissolved into deionised water to prepare nickel nitrate and nickel-iron nitrate solutions at a molar ratio of 3: 1 with addition of citric acid. These solutions were subsequently agitated and heated to 150°C for combustion, followed by calcinations in air at 450°C for 30 minutes, as exactly the same as the impregnation of catalysts in the anode. A fraction of calcined powder was pressed into a pellet and suspended into

an alumina tube, which was sealed by a thick YSZ pellets with two silver wires attached on the two electrodes. The atmosphere in the tube can be controlled by the flowing rates of the inserted water steam, hydrogen and nitrogen and be monitored by the OCV measurements on the silver electrodes with YSZ as electrolyte, as shown in Figure 2.6. By adjusting the flowing rates of gases ($H_2$, $N_2$ and steam), an OCV value between 0.55-0.6V versus the ambient air at the cathode side at 700$^{o}$C was obtained, where the powder was placed for 12h. Under this voltage, the oxygen partial pressure in the chamber can be calculated around $10^{-13}$atm. Another fraction of the calcined powder was reduced at 900$^{o}$C for 12h in a 5% $H_2$-Ar atmosphere. The powders calcined at 450$^{o}$C in air and reduced at the oxygen partial pressure of $10^{-13}$atm and 5% $H_2$-Ar were characterized by XRD. The relevant results are presented in section 4.3.5 and 4.3.6.

### 2.2.2 Scanning Electron Microscopy (SEM) and Back-Scattered Electron (BSE)

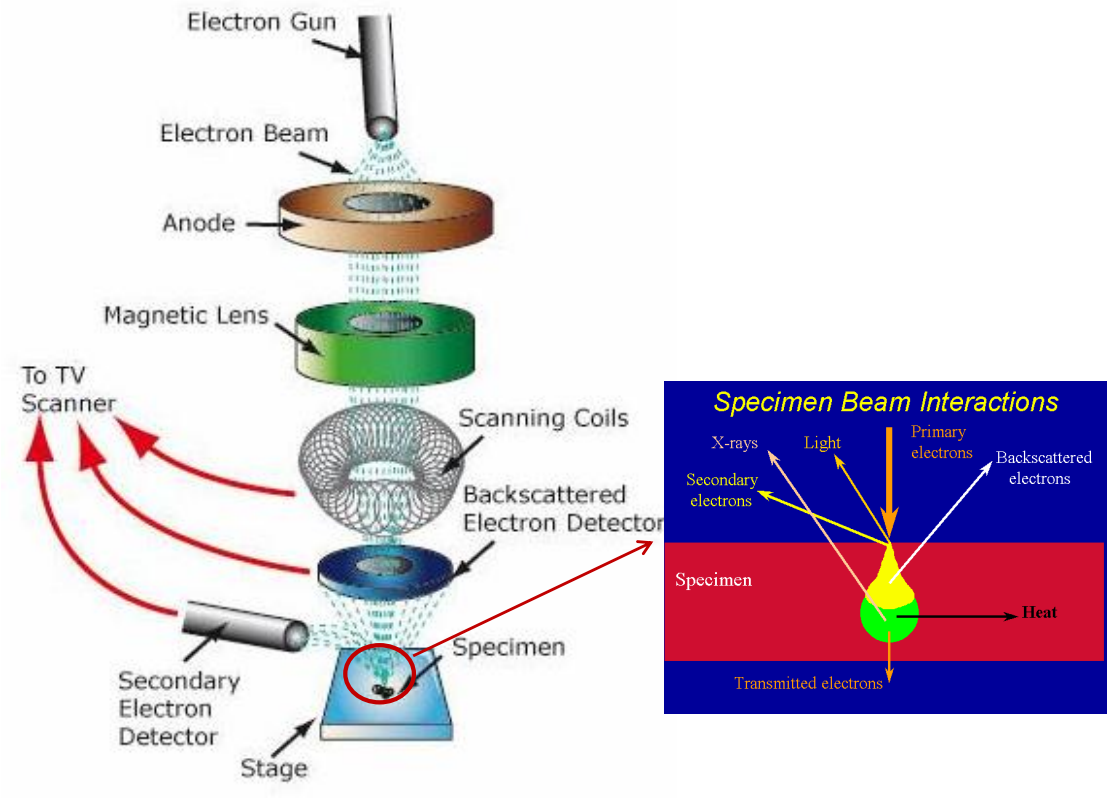


Figure 2.7 Principle of SEM and BSE. Images are taken from references [206,207]

Scanning Electron Microscopy (SEM) is a useful tool to reveal the microstructure of materials at a range of microscale and nanoscale. The focused electron beam emitted by the electron gun travels through electromagnetic lenses, which focus the beam down toward the sample, as shown in Figure 2.7. When the electron beam hits the sample surface, a series of signals are produced by the interaction between the electrons and the sample, including secondary electrons (electrons generated from the sample itself), backscattered electrons (electrons resulted from the collision between the electron beam and the nuclei of atoms in the samples), X-rays, heat, light and transmitted electrons (beam electrons that pass through the sample).

The generated secondary electrons and back-scattered electrons can be detected by the corresponding detectors, producing the SEM and BSE images, respectively. SEM image gives the information about the topography of the sample surface. BSE can provide the information about the chemical composition of different regions by contrasting the brightness.

In our experiment, the morphology of $LSCT_{A-}$ powder calcined at the different temperatures were analyzed by a JEOL model JSM 6700 Field emission gun (FEG) scanning electron microscope (see section 3.1.3). SEM experiments were also performed on the fractured cross section of Ni and $CeO_2$+Ni impregnated anode before and after the electrochemical testing at 700-800$^oC$ in humidified hydrogen (3% $H_2O$) (see section 3.3).

BSE experiments were performed on the sintered tapes made from the $LSCT_{A-}$ powder calcined at different temperatures plus varied weight percent of graphite (see section 3.2). The pellets sintered at 1350$^oC$ were mounted in the epoxy resin, ground to 1200-grit sandpaper after drying and then polished on the polishing clothes with diamond polishing paste of 1μm. The polished sample was fixed on the SEM holder and coated with a thin layer of gold. The 'ImageJ' image analysis software was used to evaluate the porosity of the porous anode scaffold on BSE images.

In order to study the evolution of microstructure, morphology and chemical composition on the impregnated anodes upon the stability testing, SEM and BSE images were taken on the cross section of the samples using JSM 6700 scanning

electron microscope, and chemical elements were analyzed by an Oxford Inca Energy Dispersive X-ray spectroscopy (EDX) equipped with JSM 6700 microscope. The cells after the stability testing in humidified hydrogen (3% $H_2O$) at 700$^oC$ have been polished by the Focused Ion Beam (FIB) to get a flat surface. In order to obtain clear and informative SEM/BSE images, the sample was mounted to the SEM specimen holder using the carbon tape and then coated with a thin layer of gold prior to the SEM measurements. The SEM and BSE images were taken on the functional layer in the $LSCT_{A-}$ anode near the anode/electrolyte interfaces.

### 2.2.3 Energy Dispersive X-ray (EDX) spectroscopy

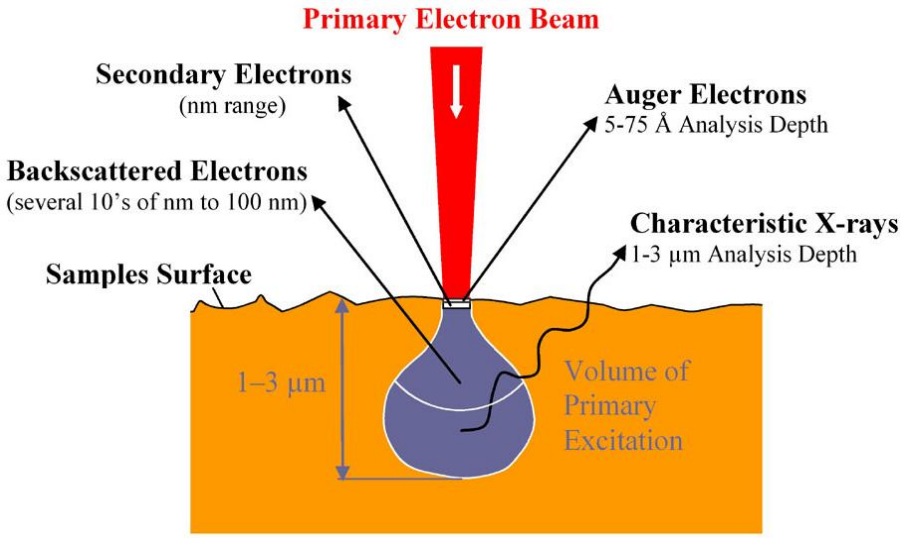


Figure 2.8 Interaction volume of the different signals in the sample. Image is taken from reference [208].

Energy Dispersive X-ray (EDX) spectroscopy embedded in SEM is an analytical technique used for the elemental analysis of a sample [209]. It relies on the characteristic X-rays generated in a sample by the interaction of the electron beam and the sample. The X-ray detector is used to absorb X-ray energy and convert into voltage signal. Then the signal is recorded as a spectrum with intensity versus X-ray energy.

The spatial resolution of EDX analysis in the SEM depends on the size of the interaction volume, which in turn is controlled by the accelerating voltage and the

mean atomic number of the sample, $Z$ [210]. In general, the spatial resolution for EDX is on the order of a few microns due to deep interaction volume by X-rays penetrated into the sample, as demonstrated in Figure 2.8. Compared with X-rays, the interaction volume of secondary electrons and backscattered electrons are much smaller, at the range of nanometers. An accelerating voltage of 15-30kV is commonly used to efficiently generate at least one family of X-ray lines for all elements; however, high-energy primary electron beam could damage the sample or increase the interaction volume. The electron beam current (or spot size) is another parameter and should be adjusted to minimize spectral artefacts and generate sufficient X-rays to allow reliable quantification.

### 2.2.4 Transmission Electron Microscopy (TEM)

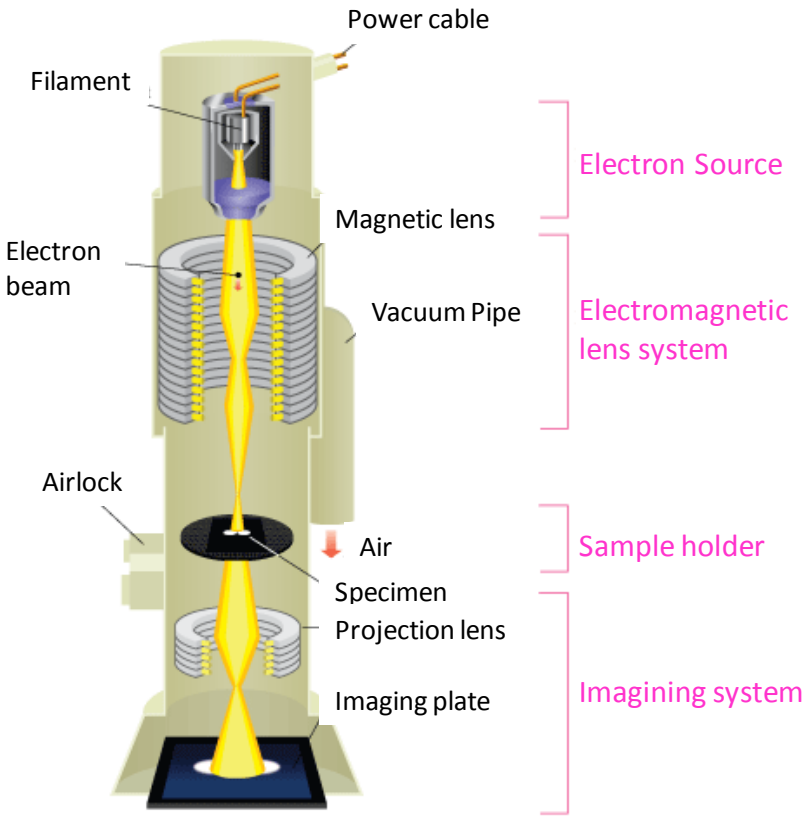


Figure 2.9 Principle of TEM. Image is taken from reference [211].

Transmission Electron Microscopy (TEM) is capable to not only provide more detailed information of specimen microstructure than SEM, but also show the

information on element and compound structure on a molecular level. Figure 2.9 shows the principle of a TEM. The electron beam is emitted from the cathode made of a tungsten filament when being heated and accelerated by the magnetic lens when it travels towards to the sample. The high-speed electron beam that passes through the thin sample will travel down the column and project the enlarged image on the screen after travelling through the projection lens.

Because TEM samples should be beam transparent (usually ≤ 100nm), the interaction volume in the path of transmission electrons is much smaller than it would be in the SEM [212], which has been illustrated in Figure 2.8. Therefore, the spatial resolution of EDX fitted within TEM is much better than that of EDX equipped within SEM.

JEOL TEM 2011 transmission electron microscopy equipped with Oxford Isis EDS detector was used to analyze the detailed microstructure and chemical composition of the impregnated catalysts in the electrodes. The TEM samples were prepared in the following way: at first, the samples were fixed into Gatan G-1 epoxy to protect the surface structures; then the cured samples were cut and thinned to electro transparency by mechanical grinding and focused ion beam polishing.

### 2.2.5 Focused Ion Beam (FIB)

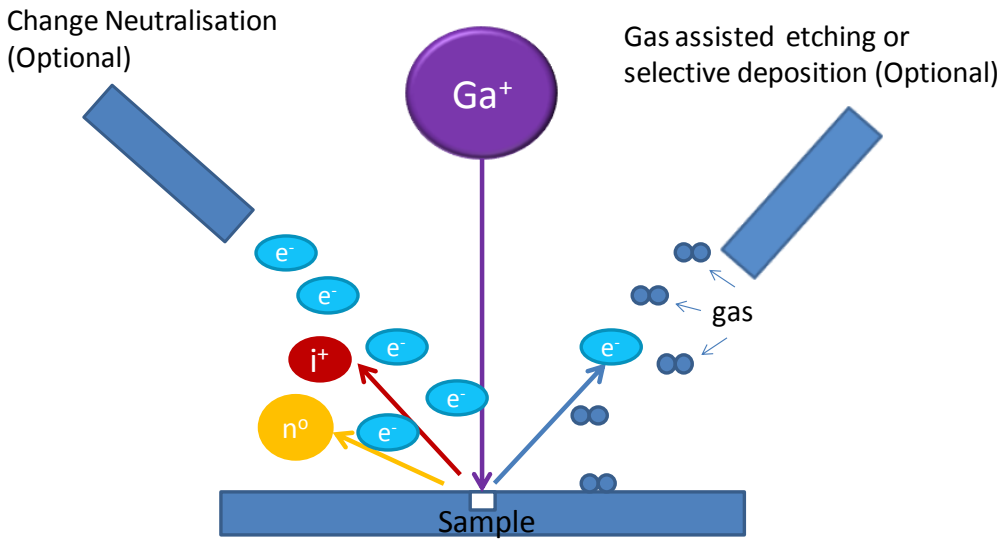


Figure 2.10 Principle of FIB

The focused ion beam (FIB) technique has been widely used for preparation of electron microscopy specimens including semiconductors, metals, ceramics, polymers and biological materials [213]. The FIB instrument setup is similar to a scanning electron microscopy (SEM), except they rely on different beam sources: an electron beam for SEM and an ion beam for FIB [213,214].

Gallium ($Ga^+$) ions are usually used in FIB system due to its low melting point, proper weight and low volatility [215]. The primary gallium ion beam approaches the sample surface and sputters a small amount of material, which leaves the surface as either secondary ions ($i^+$ or $i^-$) or neutral atoms ($n^0$) [216], as illustrated in Figure 2.10. The primary beam also generates secondary electrons ($e^-$). The signal from the sputtered ions or secondary electrons can be collected to form an image.

FIB technique allows to etch the sample surface at a range of nanoscale without destruction of surface features and the underneath atoms. In this work the impregnated cells before and after the stability testing in humidified hydrogen (3% $H_2O$) at 700$^o$C were polished using Leica EM TIC 3X triple ion beam cutter system. The Leica EM TIC 3X equipment features three saddle field ion sources located in one assembly. They are perpendicular to the sample surface, so the sample (mounted on a holder) does not require an oscillating movement to reduce shadowing/curtaining effects. And, three ion beams intersect at the centre edge of the mask forming a milling sector of 100 ° and allowing to cut the exposed sample (~20 to 100μm above the mask) until the area of interest is reached [217]. This unique triple ion beam setup could reduce the processing time, increase the milling depth and optimize the cross-section quality. Each gun allows to be controlled and switched separately, which is beneficial for a high quality milling.

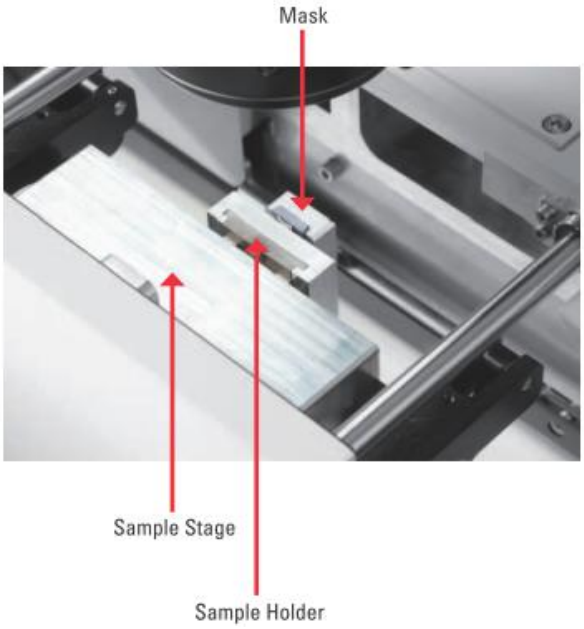


Figure 2.11 Picture of the standard sample holder of the Leica EM TIC 3X instrument used in this work. Image is taken from reference [218].

Before ion milling, the sample was treated by a mechanical process to get as close as the area of interest and in order to decrease the milling time, a final length of the sample ready for etching was around 5mm. Then the sample was pasted on the thin aluminium plate ($1 \times 1 cm^2$) using glue. Then the plate was fixed onto the sample holder using double-size copper adhesive tape. After mounting the sample, the sample holder was placed between a sample stage and a mask, as shown in Figure 2.11. The sample surface is perpendicular to the mask. The edge of the mask defines the surface to be cut. A manual high precision three axis stage allows accurate sample movement in X, Y and Z direction. Sample can be viewed in all positions by using stereo microscope equipped with the cutter system. The stage permits a cutting position accuracy of better than 10μm. All parameter settings for the milling process are operated via a single touch screen control panel [218]. The setting time used for cutting a cross-section of one anode-supported fuel cell was approximately 8h when using 3 guns under a voltage of 9.5kV and a current of 3.4mA.

### 2.2.6 Particle Size Analysis (PSA)

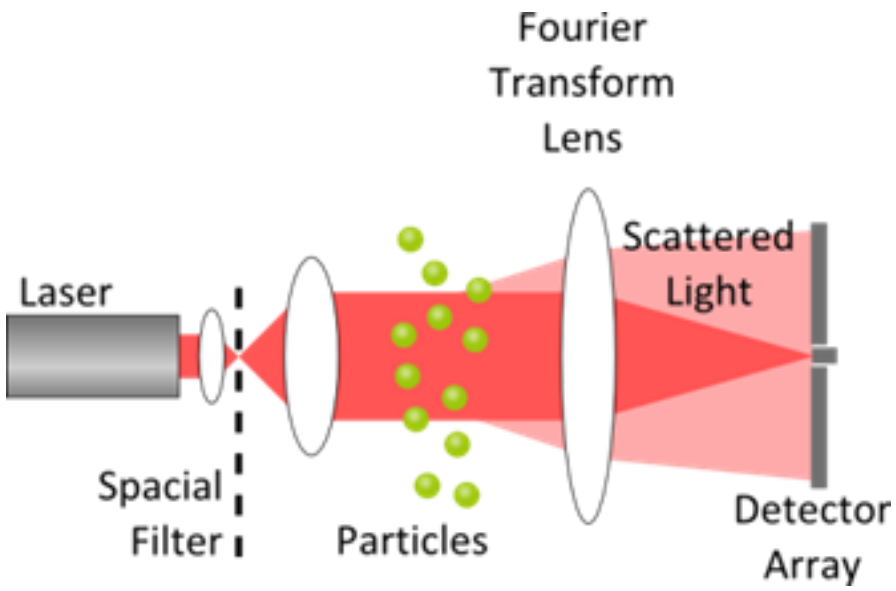


Figure 2.12 Principle of PSA using laser diffraction. Image is taken from reference [219].

Laser diffraction is a common, and fully automated, in-line method of measuring the particle size distribution of a sample [219]. As shown in Figure 2.12, when the light emitted from the laser passes through a chamber with the particles in suspension, it is scattered by the particles and then detected by a series of detector array. A particle size distribution plot can be obtained by converting the intensity of scattered light, which is collected by the detectors, using the mathematical algorithm.

In this study, particle size analysis of $LSCT_{A-}$ and YSZ powder was carried out on a Malvern Instruments Mastersizer 2000 in deionised water as solution containing 2wt.% hypermer KD6 (Croda Iberica SA) as dispersant. To eliminate particle agglomeration, the tested powder was ball milled for 24 hours in deionised water using zirconia grinding media (1cm in diameter) before the PSA measurement.

### 2.2.7 Brunauer–Emmett–Teller (BET) measurement

The specific surface area (SSA) of a sample can be determined by physical adsorption of a gas on the surface of a solid and by calculating the amount of adsorbate gas corresponding to a monomolecular layer on the surface using a fully automated

analyser [220]. The process is usually conducted at the temperature of liquid nitrogen. The amount of gas absorbed can be measured by a volumetric or continuous flow procedure. BET measurements of $LSCT_{A-}$ powder calcined at varied temperatures were obtained on a Micromeritics Tristar II 3020 instrument.

### 2.2.8 Dilatometry

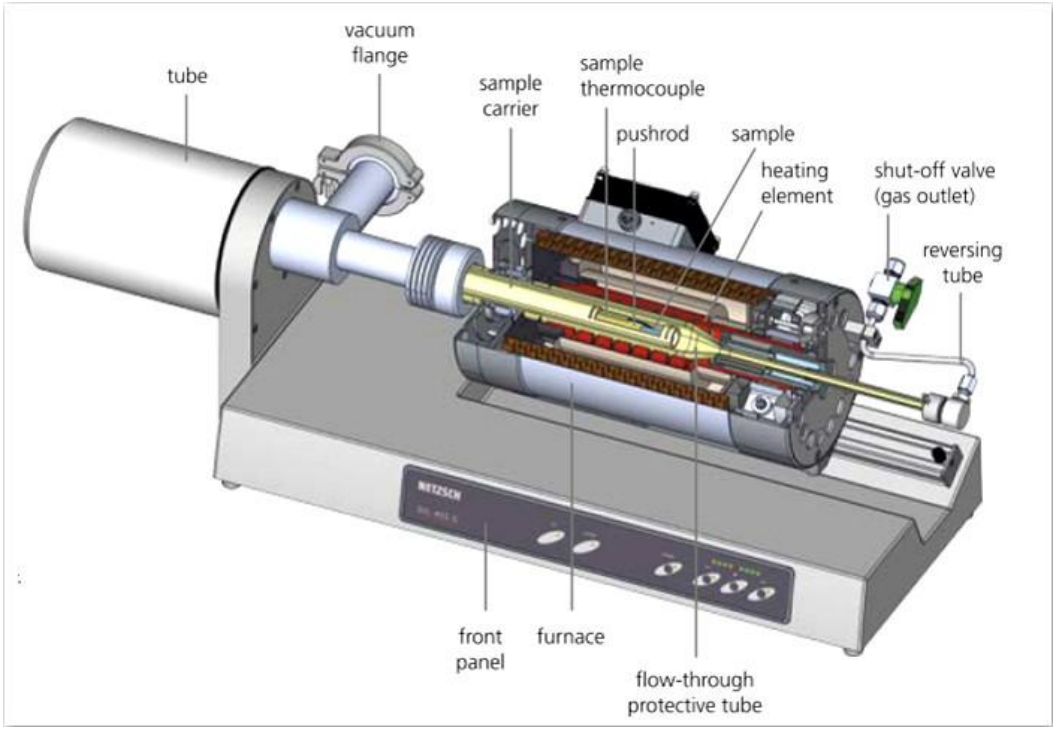


Figure 2.13 Principle of the dilatometer. Image is taken from reference [221].

Dilatometry is a method used for determining the dimensional changes of the sample versus temperature or time while the sample undergoes a controlled temperature program [221]. The measurement can be performed at different atmospheres, such as flowing air, nitrogen or 5% $H_2$-Ar.

As shown in Figure 2.13, a pellet sample sandwiched by two alumina pellets (spacers) is placed on the inside of sample carrier within a moveable furnace. The pressure is applied to the sample by pushrod, which can transmit the length change to a linear variable displacement transducer (LVDT). Then an output signal from LVDT is recorded. A thermocouple is placed next to the sample to measure the temperature. In order to eliminate the length change from the sample carrier, the front part of the

pushrod and the alumina spacers under the same temperature program as the sample, it is necessary to insert a correction curve conducted on an alumina pellet placed between the two spacers into the sample measurement.

The dilatometry measurement is used to analyze the sinterability of a green pellet and the thermal expansion coefficient (TEC) of a sintered pellet. The TEC can be calculated by the following equation:

$$\alpha = \frac{1}{L_0}\frac{\Delta L}{\Delta T} \qquad \text{(Equation 2.2)}$$

where $\alpha$ is the thermal expansion coefficient (TEC), $L_0$ is the initial length of the sintered sample, $\Delta T$ and $\Delta L$ are the change in temperature and length, respectively.

The green pellets were prepared by pressing the powder with a uniaxial pressure of either 110Mpa for $LSCT_{A-}$ or 150Mpa for 8mol.% yttria-stabilized zirconia (YSZ) powder (HSY-8, DKK, Japan), respectively, in order to create porous $LSCT_{A-}$ structure and dense YSZ structure as anode and electrolyte in the cell. The final pellets were 2mm thick and 13mm in diameter. The temperature program for the green pellets includes a heating ramp of $3^oC$/min from the room temperature to $1350^oC$, a dwelling time for 3h and a cooling ramp of $3^oC$/min from $1350^oC$ to room temperature. The flowing air was used for the sinterability experiments.

The sintered pellets with different porosity were prepared by pressing the mixture powder of $LSCT_{A-}$ and a varied amount of graphite and then firing at $1350^oC$ for 2h in air. The dimension is around 2mm in thickness and 10mm in diameter. The TEC measurement was carried out in the flowing air and 5% $H_2$-Ar atmospheres with a heating ramp of $3^oC$/min from room temperature to $1000^oC$.

The dilatometry experiments were performed on a Netzsch DIL 402 C instrument equipped with the Proteus thermal analysis software.

### 2.2.9 Thermal Gravimetric Analysis (TGA)

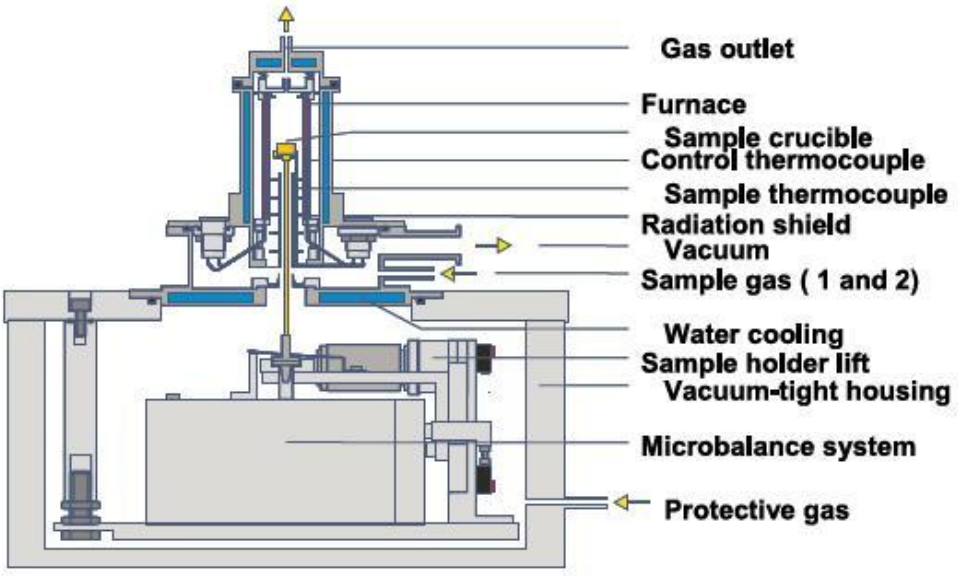


Figure 2.14 Principle of TGA. Image is taken from reference [222].

Thermal gravimetric analysis (TGA) is an analytical technique used to measure weight changes as a function of temperature and/or time in a controlled atmosphere. It can provide information about physical phenomena, such as second-order phase transitions, including vaporization, absorption and desorption, and chemical phenomena including chemisorptions, dehydration, decomposition and solid-gas reaction [223].

As shown in Figure 2.14, the sample is placed in the alumina crucible and rest on the sample holder. A thermocouple is placed next to the sample to measure the temperature. Under the temperature program, the mass change of the sample is measured by the microbalance system and recorded by the corresponding software. It allows to use different gaseous atmosphere, such as air, nitrogen, 5% $H_2$-Ar, but it is necessary to feed protective air (usually argon) to the system for the protection of the microbalance system. The TGA measurements in this work were carried out on a Netzsch TG 209 instrument.

### 2.2.10 Conductivity measurement

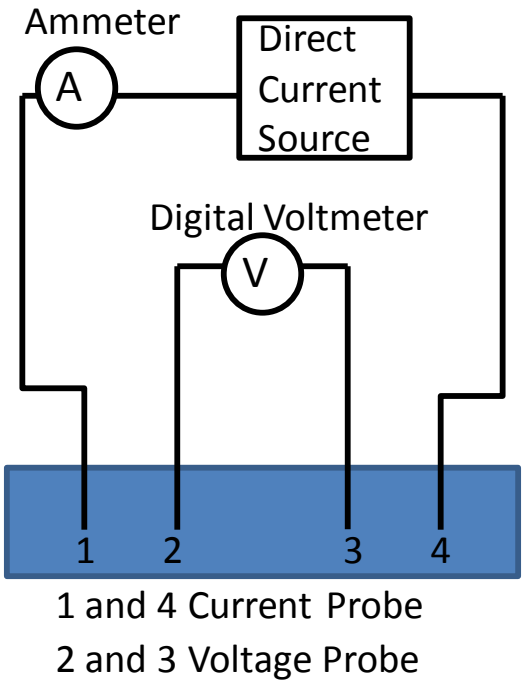


Figure 2.15 Four-probe setup for DC conductivity measurement

The conductivity of $LSCT_{A-}$ pellets was measured using four-probe setup instrument, as shown in Figure 2.15, where the two outer probes are connected to a DC current source and the two inner probes are connected to a digital voltmeter. As the current passes between the outer probes, the corresponding voltage across the inner probes will be measured [224]. The conductivity of the sample, known as reciprocal of the resistivity, is related with the resistance (the ratio of the voltage to the output current) and the geometrical characteristics of the sample. For a rectangular solid, the sample conductivity σ can be given by

$$\sigma = \frac{I}{V}\frac{S}{A} \qquad \text{(Equation 2.3)}$$

where $I$ and $V$ are the current and voltage measured from the outer and inner probes, respectively, $S$ is the separation between the two inner probes, and $A$ is the cross-sectional area of the sample.

In this work the conductivity measurement was carried out using four-probe system in 5% $H_2$-Ar atmosphere as a function of temperature. The samples were prepared by tape casting technique using the same $LSCT_{A-}$ slurries for the anode green tapes and sintering at 1350$^{o}$C in air. The slabs were 11×11mm in area and 0.5mm in thickness. Four platinum foil contacts were attached on the surface of the sample using platinum paste and consolidated by firing at 900$^{o}$C for 30 minutes.

## 2.3 Electrochemical testing techniques

### 2.3.1 Two-electrode, four-probe testing setup

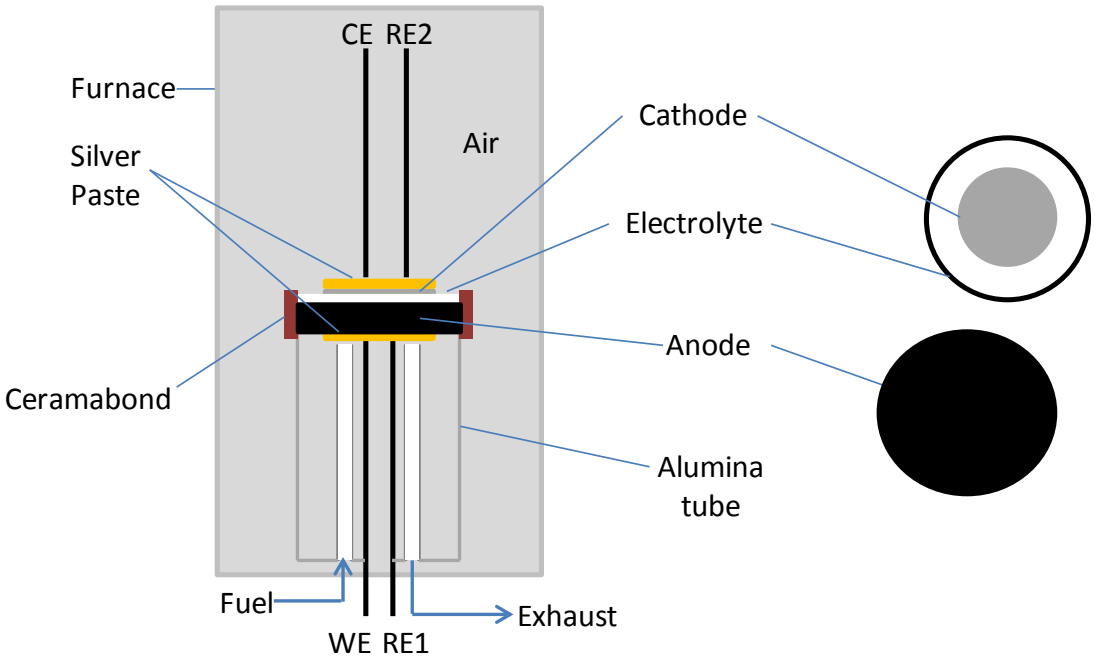


Figure 2.16 Four-probe, two-electrode setup used for the electrochemical testing of anode-supported SOFCs

The single cell was mounted on an alumina tube using a four-probe, two-electrode setup, as shown in Figure 2.16. Silver paste (ESL Europe) was used for the current collection on the anode and cathode side and silver wire (Advent) as the lead for the electrodes. A single cell was sealed onto an alumina tube using ceramic adhesive (Ceramabond 552, Aremco), which can separate the two atmospheres for the electrodes and prevent the leakage problem. A slow gas flow of Ar containing 5% $H_2$

was fed into the anode chamber to avoid the oxidation of the anode upon heating to testing temperature of 700/800$^oC$, before switching to humidified hydrogen (3% $H_2O$). In this work, humidified hydrogen (3vol.% $H_2O$) was fed into the anode chamber as the fuel at a flow rate of 30ml/min and ambient air was used as oxidant under cell operation and stability testing. The initial performance of $CeO_2$-$LSCT_{A-}$ anodes impregnated with and without metallic catalysts in humidified methane (3vol.% $H_2O$) were also evaluated at 700-800$^oC$.

### 2.3.2 Current-Voltage (I-V) measurement

Current-voltage (I-V) and current-power (I-P) curves are of importance for the evaluation of the performance of the fuel cell. An external circuit is connected to the cell through the electrical lead wires attached on the electrodes. I-V curves show the relationship between the current flowing through the external circuit and the corresponding voltage measured between the anode and cathode. I-P curves are defined as the power, the product of the voltage and current, as a function of the current. In general, the current and power are divided by the active surface area, noted as current density ($A/cm^2$) and power density ($W/cm^2$).

When there is no current passing through the cell, the electrical potential between the cell can be measured by the voltmeter connected between the two electrodes, which is known as the open circuit voltage (OCV). The actual OCV value usually is slightly lower than the theoretical OCV value predicted from the Nernst equation probably due to the fuel crossover, small internal currents or the slow reaction process. With the increasing current applied to the cell, the potential is decreased due to the polarization reactions occurring in the cell.

The current-voltage curves were measured using a Solartron 1287 Electrochemical Interface and CorrWare v3.2c software (Scribner Associates) with 4-lead configuration, as shown in Figure 2.16. The I-V measurements started at the OCV and finished at -0.7V vs OCV. The voltage was decreased at a rate of 25mV/step with each step lasting 5s (see section 3.3). In section 4.3 and 5.3, the I-V curves were scanned from OCV to -0.7V vs OCV then back to OCV at 25mV/step with single step lasting 5s. The I-V curves were measured in humidified pure hydrogen (3% $H_2O$) at

700-800$^oC$ under a cooling stage with a gas flowing rate of 30mL/min. Moreover, the ceria and metal impregnated cells were also operated in humidified pure methane (3% $H_2O$) and the I-V performances were recorded under a cooling stage from 800$^oC$ to 700$^oC$ with a gas flowing rate of 30mL/min (see section 5.3).

In this work, the best performance of the cells with the same impregnated catalysts was presented. It should be noted that cell-to-cell performance variations at a given composition were below 10%, showing a good reproducibility.

### 2.3.3 Electrochemical Impedance Spectroscopy (EIS)

#### 2.3.3.1 AC impedance

Electrochemical Impedance Spectroscopy (EIS) is a powerful tool for characterization of electrochemical properties of a material and fuel cell system by isolating the individual reaction/migration steps in multistep process. Because each reaction or migration step has a unique time constant associated with it, these steps can be separated in terms of the frequency domain [225]. By applying a small sinusoidal voltage perturbation to an equilibrium system, the corresponding current can be determined. The impedance is defined as the ratio of the voltage perturbation to the current response. The impedance measurement is carried out over a broad range of frequencies from several millihertz to several megahertz.

When a weak amplitude signal, $V(w)=V_0e^{jwt}$, under a single frequency $f=w/2\pi$, is applied to the system, a current of $I(w)=I_0e^{j(wt+\varphi)}$ can be measured. $V$ and $I$ are out of phase and frequency-dependent. The complex resistance can be given by

$$Z(w) = \frac{V(w)}{I(w)} = \frac{V_0 e^{jwt}}{I_0 e^{j(wt+\varphi(w))}} = \frac{V_0}{I_0}(cos\varphi(w) - jsin\varphi(w)) \qquad \text{(Equation 2.4)}$$

Where $j$ is the imaginary unit ($j = \sqrt{-1}$) and $\varphi$ is the phase angle shift.

Therefore, the total impedance $Z$, the real part, $Re(Z)$, and the imaginary part, $Im(Z)$, of the complex impedance can be written as

$$Z = |Z|(cos\varphi - jsin\varphi) \qquad \text{(Equation 2.5)}$$

$$Re(Z) = Z' = |Z|cos\varphi \quad \text{(Equation 2.6)}$$

$$Im(Z) = Z'' = -|Z|sin\varphi \quad \text{(Equation 2.7)}$$

Where $|Z|$ is the magnitude of $Z$.

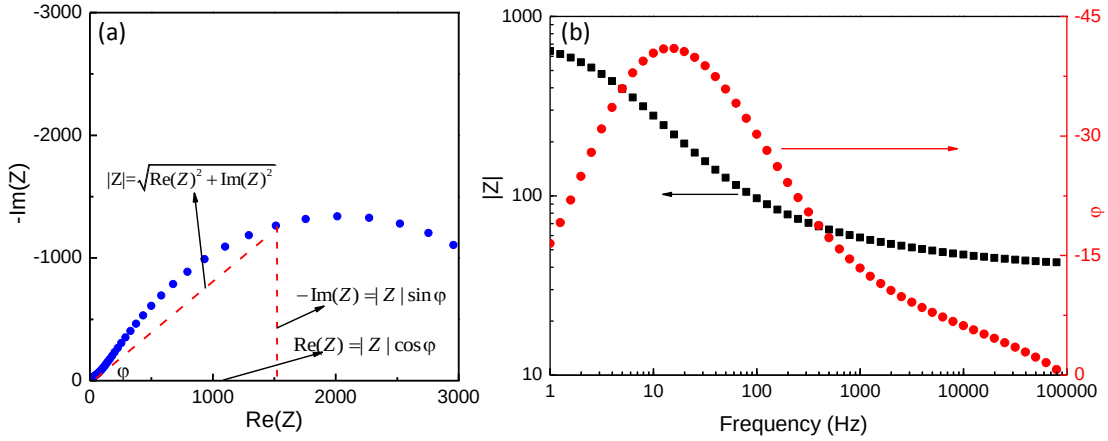


Figure 2.17 The representative impedance graphs: (a) Nyquist plot and (b) Bode plots

There are two ways to present the complex impedance graphically [226]: Nyquist plot with *–Im(Z)* as a function of *Re(Z)* and Bode plot with *log|Z|* or *φ* as a function of *logf*, as shown in Figure 2.17(a) and (b).

### 2.3.3.2 Equivalent circuit

The EIS data describe a series of electrochemical behaviours of the studied system. In order to separate and understand the different contributions, equivalent circuit is proposed to fit with the impedance data. The equivalent circuit consists of a number of different electrical elements (such as resistor, capacitor, inductor, constant phase element (CPE) etc.) in parallel, in series, or in combination of both. The reasonable explanation for the studied system depends on the selection of the electrical elements and their interconnections.

The commonly used elements in the equivalent circuit, along with their impedances and admittances are listed in Table 2.1. R is a resistor, representing the conductive pathways for electron and ion transport. L is an inductor, which is associated with adsorption/desorption processes at an electrode. C is a capacitor, which is associated

with the charge/discharge processes between the electrochemical double layers. Inductor and capacitor can be referred to space-charge polarization regions [227]. Besides the three ideal elements, the constant phase element (CPE) and Warburg element (W) have been found widespread use in the real system because the processes occurring in the real system is not distributed in time and space ideally. The impedance behaviour of CPE depends on the exponent *n (0 ≤ n ≤ 1)*. For a condition *n = 1*, CPE becomes a pure capacitor C with $Q = C$; for a case *n = 0*, CPE represents an ideal resistor with $Q = 1/R$. In a real application of CPE, *n* is determined from a slope of a plot of *logIm(Z)* VS *logf* and defined between 0 and 1. When *n = 0.5*, CPE describes the Warburg impedance for homogeneous semi-infinite diffusion [228].

Table 2.1 Impedances and admittances of the commonly used electrical elements [229]

| Element | Symbol | Impedance | Admittance |
|---|---|---|---|
| Resistor | R | $R$ | $\frac{1}{R}$ |
| Inductor | L | $j\omega L$ | $\frac{1}{j\omega L}$ |
| Capacitor | C | $\frac{1}{j\omega C}$ | $j\omega C$ |
| Constant Phase Element (CPE) | Q | $\frac{1}{Q(j\omega)^n}$ | $Q(j\omega)^n$ |
| Warburg element | W | $\frac{1}{Q\sqrt{j\omega}}$ | $Q\sqrt{j\omega}$ |

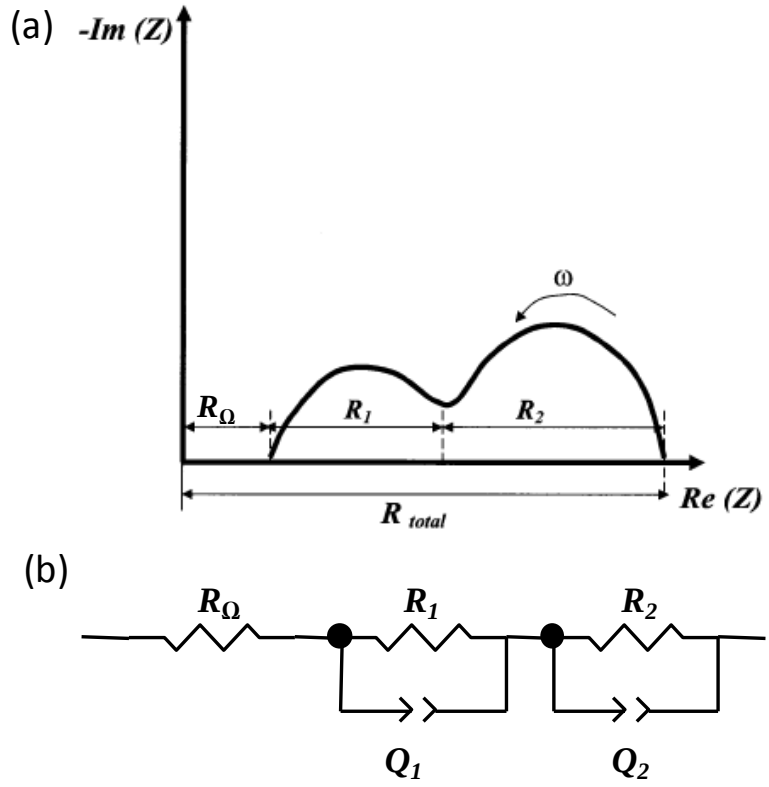


Figure 2.18 (a) Nyquist diagram of impedance and (b) the corresponding equivalent circuit of a typical fuel cell under OCV

Figure 2.18 shows EIS response and the corresponding equivalent circuit of a typical fuel cell under OCV and operating condition. The impedance graph in Figure 2.18(a) is composed of two semicircles referred to as HF for high frequency and LF for low frequency. Two clearly separated arcs in the different frequency domains indicate that the electrochemical reaction of the cell is controlled by two different electrode polarization processes. In general, the HF arc is associated to charge transfer reaction at the electrode/electrolyte interfaces and TPBs [199]; while the LF arc corresponds to the gas diffusion reaction within the electrodes [230]. The ohmic resistance of the cell ($R_s$), determined from the high-frequency intercepts with the abscissa as shown in Figure 2.18(a), primarily comes from the fuel cell electrolyte, as well as electrical resistance in the electrodes and lead wires. To analyze the polarization resistance of electrodes ($R_p$), which is represented by the distance between the high and low frequency intercepts of the curve with the abscissa, an equivalent circuit of $R_\Omega(R_1Q_1)(R_2Q_2)$ (Figure 2.18(b)) is used to fit the electrochemical impedance spectra. In the circuit, $R_\Omega$ is the ohmic resistance, $R_1$ and $R_2$ are polarization resistance in HF

and LF domain, and Q a constant phase element (CPE) relating to the nonohmic processes in the electrodes. The sum of $R_1$ and $R_2$ is considered to be the total polarization resistance of electrodes ($R_p$).

In this study, electrochemical impedance testing was carried out with two-electrode configuration (shown in Figure 2.16) using a combination of Solartron 1255 Frequency Response Analyser, Solartron 1287 Electrochemical Interface and ZPlot v3.2c software (Scribner Associates). The frequency in the cell impedance testing ranged between 1MHz and 0.04Hz, and a sinusoidal voltage with the amplitude of 10mV was applied to the system as a perturbation signal. The EIS testing results were recorded at OCV condition. Some of the impedance data were simulated using the equivalent circuit by ZView 3.1 software (Scribner Associates) in this study (see section 3.3).

#### 2.3.3.3 Studying the electrical properties of bulk using impedance spectroscopy

Electrochemical Impedance Spectroscopy (EIS) has been extensively used to study the electrochemical behaviour of materials and interfaces. Besides the fact that it can be used to analyze the different processes that occur in the whole fuel cell, it also can be used to describe the electrical properties of a bulk material for understanding the conduction mechanism by separating the bulk and grain boundary resistance.

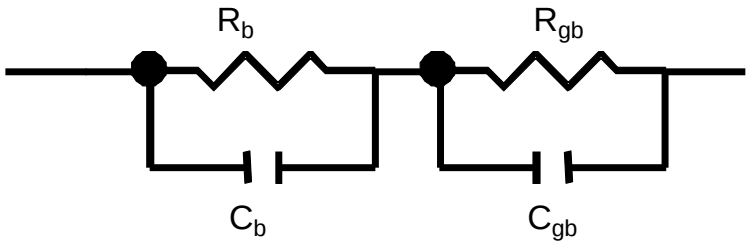


Figure 2.19 Equivalent circuit of the impedance spectrum for a bulk electroceramic: two parallel RC elements in series

For a ceramic material, bulk and grain boundary controlled processes can generally be described by placing a resistor and a capacitor in parallel, known as parallel RC element. In this case, an equivalent circuit containing two parallel RC elements in

series can represent the electrochemical phenomena of a ceramic sample: bulk and grain boundary transport, respectively. Figure 2.19 shows an equivalent circuit for describing the electrical properties in a ceramic bulk. For the individual parallel RC element, the relaxation time, $\tau$ can be expressed by:

$$\tau = \frac{1}{\omega_{summit}} = RC \qquad \text{(Equation 2.8)}$$

Where, $\omega_{summit}$ represents the summit frequency of the semicircle that is descried by the parallel RC element. R and C are the bulk or grain boundary resistance and capacitance, respectively.

Under an assumption that the studied ceramic behaves as a flat plane capacitor, the capacitance is strongly associated with its geometry, A/d (A and d are the surface area of one plate and the distance between two plates, respectively) and its dielectric constant, $\varepsilon_r$. The capacitance can be given by the following equation:

$$C = \frac{\varepsilon_0 \varepsilon_r A}{d} \qquad \text{(Equation 2.9)}$$

Where $\varepsilon_0$ is the permittivity of vacuum, $8.854 \times 10^{-12}$F/m. In a typical sintered sample where A/d is expected to be 1-10 cm and the dielectric constant ~10, the bulk capacitance can be calculated by the equation (2.9) in the order of $10^{-11}$-$10^{-12}$F [231].

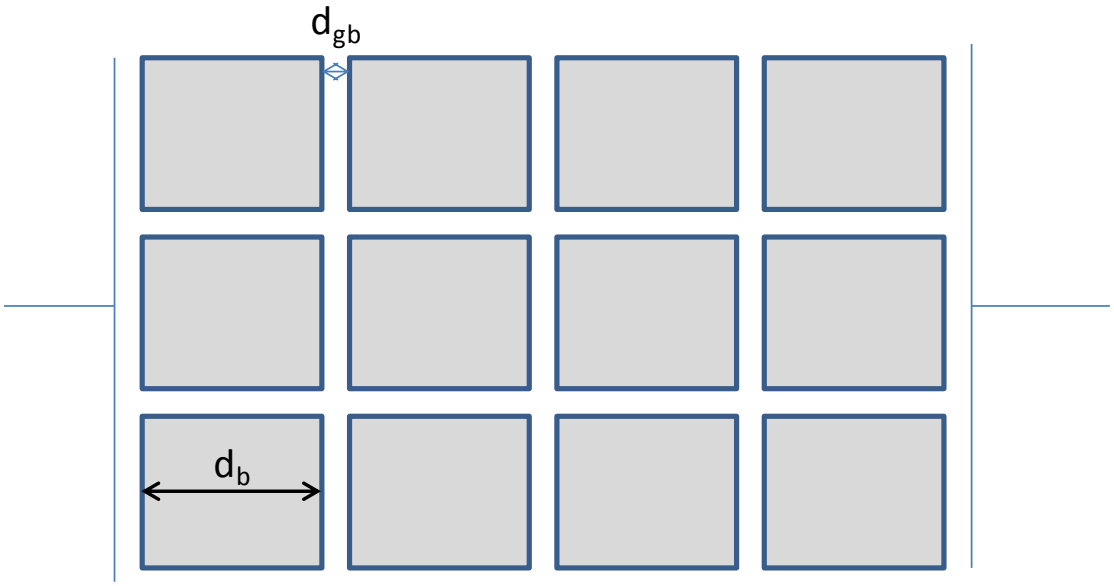


Figure 2.20 A brickwork model for the sintered sample, where $d_b$ and $d_{gb}$ are the bulk dimension and grain boundary thickness, respectively

A brickwork model is used to describe an idealized ceramic sample, as shown in Figure 2.20. In this model, a ceramic sample is comprised of cube-shaped grains with bulk dimension (or grain size) $d_b$, separated by a grain boundary with thickness $d_{gb}$. Then the relationship of bulk capacitance $C_b$ and grain boundary capacitance $C_{gb}$ can be obtained:

$$\frac{C_b}{C_{gb}} = \frac{d_{gb}}{d_b} \qquad \text{(Equation 2.10)}$$

The subscripts b and gb stand for bulk and grain boundary, respectively. According to this equation, the well-sintered sample with narrow grain boundary thickness will have a higher grain boundary capacitance. It is found that a typical capacitance of grain boundary is in the range of $10^{-11}$-$10^{-8}$F [231].

Besides the bulk and grain boundary effects can be extracted from the impedance data, the electrode processes, such as charge transfer, adsorption/desorption of electrochemical species, electrochemical reaction etc., can be distinguished at the low frequency with a higher capacitance [232]. The capacitance associated with the electrode processes lie in the range of $10^{-7}$-$10^{0}$F.

In order to get better contact between the lead wire and the sample, platinum paste was applied on both the flat surfaces of the sintered $LSCT_{A-}$ pellet and then fired at $900^oC$ for 30 minutes in air. The AC impedance measurements were carried out using the two-electrode configuration in the frequency range of 10MHz to 1Hz and the temperature range of 290-$675^oC$ in air. The impedance data were taken using a Solartron 1260 impedance/gain-phase analyzer. A thermocouple was placed next to the pellet to record the temperature. The measured impedance data were then analyzed by the Zview software and the values of capacitances and resistances were extracted by fitting the experimental data with RC elements to segregate the contribution of grain and grain boundary.

# Chapter 3. Characterization of $LSCT_{A-}$ powder and its initial performance for anode-supported SOFCs prepared by aqueous tape casting

## 3.1 Characterization of $LSCT_{A-}$ powder

### 3.1.1 Analysis of X-ray Diffraction (XRD)

$La_{0.2}Sr_{0.25}Ca_{0.45}TiO_3$ ($LSCT_{A-}$) powder was supplied by Topsoe Fuel Cells as part of the EU FCH-JU project SCOTAS and was calcined at different temperature ranging from 900°C to 1300°C for 5h. Figure 3.1 presents the X-ray diffraction (XRD) pattern spectra of $LSCT_{A-}$ powder calcined at varied temperatures, demonstrating that a pure perovskite structure has obtained. All the peaks were indexed to orthorhombic (Pbnm) structure using WinXPOW software and identified by the corresponding miller indices (h, k, l values) in Figure 3.1.

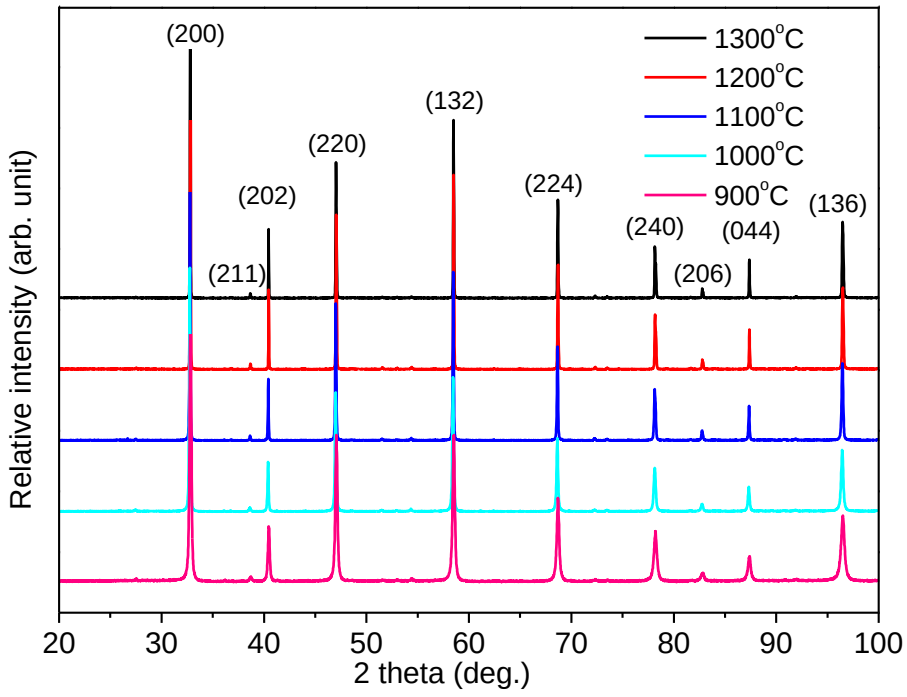


Figure 3.1 X-ray diffraction (XRD) patterns of $LSCT_{A-}$ powders calcined at different temperatures ranging from 900 to 1300°C for 5h

At room temperature, A-site deficient $La_{0.2}Sr_{0.7}TiO_3$ and $La_{0.2}Ca_{0.7}TiO_3$ respectively show cubic (Pm3m) [135] and orthorhombic (Pbnm) structure [233]. With the increasing Ca content $La_{0.2}Sr_{0.7-x}Ca_xTiO_3$ system undergoes from cubic (Pm3m) for x=0 to tetragonal (I4/mcm) for x=0.1-0.4 to orthorhombic (Pbnm) for x≥0.45 [189]. The symmetry of lanthanum strontium titanate has been decreased by the substitution of smaller size $Ca^{2+}$ (1.34Å) for larger size $Sr^{2+}$ (1.44Å) due to the enhanced distortion of perovskite structure by decreasing the tolerance factor [234]. The Goldschmidt tolerance factor (*t*) generally refers to defect-free perovskite and is a dimensionless value associated with the structure stability, which can be expressed as:

$$t = \frac{r_A + r_O}{\sqrt{2}(r_B + r_O)} \qquad \text{(Equation 3.1)}$$

Where $r_A$, $r_B$ and $r_O$ are the radii of the A cation, B cation and oxygen anion, respectively. Assuming that the A-site vacancies can be seen as the occupied sites with the radius equivalent as zero, the tolerance factor of cubic $La_{0.2}Sr_{0.7}TiO_3$ is calculated to be 0.945, and it has been decreased to 0.929 for orthorhombic $LSCT_{A-}$, which is in good agreement with the transformation of the symmetry of the crystal structure.

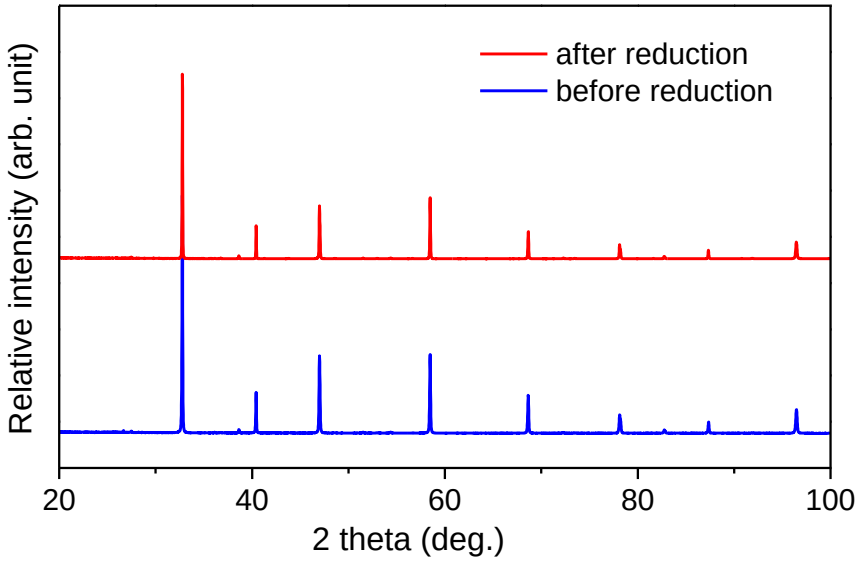


Figure 3.2 X-ray diffraction (XRD) patterns of $LSCT_{A-}$ powder calcined at 1100°C for 5h before and after being reduced at 1000°C for 2h in 5% $H_2$-Ar mixtures

Table 3.1 The refined cell parameters and volumes in terms of the XRD patterns of $LSCT_{A-}$ powder calcined at 1100°C for 5h before and after being reduced at 1000°C for 2h in 5% $H_2$-Ar mixtures

| Sample | Space group | a (Å) | b (Å) | c(Å) | Volume($Å^3$) |
|---|---|---|---|---|---|
| Before reduction | Pbnm | 5.4681(8) | 5.4670(3) | 7.7329(5) | 231.17(4) |
| After reduction | Pbnm | 5.473(9) | 5.4671(8) | 7.733(3) | 231.4(4) |

After reduction at 1000°C in 5% $H_2$-Ar atmosphere, the colour of the sample changes from light yellow to black, while the composition retaining its perovskite structure and no extra peaks were observed (Figure 3.2). The refined cell parameters and volumes for $LSCT_{A-}$ sample calcined at 1100°C without and with reduction are listed in the table 3.1, showing an expansion of cell parameter after reduction, especially the value a. The increase in the lattice parameter for the reduced sample is most likely due to the formation of the higher volume of $Ti^{3+}$ ions (ionic radius of 0.67Å compared to 0.60Å for $Ti^{4+}$, CN=6) under reducing conditions; however, the formation of oxygen vacancies by the removal of oxygen anions from the lattice could result in the decease of the lattice parameter [235]. So the combination of two contrary effects determines the change of the lattice parameters. The small variation in the lattice parameter suggests that the compound has high stability against redox cycles during operation.

The XRD of mixed $LSCT_{A-}$ and YSZ powder fired at 1400°C for 2h is shown in Figure 3.3, along with XRD patterns of pure $LSCT_{A-}$ and YSZ as comparison. No evidence of impurity phases due to a chemical reaction is found. It has been pointed out in the previous study [236], that the chemical stability with YSZ is likely to be improved by the introduction of A-site deficiency.

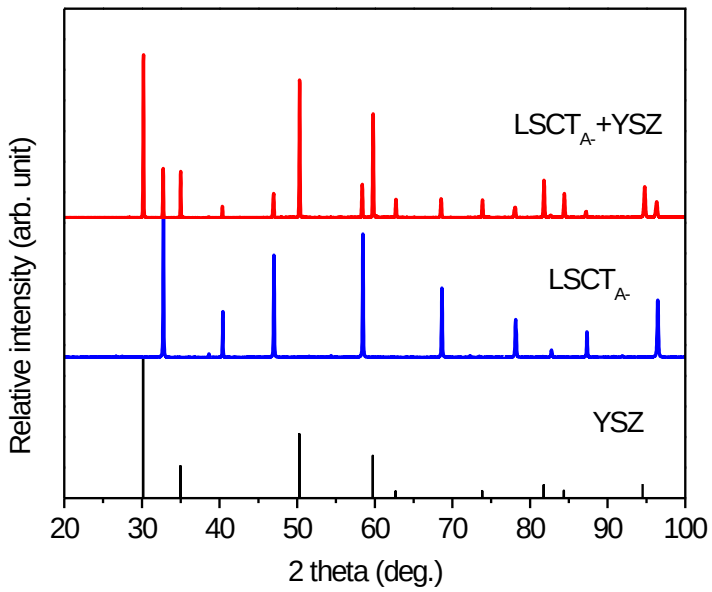


Figure 3.3 X-ray diffusion (XRD) patterns of mixture of $LSCT_{A-}$ and YSZ powders fired at 1400°C for 2h (the upper one), $LSCT_{A-}$ powder calcined at 1100°C for 5h (the middle one) and 8YSZ (the bottom one) (PDF card No.00-30-1468)

### 3.1.2 Particle Size Analysis (PSA) and Specific Surface Area (SSA)

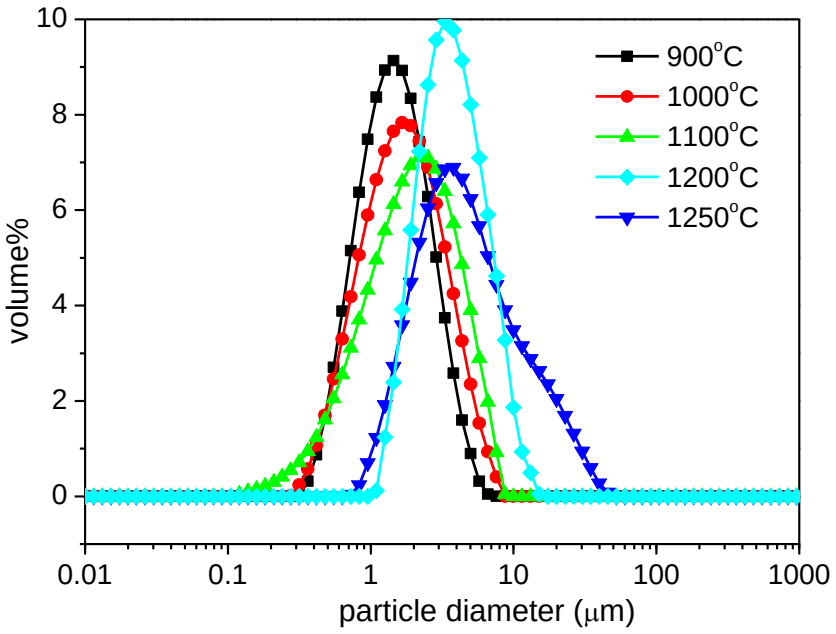


Figure 3.4 Particle size distribution of $LSCT_{A-}$ powder after calcination at 900-1250°C for 5h in air and ball milling for 24h

Table 3.2 Mean particle size and specific surface area (SSA) of $LSCT_{A-}$ powder after calcination at varied temperatures and ball milling

| Calcination Temp (℃) | $d_{(0.5)}$ (μm) | SSA ($m^2g^{-1}$) |
|---|---|---|
| As-received powder | - | 35.84 |
| 900 | 1.542 | 9.62 |
| 1000 | 1.781 | 6.17 |
| 1100 | 2.198 | 2.14 |
| 1200 | 3.774 | 0.66 |
| 1250 | 4.212 | 0.47 |

The particle size of $LSCT_{A-}$ powder is an important parameter to the tape-casting slurry in respects of dispersion, homogeneity of ceramics particles, viscosity of the slurry, the sintering behaviours of green tapes and the final structure. Because the calcination process is likely to cause the agglomeration of fine particles, all the powders for the particle size analysis have been ball milled for 24h in deionised water with addition of dispersant in advance. The PSA results of $LSCT_{A-}$ powders after thermal treatment and ball milling are presented in Figure 3.4. A narrow and unimodal distribution is observed for all the cases. When calcination temperature is increased from 900$^oC$ to 1250$^oC$, the distribution shifts from the fine particles to coarser particles.

The mean particle size $d_{(0.5)}$ and specific surface area (SSA) of all samples are presented in Table 3.2. The SSA of the as-received powder is 35.84$m^2g^{-1}$, much larger than calcined powders, indicating that it is composed of much smaller particles. The specific surface area (SSA) decreases with increasing calcination temperature, demonstrating a quick growth process of $LSCT_{A-}$ powder under calcination, which is in good agreement with the tendency of the mean particle size due to the inverse relationship between particle size and surface area.

### 3.1.3 Scanning Electron Microscopy (SEM)

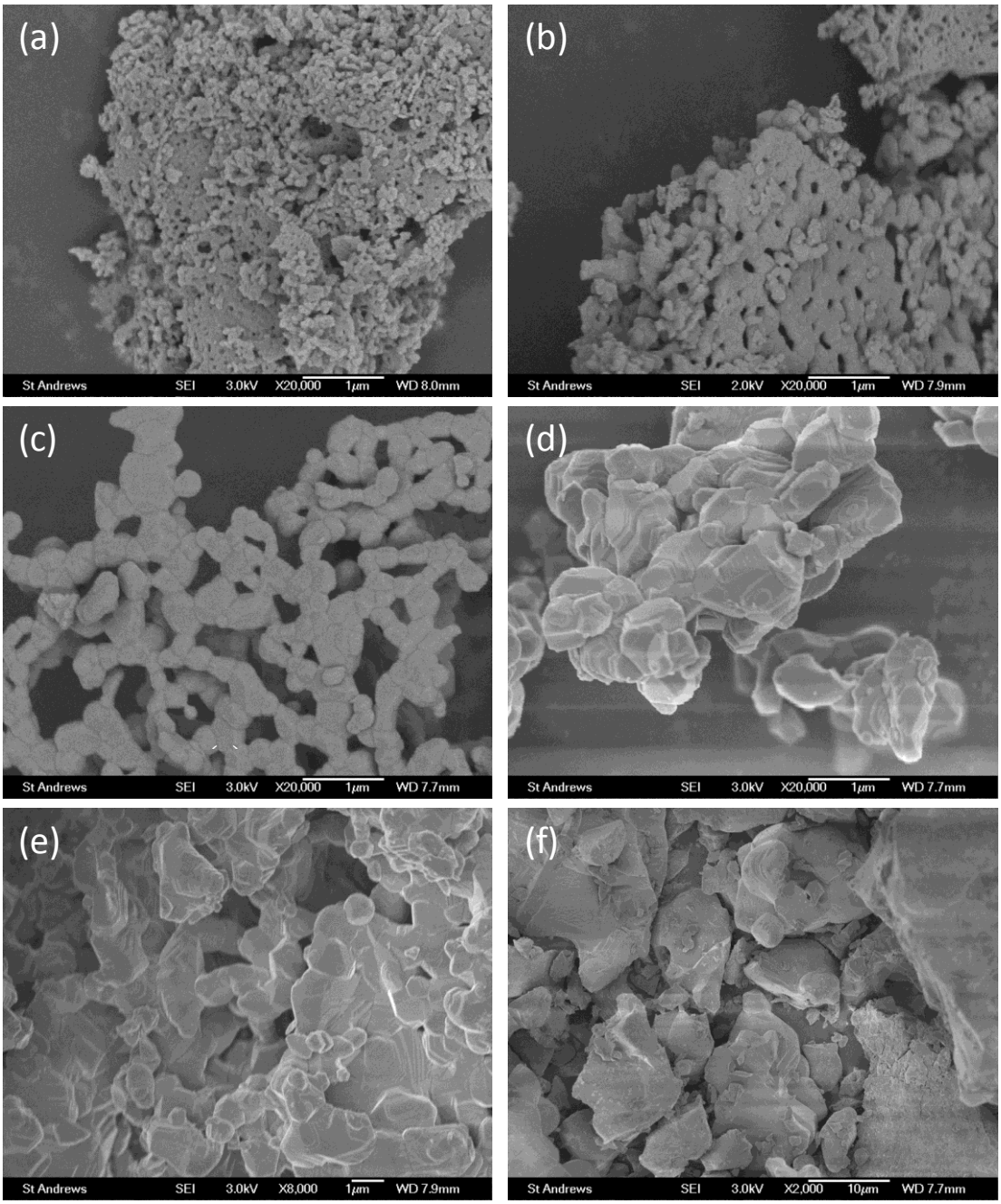


Figure 3.5 Scanning electron microscopy (SEM) images of $LSCT_{A-}$ powder after calcination at (a) 900°C, (b) 1000°C, (c) 1100°C, (d) 1200°C, (e) 1250°C and (f) 1300°C

Scanning electron microscopy (SEM) analysis (Figure 3.5) of $LSCT_{A-}$ powders calcined at different temperatures shows increasingly large grain size with the increasing heating temperature. The increase in the grain size of the powders is

induced by the agglomeration, absorption and sintering of small grains due to thermally activated diffusion process, which has been introduced in the previous study [237]. It has been noted that the powder calcined at 900°C is comprised of fine and isolated grains with average grain size of 100nm (Figure 3.5(a)); after calcinations at 1000 and 1100°C, the necking between grains is formed with the average grain size being hundreds of nanometres (Figure 3.5(b) and (c)); when the calcination temperature is increased above 1200°C, the powder shows apparent clusters and agglomeration forming micro-sized particles.

### 3.1.4 Dilatometry

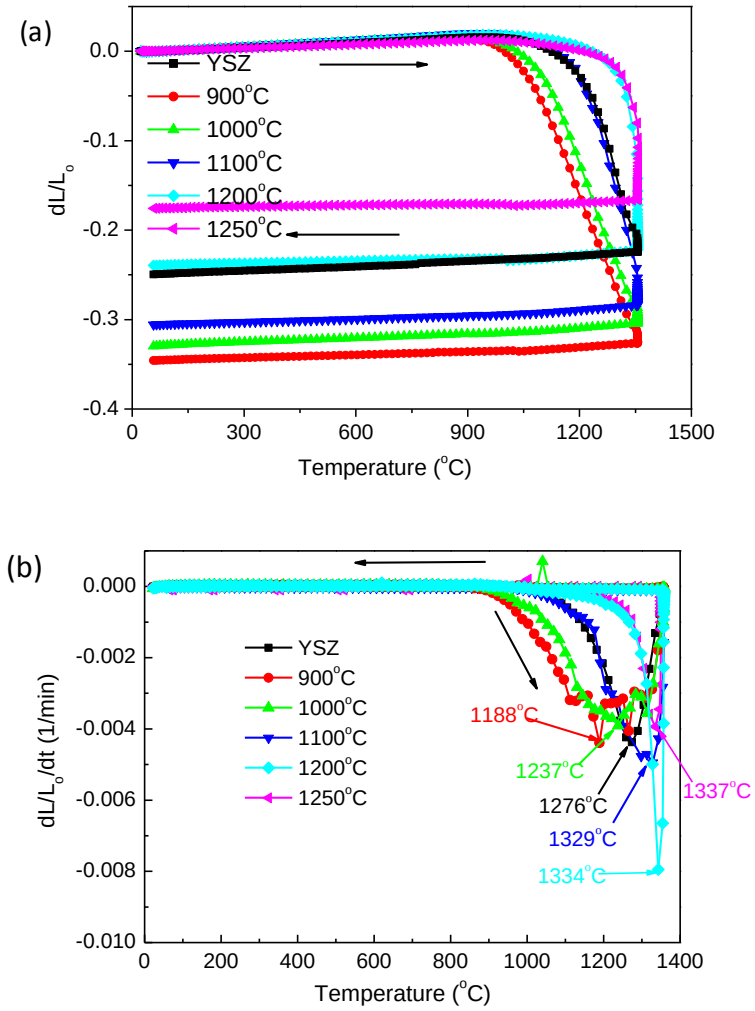


Figure 3.6 (a) Sintering and (b) shrinkage rate curves for $LSCT_{A-}$ powders calcined at different temperatures and YSZ powder as a function of temperature in air

In this study, YSZ and $LSCT_{A-}$ powders are used for the electrolyte and anode, respectively. Therefore, the sinterability of $LSCT_{A-}$ and YSZ is very important to avoid the defect of the cell in terms of delamination or cracks because of the stresses between the electrolyte and anode originated from the mismatch of sintering process.

Precalcination is used to tailor the commercial $LSCT_{A-}$ powder to match the sinterability with the YSZ electrolyte in this study. Because the sintering process of ceramic powder at high temperature involves the vacancy diffusion on the surface and through the grain boundary, the precalcined powder is very effective in tuning the properties of the ceramic for a porous support through high temperature sintering. The shrinkage extent and the onset sintering temperature are the main parameters to determine the compatibility of two powders. The dilatometer curves and the corresponding shrinkage rate of calcined $LSCT_{A-}$ and YSZ powder in air are used to scope the sinterability of the two powders, as shown in Figure 3.6. Most of the shrinkage occurred during the heating stages, indicating the shrinkage process of the heating stage is the main cause of the residual stresses produced in the cell. YSZ sample expands with increasing temperature up to around 1100$^{o}$C because of the thermal expansion, and then shrinks abruptly to the maximum shrinkage rate at 1276$^{o}$C (Figure 3.6(b)), followed by a lower shrinkage rate to 1350$^{o}$C, revealing that the sintering process approaches to the final stage. The onset sintering temperature of $LSCT_{A-}$ powder calcined below 1000$^{o}$C is lower than that of YSZ, and the total shrinkage is much larger than YSZ, reaching 34.5% and 32.9% for the powder calcined at 900$^{o}$C and 1000$^{o}$C, respectively, while the final shrinkage of YSZ powder is only 24.9%. The $LSCT_{A-}$ powders calcined below 1000$^{o}$C seem to approach the maximum shrinkage rate at lower temperature than YSZ. The $LSCT_{A-}$ powder precalcined at 1100$^{o}$C shows a very similar sintering curve to the YSZ until the temperature reaches 1276$^{o}$C corresponding to the maximum shrinkage rate for YSZ: a continued fast sintering of the $LSCT_{A-}$ powder after this temperature causes the mismatch of final shrinkage. The $LSCT_{A-}$ powders calcined at 1200 and 1250$^{o}$C display a higher initiating temperature of densification and a smaller overall shrinkage than those of YSZ, which is in good agreement with the aforementioned BET analysis results. The temperature for the maximum shrinkage rate has been increased to 1334 and 1337$^{o}$C for the powder calcined at 1200 and 1250$^{o}$C, respectively. The evident

discrepancy of the temperature of the maximum shrinkage rate between $LSCT_{A-}$ and YSZ may induce the local stresses between electrolyte and anode, causing the crack and delamination of the cell [238]. The final shrinkage and temperature for the maximum shrinkage rate are shown in Table 3.3.

Table 3.3 Final shrinkage and temperature for the maximum shrinkage rate of $LSCT_{A-}$ powder calcined at different temperatures from 900 to 1250°C, along with YSZ as a comparison

| Powder | Total shrinkage (%) | Temperature for the maximum shrinkage rate (°C) |
|---|---|---|
| YSZ | 24.9 | 1276 |
| $LSCT_{A-}$ 900°C | 34.5 | 1188 |
| $LSCT_{A-}$ 1000°C | 32.9 | 1237 |
| $LSCT_{A-}$ 1100°C | 30.5 | 1329 |
| $LSCT_{A-}$ 1200°C | 23.8 | 1334 |
| $LSCT_{A-}$ 1250°C | 17.6 | 1337 |

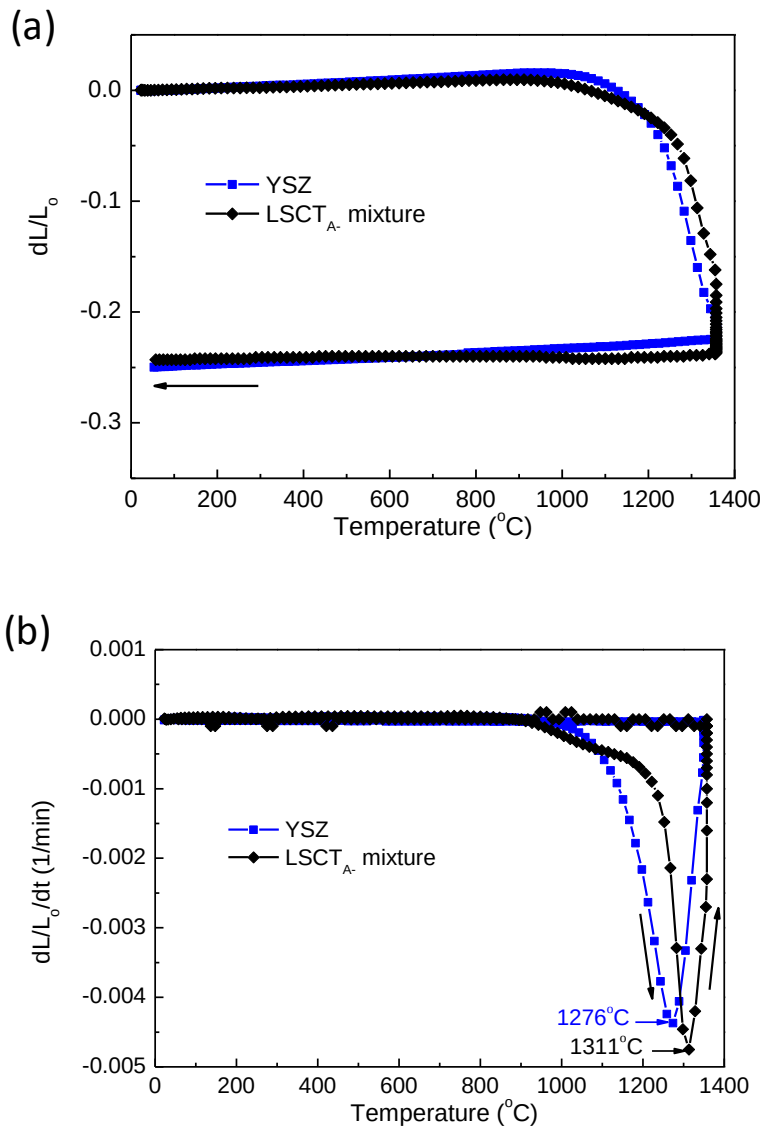


Figure 3.7 (a) Sintering and (b) shrinkage rate curves for mixed $LSCT_{A-}$ powder calcined at 1100°C (10wt.%) and 1250°C (90wt.%) compared with YSZ powder as a function of sintering temperature in air

Based on the comparison of the dilatometric sintering results of $LSCT_{A-}$ powder precalcined at different temperatures with YSZ powder, it can be concluded that the shrinkage behaviour of $LSCT_{A-}$ powder calcined at a certain temperature is not compatible with the YSZ electrolyte. The mismatch could cause the delamination or cracks on the cell components during sintering, resulting in the disfunction of the whole cell. In order to make a better match in both the overall shrinkage and shrinkage rate with YSZ, the mixed $LSCT_{A-}$ powder containing 10wt.% calcined at

1100°C and 90wt.% calcined at 1250°C was used. The mixture shows a very similar sintering shrinkage with YSZ, 24.3% for the mixed $LSCT_{A-}$ pellet and 25.0% for YSZ pellet (Figure 3.7(a)). It is important to notice that during 3h dwelling at 1350°C, $LSCT_{A-}$ green pellet shows a much larger shrinkage than YSZ (7.4% comparing with 2.3%), so for co-sintering process the dwelling time is crucial to keep the YSZ and $LSCT_{A-}$ bonded to each other. The discrepancy of the temperature corresponding to the maximum shrinkage rate between $LSCT_{A-}$ mixture and YSZ can be observable in Figure 3.7(b) (1311°C for $LSCT_{A-}$ mixture and 1276°C for YSZ), but the pores from the graphite in $LSCT_{A-}$ green tape might alleviate the strain through the rearrangement of $LSCT_{A-}$ powder.

### 3.1.5 Thermal Expansion Coefficient (TEC)

The thermal compatibility between the anode materials and other fuel cell components is crucial during fabrication or at thermal cycles during operation. According to the reported TEC values for dense and porous LST samples [154], the porosity of anode could play an important role in affecting the TEC values. The anode material requires to present sufficient porosity in order to allow gas diffusion to the triple phase boundary (TPB) for the electrochemical reaction so the relationship between the anode porosity and thermal compatibility of anode and other fuel cell components should be considered. In general, the porosity and the relative density of a sample have an inverse relationship. Therefore, the prepared samples are characterized by the corresponding relative densities.

In this work, the relative density, $\rho_r$ , is expressed as a ratio of the experimental density to the theoretical density

$$\rho_r = \frac{\rho_e}{\rho_t} \times 100\% \qquad \text{(Equation 3.2)}$$

Where $\rho_e$ and $\rho_t$ are the experimental and theoretical density, respectively.

The experimental density in $g/cm^3$ is calculated by the geometry of the sintered samples, which can be given by the following equation

$$\rho_e = \frac{mass}{volume} = \frac{4mass}{\pi d^2 l} \qquad \text{(Equation 3.3)}$$

Where $l$ and $d$ are the thickness and diameter of the sintered pellet in cm, respectively.

The theoretical density in $g/cm^3$ is calculated by using the cell parameters according to the following equation

$$\rho_t = \frac{m}{V} = \frac{\frac{M}{N} \times Z}{V} = \frac{MZ}{NV} \qquad \text{(Equation 3.4)}$$

Where $m$ and $V$ are the mass and volume of the unit cell, $M$ is the formula weight of the ceramic composition in g/mol, $Z$ is the number of formula units in one unit cell, $N$ is the Avogadro number known as $6.022 \times 10^{23}$/mol.

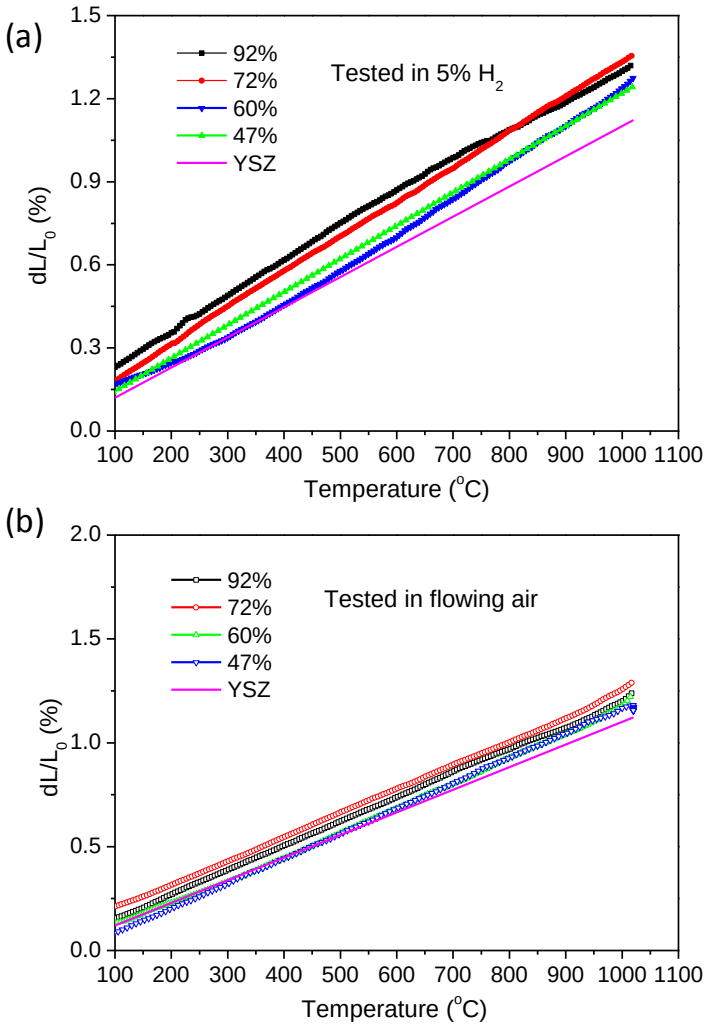


Figure 3.8 Thermal expansion curves for $LSCT_{A-}$ samples with different relative density (47-92%) sintered in air at 1350°C for 2h, measured in (a) 5% $H_2$-Ar atmosphere and (b) flowing air

The thermal expansion behaviours of $LSCT_{A-}$ pellets sintered at 1350°C for 2h in various atmospheres are plotted in Figure 3.8 and compared with the thermal expansion of the YSZ electrolyte. The thermal expansion coefficients (TEC) are calculated and summarized in Table 3.4. The TEC values on both heating and cooling stages for every sample are very reproducible so only the data on cooling are shown above. It is found that all the samples with varied relative density in reducing atmosphere and air at the range of 100-1000°C present similar TEC values. Therefore, in our cases, the TEC values are not associated with the porosity (or relative density) of the samples in two atmospheres. There values are close to those of $11\text{-}12 \times 10^{-6} K^{-1}$

in the temperature range 50-1000$^oC$ for $La_xSr_{1-x}TiO_{3+\delta}$ (x=0.1-0.4) samples [134]. The samples with relative density between 47 and 92% show lower thermal expansion coefficient (TEC) values in air than those in reducing conditions but still slightly higher than that of a typical zirconia based electrolyte. The slightly higher TEC values in reducing atmosphere than those in air could be attributed to the formation of $Ti^{3+}$ ions in reducing atmosphere. However, the small difference of TEC values between YSZ and porous $LSCT_{A-}$ may be a cause of possible fuel cell testing problems, e.g. spalling of YSZ from $LSCT_{A-}$ anode during operation or cracking upon thermal cycles.

Table 3.4 Thermal expansion coefficients (TECs) for $LSCT_{A-}$ pellets with different relative density (44-92%) in various atmospheres from 100 to 1000$^oC$

| Atmosphere | Relative density (%) | TEC ($\times 10^{-6}K^{-1}$) |
|---|---|---|
| 5% $H_2$-Ar | 92 | 12.0 |
| | 72 | 12.7 |
| | 60 | 12.1 |
| | 47 | 12.0 |
| Flowing air | 92 | 11.6 |
| | 72 | 11.5 |
| | 60 | 11.6 |
| | 47 | 11.8 |
| 8mol.% yttria-stabilized zirconia (YSZ) [88] | | 10.6-10.9 |

### 3.1.6 Electrical conductivity

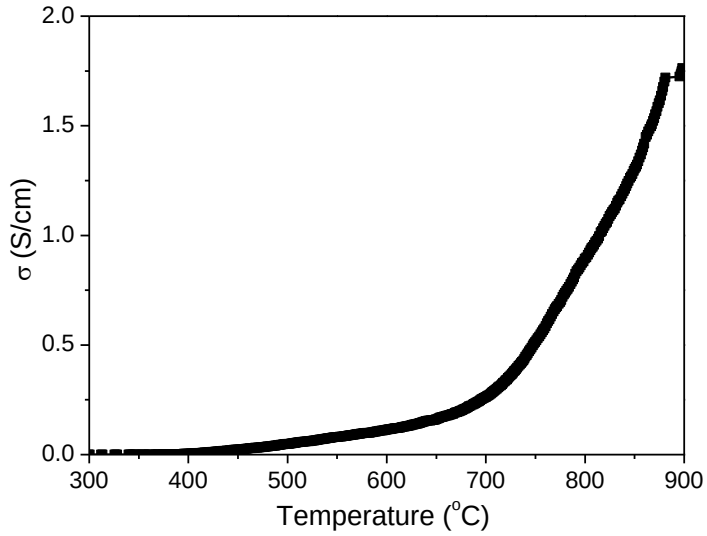


Figure 3.9 Electrical conductivity of $LSCT_{A-}$ sample with a relative density of 60% in 5% $H_2$-Ar atmosphere as a function of temperature

It has been noted that the electrical conductivity of LST or YST depends to a very large extent on the preparation and processing procedure leading to different porosity and concentration of $Ti^{3+}$ ions [235,239]. The desired electrical conductivity of anode materials as a porous support is set to be greater than 1S/cm [240]. In dense form, the conductivity would need to be at least one order of magnitude greater. The conductivity of the $LSCT_{A-}$ sample with a high relative density around 91% has been reported that after pre-reduction at 1050°C under 5% $H_2$-Ar condition for 72h, it could be 30S/cm [189], while a very slow reduction process at 880°C [234] implies that high-temperature reduction may be required for $LSCT_{A-}$ anode support to maintain its high electrical conductivity.

Because the anode support requires to be sufficiently porous for the diffusion of fuel, the samples for conductivity measurement were prepared by the tape casting technique and sintering at 1350°C in air for 2h, the same as the fuel cell anode fabrication. The electrical conductivity of a porous $LSCT_{A-}$ sample with a relative density of 60% was carried out in 5% $H_2$-Ar atmosphere with the increasing temperature to 900°C, as shown in Figure 3.9. It was found that the conductivity increase with temperature suggesting a semiconducting behaviour. At 900°C, the

conductivity can reach 1.7S/cm due to the reduction of $Ti^{4+}$ to $Ti^{3+}$, which is sufficient to provide electrical pathways for SOFC anodes. However, at the operation temperature of 700°C, the conductivity is only 0.25S/cm, indicating a high ohmic resistance could be caused by the low conductivity of the anode, leading to the inferior performance; for example, for an anode support with thickness of 0.5mm, an ohmic loss of $0.2\Omega cm^2$ could be obtained for the anode.

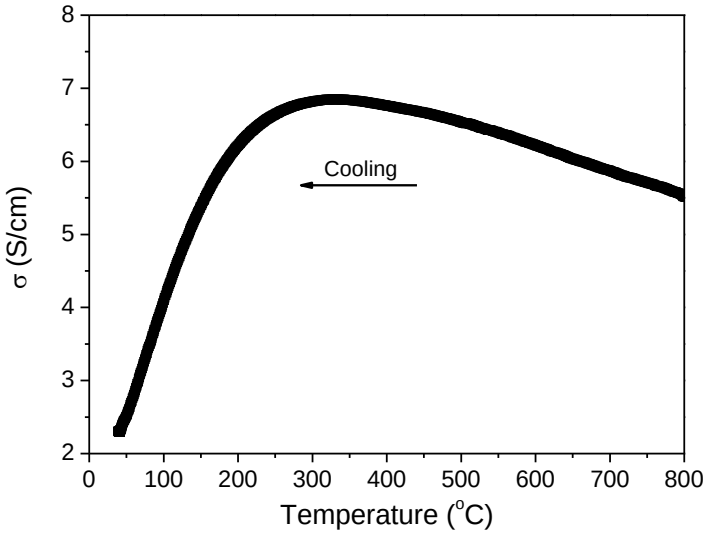


Figure 3.10 Temperature dependence of the electrical conductivity of a pre-reduced $LSCT_{A-}$ sample with a relative density of 60% in 5% $H_2$-Ar atmosphere on cooling stage

In order to investigate the influence of the pre-reduction condition on the conductivity, a porous sample with a relative density of 60% was sintered at 1350°C in air, followed by pre-reduction at 1000°C for 24h in tube furnace under a constant purge flow of 5% $H_2$-Ar before conductivity measurement. To avoid the re-oxidation of the pre-reduced sample, 5% $H_2$ was fed into the jig with the sample in place for one hour to flush away the residue air before increasing the temperature for measurement. The temperature dependence of the electrical conductivity in reducing atmosphere is shown in Figure 3.10. The measurement was carried out upon cooling from 800°C to room temperature after being kept at 800°C for 24h under $PO_2<10^{-22}$atm in 5% $H_2$-Ar atmosphere. The conductivity increases with the decreasing temperature until 300°C, and below this temperature, the conductivity decreases with the decrease of the

temperature, showing a metal–semiconductor transition from high temperature to room temperature. At 700°C, a conductivity of 5.9S/cm is obtained for a porous sample, which is quite promising for the electronic transport as an anode support. However, the conductivity value is much lower than the one reported for porous $La_{0.4}Sr_{0.4}TiO_3$ samples, probably due to more A-site vacancies and substitution of $La^{3+}$ for $Sr^{2+}$, and higher reducing temperature up to 1100-1300°C [235] leading to the massive formation of $Ti^{3+}$ ions.

According to the conductivity measurement, $LSCT_{A-}$ is a good candidate as anode material for intermediate temperature SOFCs after pre-reduction at high temperature around 1000°C. However, careful consideration should be made when impregnating catalyst into the electrodes to prevent the re-oxidation of reduced anode during thermal treatment of the catalyst precursors.

## 3.2 Cell fabrication

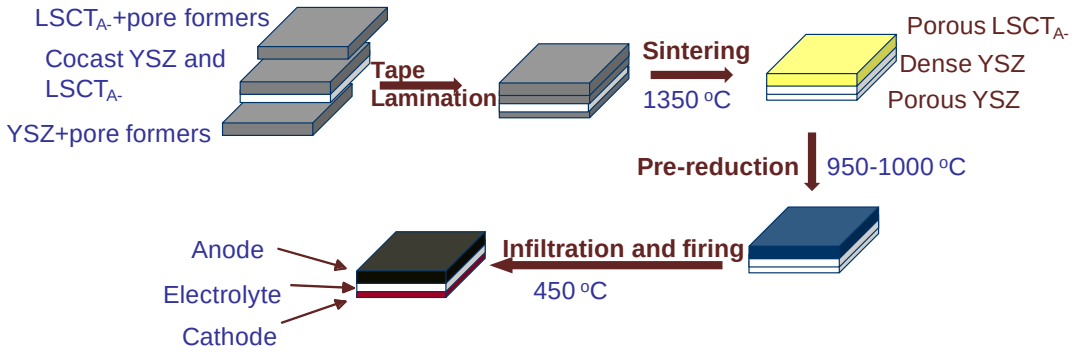


Figure 3.11 Process for the fabrication of $LSCT_{A-}$ anode-supported fuel cells

In this chapter, the button fuel cells were fabricated by an aqueous tape casting and co-casting technique with co-sintering of dense YSZ electrolytes bonded to porous skeletal electrodes ($LSCT_{A-}$ and YSZ). The resulting cells then were pre-reduced in reducing atmosphere, followed by multi-infiltration of catalyst or ionic/electronic conductors in the electrodes, as illustrated in Figure 3.11.

The slurry formulation is the most crucial step for tape casting, the green tapes and hence the sintered samples. The general procedure is as follows. In the first step, the ceramic powder ($LSCT_{A-}$ for anode and YSZ for cathode) and flake graphite (Alfa

Aesar) were mixed and ball milled at a fast rate for 24h with addition of de-ionised water as solvent and hypermer KD6 (Croda Iberica SA) as dispersant. In the second step, another 24-h ball-milling was carried out after Poly(ethylene glycol) (PEG, Sigma-Aldrich) and Glycerol (Fisher Scientific UK Limited) as plasticizer, Polyvinyl alcohol (PVA, Alfa Aesar) as binder and containing Ethoxylated 2, 4, 7, 9-Tetraethyl 5 Decyn-4, 7-diol (Haikutech Europe BV) as defoamer were added to the homogenized powders, successively. Then the mixed suspension was de-aired by slow ball milling and cast onto a Mylar film to produce a ceramic green tape.

### 3.2.1 $LSCT_{A-}$ tapes made from the powder calcined at single temperature

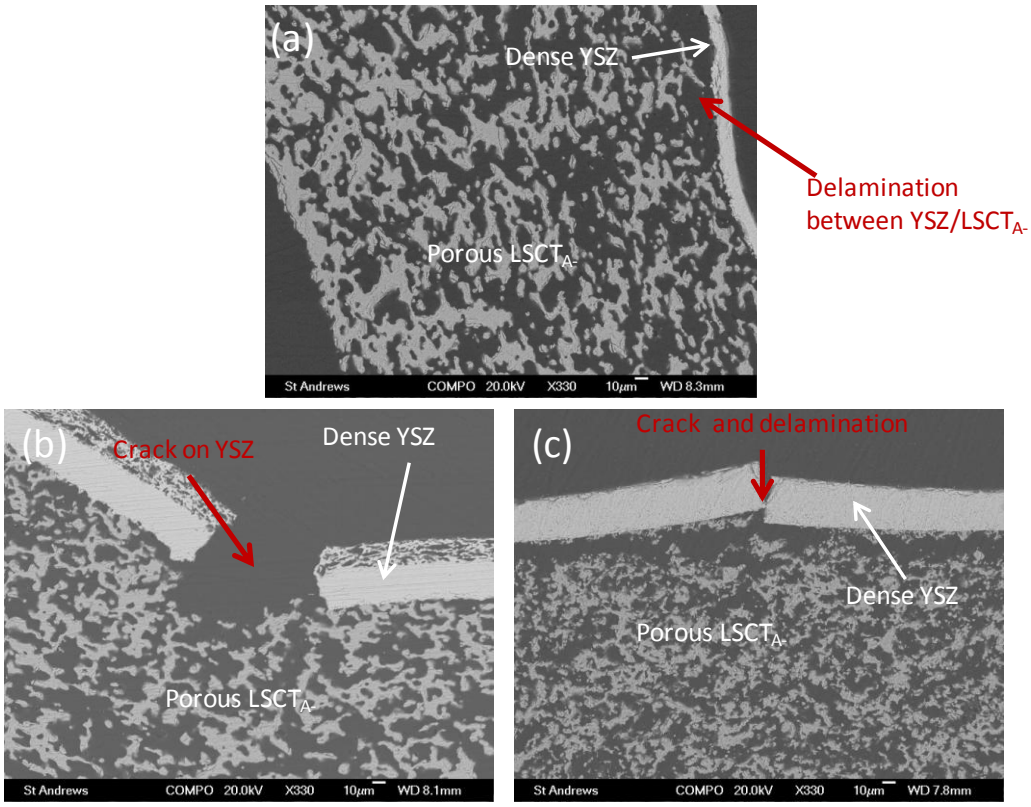


Figure 3.12 Back-scattered electron (BSE) images of anode from $LSCT_{A-}$ powder (a) calcined at 1100°C with addition of 120wt.% graphite, (b) calcined at 1200°C with addition of 70wt.% graphite and (c) calcined at 1250°C with addition of 35wt.% graphite. The weight percentage of graphite is relative to the mass of the $LSCT_{A-}$ ceramic powder used in the slurry. The laminated tapes shown above were sintered at 1350°C in air for 2h.

The BSE images of the sintered tapes made from $LSCT_{A-}$ powder calcined at different temperatures for 5h with varied weight ratios of graphite are shown in Figure 3.12. A porosity of 58% can be obtained on the $LSCT_{A-}$ anode after sintering at 1350°C for 2h when 120wt.% graphite was added into the slurry consisting of $LSCT_{A-}$ powder calcined at 1100°C, while delamination between YSZ and $LSCT_{A-}$ layers occurred due to the mismatched sintering process of two materials (see section 3.1.4). The total shrinkage of YSZ, around 25% after firing at 1350°C, is much smaller than $LSCT_{A-}$ powder calcined at 1100°C. Under this effect, a warped and detached YSZ electrolyte on the $LSCT_{A-}$ anode was formed after high-temperature sintering, as shown in Figure 3.12(a).

A porosity of 60% was observed from the mixed slurry of $LSCT_{A-}$ powder calcined at 1200°C for 5h with 70wt.% graphite, shown in Figure 3.12(b). It can be seen that the dense YSZ electrolyte was broken mainly because of the different shrinkage onset temperature in the early sintering stage. The dilatometry measurement of $LSCT_{A-}$ powder calcined at 1200°C shows an onset of densification at around 1200°C, higher than 1100°C of YSZ powder. When the sintering temperature reaches at 1100°C, YSZ green tapes begin to shrink while $LSCT_{A-}$ powder calcined at 1200°C remains unchangeable, resulting in crack on the YSZ surface especially on the edge. Moreover, a larger shrinkage of YSZ than $LSCT_{A-}$ towards the sintering process could accelerate the formation of crack on the thin YSZ layer.

The anode prepared by the $LSCT_{A-}$ powder thermally treated at 1250°C plus 35wt.% graphite as pore former is presented in Figure 3.12(c), where the porosity of 45% was anticipated. As discussed in the dilatometry measurements, because YSZ has a lower shrinkage onset temperature than $LSCT_{A-}$ powder calcined at 1250°C, when the sintering temperature reached 1100°C, the shrinkage stress produced in the thin YSZ electrolyte could result in the fragmentation of YSZ layer. Furthermore, the mismatched shrinkage between YSZ and $LSCT_{A-}$ could deteriorate the adherence of the thin YSZ layer on $LSCT_{A-}$ anode. The porosity of the anodes fabricated from $LSCT_{A-}$ powder calcined at different temperatures with an addition of various proportions of graphite is listed in Table 3.5. It is noted that the formed porosity is not

only relevant to the amount of graphite but also related with the grain size of the $LSCT_{A-}$ powder used in slurry.

Table 3.5 The porosity of the $LSCT_{A-}$ anode made from the powder calcined at different temperatures (1100, 1200 and 1250$^{o}$C) with an addition of graphite (The density of $LSCT_{A-}$ was calculated using the cell parameters; Average density of graphite is 2.15g/cm$^3$)

| Calcined Temperature ($^{o}$C) | Graphite (wt.% )* | Graphite (vol.% )* | Porosity (%) from ImageJ |
|---|---|---|---|
| 1100 | 120 | 277 | 58 |
| 1200 | 70 | 162 | 60 |
| 1250 | 35 | 81 | 45 |

*relative to mass/volume of $LSCT_{A-}$ powder

### 3.2.2 $LSCT_{A-}$ tapes made from the mixed powder calcined at two temperatures

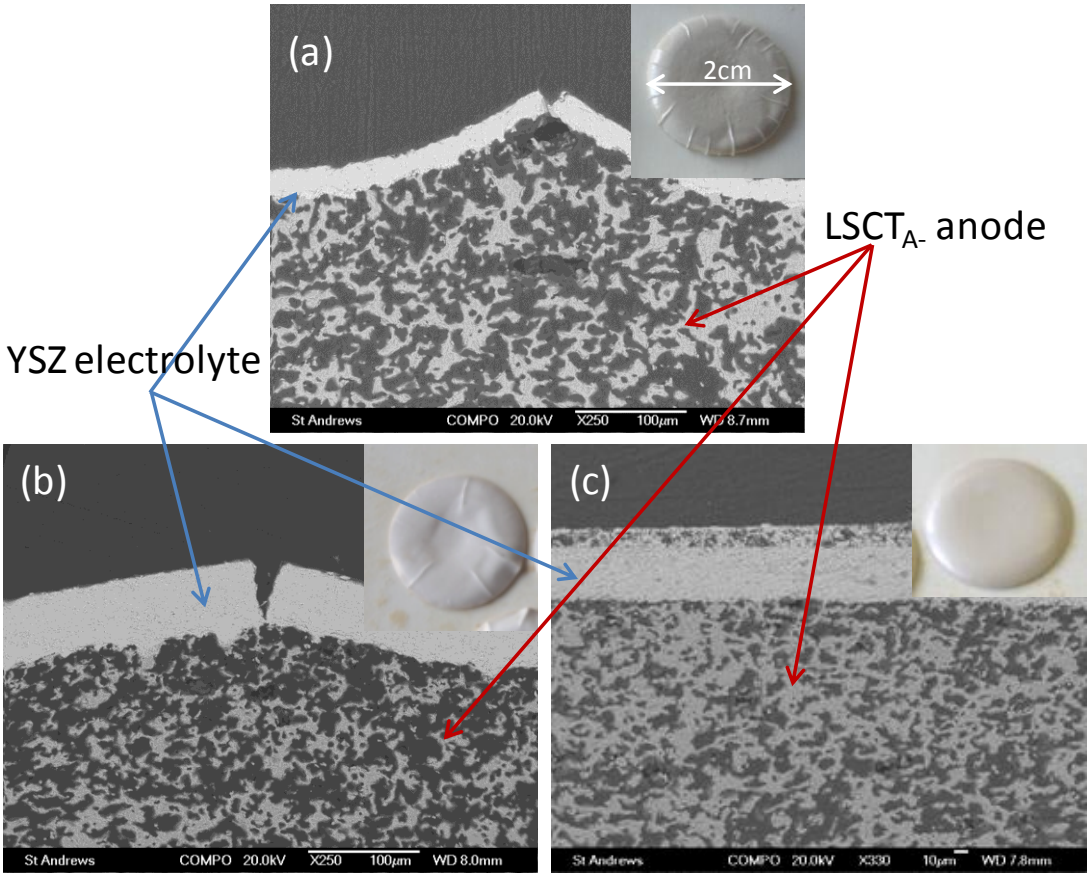


Figure 3.13 Back-scattered electron (BSE) images of anode from $LSCT_{A-}$ powder (a) calcined at 1100°C (20wt.%) and 1250°C (80wt.%) with 40wt.% graphite, (b) calcined at 1100°C (15wt.%) and 1250°C (85wt.%) with 40wt.% graphite, and (c) calcined at 1100°C (10wt.%) and 1250°C (90wt.%) with 30wt.% graphite. The weight percentage of graphite is relative to the mass of the $LSCT_{A-}$ ceramic powder used in the slurry. The laminated tapes shown above were sintered at 1350°C in air for 2h.

The picture of half cell made from $LSCT_{A-}$ powder calcined at 1100°C (20wt.%) and 1250°C (80wt.%) plus 40wt.% graphite in the inset of Figure 3.13(a) reveals the formation of the wrinkles on the edge of YSZ surface. The BSE image of the cross section on the edge of the sample is shown in Figure 3.13 (a), demonstrating a good connectivity between YSZ and $LSCT_{A-}$ but coupled with the crack and arch formed on the YSZ electrolyte. The optimized half cell using $LSCT_{A-}$ powder calcined at 1100°C (15wt.%) and 1250°C (85wt.%) with an addition of 40wt.% graphite is

presented in Figure 3.13(b). Compared with the former sample, the latter sample has a longer wrinkle on the edge of YSZ surface, but the arch of YSZ layer is less evident. When 30wt.% graphite was added into the $LSCT_{A-}$ powder calcined at 1100°C (10wt.%) and 1250°C (90wt.%) and an alumina plate was applied on the top of the green tapes during sintering, a high-quality cell was obtained. The BSE image in Figure 3.13(c) shows a good adherence of the different layers.

Therefore, the anode material we used in the slurry is the mixture of 10wt.% $LSCT_{A-}$ calcined at 1100°C and 90wt.% $LSCT_{A-}$ calcined at 1250°C in respects of the matched dilatometric curves with YSZ electrolyte upon sintering. The dense YSZ green tapes were fabricated using the same chemicals without pore former. To maximize the bonding of $LSCT_{A-}$ anode and YSZ electrolyte, co-casting of $LSCT_{A-}$ and YSZ green tapes was employed, where the mixed suspension of $LSCT_{A-}$ was cast on the top of the thin YSZ green slip. The recipes of YSZ and $LSCT_{A-}$ tapes used in our experiments are summarized in Table 3.6 and Table 3.7.

Table 3.6 Recipes of dense/porous YSZ tapes using aqueous tape casting technique

| Stage | Ingredients | Dense YSZ tape (g) | Porous YSZ tape (g) |
|---|---|---|---|
| Stage 1 milling | YSZ | 20 | 20 |
| | Graphite | - | 12.3 |
| | Deionised water | 12 | 18 |
| | Hypermer KD6 | 0.28 | 0.42 |
| Stage 2 milling | PEG | 1.2 | 2.0 |
| | Glycerol | 2.4 | 4.0 |
| | PVA[a] | 12 | 20 |
| | Defoamer | 0.28 | 0.42 |
| [a]: 15wt.% PVA dissolved in deionised water | | | |

Table 3.7 Recipes of co-cast/supported $LSCT_{A-}$ tapes using aqueous tape casting

| Stage | Ingredients | Co-cast $LSCT_{A-}$ layer (g) | $LSCT_{A-}$ support (g) |
|---|---|---|---|
| Stage 1 milling | $LSCT_{A-}$ (1100°C) | 1.5 | 2.5 |
| | $LSCT_{A-}$ (1250°C) | 13.5 | 22.5 |
| | Graphite | 4.5 | 6.0 |
| | Deionised water | 14 | 23 |
| | Hypermer KD6 | 0.32 | 0.48 |
| Stage 2 milling | PEG | 1.5 | 2.3 |
| | Glycerol | 3.0 | 4.6 |
| | PVA[a] | 14 | 21 |
| | Defoamer | 0.32 | 0.48 |
| [a]: 15wt.% PVA dissolved in deionised water | | | |

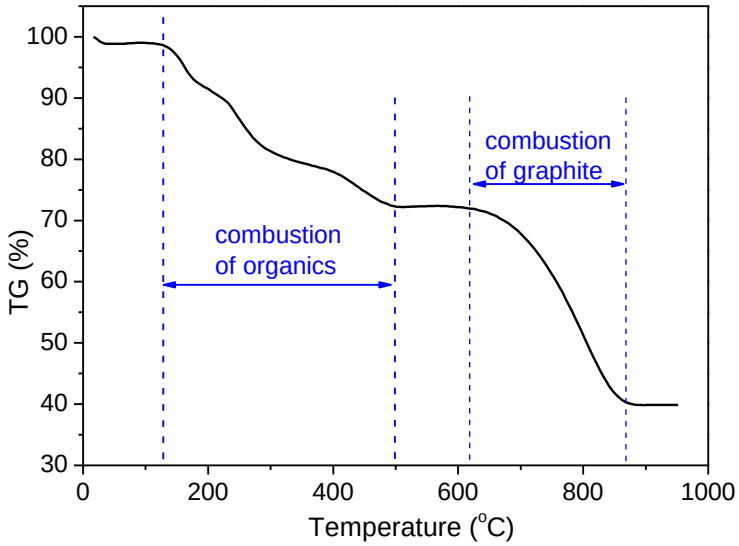


Figure 3.14 TGA curve for the porous YSZ tape at a heating ramp of 3°C/min

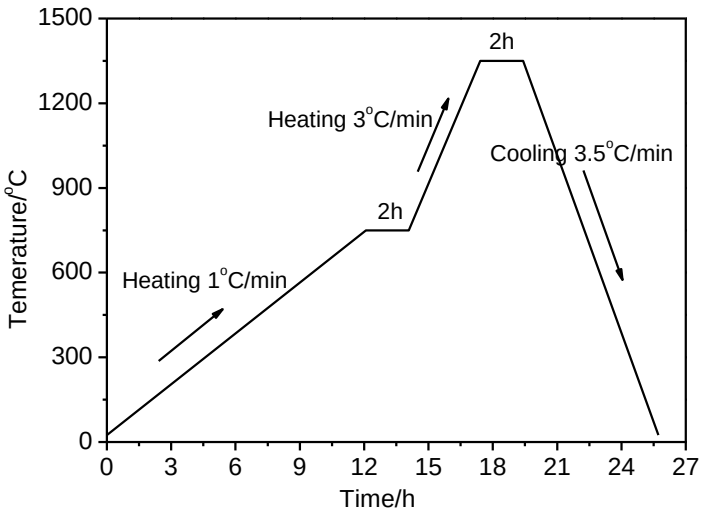


Figure 3.15 Temperature program for co-sintering of the green tapes

After drying overnight at room temperature, the green tapes were cut to an appropriate size and laminated, followed by co-sintering at 1350°C for 2h in air. The sintering program is crucial for the formation of a defect-free ceramic cell, and can be determined by the TGA of the porous YSZ tape with temperature at a heating ramp of 3°C/min, as shown in Figure 3.14. The mass of the tape starts to decrease at 120°C, when the organic chemicals added to the tape as plasticizer and binder begins to burn out. This process is required to be gentle to avoid a rapid increase of gas pressure, otherwise, it can cause damage to the cell, such as deformation, crack and stresses. The mass reduction above 600°C can be attributed to the combustion of graphite.

In terms of temperature dependence of TGA, the sintering program is settled and shown in Figure 3.15. In order to avoid the formation of the defects resulting from the combustion of organics and graphite, a slow ramping rate of 1°C/min up to 750°C was used. Then a dwelling stage of 2h at 750°C was followed to burn off graphite and organic residues completely. The temperature was raised to 1350°C at a faster ramp rate of 3°C/min and kept for 2h to allow the final shrinkage and produce a fully dense electrolyte. At the cooling stage, the temperature was cooled down to room temperature at a ramp rate of 3.5°C/min. The sintered samples of 2cm in diameter were subjected to a reduction process at 1000°C for 12h in a 5% $H_2$-Ar atmosphere. Upon reduction, the colour of $LSCT_{A-}$ changes from light yellow to black.

The cathode side of pre-reduced samples was impregnated with precursor solutions containing $La_{0.8}Sr_{0.2}FeO_3$ (LSF) and $La_{0.8}Sr_{0.2}CoO_3$ (LSC) successively and fired at 450$^o$C in air to decompose nitrate while avoid the re-oxidation of $LSCT_{A-}$. The loadings of impregnates into the YSZ cathode scaffold were 15wt.% LSF and 5wt.% LSC. Anode catalyst materials including $CeO_2$ and Ni were impregnated into the porous $LSCT_{A-}$ anode scaffold using solutions from $Ce(NO_3)_3.6H_2O$ and $Ni(NO_3)_2.6H_2O$. Multiple cycles of impregnation and calcination at 450$^o$C were used until the desired loading of impregnates of oxides was reached. Figure 3.16 shows the BSE image of the cross-section of $LSCT_{A-}$ anode/YSZ electrolyte interface after the impregnation of ceria and nickel in the anode side and the firing process. It can be seen that the impregnated catalysts have successfully diffused into the interfacial area across the thick anode support.

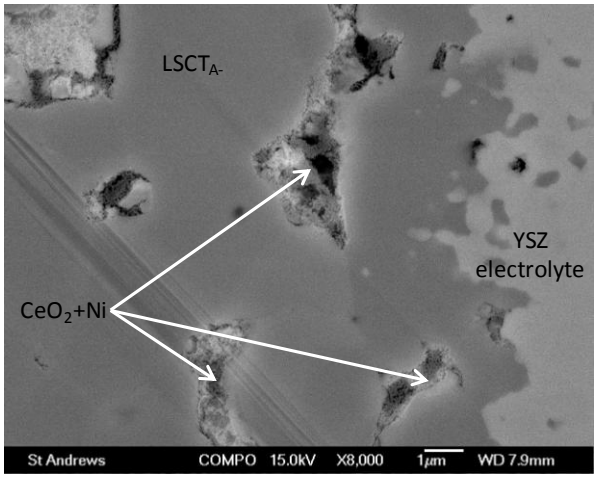


Figure 3.16 (a) Back-scattered electron (BSE) image of the cross section of the $LSCT_{A-}$ anode/YSZ electrolyte after impregnation of $CeO_2$+Ni and firing

## 3.3 Performance of $LSCT_{A-}$ anode-supported cells

### 3.3.1 Microstructure of the cells

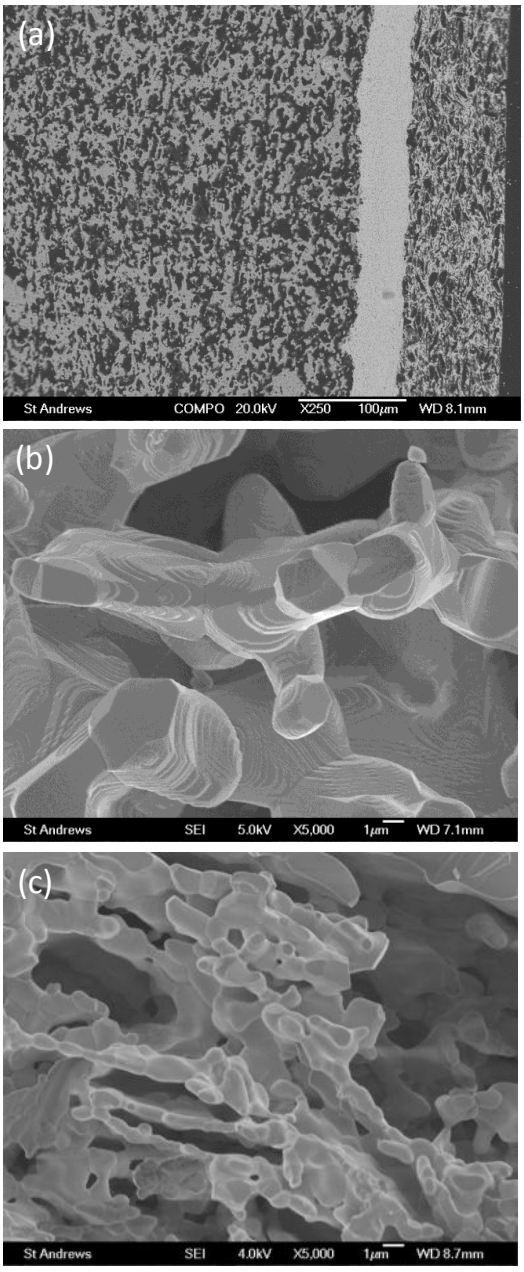


Figure 3.17 (a) Back-scattered electron (BSE) image of the cross section of anode-supported cell produced by aqueous tape casting (from left to right: porous $LSCT_{A-}$ anode, dense YSZ electrolyte and porous YSZ cathode); scanning electron micrographs (SEM) images of (b) porous $LSCT_{A-}$ anode backbone and (c) porous YSZ cathode backbone prior to impregnation

A BSE micrograph of the cross-section of the anode-supported button cells produced by aqueous tape casting is presented in Figure 3.17(a), showing the dense YSZ electrolyte adhering well with two porous electrode skeletons. In this study, the cells consisted of a 40μm thick dense YSZ disk sandwiched by an 85μm thick porous YSZ layer on one side and a 450μm thick porous $LSCT_{A-}$ layer on the other side. A crack-free dense YSZ electrolyte has been successfully obtained on the $LSCT_{A-}$ anode substrate after co-sintering technique without open pores. As shown in the magnified SEM image of the fractured $LSCT_{A-}$ layer before impregnation (Figure 3.17(b)), the necks between the $LSCT_{A-}$ particles are difficult to distinguish, indicating that a well-sintered scaffold has formed possibly due to the addition of fine particles from $LSCT_{A-}$ powder calcined at $1100^oC$. The porous YSZ layer in Figure 3.17(c) shows a much smaller homogeneous particle size of 1μm surrounded by the random pores between 1 and 5μm in size. The coarse pores formed in the porous electrodes are caused by the burnout of pore formers, which favours the easy transport of gas even after impregnation. The flake-like pores are attributed to the shape of graphite that is pore-forming agent in the porous tapes.

### 3.3.2 Electrochemical testing

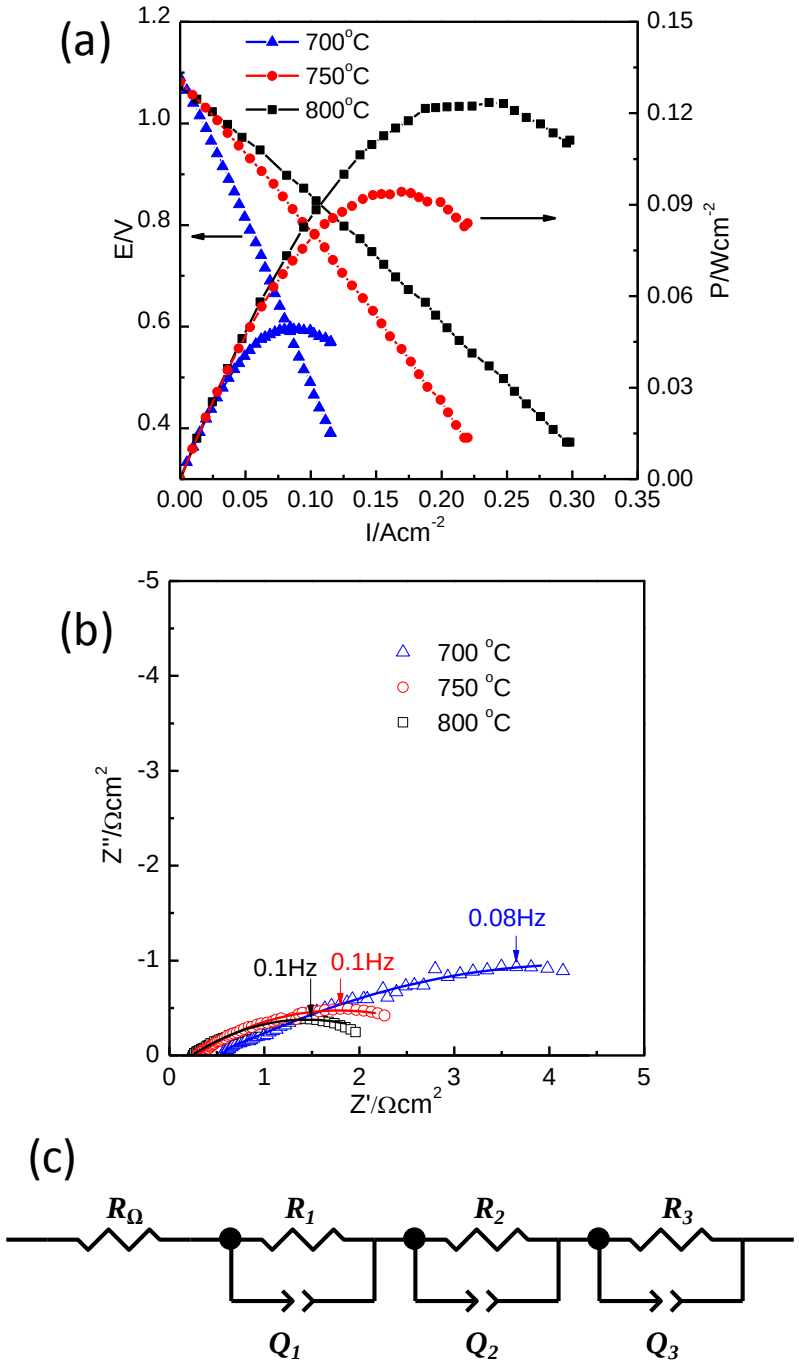


Figure 3.18 (a) I-V and power density curves and (b) impedance spectra for single-phase $LSCT_{A-}$ anode-supported cell in humidified hydrogen as a fuel gas and air as an oxidant gas collected at the following temperatures upon cooling: 700, 750 and 800°C. The impedance spectra were measured at open circuit voltage (OCV). Symbol and line in (b) represent the experimental data and fitting data using the equivalent circuit, respectively. (c) Equivalent circuit of the impedance spectra in this study

The fuel cell was directly mounted and sealed onto an alumina tube, and a gas flow of Ar containing 5% $H_2$ was fed into the anode chamber to avoid the oxidation of the anode upon heating to testing temperature 800$^o$C, before switching to humidified hydrogen (3vol.% $H_2O$). The $LSCT_{A-}$ anode-supported button fuel cells ($LSCT_{A-}$/YSZ/LSF-LSC-YSZ) with an active area of 0.8cm$^2$ were electrochemically characterized at 700-800$^o$C using humidified $H_2$ (3vol.% $H_2O$) as fuel and ambient air as oxidant. The data were collected upon cooling down from 800 to 700$^o$C. In Figure 3.18(a), the open circuit voltages (OCVs) recorded are 1.09, 1.08 and 1.07V at 700, 750 and 800$^o$C, respectively, which is close to the theoretical values calculated from the Nernst equation. The high OCV values indicate that the thin electrolyte is sufficiently dense and the cell is well sealed onto the testing jig. The initial Area Specific Resistance (ASR) values calculated as the slope of the I-V curves are 6.3, 3.2 and 2.4Ωcm$^2$ at 700, 750 and 800$^o$C, respectively. The maximum power densities (Figure 3.18(a)) for the cell without catalysts on the anode side are 50, 94 and 124mWcm$^{-2}$ at 700, 750 and 800$^o$C, respectively. In order to understand the factors limiting cell performance, the electrochemical impedance spectra measured at OCV from 700 to 800$^o$C are presented in Figure 3.18(b). The ohmic resistances of the cell ($R_s$), determined from the high-frequency intercepts with the abscissa, range from 0.55Ωcm$^2$ at 700$^o$C to 0.25Ωcm$^2$ at 800$^o$C. According to the conductivity of YSZ in the literature [41], the contribution of the 40-μm thick YSZ electrolyte to the ohmic resistance is around 0.20Ωcm$^2$ at 700$^o$C and 0.10Ωcm$^2$ at 800$^o$C. The measured ohmic losses are much larger than the calculated values of YSZ electrolyte, because they also include the ohmic resistance of electrodes and current collection of silver paste, and electrode/electrolyte interfacial resistance. The low contribution of ohmic losses from the electrodes demonstrates that $LSCT_{A-}$ backbone has a reasonable electronic conductivity. The cell losses are dominated by the polarization resistance of electrodes ($R_p$), which are represented by the distance between the high and low frequency intercepts of the curve with the abscissa. In order to analyze the nonohmic losses, an equivalent circuit of $R_\Omega(R_1Q_1)(R_2Q_2)(R_3Q_3)$ (in Figure 3.18(c)) was used to fit the impedance spectra, where R is a resistance and Q a constant phase element (CPE). The fitting results reveal three distinct electrode processes corresponding to the high-frequency (~3kHz), medium-frequency (~5Hz), and low-frequency frequency (~0.1Hz) arcs. The sum of $R_1$, $R_2$ and $R_3$ is considered to be the total

polarization resistance of electrodes ($R_p$). The fitted impedance parameters are listed in Table 3.8.

Table 3.8 The fitting parameters ($\Omega cm^2$) for Impedance Spectra of the $LSCT_{A-}$ backbone cell tested at different temperatures in humidified hydrogen (3vol.% $H_2O$)

| Resistance | 700°C | 750°C | 800°C |
|---|---|---|---|
| $R_1$ | 0.52 | 0.11 | 0.036 |
| $R_2$ | 1.20 | 0.92 | 0.70 |
| $R_3$ | 3.98 | 1.50 | 1.12 |
| $R_p$ | 5.70 | 2.53 | 1.86 |

The primary non-ohmic resistance is attributed to the low-frequency response with summit frequency value of ~0.1Hz. The appearance of thermally activated low-frequency arc may suggest that the dissociative adsorption of gaseous species and surface diffusion are the arc-related processes. The high- and medium-frequency arcs are probably related with the charge transfer (oxygen ions and electron) between bulk and surface of the electrodes. However, it is difficult to separate the losses from the anode and cathode. The $R_p$ values simulated from the equivalent circuit ($R_p=R_1+R_2+R_3$) range from 5.70$\Omega cm^2$ at 700°C to 1.86$\Omega cm^2$ at 800°C, demonstrating a poor electrocatalytic activity of the $LSCT_{A-}$ backbone for hydrogen oxidation, because the non-ohmic losses of the cathode are estimated to be around 0.13$\Omega cm^2$ at 700°C [59]. It is noteworthy that the polarization resistance values were much smaller than those of electrolyte-supported cell with $LSCT_{A-}$ backbone anode at 900°C (45$\Omega cm^2$) [143] and LST single-phase anode at 800°C (9.6$\Omega cm^2$) [172], and cathode-supported cell with mixed YST and YSZ as anode at 800°C (2.9$\Omega cm^2$) [158]. For the first two cells, the polarization resistance from the screen printed LSM-YSZ composite cathode could be negligible, around 0.5-0.8$\Omega cm^2$ at 800-950°C [241]. The improved $R_p$ values can be explained by the generated oxygen vacancies with the formation of $Ti^{3+}$ upon high-temperature reduction, therefore increasing the reaction

sites and improving the performance when using $LSCT_{A-}$ scaffold as the ionic and electronic conductive channel.

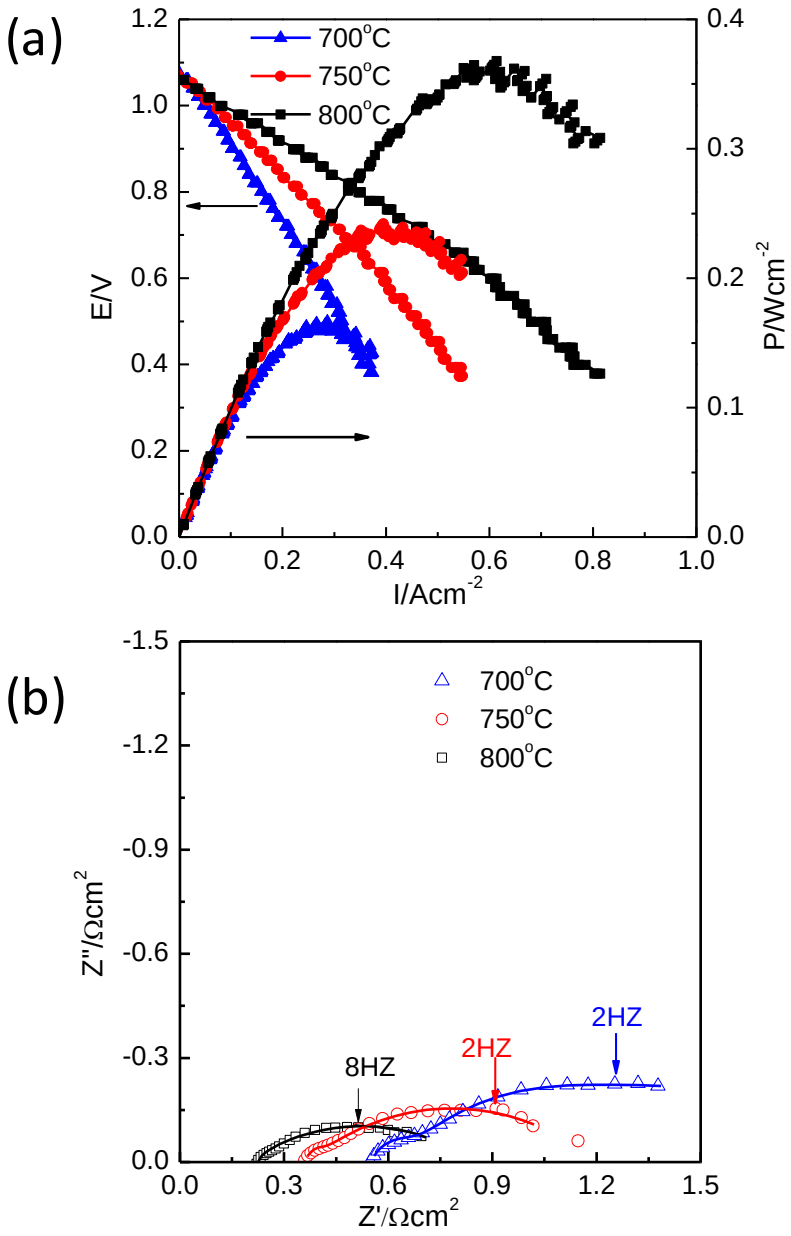


Figure 3.19 (a) I-V and power density curves and (b) impedance spectra for 3wt.% Ni impregnated $LSCT_{A-}$ anode-supported cell in humidified hydrogen as a fuel gas and air as an oxidant gas collected at the following temperatures upon cooling: 700, 750 and 800°C. The impedance spectra were measured at open circuit voltage (OCV). Symbol and line in (b) represent the experimental data and fitting data using the equivalent circuit, respectively.

The addition of 3wt.% nickel enhances the performance significantly, as shown in Figure 3.19(a): maximum power densities of 162, 237 and 367mW $cm^{-2}$ are achieved at 700, 750 and 800°C, respectively, while the impregnated cell exhibits the reasonable OCV values between 1.07 and 1.09V. The initial ASR values of unit cell calculated as the slope of the I-V curves are 1.97, 1.33 and 0.87Ω$cm^2$ at 700-800°C, respectively. These values are significantly lower than those of $LSCT_{A-}$ single phase cell at the same operation temperature.

The impedance spectra shown in Figure 3.19(b) are used to explain the losses of the cell. The ohmic resistances obtained from the EIS graph are 0.55-0.23Ω$cm^2$ at the temperature range 700-800°C, close to those of the $LSCT_{A-}$ backbone cell. The addition of Ni did not alter the ohmic resistances probably because the electrical conductivity of the anode backbone material after the pre-reduction process is sufficient to ensure that the resistance from the anode does not limit the cell performance. Moreover, the nickel loading is insufficient to form an interconnected layer for electronic conduction. The addition of nickel catalyst causes a dramatic drop of the non-ohmic losses, from 1.86Ω$cm^2$ for the cell without impregnation to 0.60Ω$cm^2$ for the cell impregnated with Ni at 800°C. The decrease of the $R_p$ value for Ni impregnated cell confirms that the high electrode losses can be attributed to the anode of the cell without catalyst. This result is consistent with what has been reported for infiltrating LST [140,242], LSTM [159] and LSCM [243~245] as anodes.

Three responses presented at high, medium and low frequencies can be observed from the impedance spectra and analyzed by using the equivalent circuit of $R_\Omega(R_1Q_1)(R_2Q_2)(R_3Q_3)$, as shown in Figure 3.18(c). For example, at 700°C the three main responses can be separated by the corresponding frequency values: 2000Hz for high-frequency response, 80Hz for medium-frequency response and 2Hz for low-frequency response. The major electrode losses are from the low-frequency process, which is temperature dependent, suggesting that the adsorption and surface diffusion of reactant species are the dominant rate-limiting step in the anode.

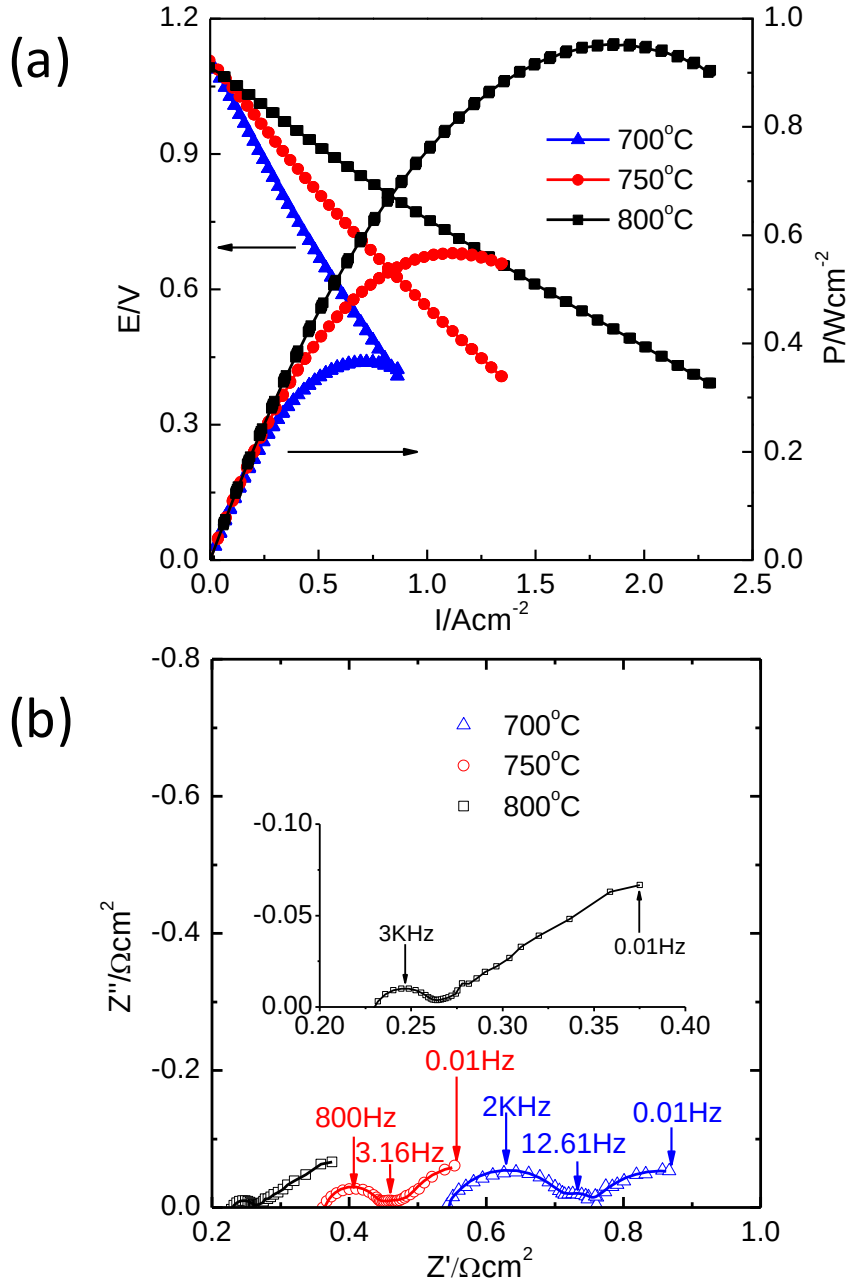


Figure 3.20 (a) I-V and power density curves and (b) impedance spectra for 6wt.% $CeO_2$ and 3wt.% Ni impregnated $LSCT_A$- anode-supported cell in humidified hydrogen as a fuel gas and air as an oxidant gas collected at the following temperatures upon cooling: 700, 750 and 800°C. The impedance spectra were measured at open circuit voltage (OCV). Symbol and line in (b) represent the experimental data and fitting data using the equivalent circuit, respectively.

The performance of the cell impregnated with 6wt.% $CeO_2$ and 3wt.% Ni into the $LSCT_{A-}$ was studied and presented in Figure 3.20. In Figure 3.20(a), the cell obtained high OCV values of 1.08-1.10V at the temperature range 700-800$^oC$, which is close to the theoretical OCV value considering the fuel is pure hydrogen containing 3vol.% $H_2O$. With the infiltration of combined ceria and nickel, the maximum power densities exceeded those of the nickel impregnated cell by a factor of two at the operation temperatures. The maximum power densities observed in Figure 3.20(a) are 367, 568 and 960mW/$cm^2$ at 700, 750 and 800$^oC$, respectively. The initial ASR values of unit cell calculated as the slope of the I-V curves are 0.80, 0.52 and 0.30Ω$cm^2$ at 700-800$^oC$, respectively. These values are significantly lower than those of $LSCT_{A-}$ single phase cell and Ni-impregnated cell at the same operation temperature.

The impedance spectra at OCV are presented at Figure 3.20(b). The ohmic losses are quite similar to those of the cells with Ni catalyst and without catalyst. The polarization resistance ($R_p$) has been significantly decreased with addition of ceria and nickel. The separation of the three main responses at high, medium and low frequency are much more evident than the other two cells, especially at low temperature. At 700$^oC$, the maximum frequencies for the corresponding electrode processes are 2000, 12.61 and 0.01Hz for high-, medium- and low-frequency arc, respectively. Compared to the cell impregnated with Ni only, the impregnation of ceria in addition can possibly provide extra oxygen ionic conductivity and exchange sites, so enlarging the electrochemical reaction zones. Usually, on such impedance spectra, the reaction of charge transfer at high frequency, the absorption and surface diffusion process at medium frequency, and gas diffusion process at low frequency is registered [143,246]. The resistance values across the high and medium frequency are thermally activated and strongly dependent on microstructure and anode composition. A significant decrease of the polarization resistance determined by absorption and surface diffusion process can be observed on the $CeO_2$ and Ni co-impregnated cell compared with the anode without catalyst and with Ni only, suggesting that the appearance of the ceria layer increases the TPBs, which might correlate with the ionic conductivity of ceria. In an anode where YSZ is used as a scaffold, ceria is not seen to have such an enhancing effect on the performance [247,248], as YSZ provides sufficient oxygen

ionic conductivity, whereas ceria on an $LSCT_{A-}$ scaffold plays the role of both ionic conductor and catalyst. The low-frequency arcs are temperature independent, with a relaxation time ~0.01Hz, pointing out the gas diffusion and fuel delivery at the anode as the process associated with this arc.

### 3.3.3 Microstructure of impregnated anode

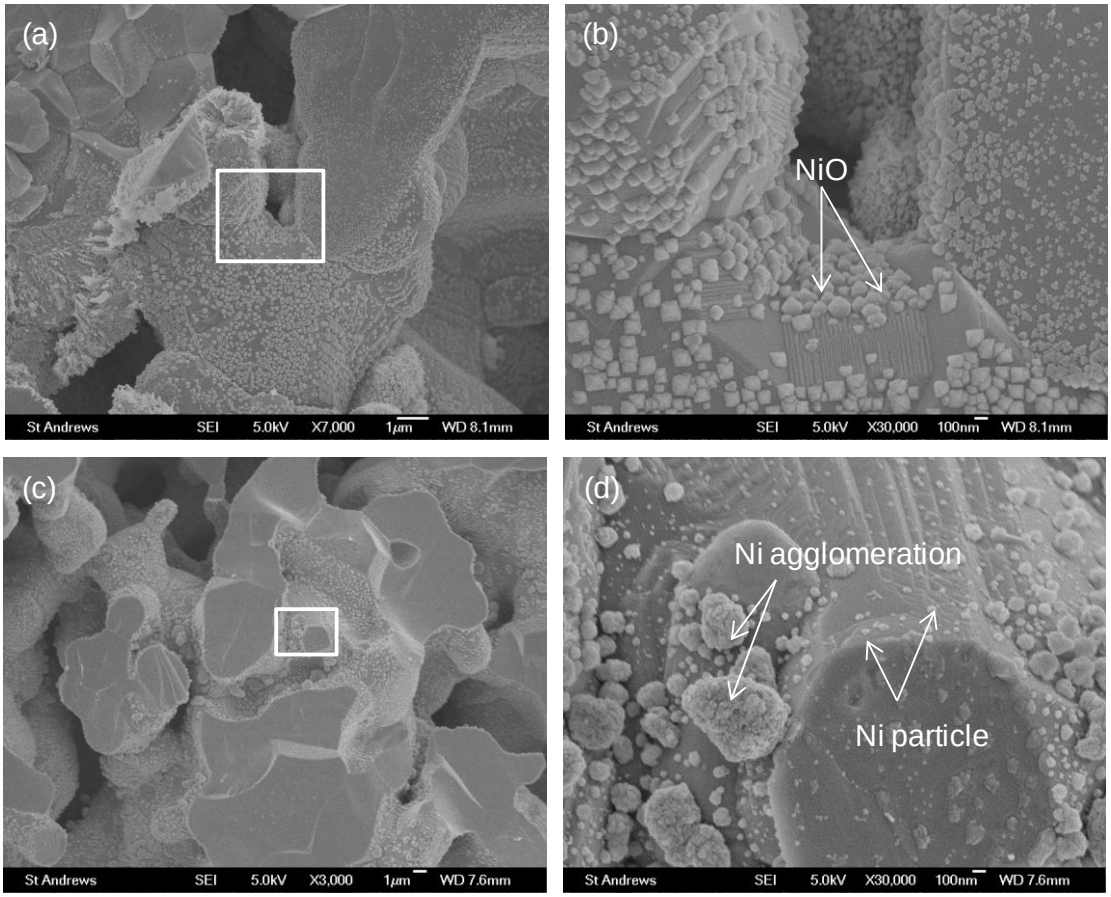


Figure 3.21 Scanning electron microscopy (SEM) images of the 3wt.% Ni impregnated $LSCT_{A-}$ (a) fired at 450°C before electrochemical measurements and (c) after electrochemical measurements at 800°C; (b) and (d) the magnified view of impregnated coating in (a) and (b), respectively (rectangular part).

The SEM images of the anodes with impregnated NiO before and after electrochemical testing are shown in Figure 3.21. In Figure 3.21(a) and (b), after the annealing at 450°C in air, NiO forms a coating of 100nm particles on the surface of $LSCT_{A-}$ backbone, which plays an important role in electrochemical catalytic activity. After testing at 800°C (Figure 3.21(c) and (d)), two different Ni particle sizes can be

seen on the $LSCT_{A-}$ structure: a finer nickel structure is visible on the convex regions of $LSCT_{A-}$ surface and a coarser nickel particle with agglomeration is formed on the concave zones of $LSCT_{A-}$ surface. This can be explained by the uneven deposition process, which is driven by capillary action, resulting in a thinner layer formed on convex surfaces and a thicker layer located on concave surfaces [249]. Most of agglomerations of nickel particles are located on the concave surface of $LSCT_{A-}$, resulting from a thicker layer of NiO forming upon the process. It is necessary to optimize the distribution and retard the agglomeration and growth of Ni particles on the anode surface during the electrochemical testing.

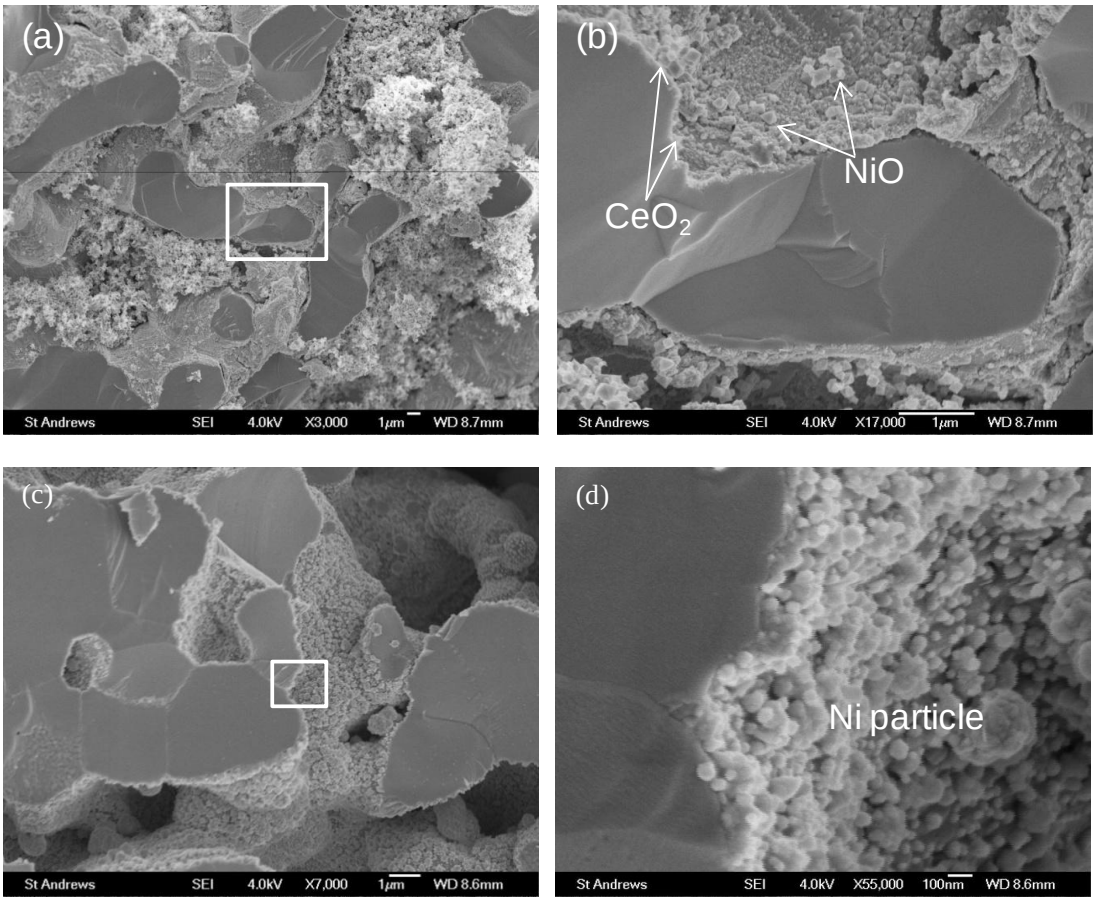


Figure 3.22 Scanning electron microscopy (SEM) images of the 6wt.% ceria and 3wt.% Ni impregnated $LSCT_{A-}$ (a) fired at 450°C before electrochemical measurements and (c) after electrochemical measurements at 800°C; (b) and (d) the magnified view of impregnated coating in (a) and (b), respectively (rectangular part).

Figure 3.22 shows the SEM images of the anodes with impregnated $CeO_2$ and NiO before and after electrochemical testing. Figure 3.22(a) is the micrograph obtained on

the $LSCT_{A-}$ anode after the addition of 6wt.% ceria and 3wt.% Ni and then the annealing at 450°C in air. The figure demonstrates that a loosely packed structure of $CeO_2$ and NiO has been filled into the pores of $LSCT_{A-}$ particles. From the magnified image of impregnates in Figure 3.22(b), a thin layer of ceria is observed, along with bright and rectangular NiO particles on the ceria coating. This morphology can possibly increase the ionic conductivity of the backbone and provide more TPBs for electrochemical reaction, which is in good agreement with the electrochemical testing results. After testing at 800°C, it is difficult to discern the ceria layer from nickel particles formed on the $LSCT_{A-}$ surface, as shown in Figure 3.22(c) and (d). By contrast to Ni-impregnated $LSCT_{A-}$ structure with and without ceria, it has been noted that the existence of ceria layer slows down the growth and agglomeration of nickel nanoparticles during testing, which is supposed to favour the performance as well as the long-term operation. In order to further improve the performance, the optimization of catalyst impregnation method and understanding of scaffold-catalyst interactions is necessary and will be studied.

## 3.4 Conclusion

A-site deficient strontium titanate $La_{0.2}Sr_{0.25}Ca_{0.45}TiO_3$ ($LSCT_{A-}$) after pre-reduction at high temperature (i.e. 1000°C) is a good candidate for anode support of SOFCs. The fuel cells using $LSCT_{A-}$ perovskite as an anode support show a promising electrochemical performance after impregnation of catalyst. The addition of catalysts into $LSCT_{A-}$ anode significantly reduces the polarization resistance of the cells, suggesting an insufficient electrocatalytic activity of the $LSCT_{A-}$ backbone for hydrogen oxidation, but $LSCT_{A-}$ can provide the electrical conductivity required for anode.

# Chapter 4. Stability studies of metal-impregnated $LSCT_{A-}$ anode as support for SOFCs

## 4.1 Introduction

The electrochemical reaction in the SOFC electrodes predominantly occur at the triple phase boundaries (TPBs) between the electronic conductor, ionic conductor and gas phases. Therefore, changes in the microstructure and surface properties of anode materials have a significant impact on the performance and durability of SOFCs [250].

The agglomeration and particle coarsening of the metallic Ni is considered to be the predominant microstructural change in the Ni-YSZ anode concerning the degradation of fuel cell performance under operation. It is widely assumed [94,251,252] that the increase in nickel particle size can diminish triple phase boundaries (TPB) and the contact within the nickel phase, leading to the reduction of chemically active areas for fuel oxidation and electrical pathways in the anode, and finally the increasing losses of power output. Besides the increase of nickel particle size, the interaction between catalyst and scaffold material under operation condition is not clear, which could to some extent deteriorate the cell performance. A more detailed microstructure of the interface between the catalyst and anode backbone will be presented to fully understand the mechanism of degradation in terms of microstructure change.

Recently, in order to address the problems caused by Ni-YSZ anodes, increasingly more attention has been attracted by the Ni-Fe bimetal anodes. Ishihara et al. [253] reported a high performance for Ni-Fe-SDC anode on the dense LSGM/SDC electrolyte due to the improved activity of reaction site on Ni by addition of Fe. A maximum power density of 3270mW/$cm^2$ was achieved at 700$^oC$ for the cell with LSGM/SDC as electrolyte, Ni-Fe-SDC as anode and SSC ($Sm_{0.5}Sr_{0.5}CoO_3$) as cathode. $Ni_{0.75}Fe_{0.25}$-GDC anode supported cells show a much higher performance in humidified hydrogen than that of Ni-GDC because iron doping could not only enhance the catalytic activity of anode reaction and lower the ohmic resistance, but also improve the anode microstructure and increase the reaction sites [254]. It is also found that the addition of iron into Ni/GDC or Ni/LSGM anodes significantly

improved the long-term stability in methane due to the optimized catalytic properties for fuel oxidation [255,256].

In this study, electrochemical tests were carried out on $LSCT_{A-}$ anode supported fuel cells with metallic catalysts and/or ceria impregnated into the anode. It is interesting to compare the performance and stability of Ni and Ni-Fe bimetal infiltrated anode and explore the possible reasons for the presented properties. High-resolution electron microscopy techniques would be utilized, allied with ion beam preparation to preserve fine structure on the cross-sections and interfaces, allowing a detailed survey over large areas of infiltrated anode so developing an improved understanding of how these anode structures behave and mature during cell operation. In this way, the relationship of cell performance and microstructure at different time was established and studied.

## 4.2 Cell fabrication

In this chapter, the button fuel cells were fabricated by organic tape casting and co-casting techniques. Compared with water-based tape casting, organic tape casting technique has a lot of advantages, such as a high solvent evaporation rate, low concentration binder in slurry, insensitive slurry to the process parameters and easy to form smooth dense tape [257]. It is much easier to fabricate the defect-free co-cast layers using organic tape casting technique.

The slurry formulation and chemicals are playing an important role in the property of the green tapes and hence the sintered samples. The organic chemicals were added according to the following order. In the first step, the ceramic powder ($LSCT_{A-}$ for anode and YSZ for cathode) and flake graphite (Alfa Aesar) were mixed and ball milled at a fast rate for 16h with addition of solvent and triton as dispersant. The anode material we used in the slurry is the mixture of 10wt.% $LSCT_{A-}$ calcined at $1100^oC$ and 90wt.% $LSCT_{A-}$ calcined at $1250^oC$ in respect of the matched dilatometric curves with YSZ electrolyte upon sintering. In the second step, another 6h ball-milling was carried out after Poly(ethylene glycol) (PEG) and Di-n-butyl phthalate (DBP) as plasticizer, and Polyvinyl Butyral (PVB) as binder were added to the homogenized powders, successively. Then the mixed suspension was de-aired by

slow ball milling and cast onto a Mylar film to produce a ceramic green tape. The dense YSZ green tapes were fabricated using the same recipe without pore former. To maximize the bonding of $LSCT_{A-}$ anode and YSZ electrolyte, co-casting of $LSCT_{A-}$ and YSZ green tapes was employed, where the mixed suspension of $LSCT_{A-}$ was cast on the top of the thin YSZ green slip. The recipes of YSZ and $LSCT_{A-}$ tapes are summarized in Table 4.1 and Table 4.2.

Table 4.1 Recipes of dense and porous YSZ tapes using organic tape casting technique

| Stage | Ingredients | Dense YSZ tape (g) | Porous YSZ tape (g) |
|---|---|---|---|
| Stage 1 milling | YSZ | 20 | 20 |
| | Graphite | - | 12.32 |
| | Solvent[a] | 15 | 28 |
| | Triton | 0.23 | 0.35 |
| Stage 2 milling | PEG | 1.69 | 2.53 |
| | DBP | 1.43 | 2.19 |
| | PVB | 2.24 | 3.36 |
| [a]: 33wt.% ethanol dissolved in Methyl Ethyl Ketone (MEK) | | | |

Table 4.2 Recipes of co-cast and supported porous $LSCT_{A-}$ tapes using aqueous tape casting technique

| Stage | Ingredients | Co-cast $LSCT_{A-}$ layer (g) | Porous $LSCT_{A-}$ support (g) |
|---|---|---|---|
| Stage 1 milling | $LSCT_{A-}$ (1100°C) | 2.5 | 1.5 |
| | $LSCT_{A-}$ (1250°C) | 22.5 | 13.5 |
| | Graphite | 6.25 | 4.5 |
| | Solvent[a] | 23 | 17 |
| | Triton | 0.32 | 0.22 |
| Stage 2 milling | PEG | 2.49 | 1.80 |
| | DBP | 2.13 | 1.56 |
| | PVB | 3.20 | 2.54 |
| [a]: 33wt.% ethanol dissolved in Methyl Ethyl Ketone (MEK) | | | |

After drying, the green tapes were cut into an appropriate size and laminated, followed by co-sintering at 1350°C in air, using the same temperature program as mentioned in last chapter. Then the sintered samples of 2cm in diameter were subjected to a reduction process at 900°C for 12h in a 5% $H_2$-Ar atmosphere.

The cathode side of pre-reduced samples was impregnated with precursor solution containing $La_{0.8}Sr_{0.2}Co_{0.2}Fe_{0.8}O_3$ (LSCF) and fired at 450°C in air to decompose the nitrate but avoiding the re-oxidation of $LSCT_{A-}$. The loadings of impregnates in the YSZ cathode were 20-25wt.% LSCF. Anode catalyst materials including Ni and $Ni_{0.75}Fe_{0.25}$ were impregnated into the porous $LSCT_{A-}$ scaffold using solutions from $Ni(NO_3)_2.6H_2O$ (Newburyport, MA USA) and $Fe(NO_3)_3.9H_2O$ (Sigma-Aldrich, USA) with 3:1 molar ratio of Ni:Fe with additional citric acid. Multiple cycles of

impregnation and calcination at 450°C were used until the desired loading of impregnates of oxides was reached.

In this Chapter, the anode catalysts containing Ni and $Ni_{0.75}Fe_{0.25}$ after different thermal treatments were characterized by XRD to investigate the formed phases of the catalysts calcined at 450°C, and reduced at the oxygen partial pressure of $10^{-13}$atm and 5% $H_2$-Ar. The detail has been described in section 2.2.1.

## 4.3 Results and discussion

### 4.3.1 Cell microstructure

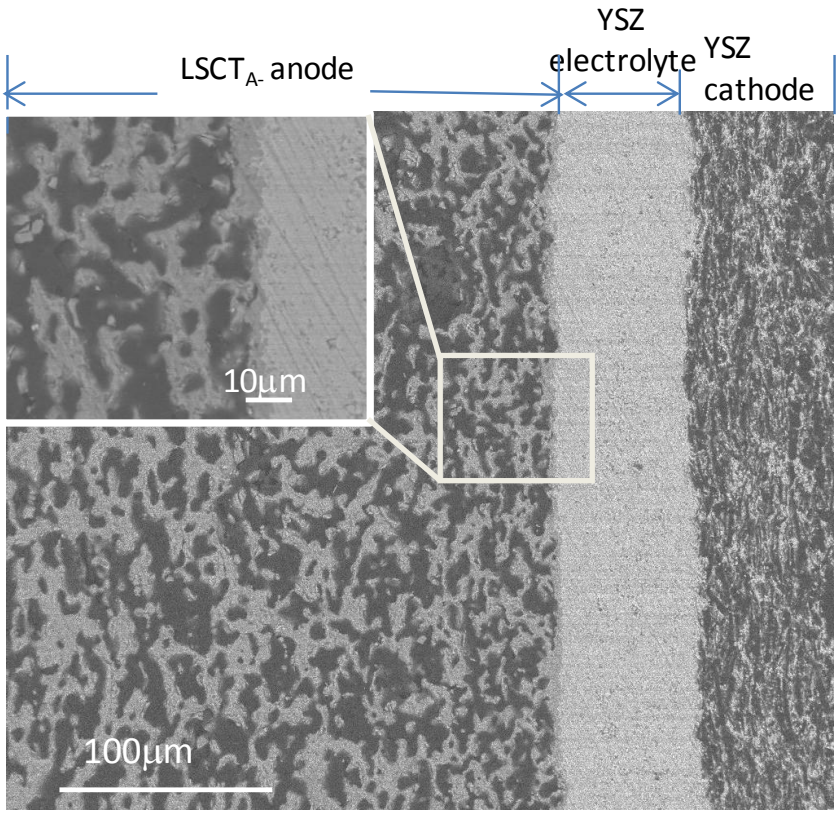


Figure 4.1 Back-scattered electron (BSE) image of the cross section of the cell after reduction, showing the anode to the left and the cathode to the right of the dense electrolyte. The inset is the magnified image of the anode/electrolyte interface, as shown in the rectangle.

After being reduced at 900$^{o}$C for 12 hours and LSCF impregnated into the YSZ cathode, the cross-sectional image of the cell is shown in Figure 4.1. It can be seen that the electrolyte is about 60μm thick and adheres well to both cathode and anode with the average thickness of 60 and 300μm, respectively. The electrolyte seems to be homogeneous in thickness. It is widely known [258] that the chemical expansion due to the loss of oxygen and change of ionic radii of $Ti^{3+}/Ti^{4+}$ would threaten the bonding between the anode and electrolyte. Fortunately, the microstructure indicates that neither volumetric change during the reduction at 900$^{o}$C or thermal cycles between 450$^{o}$C and room temperature during the infiltration process harm the integrity of the fuel cell. The coarse pores are observed in the anode support, which are sufficient to provide pathways for fuel transport into the TPBs. The inset of Figure 4.1 is the magnified BSE image of the electrolyte/anode interface. It demonstrates that a good intimacy has been successfully formed between perovskite anode and YSZ electrolyte by co-casting and co-sintering techniques. A thin and discontinuous $LSCT_{A-}$ layer on the interface could provide more surface areas for anode chemical reaction on the electrolyte/anode interface, where YSZ, $LSCT_{A-}$ and fuel meet together because $LSCT_{A-}$ does not have sufficient ionic conductivity to allow the transport of oxygen ions from the YSZ electrolyte within the $LSCT_{A-}$ anode.

### 4.3.2 EIS of symmetric LSCF-YSZ cell

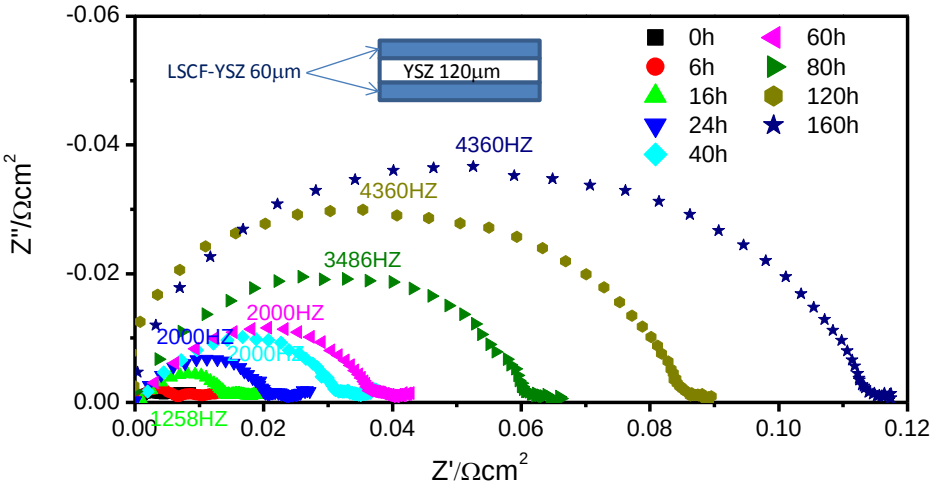


Figure 4.2 Nyquist plots of AC-impedance data obtained from the LSCF-YSZ symmetric cell at 700°C in air at different time. The high-frequency intercepts have been offset to zero.

In order to evaluate the resistance from the cathode side, the symmetric LSCF-YSZ cells were made by lamination of porous and dense YSZ tapes and co-sintering at 1350°C for 2h, followed by infiltration of precursor solutions containing $La_{0.8}Sr_{0.2}Co_{0.2}Fe_{0.8}O_3$ (LSCF) and firing at 450°C in air. The YSZ electrolyte and LSCF-YSZ electrode are 120 and 60μm in thickness, as shown in the inset of Figure 4.2. The structure, thickness and impregnate loading of the electrode of the symmetric cells are the same as those of LSCF-YSZ cathode of button cells.

Figure 4.2 shows the impedance spectra of the symmetric cell measured at 700°C in air at the different time. The ohmic contribution from YSZ electrolytes, current collectors and lead wires has been removed and the impedance data were divided by 2 because there are two identical electrodes contributing to the impedance. All the impedance spectra are comprised of a depressed semicircle and a small tail at the low frequency. The polarization resistance, $R_p$, has increased from 0.01 to 0.115Ω/cm$^2$ after 160-h ageing at 700°C due possibly to the growth and agglomeration of impregnated LSCF particles on the YSZ surface leading to the decrease of the Triple Phase Boundaries (TPB) on the cathode, where YSZ, LSCF and oxygen meet together.

The effects of calcination temperature and duration on the polarization resistance of the impregnated cathode, such as LSF-YSZ and LSCF-GDC symmetric cells, have been reported previously, demonstrating that coarsening of the infiltrated nano-particles were responsible for the degradation of oxygen reduction at the cathode [259~261].

### 4.3.3 Effects of metallic infiltration on the initial performance

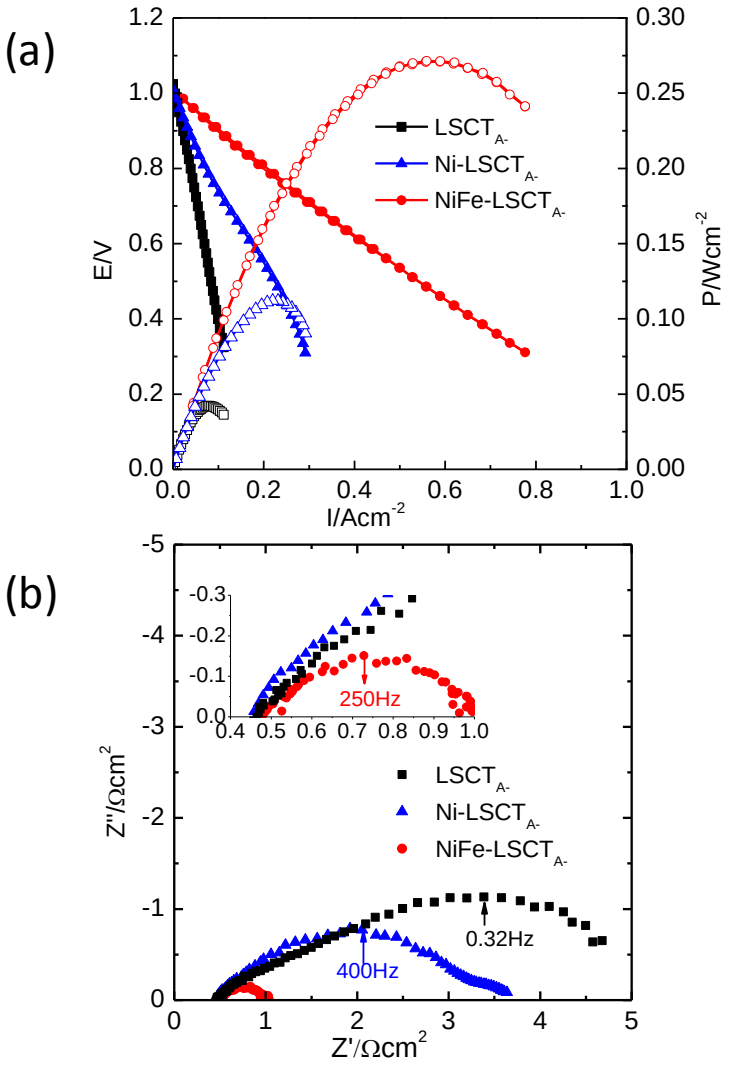


Figure 4.3 (a) I-V and I-P curves and (b) EIS curves of the cells tested at 700°C in humidified hydrogen (3% $H_2O$) with different anodes: $LSCT_{A-}$ backbone, Ni and Ni-Fe impregnated $LSCT_{A-}$. I-V and I-P curves in (a) are signified by solid and open symbols, respectively. The inset in the Nyquist plots magnifies the high-frequency intersection with x-axis.

After being impregnated with the precursor solutions in the electrodes and attached with silver wires on the electrodes, the fuel cells were directly mounted and sealed onto an alumina tube, and a gas flow of Ar containing 5% $H_2$ was passed over to the anode to avoid the oxidation of the anode upon heating to testing temperature 700$^oC$, before switching to humidified hydrogen (3% $H_2O$). The initial performance of the fuel cell without catalyst, and with 3wt.% nickel and 3wt.% Ni-Fe on the anode at 700$^oC$ is shown in Figure 4.3. All the three cells show an open circuit voltage (OCV) of 1.02V (Figure 4.3(a)), which is slightly lower than the theoretical OCV of 1.09V from Nernst equation using humidified $H_2$ containing 3% $H_2O$. The addition of nickel to the bare $LSCT_{A-}$ anode doubles the peak power density. Compared to the cell with Ni as catalyst, the substitution of 25mol.% Fe for Ni as catalyst enhances the peak power density by a factor of two as shown in Figure 4.3(a). The three cells show a similar series resistance, $R_s$, which can be estimated by the high frequency intersection of the Nyquist plot and x-axis in Figure 4.3(b). The addition of iron decreases the polarization resistance, $R_p$, which can be determined by subtracting $R_s$ from the modulus of the low frequency intersection of the Nyquist plot with x-axis. The decrease of the $R_p$ value for impregnated cell confirms that the high electrode losses can be attributed to the bare $LSCT_{A-}$ anode, in good agreement with the results in last chapter. Since the comparison of the impregnated materials between Ni and ceria+Ni indicates that the rate limiting step for $LSCT_{A-}$ anode with metal catalyst is the insufficient ionic conduction through the backbone, the enhancement by impregnation of bi-metal can possibly be the result of ionic conductivity of Wustite $Fe_{1-x}O$, present in the system from the incomplete reduction of the oxides; however, another possible explanation could be that the enhancement results from the better microstructure in the bi-metal system. The defect in Wustite $Fe_{1-x}O$ is generally regarded as the iron vacancy in a rocksalt oxygen lattice, and it is possible that the ferric iron in a tetrahedral interstices could be compensated, in part, by interstitial oxygen [262], which may contribute to the oxygen ionic conductivity. Moreover, the addition of a small amount of Fe into Ni could significantly decrease the aggregation of Ni during heating process to operating temperature and improve the number of active sites on Ni and the activity of those sites by decreasing the activation energy. In this case, both the charge transfer and the diffusion process are accelerated by the Fe addition [263].

### 4.3.4 Stability of bare $LSCT_{A-}$ anode

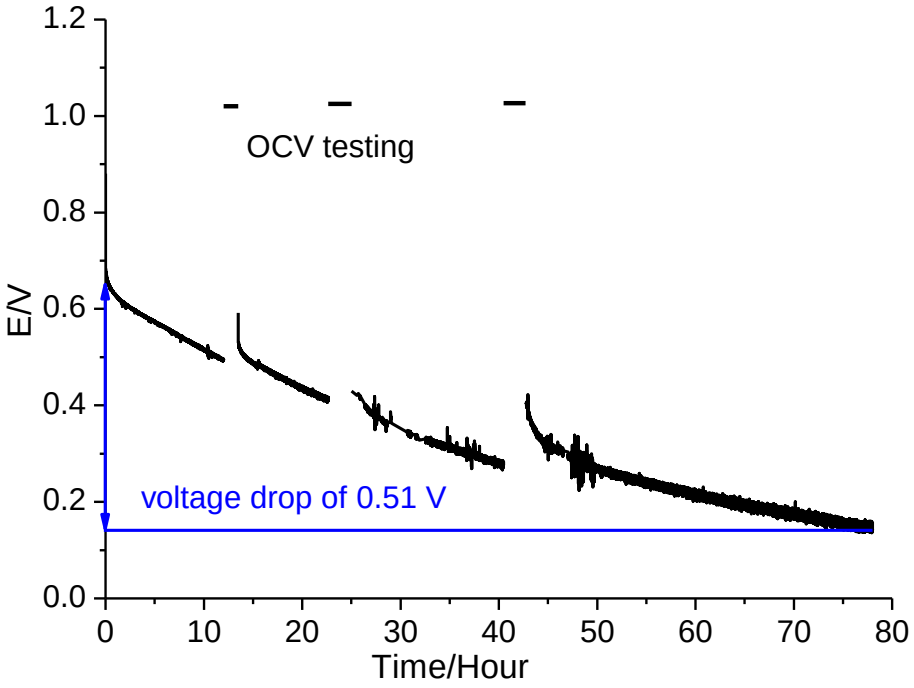


Figure 4.4 Stability testing of the bare $LSCT_{A-}$ anode at 700°C in humidified hydrogen (3% $H_2O$) under the current density of 60mA/cm$^2$

As well as the initial performance, the stability of the cells without catalyst, and with Ni or Ni-Fe as catalyst was examined. The current densities were set to give a starting voltage ~0.7V in each of the cells.

The voltage variation with time at current densities of 60mA/cm$^2$ for the $LSCT_{A-}$ backbone cells at 700°C is shown in Figure 4.4. The OCV of the cell tested at intervals between the stability testing is stable, about 1.02V, throughout the whole testing duration, which indicates the decrease of the voltage is coming from the area specific resistance of the fuel cell under constant fuel utilization. The $LSCT_{A-}$ backbone shows a drastic degradation from 0.66V to 0.15V in 80h, which has so far been attributed to the re-oxidation of the scaffold under relatively high oxygen partial pressure resulted from transporting oxygen ions at the low voltages. The partial oxidation of $LSCT_{A-}$ surface causes a decrease in both ionic and electronic conductivities, and therefore results in a deterioration of the performance. It should be

noted that the performance of the cell slightly increases even after the short-time relaxation at OCV.

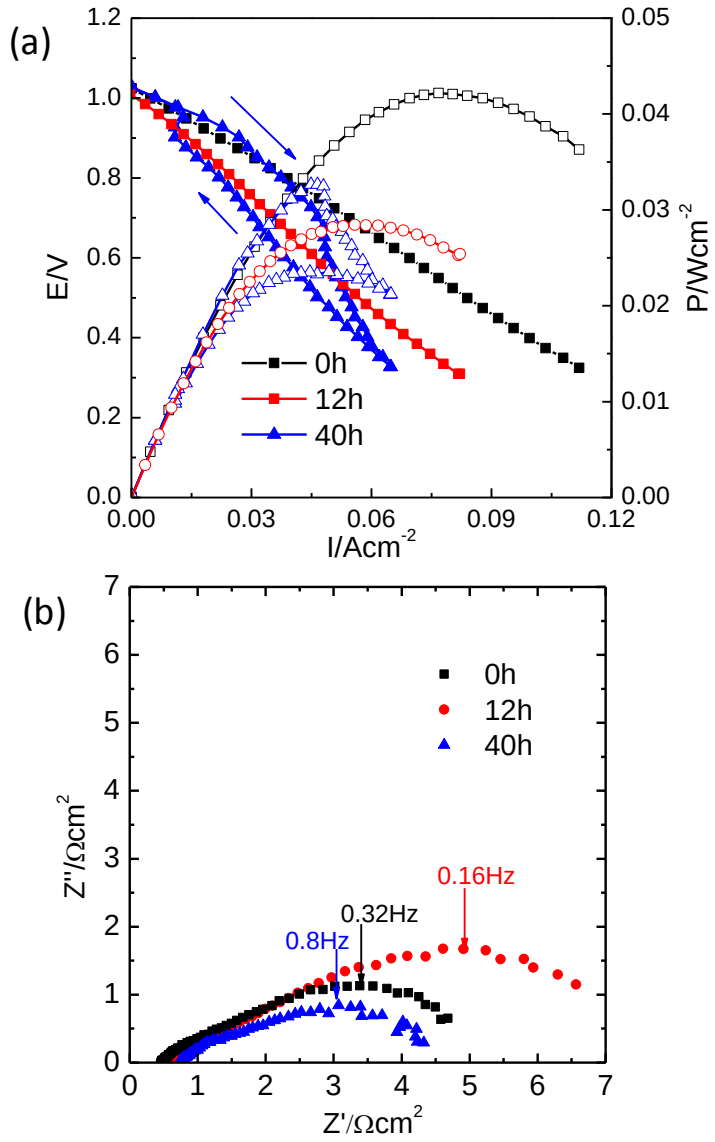


Figure 4.5 (a) I-V and I-P curves and (b) EIS curves of the bare $LSCT_{A-}$ anode at different time upon stability testing at 700°C in humidified hydrogen (3% $H_2O$). I-V and I-P curves in (a) are signified by solid and open symbols, respectively. The impedance data were recorded under OCV.

The performance of bare $LSCT_{A-}$ anode at different time upon stability testing at 700°C in wet hydrogen is shown in Figure 4.5. The OCV values at different time are around 1.02V, lower than the theoretical value calculated from Nernst equation but

stable over the testing time. Upon reaching the testing temperature 700$^{o}$C, the cell achieves a maximum powder density of 42mW/cm$^2$, which is comparable with that of $LSCT_{A-}$/YSZ/LSF-LSC-YSZ cell prepared by aqueous tape casting (see section 3.3.2). After 12-h testing under a constant current density, the maximum power density of the cell decreased by 33%. It is more interesting to note that after the stability testing for 40 h a different behaviour of the voltage dependence on the current density can be observed upon the I-V testing. When the current density increases from zero to 0.65A/cm$^2$, the resistance calculated from the slope of the voltage to the current density at low current density is much smaller than that at the high current density; however, when the current density goes back to zero, the resistance of voltage/current density slope is a constant value except at the low current density close to zero where the collected voltage jumps to and coincides with the original curve. In this way, a loop has been formed under the cycle of the current density with the maximum power density of 33 and 23mW/cm$^2$ at the rising and declining phase of the current density, respectively. The appearance of the loop can be attributed to the reduction of re-oxidised surface of $LSCT_{A-}$ backbone during stability testing under an OCV value leading to the recovery of performance at the low current density and the re-oxidation at the high current density segment. The impedance spectra under OCV of the $LSCT_{A-}$ cell at the different time upon stability testing are shown in Figure 4.5(b). A small increase of ohmic resistance can be observed, probably because the body of the $LSCT_{A-}$ backbone maintains the high conductivity during testing. The main losses for the cell are from the polarization resistance due to insufficient ionic conductivity and catalytic activity of the anode material for hydrogen oxidation, which increase significantly after 12-h testing. The increase of polarization resistance resulting from the coarsening process of impregnated LSCF in the YSZ cathode can be neglected by comparing with the magnitude of polarization resistance between the LSCF-YSZ cathode and the whole cell. So far the increase of polarization resistance is ascribed to the re-oxidation of $LSCT_{A-}$ surface leading to the reduction of ionic pathways on the anode surface and reaction sites for hydrogen oxidation. After a stability testing for 40h, the cell shows a decreased polarization resistance as compared with that at 0h. The decrease of polarization resistance under OCV can be explained by the accelerated reaction of hydrogen oxidation due to the electrolyte/anode interfacial enrichment of oxygen ions from the cathode side.

### 4.3.5 Stability of nickel impregnated $LSCT_{A-}$ anode

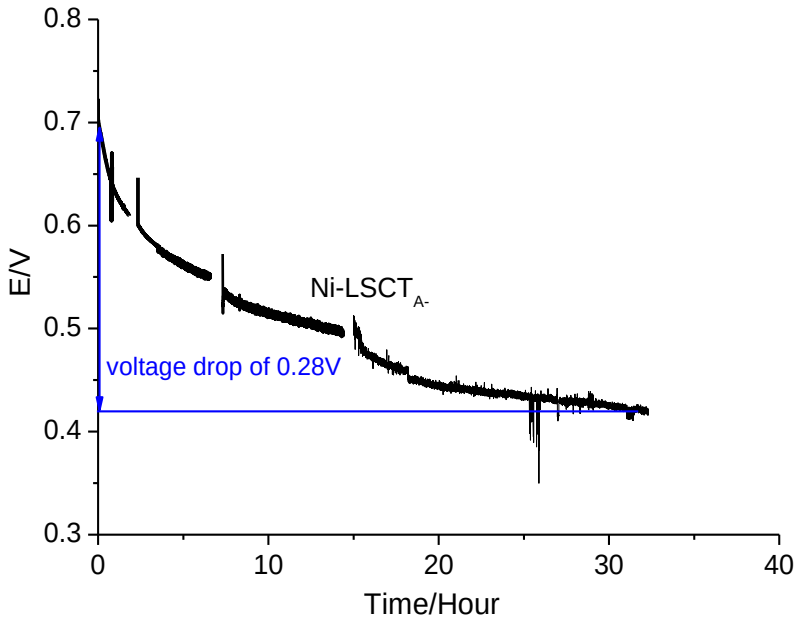


Figure 4.6 Stability testing of the 3wt.% nickel-impregnated $LSCT_{A-}$ anode at 700°C in humidified hydrogen (3% $H_2O$) under the current density of 130mA/cm$^2$

The time dependence of the voltage for 3wt.% nickel-impregnated $LSCT_{A-}$ cell under a current density of 130mA/cm$^2$ is shown in Figure 4.6. Likewise, the OCV measurement was carried out at the intervals during the stability testing and a stable OCV value around 1.01V indicates the integrity of the cell except small pinholes on the YSZ electrolyte or sealant. It can be seen that the nickel-impregnated cell shows a faster degradation rate during the first 20h, comparable with that of bare $LSCT_{A-}$ cell, but in the following testing time the impregnated sample demonstrates a more stable status than the one without catalyst. The appearance of nickel catalyst on the $LSCT_{A-}$ backbone prevents the successive deterioration of the anode performance.

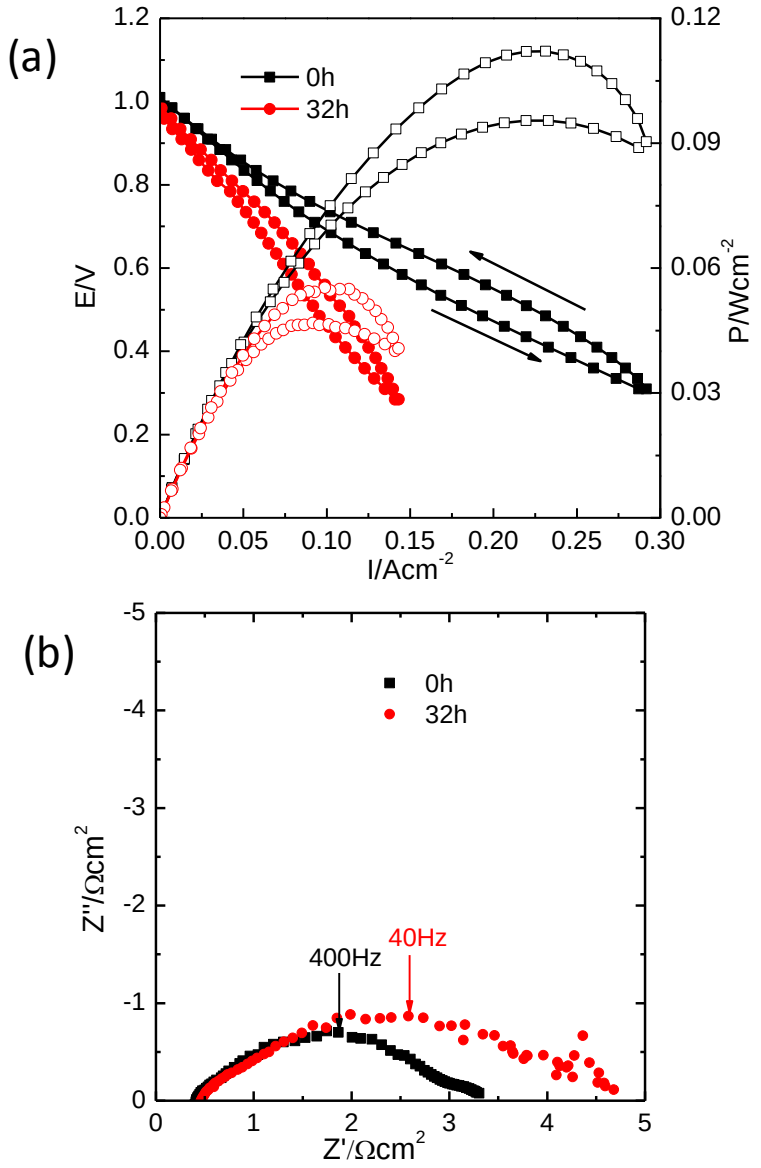


Figure 4.7 (a) I-V and I-P curves and (b) EIS curves of the 3wt.% nickel impregnated $LSCT_{A-}$ anode at different time upon stability testing at 700°C in humidified hydrogen (3% $H_2O$). I-V and I-P curves in (a) are signified by solid and open symbols, respectively. The impedance data were recorded under OCV.

Figure 4.7 shows the performance of 3wt.% nickel-impregnated $LSCT_{A-}$ cell before and after stability testing for 32h at 700°C in humidified hydrogen under the current density of 130mA/cm$^2$. After 32-h testing, the maximum power density has been decreased by around 50%. The EIS data shown in Figure 4.7(b) demonstrate that the main losses of the cell performance are from the polarization resistance of the whole

cell. By comparing with the polarization resistance of LSCF-YSZ electrode with the cell, it is allowed to summarise that the degradation of the cell performance is mainly attributed to the anode, such as the agglomeration and growth of nickel particles on $LSCT_{A-}$ surface, and partial oxidation of $LSCT_{A-}$ surface under the low voltage.

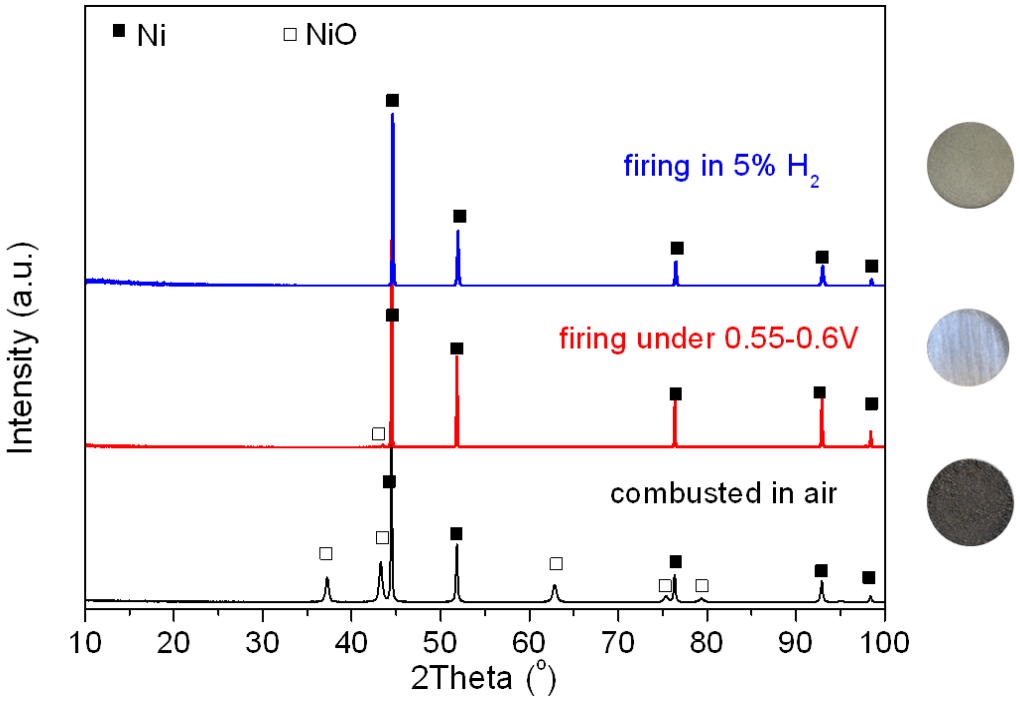


Figure 4.8 XRD patterns of the prepared Ni(O) powder calcined at 450°C and reduced at the oxygen partial pressure ~$10^{-13}$atm and 5% $H_2$-Ar

In order to explore the phases of the prepared catalyst under different atmospheres, nickel nitrate solution was prepared with addition of citric acid, and after evaporation, the sample was calcined at 450°C in air for 30min, followed by being reduced at the oxygen partial pressure ~$10^{-13}$atm or argon containing 5% hydrogen for 12h. As displayed in Figure 4.8, after annealing at 450°C, the sample is dark and comprised of NiO and Ni. The formation of nickel is possibly due to the reduction condition caused by combustion of citric acid. Upon reduction in reducing condition, the sample becomes brown and metallic after being polished, and is composed of a single phase of metallic nickel. Therefore, during the stability testing, the catalyst in the anode is likely to be metallic nickel rather than nickel oxide.

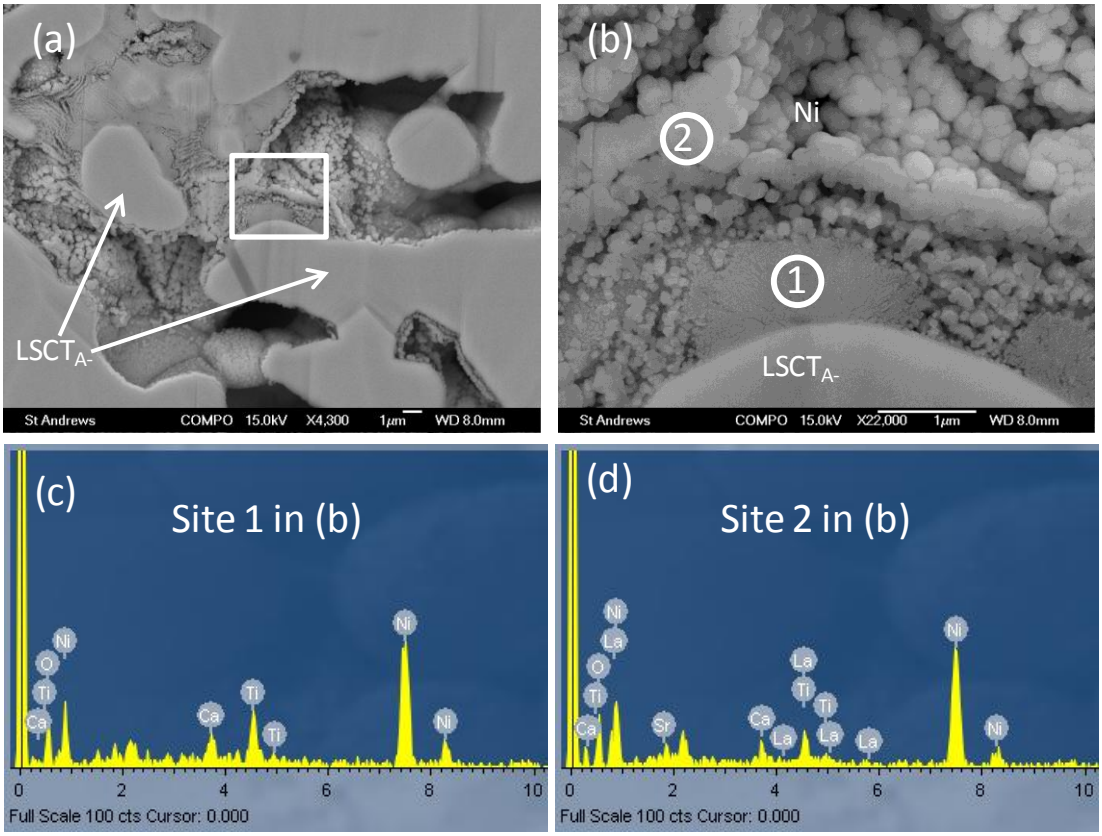


Figure 4.9 Back-scattered electron (BSE) images of Ni-impregnated LSCT$_{A-}$ (a, b) after firing at 450$^{o}$C in air for 30min and (c, d) energy dispersive X-ray analysis (EDX) of the areas marked by the sites 1 and 2 in (b), respectively. (b) is the enlarged image of the rectangular area in the general images (a).

Since the addition of catalyst improves both the performance as well as the durability of the cell under working condition, it would be interesting to investigate the correlation between the performance and the microstructure of LSCT$_{A-}$-based anode. Figure 4.9 shows the back-scattering images (BSE) of the Ni-LSCT$_{A-}$ anode after firing at 450$^{o}$C in air for 30min and before the stability testing. From the microstructure after impregnation and low-temperature firing, a uniform coating of nano-sized NiO has formed on the LSCT$_{A-}$ particle surface (Figure 4.9(a, b)). The fine particles, around 50nm, can be visible on the edges around the LSCT$_{A-}$ particles, especially around the convex areas, and the coarse particles with 200nm in diameter are concentrated on the concave surfaces. The difference in the size of catalysts is attributed to the uneven deposition process driven by capillary action, resulting in a thinner layer formed on convex surfaces and a thicker layer on concave surfaces [249].

The EDX spectra (Figure 4.9(c) and (d)) show the composition at site 1 and 2: a large proportion of La, Sr, Ca and Ti can be found in the porous particles. The decomposition of nitrate and citric acid produce a local acidic condition and therefore induces a partial dissolution of the backbone at the firing process.

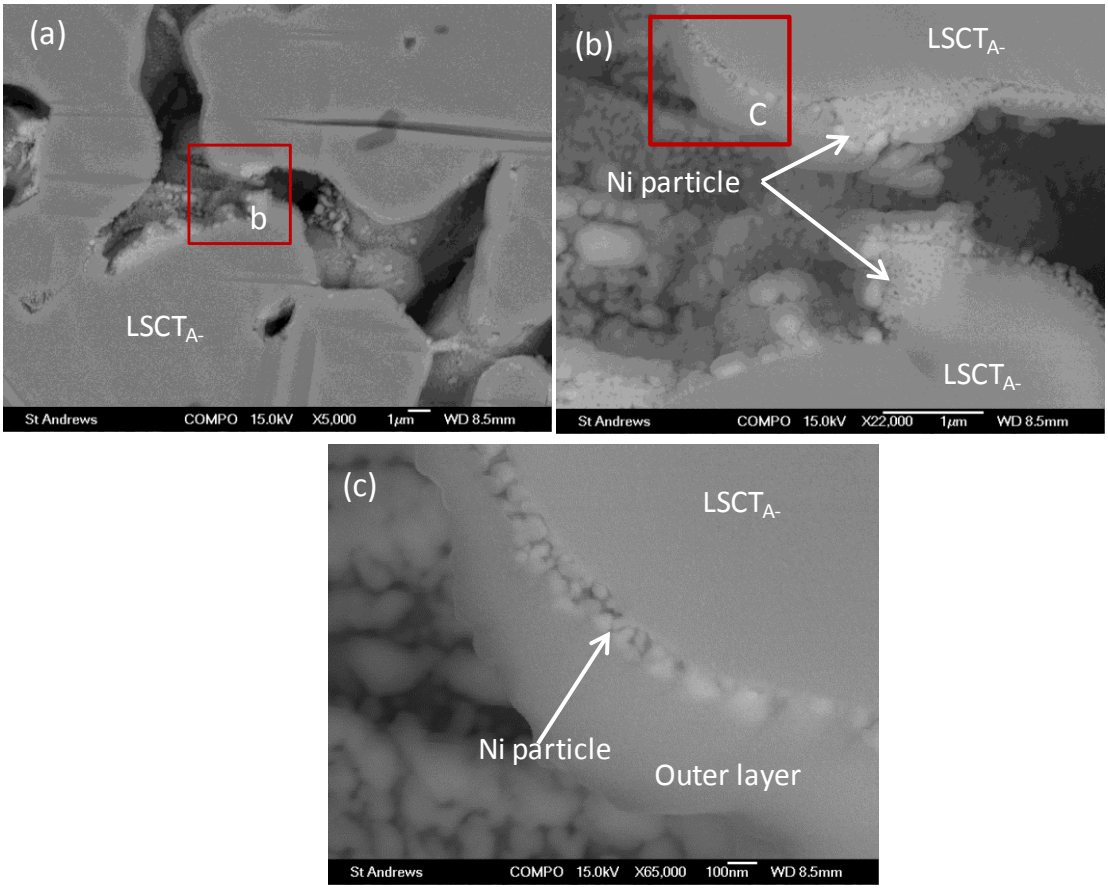


Figure 4.10 Back-scattered electron (BSE) images of Ni-impregnated $LSCT_{A-}$ after the stability testing at 700°C for 32h in humidified hydrogen (3% $H_2O$). (b) and (c) are the enlarged images of the rectangular areas in the images (a) and (b), respectively.

There is a significant change in the microstructure after 32 hours in humidified hydrogen at 700°C as shown in Figure 4.10. The surface of $LSCT_{A-}$ backbone around the pores is covered by the catalyst particles (Figure 4.10(a)). A continuous bright layer contains nanoparticles of 50nm, which tend to line up along the edge of $LSCT_{A-}$ particles but agglomerate on the corners (Figure 4.10(b) and (c)). A layer even darker than the backbone can be distinguished outside the bright layer, whose composition is not clear yet.

### 4.3.6 Stability of bimetallic $Ni_{0.75}Fe_{0.25}$ impregnated $LSCT_{A-}$ anode

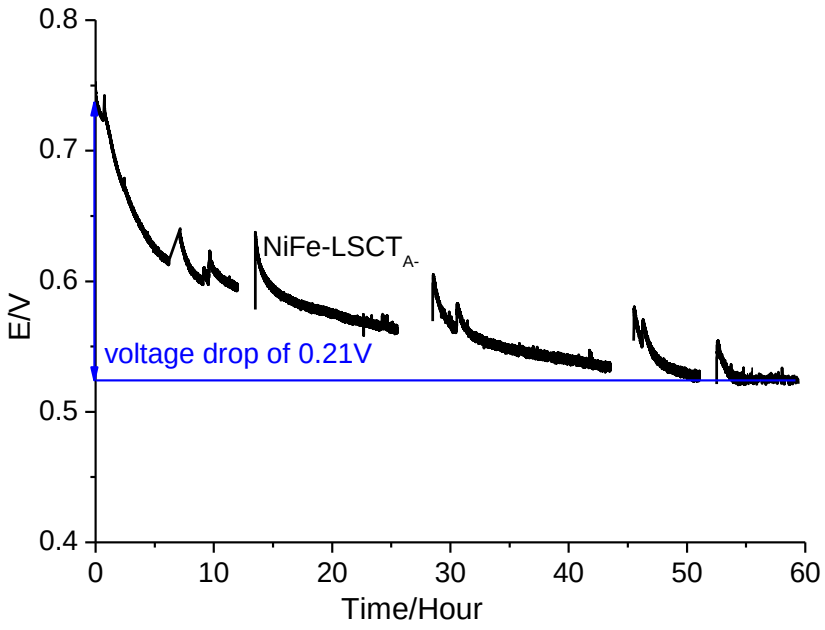


Figure 4.11 Stability testing of the 3wt.% metallic $Ni_{0.75}Fe_{0.25}$-impregnated $LSCT_{A-}$ anode at 700°C in humidified hydrogen (3% $H_2O$) under the current density of 280mA/cm$^2$

The time dependence of the voltage for 3wt.% $Ni_{0.75}Fe_{0.25}$-impregnated $LSCT_{A-}$ cell under a current density of 280mA/cm$^2$ is shown in Figure 4.11. At the first 20h, the degradation rate is similar with bare $LSCT_{A-}$ and nickel impregnated $LSCT_{A-}$ cells. However, in the following testing time, the degradation rate of the cell catalysed with nickel-iron composite is much slower than that with pure nickel. Within 32 hours, the voltage of Ni-$LSCT_{A-}$ cell drops below 0.45V shown in Figure 4.6, while that of Ni-Fe composite impregnated $LSCT_{A-}$ cell stabilizes at 0.53V after 60 hours. The prevention of the nickel aggregation by the addition of iron could be one of the reasons responsible for the improved stability [263].

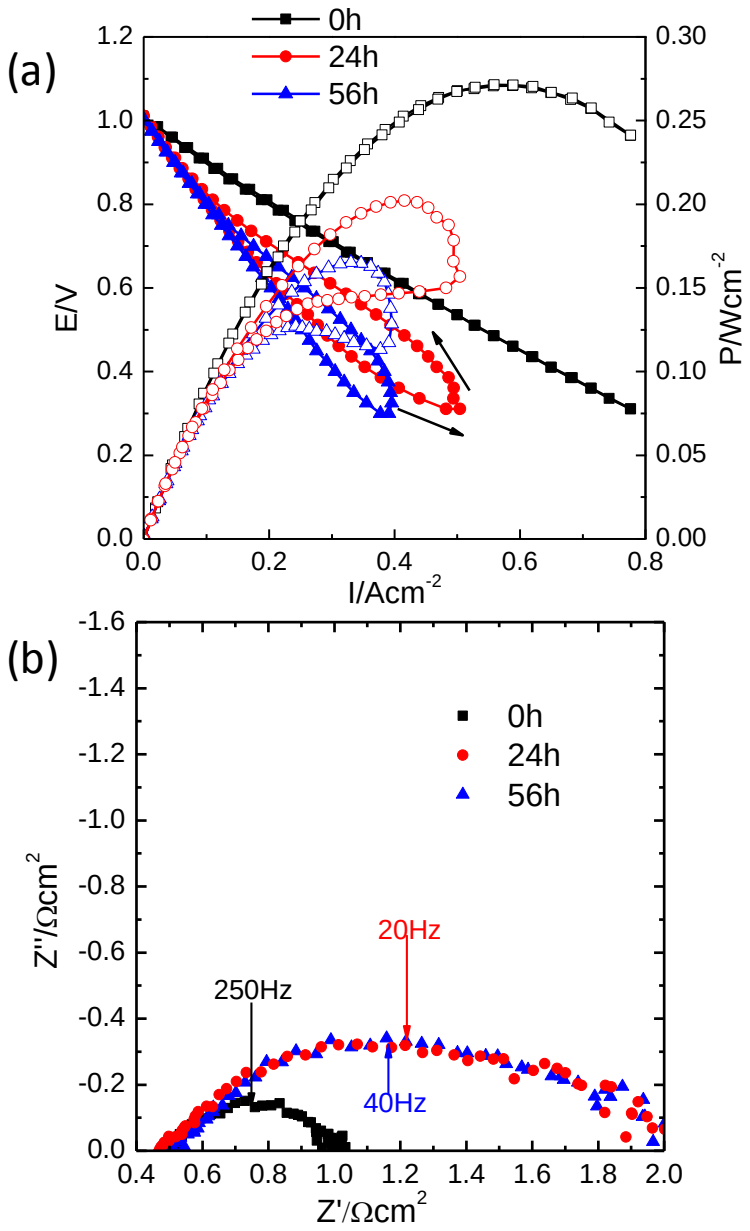


Figure 4.12 (a) I-V and I-P curves and (b) EIS curves of the 3wt.% $Ni_{0.75}Fe_{0.25}$-impregnated $LSCT_{A-}$ anode at different time upon stability testing at 700°C in humidified hydrogen (3% $H_2O$). I-V and I-P curves in (a) are signified by solid and open symbols, respectively. The impedance data were recorded under OCV.

Figure 4.12 shows the I-V and I-P curves of the cell infiltrated with 3wt.% Ni-Fe bimetallic catalyst at different time by applying a constant current density to the cell in humidified hydrogen at 700°C. Before the stability test, the cell gives a high power density with the peak density of 270mW/cm$^2$ and shows a reversible behaviour of

voltage with the changing current density. A significant decrease of performance can be observed on the cell after 24-h testing under a constant current density. The formation of a broad loop could possibly be due to the sensitive transformation between oxide and metal under low/high current density. The degradation is enhanced with time, but the rate is relatively moderate. The losses from the cell are mainly from the polarization resistance, as shown in impedance spectra of the cell under OCV.

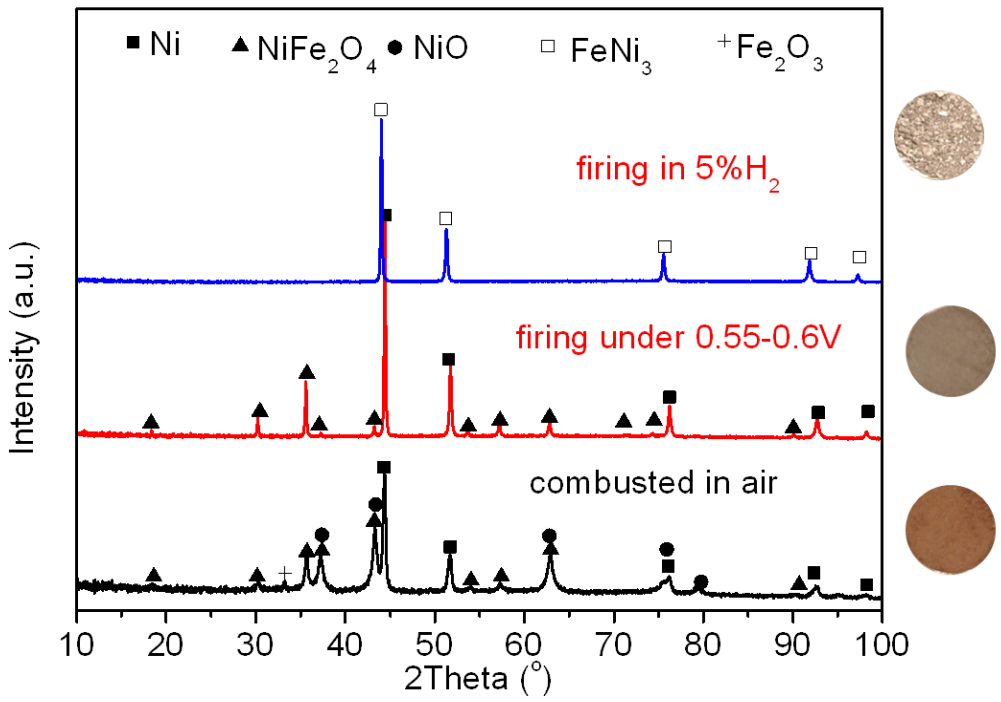


Figure 4.13 XRD patterns of the prepared $Ni_{0.75}Fe_{0.25}$ catalyst calcined at 450°C and reduced at the oxygen partial pressure ~$10^{-13}$atm and 5% $H_2$-Ar

In order to study the phases of the prepared catalyst under different atmospheres, nickel and iron nitrate were dissolved into deionised water with addition of citric acid, followed by being calcined at 450°C in air for 30min and then being reduced at the oxygen partial pressure ~$10^{-13}$atm and argon containing 5% hydrogen for 12h, respectively. The molar ratio of Ni to Fe in this study is 3:1. Figure 4.13 shows XRD patterns of Ni-Fe catalyst under different conditions. Before reduction, the sample powder is in brown colour on the exterior. The main phases include NiO, $NiFe_2O_4$ and Ni; however, a small diffraction peak, attributed to cubic $Fe_2O_3$ phase (JCPDs 00-002-1047), was also detected. Upon reduction in argon containing 5% hydrogen, the

sample becomes metallic colour, the diffraction peaks of which can assigned for cubic awaruite $FeNi_3$ (JCPDs 00-038-0419). Therefore, during the stability testing, the catalyst in the anode is likely to maintain as metallic nickel and iron oxide rather than $FeNi_3$.

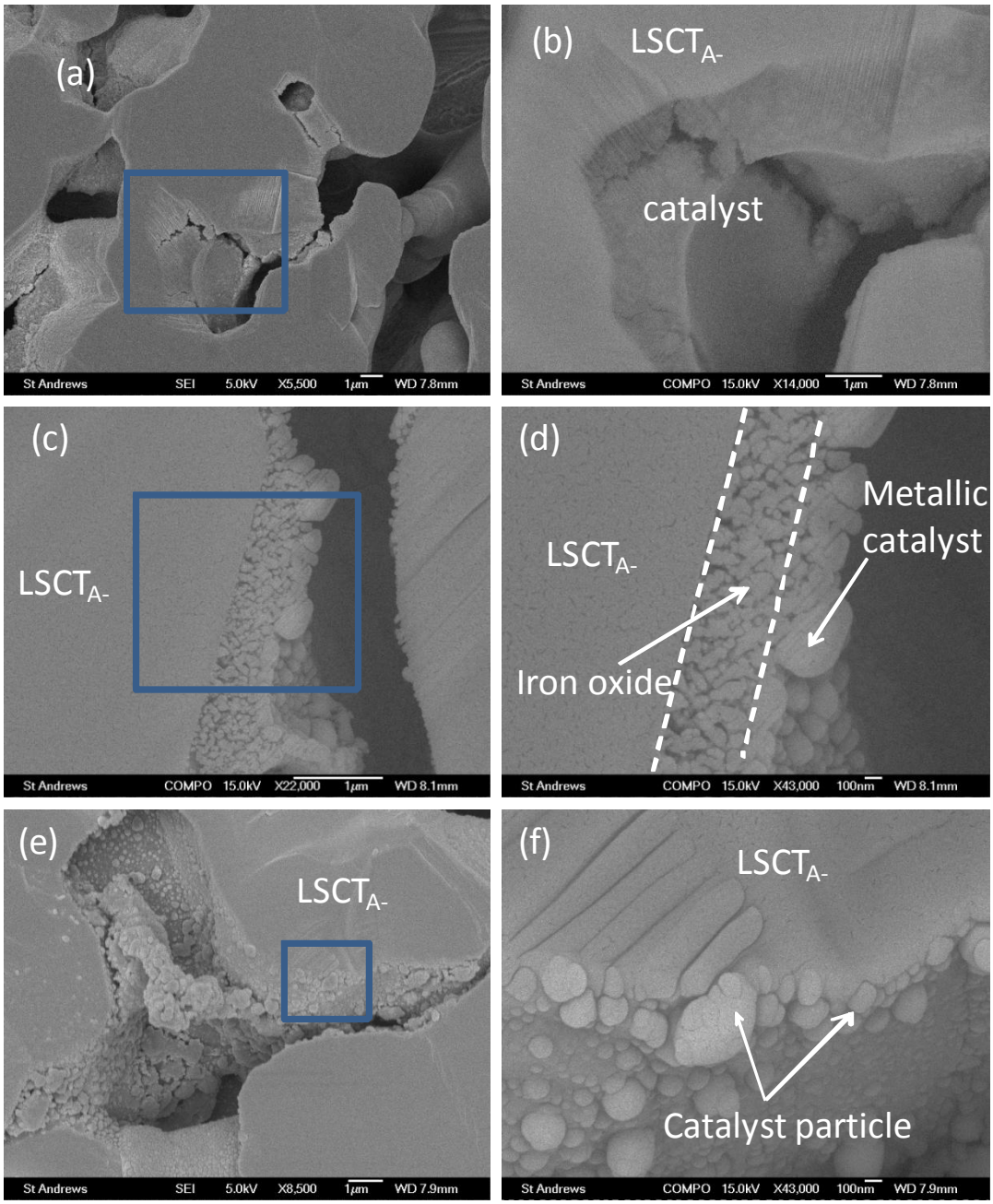


Figure 4.14 Secondary electron microscopy (SEM) and Back-scattered electron (BSE) images of Ni-Fe impregnated $LSCT_{A-}$ (a, b) before testing, (c, d) and (e, f) after testing for 24 and 60h, respectively, at 700$^{o}$C. (b), (d) and (f) the enlarged images of the rectangular areas in the general images (a), (c) and (e), respectively.

It is of importance to monitor the potential structural changes of impregnated anode upon testing in fuel cell condition in order to understand the mechanics for the cell degradation with time. The microstructure of Ni-Fe impregnated $LSCT_{A-}$ anode at different testing time is shown in Figure 4.14. After firing at 450$^{o}$C, a dense layer of bi-metallic oxide is formed covering the surface of the backbone particles (Figure 4.14(a)). In particular, the thickness of the catalyst can reach around 1μm at the bottom side (Figure 4.14(b)). A comparison of the SEM image (Figure 4.14(a)) and BSE image (Figure 4.14(b)) implies a seamless bonding between the catalyst and backbone. After 24-h reduction at 700$^{o}$C, the dense layers become a porous coating comprising of metallic particles of 200nm in diameter on the very top but 50nm in diameter between top layer and the backbone (Figure 4.14(d)). The positional variation of particle size could be a result of the difference in oxygen partial pressure on the surface and bottom in the Ni-Fe layer: the higher content of $Fe^0$ because of lower oxygen partial pressure could assist the grain growth of the catalyst. A dark circle with thickness of 50-100nm is detected on the surface of the large catalyst. The nature of this dark area is not certain so far, but should be oxides from the backbone due to the low molar mass per atom indicated by BSE images. Their compositions will be examined using EDX on a TEM to avoid the large interaction volume of the electron beam with a thick substrate as encountered when using EDX on a SEM. From the Figure 4.14(e), the spalling of the thick catalyst layer after 60-h reduction may be a contributing reason for the degradation of the performance.

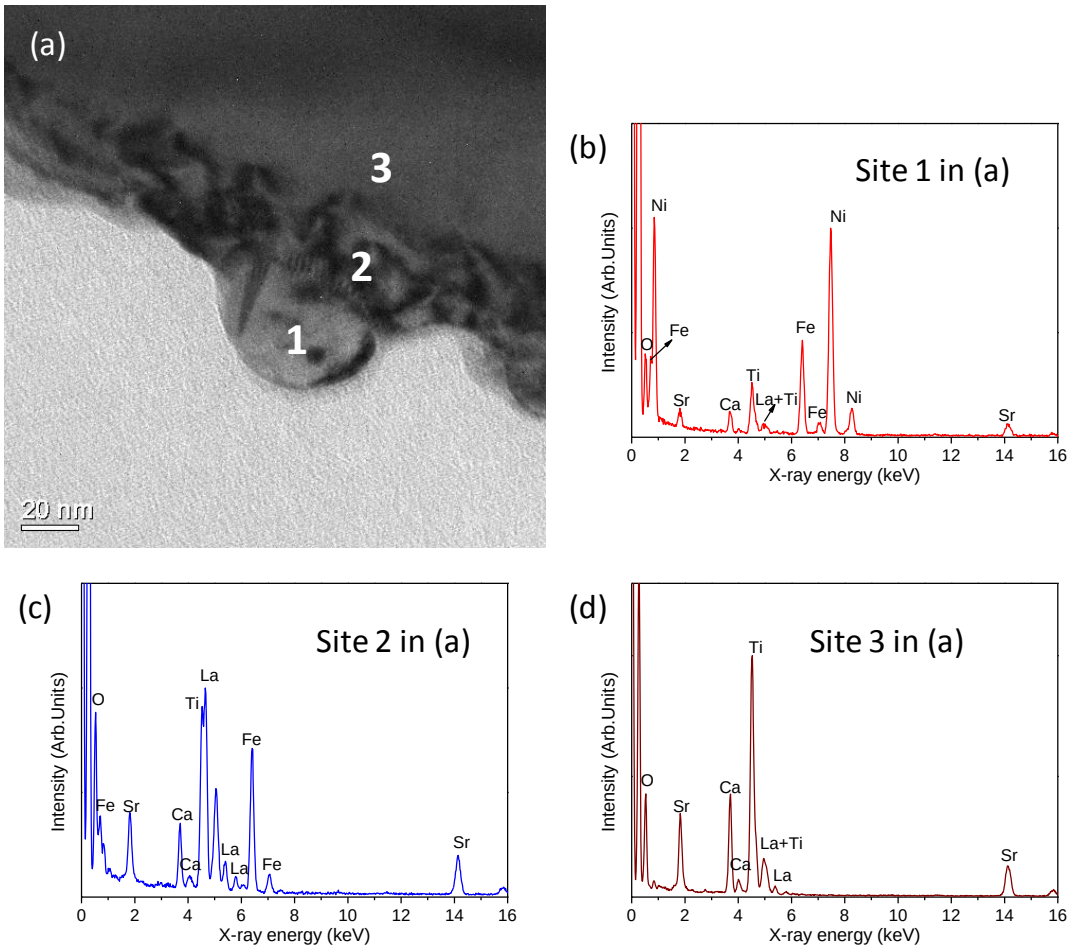


Figure 4.15 (a) Transmission electron microscopy (TEM) image of $LSCT_{A-}$ anode coated with a Ni-Fe layer on the surface after stability testing for 24h at 700°C in humidified hydrogen and (b), (c) and (d) the corresponding EDX spectra of the marked areas by numbers 1, 2 and 3

A TEM micrograph with EDX is able to reveal more detail of impregnated catalyst on the backbone and identify the elemental composition of the different layers. The TEM image of an interface between the $LSCT_{A-}$ backbone and catalyst after testing in fuel cell condition for 24h is shown in Figure 4.15, along with the corresponding EDX spectra. Two different structures on the $LSCT_{A-}$ backbone can be observed, including a nanoparticle on the very top and a relatively dense layer between the backbone and top layer, consistent with the analysis result of SEM images. According to the EDX spectra of coating, there is chemical interaction between Ni-Fe and $LSCT_{A-}$ backbone. The microstructure of catalyst on the $LSCT_{A-}$ surface play an important role in the cell performance: on the very top the nanoparticle is mainly comprised of Ni and Fe; the

layer between Ni-Fe nanoparticles and $LSCT_{A-}$ backbone, as indicated by site 2, shows a strong interaction between iron and the backbone, possibly consisting of $LaFeO_3$ [264] and titanate.

The growth of nano-sized metal catalyst due to thermal instability is always quoted to be the major reason for the performance degradation of a cell prepared with infiltration [112]. The nano particle growth has two ramifications: it will decrease the reaction site of hydrogen oxidation or oxygen reduction, and increase the series resistance by creating layer intergranular gap. In our anode-supported cell where $LSCT_{A-}$ provides most of the electric conductivity, the degradation comes mostly from the catalysis of the anode. The growth of metal particles is obvious from the SEM images, but the interaction between the metal particles and the $LSCT_{A-}$ backbone may contribute extra degradation of the anode. The substitution of Fe for Ni could greatly decrease the aggregation of Ni particles [263]; on the other hand, the less extent of the direct interaction between the metallic catalysts and the $LSCT_{A-}$ backbone could decrease the blockage of the effective electrochemical reaction sites by the backbone oxides.

### 4.3.7 The effect of anode porosity on the performance of bimetallic $Ni_{0.75}Fe_{0.25}$ impregnated $LSCT_{A-}$ anode (see section 4.3.6)

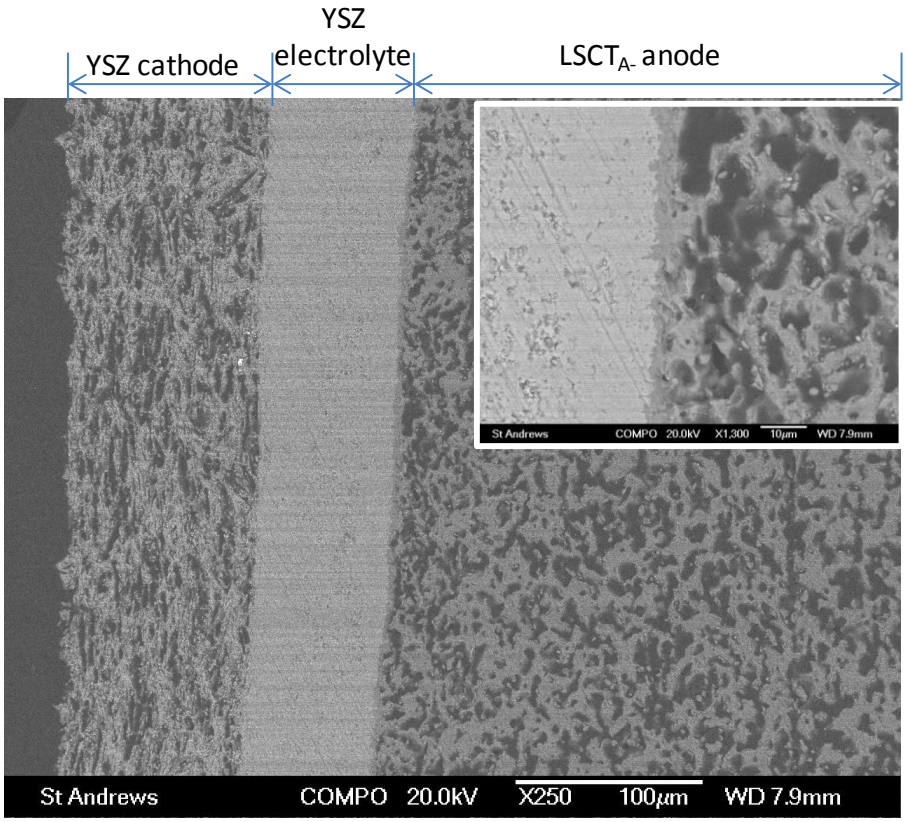


Figure 4.16 Back scattered electron (BSE) image of the cross section of the cell with less porosity (~ 35%) on the anode after reduction. The inset is the magnified image of the anode/electrolyte interface.

The decrease of the porosity of $LSCT_{A-}$ backbone anode is conducive to improving the electronic conductivity of the anode and more importantly, coordinating the TECs between anode backbone and electrolyte during pre-reduction and subsequential multi low-temperature firing. This can be drawn by comparing the number of cells with different porosity ready for fuel cell testing after multi-impregnation of electrodes. The content of graphite in the co-casted and laminated $LSCT_{A-}$ layer has been decreased to 20 and 25wt.% corresponding to the weight of $LSCT_{A-}$ powder. The microstructure of the cell is shown in Figure 4.16, consisting of a dense electrolyte layer sandwiched by porous YSZ cathode and $LSCT_{A-}$ anode. As displayed in the inset, a dense and thin layer of $LSCT_{A-}$ has formed on the interface between the

porous anode and the dense electrolyte, which could inhibit the diffusion of hydrogen to the reaction sites on the anode/electrolyte interface. Simultaneously, the reduction of porosity in the laminated $LSCT_{A-}$ layer could also slow down the diffusion of fuel to the TPBs leading to a limitation of cell performance.

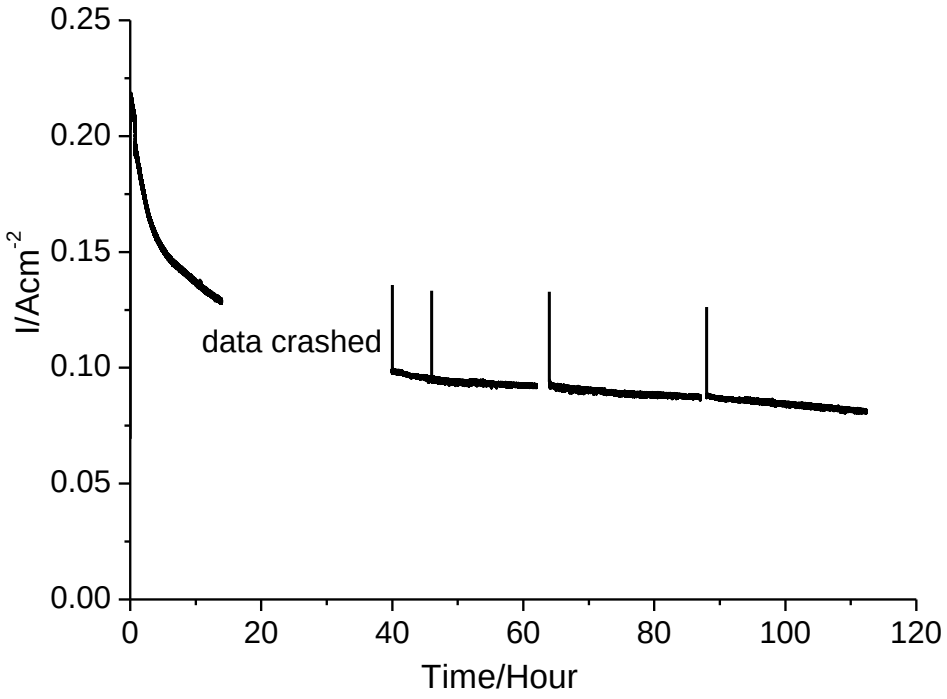


Figure 4.17 Stability testing of the 3wt.% metallic $Ni_{0.75}Fe_{0.25}$-impregnated $LSCT_{A-}$ anode with low porosity (~ 35%) at 700°C in humidified hydrogen (3% $H_2O$) under a constant voltage of 0.7V

The time dependence of current density for Ni-Fe impregnated $LSCT_{A-}$ anode with a low porosity under a constant voltage of 0.7V in fuel cell testing condition is shown in Figure 4.17. A relatively fast degradation of cell performance with time is observed in the first 40h, even the data between 14 and 40h have been crashed. This rapid decrease of current density could be attributed to the nanoparticle growth of catalyst and the interaction of catalyst and anode scaffold, especially the chemical interaction between the iron composites in the inner layer and $LSCT_{A-}$ backbone, which has been illustrated in Figure 4.15. With increasing testing time the current density is becoming more stable.

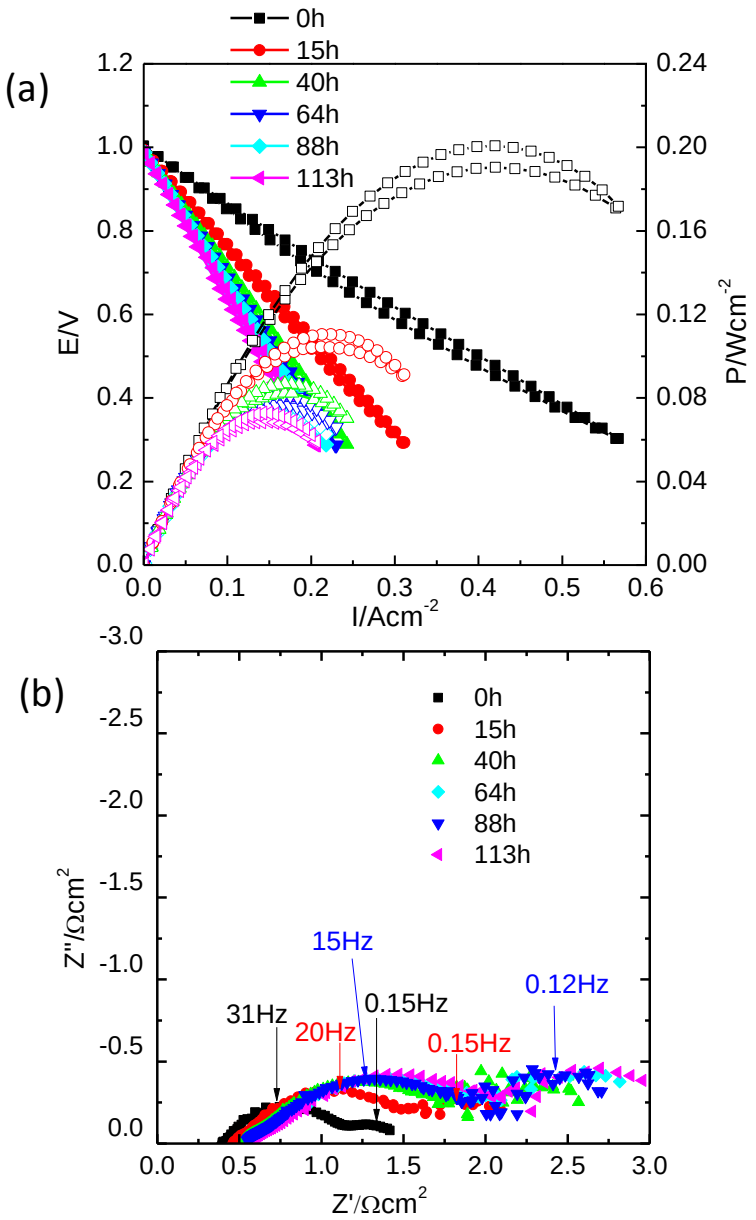


Figure 4.18 (a) I-V and I-P curves and (b) EIS curves of the 3wt.% $Ni_{0.75}Fe_{0.25}$-impregnated $LSCT_{A-}$ anode with low porosity (~ 35%) at different time upon stability testing at 700°C in humidified hydrogen (3% $H_2O$). I-V and I-P curves in (a) are signified by solid and open symbols, respectively. The impedance data were recorded under OCV.

By comparing the maximum power density of the cells infiltrated by the same catalyst with different porosity, it can be seen that the performance has been remarkably decreased due to the reduction of porosity, shown in Figure 4.18. The degradation

mainly occurs at the first 15h, and with time the degradation rate is becoming more and more flat. Even the testing measurements are different for the two cells: potentiostatic and galvanostatic methods, but the variation trends with time are identical, suggesting that the factors contributing to the cell degradation are the same. The impedance data in Figure 4.18(b) show that a low performance for the relatively dense cell can be attributed to the enlarged low-frequency arc, compared with the more porous cell shown in Figure 4.12(b). The low-frequency arc is related to the fuel diffusion from the anode surface to the effective TPBs across the anode functional layer and on the electrolyte/anode interface. During the first 40h, the impedance arcs at the medium frequency (15-30Hz) and low frequency (~0.15Hz) increase drastically; however, in the next following dozens of hours, the performance degradation is mainly ascribed to the gradual increase of low-frequency arc (~0.15Hz). The increase of impedance arc is likely due to the the growth of catalyst leading to a significant decrease of the electrochemical reaction sites for hydrogen oxidation, respectively.

## 4.4 Conclusion

The cell with nickel and iron impregnated $LSCT_{A-}$ anode exhibits a maximum powder density of 272mWcm$^{-2}$ at 700$^{o}$C, much larger than 43mWcm$^{-2}$ for the cell without impregnation and 112mWcm$^{-2}$ for the cell with nickel impregnation. The impregnation of bimetal Ni-Fe can remarkably improve the electrochemical performance possibly due to the optimized microstructure of catalyst. Moreover, the Fe addition improves the number of active sites on Ni and the activity of those sites by decreasing the activation energy, leading to an accelerated charge transfer and the diffusion process [263].

The impregnated samples demonstrate a more stable performance than the one without catalyst during testing in humidified hydrogen for 60h. The significant microstructure evolution for the impregnated cells before and after testing might explain the degradation mechanism of the cells: the growth of catalyst and the interaction between the catalyst and $LSCT_{A-}$ backbone are the main reasons for the degradation of the cell performance. The combined Ni-Fe catalyst can effectively improve the stability compared with the nickel impregnated cell as the agglomeration

and growth of nickel particles have been optimized by the addition of Fe. On the other hand, the chemical interaction between the metallic catalyst and $LSCT_{A-}$ backbone is to some extent inhibited by the Fe-rich layer on the inner layer attached to the anode backbone.

# Chapter 5. Performance of $LSCT_{A-}$ anode infiltrated with $CeO_2$ and metal as catalyst

## 5.1 Introduction

Ceria-based oxides have attracted considerable attention as catalyst, particularly for environmental applications and energy conversion systems. Ceria has a fluorite structure with space group of Fm3m, containing 4 coordinate $O^{2-}$ and 8 coordinate $Ce^{4+}$ in the ideal structure. Under reducing atmosphere and high temperature, ceria can be reduced into a non-stoichiometric state, where the anion-deficient oxide still retains the fluorite structure. Under this condition, $Ce^{4+}$ ions are reduced into $Ce^{3+}$, and meanwhile oxygen vacancies are formed due to the charge compensation, expressed by the following equation:

$$2Ce_{Ce}^{\times} + O_O^{\times} = 2Ce_{Ce}^{'} + V_O^{\bullet\bullet} + \frac{1}{2}O_2(g) \qquad \text{(Equation 5.1)}$$

The number of $V_O^{\bullet\bullet}$ increases linearly with the the formation of $Ce^{3+}$ ions, which are the carriers for ionic and electronic conduction, respectively. The final non-stoichiometry and ionic and electronic conductivity are considerably dependent on the oxygen partial pressure and temperature.

Another major role for ceria-based oxides is as a diffusion barrier in order to prevent the chemical reaction of the two adjacent components resulting in insulating layers and decrease in performance losses, for example, zirconia electrolyte and Co-rich perovskite cathode [265, 266]. In theory, the formation of electrically resistive interfacial $SrZrO_3$ layers between LSC and YSZ interfaces arises from the diffusion of Sr to YSZ and subsequential reaction between Sr and Zr. The concept using a barrier layer is to incorporate a ceria coating on the YSZ scaffold by infiltration process before infiltration of the perovskite LSC. In order to prohibit fluid-phase species from infiltrated solutions supported on ceria to interact with the underlying electrode scaffold, it is necessary to calcine the ceria coating to a high temperature in advance [267]. It has been discovered that the ceria layer is effective in minimizing the solid-

state reaction at the LSC-YSZ interfaces after infiltrated with SDC precursors and firing up to 1200$^{o}$C.

Ceria is also an intriguing anode backbone material; unlike YSZ which offers ionic conductivity only, ceria can provide ionic and electronic conductivity. In a case where ceria is used to replace YSZ in the conventional Ni-YSZ anode, the TPBs will be considerably expanded because the pathways for the electronic conduction has been greatly increased from Ni percolation to the whole anode, and accordingly the polarization resistance will be drastically reduced.

In addition, the use of infiltrated ceria on the highly conductive titanate-based anode forming an interconnected layer can promote a significant improvement of the polarization resistance because the enhancement in the ionic conductivity of the anode and therefore the efficient active areas for the electrochemical reaction of fuel [136,159]. Furthermore, an underlying ceria layer supporting metal catalyst can remarkably enhance the thermal stability of catalyst nanoparticles and prevent them from agglomeration and sintering [268].

It is also found that the introduction of ceria into the Ni-based anode is able to reduce the carbon deposition when using hydrocarbon as a fuel in a low humidity because ceria can store and release oxygen under oxidizing and reducing atmosphere, respectively. Oxygen originating from ceria can oxidize the deposited carbon into $CO/CO_2$ on the anode surface. Chen et al. [269] have impregnated ceria into the conventional Ni-YSZ anode successfully, and found that a layer of fine $CeO_2$ particles, approximately 100nm in size are formed covering the Ni-YSZ particles after sintering at 900$^{o}$C in air. The formation of a ceria layer can not only prevent the carbon deposition on Ni surface but also improve the electrochemical performance at a temperature as high as 850$^{o}$C.

Although ceria has the favourable properties as an anode material mentioned above, it has its own disadvantages, making it unsuitable to be used in the anode by itself. At first, ceria undergoes a volumetric expansion when $Ce^{4+}$ ions are reduced into bigger $Ce^{3+}$ under the anode operating condition. The volumetric change is capable of causing the volumetric mismatch between the anode and electrolyte, leading to a

crack of the cell. Secondly, the electronic conductivity of ceria-based oxides is not high enough to provide a reasonable ohmic resistance, especially since anode is required to be porous. Besides, compared with Ni the catalytic activity for hydrogen oxidation is insufficient. The attractive features of ceria make it more suitable to use as wetting material underneath the nickel catalyst on the surface of the electronically conducting anode backbone.

## 5.2 Infiltration

In this chapter, the cells were fabricated using the same recipes with non-aqueous tape casting technique, followed by a high-temperature sintering process at 1350$^{o}$C and reducing process at 900$^{o}$C, as described in last chapter. The cathode side of pre-reduced samples was impregnated with precursor solutions containing $La_{0.8}Sr_{0.2}Co_{0.2}Fe_{0.8}O_3$ (LSCF) and fired at 450$^{o}$C in air. To prepare a ceria supporting layer on the anode surface, an aqueous solution of $Ce(NO_3)_3.6H_2O$ was infiltrated into the porous anode, followed by heating at 450$^{o}$C in air. The infiltration steps were repeated until the loading of $CeO_2$ reaches 6wt.%.

Then, the anode catalyst materials including Ni and $Ni_{0.75}Fe_{0.25}$ were impregnated into the porous $CeO_2$-$LSCT_{A-}$ electrodes using the solutions from $Ni(NO_3)_2.6H_2O$ and $Fe(NO_3)_3.9H_2O$ at a molar ratio of Ni:Fe = 3:1 with additional citric acid. Multiple cycles of impregnation and calcination at 450$^{o}$C were used until the desired loading of impregnates of oxides were achieved. The loading of metal catalyst is estimated to be 3wt.% after reduction.

After infiltration process, Ag wires were attached onto the electrodes by applying Ag paste for current collection. The cell was then sealed onto an alumina tube using a ceramic adhesive. The electrochemical performance of the infiltrated cells with time under the operation conditions was measured. The microstructure of the anode upon stability testing was also obtained to determine the factors contributing to the degradation of cell performance.

For the $CeO_2$ and Ni co-impregnated $LSCT_{A-}$ cell, the redox property was also examined, along with the I-V and impedance curves before and after every redox

cycle. To investigate the possibility to use $LSCT_{A-}$ as anode in $CH_4$ fuel, containing 3vol.% $H_2O$ methane was supplied to $CeO_2$ impregnated anode with and without metallic catalysts at a flowing rate of 30mL/min at a temperature range of 700-800$^oC$. The microstructure of the tested sample in methane was examined for evaluation the carbon coking problem on the anode surface.

## 5.3 Results and discussion

### 5.3.1 Initial performance in hydrogen

#### 5.3.1.1 $CeO_2$ impregnated $LSCT_{A-}$ cell

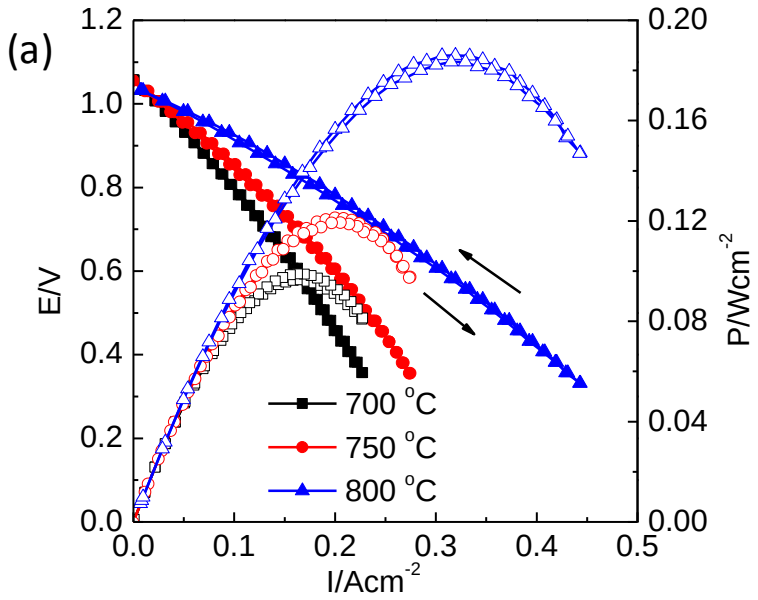


(Continued on the next page)

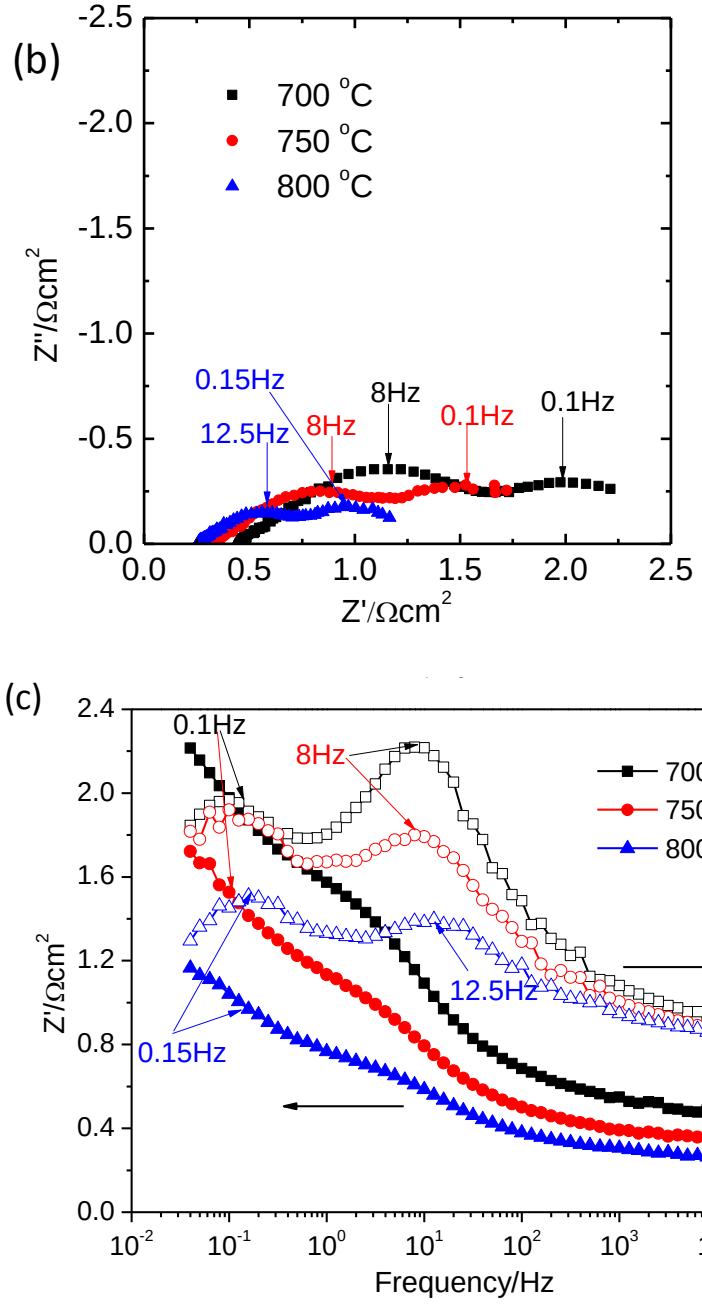


Figure 5.1 (a) I-V and I-P curves and (b) Nyquist plot and (c) Bode plot of EIS curves for the 6wt.% $CeO_2$-impregnated $LSCT_{A-}$ anode tested at 700-800°C in humidified hydrogen (3% $H_2O$). I-V and I-P curves in (a) are signified by solid and open symbols, respectively. The impedance data were recorded under OCV.

The initial performance of 6wt.% $CeO_2$-impregnated $LSCT_{A-}$ supported cell has been tested in humidified hydrogen containing 3vol.% $H_2O$ at 700-800°C, as shown in Figure 5.1. At 700°C, the maximum power density has been doubled compared with

bare $LSCT_{A-}$ cell, displayed in Figure 4.3 of the last chapter. With increasing operation temperature, the peak power density increased to 186mW/cm$^2$ at 800$^o$C. The high performance is expected because the ceria coating covering on $LSCT_{A-}$ surface is supposed to increase the ionic conductivity and therefore the reaction sites and is more likely to be further improved by the addition of metal catalysts for fuel oxidation. The impedance spectra at OCV in Figure 5.1(b) present reasonable ohmic losses at all the testing temperatures, mainly contributed by 60μm thick YSZ electrolyte and 300μm thick anode support. The main losses for the cell are from the polarization resistance. The arcs at the high- and medium-frequency overlap to each other, and the low-frequency arc associated with the mass transfer is more distinct to be separated from the other electrochemical processes. Because the $LSCT_{A-}$ backbone has a higher electronic conductivity than $CeO_2$, and in the meanwhile, the ionic conductivity of $CeO_2$ is much higher than that of $LSCT_{A-}$ material, the hydrogen oxidation is supposed to happen on the $LSCT_{A-}/CeO_2$ interface where hydrogen can reach through the ceria coating. Therefore, the change of microstructure upon heating is proposed to relate with the magnitude of polarization resistance, in particular, the medium-frequency arcs, which is observed clearly in Figure 5.1(c). The decrease in the polarization resistance from this arc with the increasing temperature shows that the processes associated with the absorption of the reactant species and surface transfer are thermally activated. The conductivity of ceria at high temperature is more prominent than that at low temperature, providing more pathways for ionic transport.

### 5.3.1.2 $CeO_2$+Ni impregnated $LSCT_{A-}$ cell

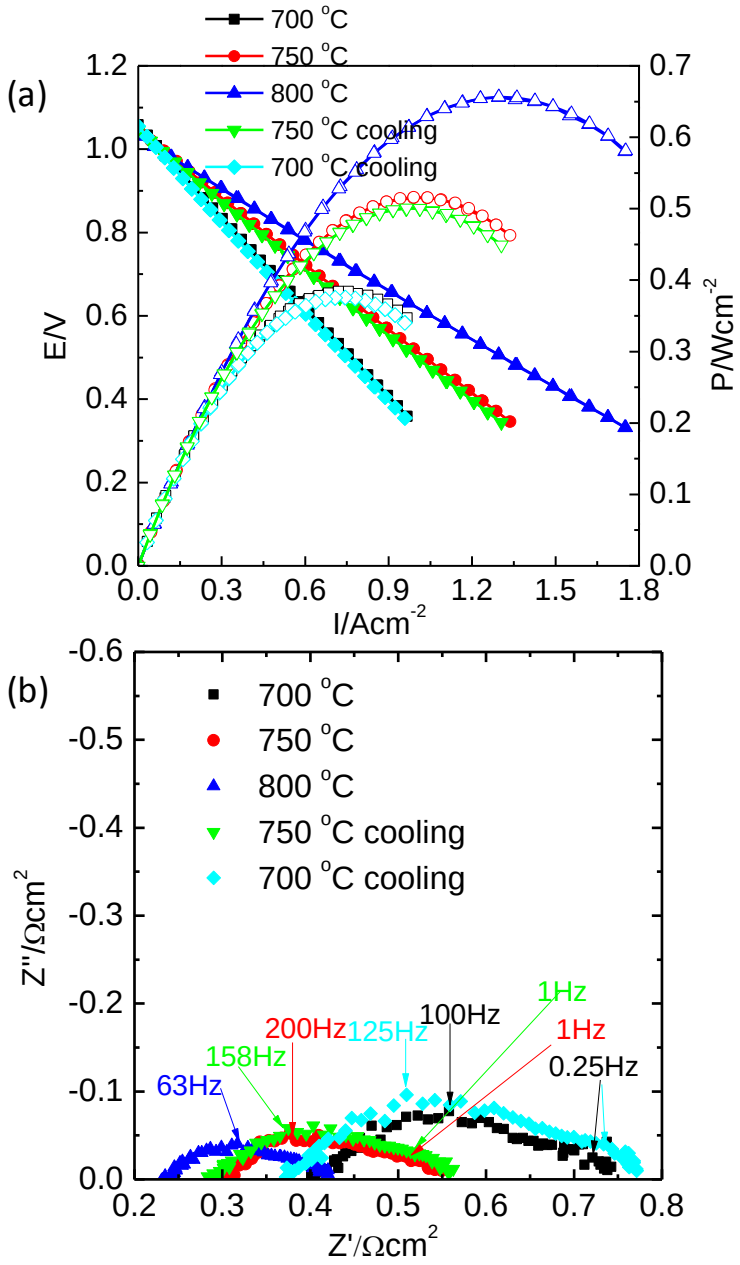


Figure 5.2 (a) I-V and I-P curves and (b) Nyquist plot of EIS curves for the 6wt.% $CeO_2$ and 3wt.% Ni co-impregnated $LSCT_{A-}$ anode tested at 700-800°C upon heating and cooling stages in humidified hydrogen (3% $H_2O$). I-V and I-P curves in (a) are signified by solid and open symbols, respectively. The impedance data were recorded under OCV.

The combination of ceria with catalytic metal for oxidation reactions, such as Ni, Cu and Pd, has been confirmed to be able to promote significantly the anode performance [248]. The catalytic metal has a profound impact on the electrode performance by offering a high catalytic activity for the oxidation of fuels, such as hydrogen and methane. The presence of a supporting ceria layer has a beneficial influence on the electrode stability due to a decrease of the agglomeration and growth of metal particles. The cell with the configuration of $CeO_2$-Ni-$LSCT_A$-/YSZ/LSCF-YSZ (the loadings of ceria and Ni in the $LSCT_A$- anode are 6 and 3wt.%, respectively) performed better than that with the infiltrated $CeO_2$ into the anode in 3% $H_2O/H_2$ atmosphere at 700-800$^oC$. Its performances are displayed in Figure 5.2. The I-V curves were measured on the heating stages to 800$^oC$ and the cooling stage from 800$^oC$. The OCVs are approximately 1.06V at 800$^oC$ and 1.04V at 700$^oC$, which are considerably close to the predicted value calculated from the Nernest equation. The maximum power densities read form the Figure 5.2(a) are around 390, 520 and 660mW/cm$^2$ at 700, 750 and 800$^oC$, respectively, which is comparable to the state-of-the-art Ni-YSZ composite cells. Compared with the anode infiltrated with ceria only, the performance has been improved by a factor of four with the addition of nickel. More interestingly, the performances tested during the cooling stage are very similar with those upon heating, suggesting that the growth of catalyst leading to the decrease of the effective reaction sites can be compensated by the increased electronic conductivity. This has been demonstrated in Figure 5.2(b). The ohmic resistances measured under OCV are 0.42, 0.31 and 0.23Ωcm$^2$ at 700, 750 and 800$^oC$, respectively, during the heating stage. Upon cooling, an optimized ohmic resistance can be observed, while the high-temperature calcination up to 800 $^oC$ can cause the growth of catalyst nanoparticles formed at 450$^oC$ and then the rise of the polarization resistance. It also has been noted that the total Area Specific Resistances (ASR) at the same temperature are very similar, in good agreement with the I-V curves where the slops of V/I are identical under the heating and cooling processes.

### 5.3.1.3 $CeO_2$+$Ni_{0.75}Fe_{0.25}$ impregnated $LSCT_{A-}$ cell

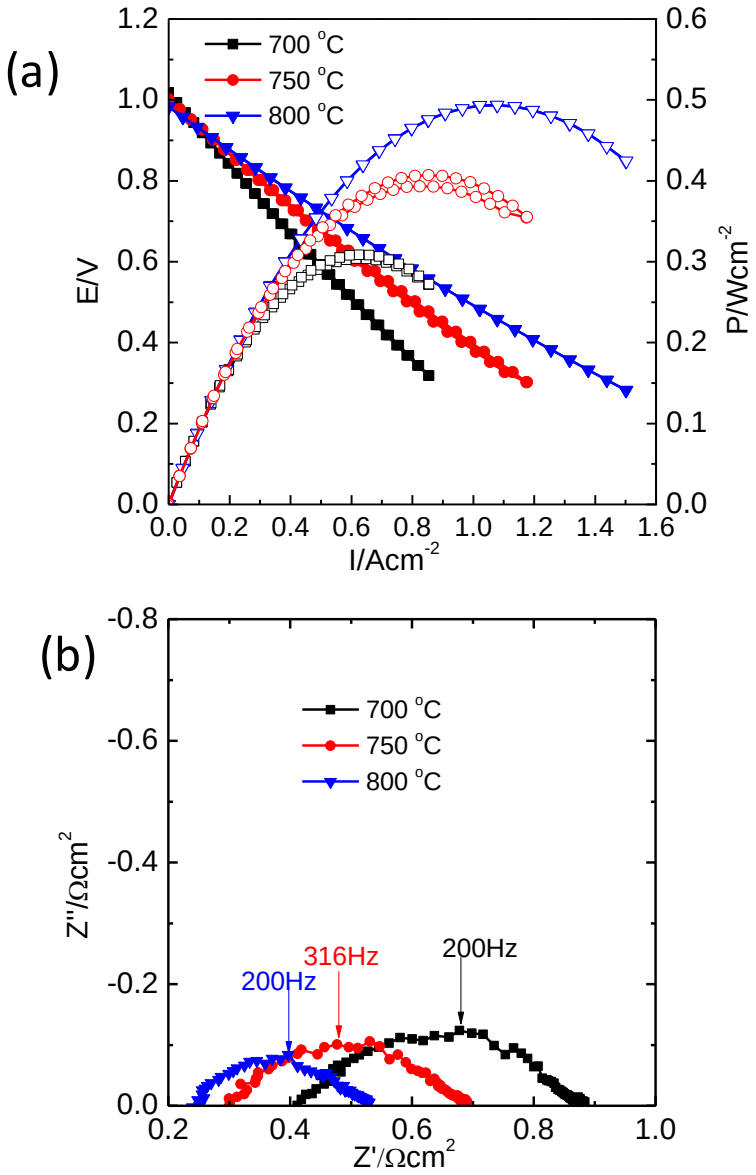


Figure 5.3 (a) I-V and I-P curves and (b) Nyquist plots of EIS curves for the 6wt.% $CeO_2$ and 3wt.% $Ni_{0.75}Fe_{0.25}$ co-impregnated $LSCT_{A-}$ anode tested at 700-800°C in humidified hydrogen (3% $H_2O$). I-V and I-P curves in (a) are signified by solid and open symbols, respectively. The impedance data were recorded under OCV.

Because the addition of the bimetal $Ni_{0.75}Fe_{0.25}$ into the $LSCT_{A-}$ backbone improves the initial performance and stability compared with the cells with the bare anode and Ni-impregnated anode, the incorporation of ceria and bimetal into the $LSCT_{A-}$ anode was also examined in this study. Figure 5.3 shows the I-V curves and impedance

spectra for the cell with 6wt.% $CeO_2$ and 3wt.% $Ni_{0.75}Fe_{0.25}$ co-impregnated $LSCT_{A-}$ anode tested at the temperature range of 700-800$^oC$ during the cooling stage in 3% $H_2O$+97% $H_2$ atmosphere. The OCVs are observed in Figure 5.3(a), ranging between 0.98-1.01V at 700-800$^oC$, which are lower than the predicted value using the Nernest equation under the same condition. The maximum power densities are 310, 406 and 495mW/$cm^2$ at 700, 750 and 800$^oC$, respectively, lower than those of the ceria and nickel co-impregnated $LSCT_{A-}$ cell, due to the lower catalytic activity of Ni-Fe bimetal than the pure nickel when the ceria layer provides ionic conductivity for the anode reaction. The ohmic resistances are quite similar with those of ceria and nickel co-impregnated cell, but the polarization resistances at the testing temperatures are slightly larger. The addition of ceria apparently enhances the initial performance compared with the same bimetal impregnated sample, suggesting that the underlying ceria layer is crucial for extending the TPB length for hydrogen oxidation.

### 5.3.2 Initial performance in methane

#### 5.3.2.1 $CeO_2$ impregnated $LSCT_{A-}$ cell

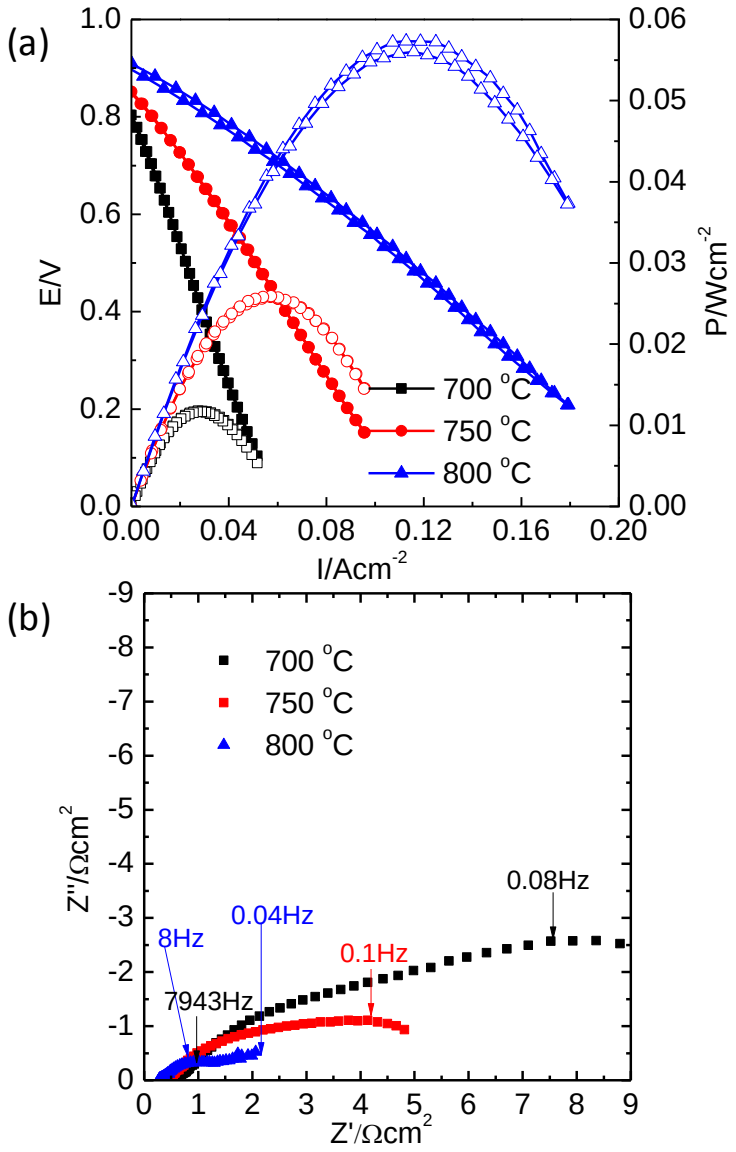


Figure 5.4 (a) I-V and I-P curves and (b) EIS curves for the 6wt.% $CeO_2$-impregnated $LSCT_{A-}$ anode tested at 700-800°C in methane with low humidity (3% $H_2O$). I-V and I-P curves in (a) are signified by solid and open symbols, respectively. The impedance data were recorded under OCV.

The direct ultilisation of methane is one of the most significant strengths for SOFCs. Figure 5.4 shows the I-V and impedance curves of the $CeO_2$ impregnated $LSCT_{A-}$ supported cell tested in slightly humidified methane (3% $H_2O$) at a flowing rate of 30mL/min at 700-800$^oC$. The cell impregnated with ceria only exhibited poor performance in methane, but still active for methane oxidation. It has been reported that the catalytic activity of methane oxidation for ceria depends on surface oxygen availability [270], so the fine particle size after low-temperature calcination may play an important role for methane oxidation. The maximum power densities are much lower in methane than in hydrogen, because $H_2$ is much more reactive than $CH_4$ in heterogeneous oxidation and displays a higher reactivity for the anode as well [109]. In addition, it is very difficult to activate methane at the electrode/electrolyte interface for the thick and complex anode structure [271], in this case, 300 μm thick $LSCT_{A-}$ anode. The OCVs are 0.8-0.9V at the testing temperatures, considerably lower than the value predicted using the Nernst equation. Gorte et al. [109] have proposed an interpretation for the low OCVs that the equilibrium is established between the hydrocarbons and partial oxidation products, since hydrocarbon oxidation on surfaces may occur in multiple steps. The impedance spectra in Figure 5.4(b) show that the ohmic losses in methane and hydrogen are nearly the same at the testing temperatures and the higher polarization losses are the main contribution of the poor performance in methane. It is indicative that ceria is not an effective catalysts for methane oxidation and the performance will be limited by the catalytic activity for cracking the strong C-H bonds [248]. To achieve a better performance in methane, it is necessary to add metal catalyst into the anode.

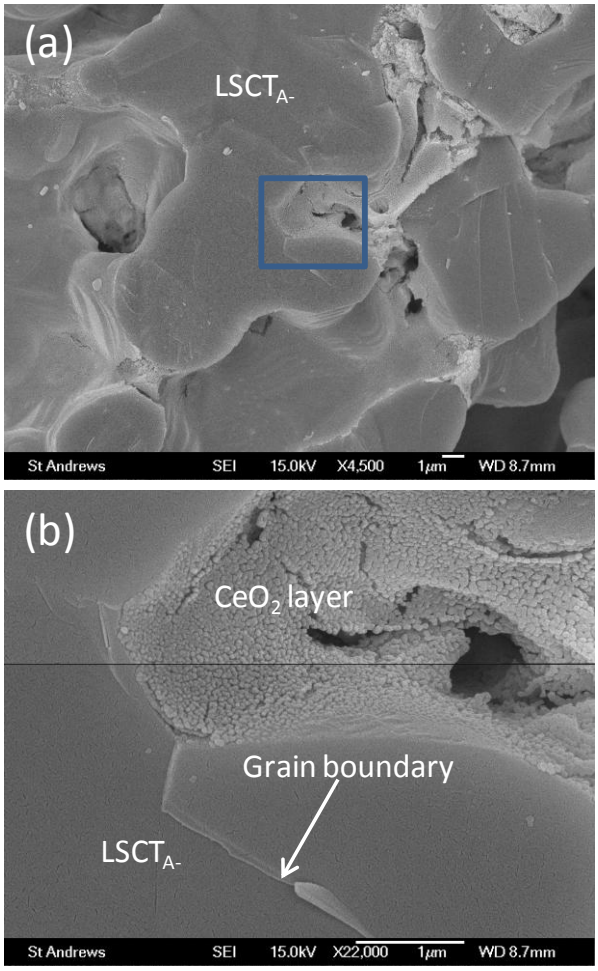


Figure 5.5 Scanning electron microscopy (SEM) images of $CeO_2$-impregnated $LSCT_{A-}$ anode after testing in $CH_4$ at 700-800$^oC$. (b) the enlarged image of the rectangular area in (a).

The SEM images (Figure 5.5) of ceria-impregnated $LSCT_{A-}$ anode undergoing the testing in methane containing 3vol.% $H_2O$ at 700-800$^oC$ show that the ceria layer comprised of nanoparticles covers the surface of $LSCT_{A-}$ backbone. It is worth noting that no carbon deposition is observed on the anode. Interestingly, the uneven distribution of ceria particles is likely to be associated with the pore shape constructed by $LSCT_{A-}$ backbone and the terraced structures of $LSCT_{A-}$ particles themselves. Most of catalyst particles are located in the narrow pores against the $LSCT_{A-}$ surface without terraced structure.

### 5.3.2.2 $CeO_2$+Ni impregnated $LSCT_{A-}$ cell

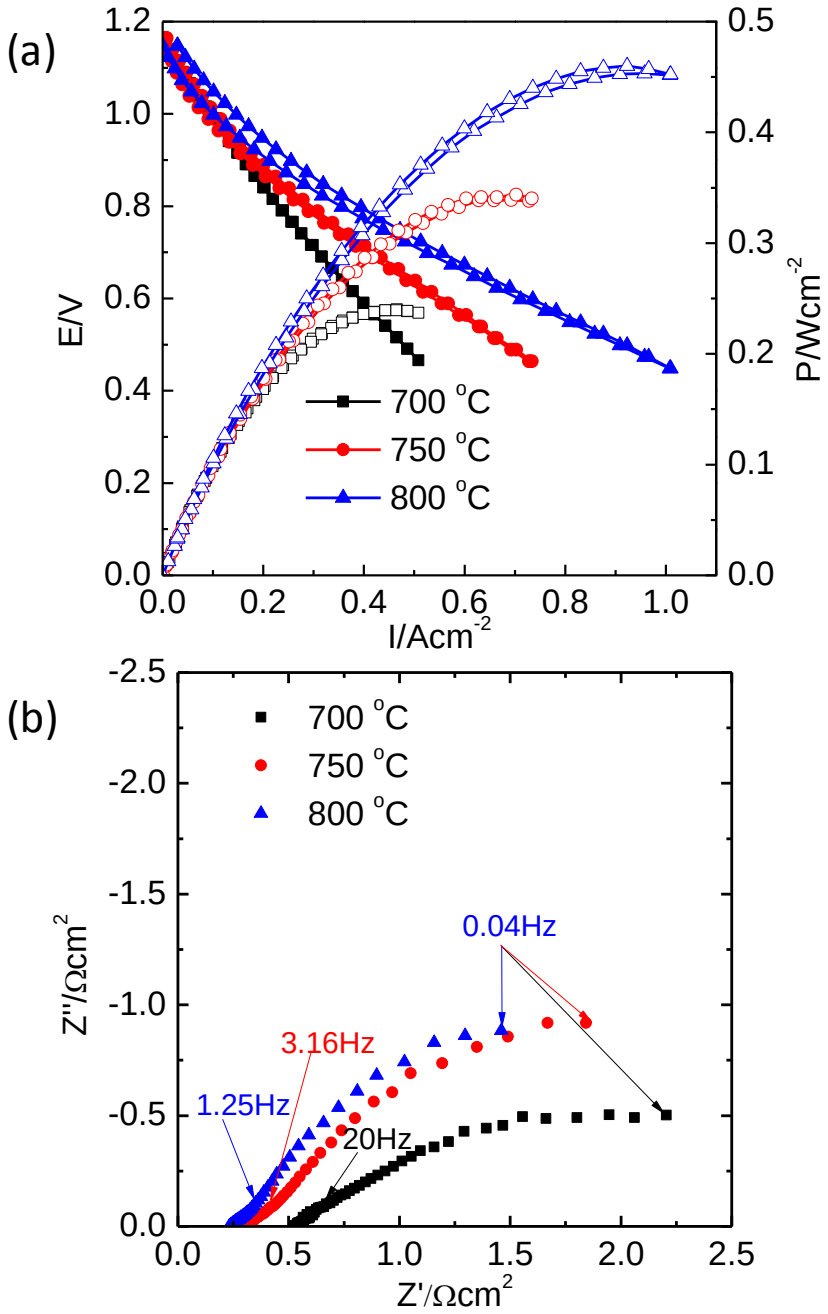


Figure 5.6 (a) I-V and I-P curves and (b) Nyquist plot of EIS curves for the 6wt.% $CeO_2$ and 3wt.% Ni co-impregnated $LSCT_{A-}$ anode tested at 700-800°C in humidified methane (3% $H_2O$). I-V and I-P curves in (a) are signified by solid and open symbols, respectively. The impedance data were recorded under OCV.

Earlier studies have investigated the potential for SOFCs to directly use hydrocarbon as fuel. The hydrocarbon needs to be reformed into hydrogen by steam at the anode before the electrochemical oxidation happens. Nickel has been known as an active, steam-reforming catalyst, so in our study, nickel has been chosen to incorporate with $CeO_2$-impregnated $LSCT_{A-}$ cells. Figure 5.6(a) shows the measurements of current density and power density versus voltage, performed on a 6wt.% ceria and 3wt.% nickel co-impregnated $LSCT_{A-}$ cell using ambient air and 3% $H_2O/CH_4$. The OCVs for methane are reasonable at ~1.16V, suggesting the humidified methane reached equilibrium at the anode. The non-linear trend of I-V curves are clearly seen at all the testing temperatures, showing the activation losses at high current densities and ohmic losses at low current densities. The high activation polarization can be attributed to the $CeO_2$ in the anode due to its lower catalytic activity for $CH_4$ oxidation reactions when compared with nickel. The maximum power densities are 460, 350 and 240mW/cm$^2$ in methane, about ~30% lower than those in the moist hydrogen fuel. The addition of nickel has been found to improve the cell performance significantly compared with the ceria-impregnated $LSCT_{A-}$ cell. Others [109,269,272] also have reported that a significant enhancement can be achieved by the addition of ceria into the metal-YSZ based anode when using hydrocarbon as fuel.

The impedance spectra recorded at OCV in humidified methane (3% $H_2O$) at 700-800$^o$C are presented in Figure 5.6(b). The ohmic resistances of the cell decrease from 0.5 to 0.25Ωcm$^2$ with the increasing temperature between 700 and 800$^o$C, including the resistance of electrodes, electrolyte and current collectors. The polarization resistances of the cell at the testing temperatures in methane are higher than those of the cell exposed in humidified hydrogen. It suggests that at the anode side the rate of the electrochemical oxidation for methane is much slower than that of hydrogen when both of the cells have the same rate for oxygen oxidation at the cathode side. The main difference is concentrating on the semicircle at the low frequency, also indicating that the fuel dissociation/adsorption or surface diffusion process on the anode catalyst surface [273] in $CH_4$ is much slower than that in $H_2$.

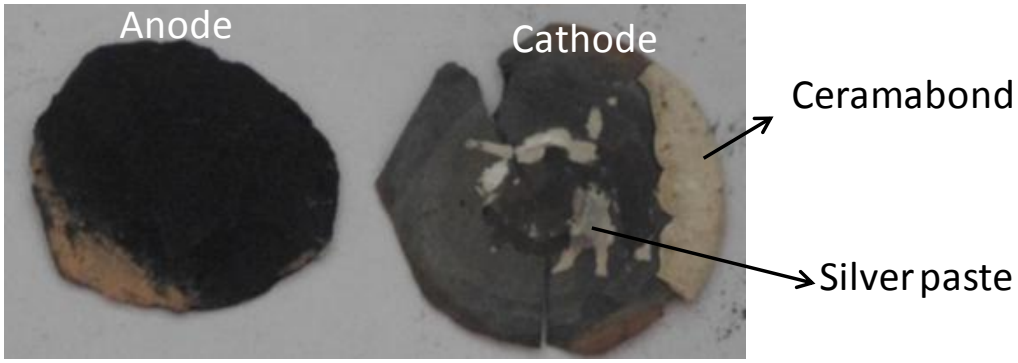


Figure 5.7 Picture of $CeO_2$+Ni impregnated cell after testing in wet methane at 700-800$^oC$ and cooling to the room temperature in the same atmosphere

After the fuel cell testing at 800$^oC$ and cooling to room temperature at moist methane (3% $H_2O$), the cell has been shown in the photograph in Figure 5.7. A serious delamination has occurred between the co-casting YSZ and $LSCT_{A-}$ due to the formation of a large amount of black carbon on the electrolyte/anode interface or the different TECs upon the rapid cooling. It has been widely acknowledged that in the presence of hydrocarbon, Ni can catalyze the formation of carbon fibres by the dissolution of carbon into the Ni bulk and precipitation of carbon as a fibre [274]. The carbon deposition on the SOFC anode can not only damage the effective TPBs but also deteriorate the mechanical strength.

As predicted, the BSE images of the $LSCT_{A-}$ anode incorporated with $CeO_2$ and Ni after the testing in methane in Figure 5.8 present that filament-like carbon has formed in the open pores. The bright clusters attaching along the surface of $LSCT_{A-}$ surface in Figure 5.8(a) are believed to be ceria and nickel catalysts, although it is impossible to distinguish both. Thin and long filaments having the thickness around 100nm can be observed mixing with catalysts (Figure 5.8(b)) and covering the catalysts on the concave region of the anode backbone (Figure 5.8(c)). The carbon deposition would have a fatal impact on the cell performance.

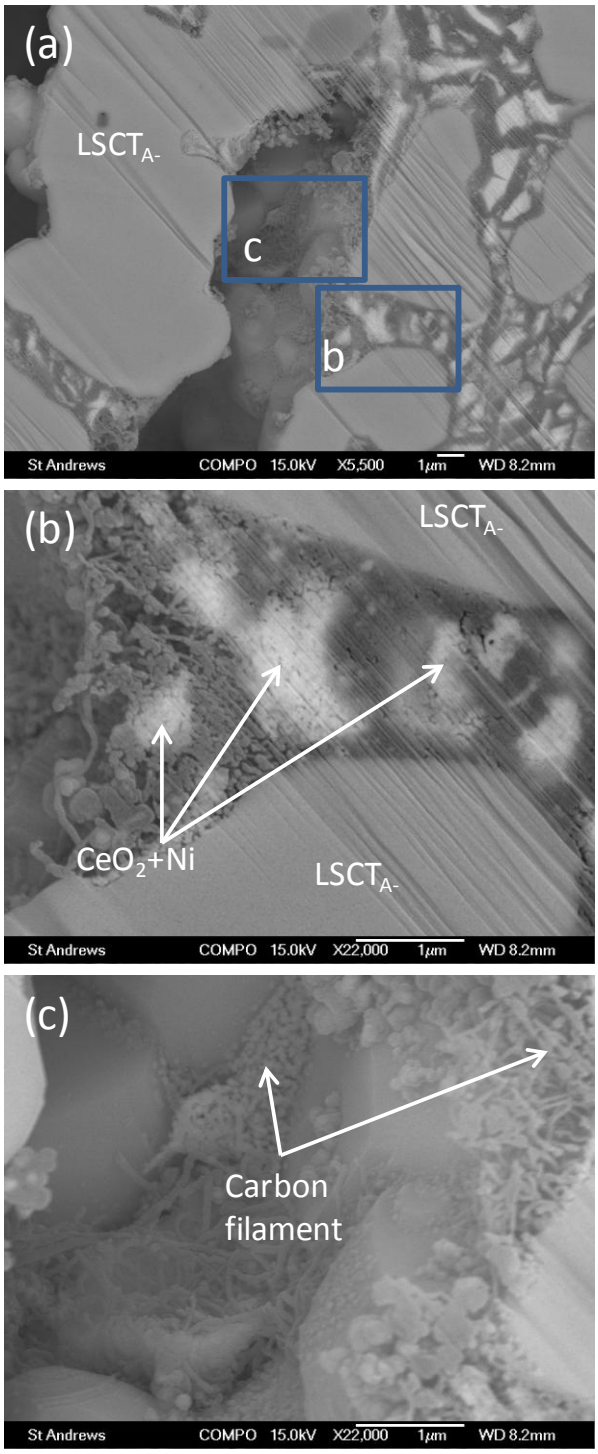


Figure 5.8 Back-scattered electron (BSE) images of $CeO_2$ and Ni-impregnated $LSCT_{A-}$ anode after testing in humidified $CH_4$ at 700-800$^oC$. (b) and (c) the enlarged images of the rectangular areas in (a).

### 5.3.2.3 $CeO_2$+$Ni_{0.75}Fe_{0.25}$ impregnated $LSCT_{A-}$ cell

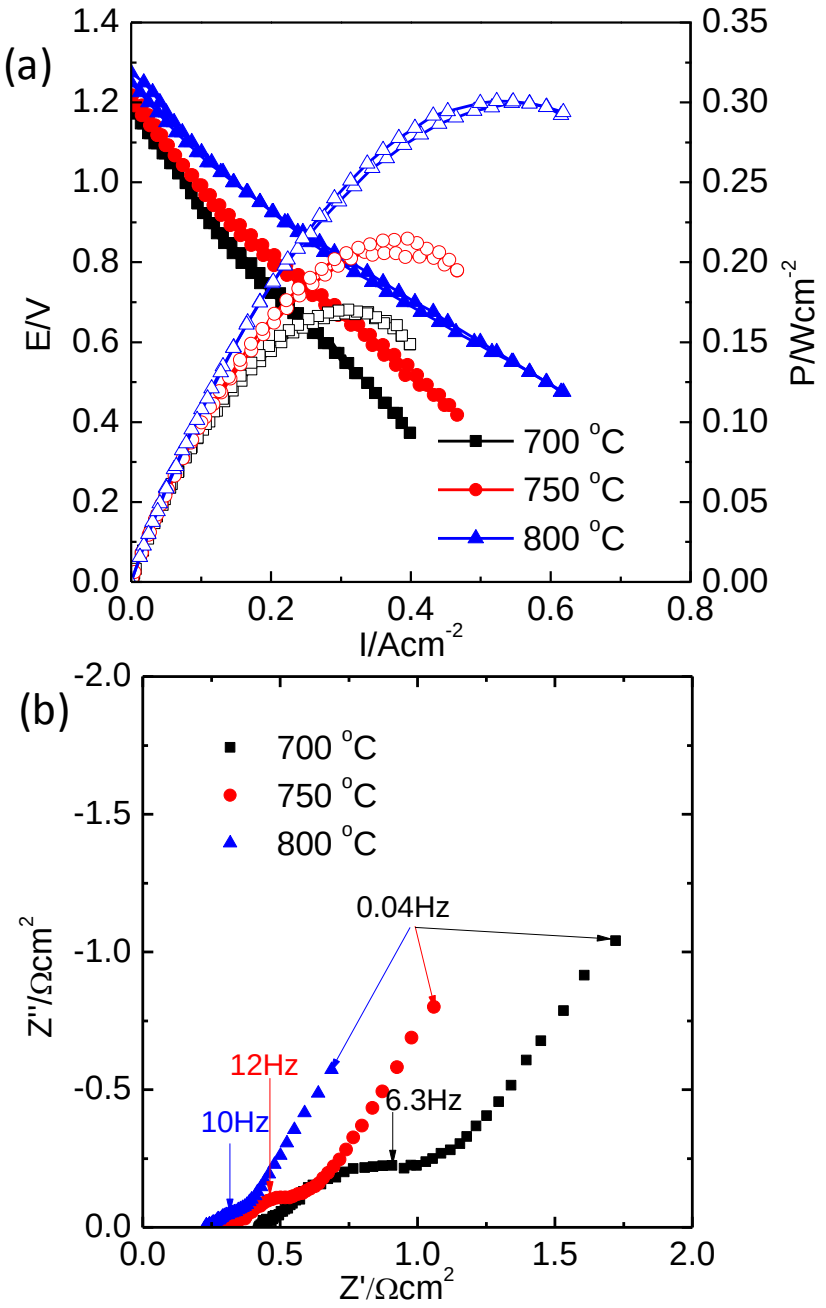


Figure 5.9 (a) I-V and I-P curves and (b) Nyquist plot of EIS curves for the 6wt.% $CeO_2$ and 3wt.% $Ni_{0.75}Fe_{0.25}$ co-impregnated $LSCT_{A-}$ anode tested at 700-800°C in humidified hydrogen (3% $H_2O$). I-V and I-P curves in (a) are signified by solid and open symbols, respectively. The impedance data were recorded under OCV.

Figure 5.9 shows the V-I curves and impedance spectra of the SOFC with $CeO_2$ and $Ni_{0.75}Fe_{0.25}$ impregnated $LSCT_{A-}$ anode at 700-800$^oC$ in humidified methane (3% $H_2O$). The anode apartment was flushed by humidified 5% hydrogen until reaching the operation temperature 800$^oC$ and then fed with humidified methane. The measurements were performed on the cell upon the cooling process. The cell exhibits the potential values of 1.15-1.28V under the operation condition, which are close to the theoretical OCV values. It is found that the OCV values in methane are significantly higher than those in hydrogen and gradually increase with increasing temperature, opposite to the tendency observed in hydrogen where the OCV values decrease slightly with the increasing temperature. The measured OCV values are consistent with the predicted potential values when the humidified methane reaches equilibrium [ 275 ]. The I-V curves are non-linear, showing distinct activation polarization at low current densities and ohmic polarization resistance at high current densities, especially at high temperature. The high activation losses can be attributed to the addition of ceria because its low catalytic activity for $CH_4$ oxidation reactions compared with nickel and iron. Beside the activation and ohmic losses, the mass transport losses typically occurring at the higher current densities are invisible in the I-V measurement, indicating that the current densities recorded are not high enough or the diffusion pathways are sufficient. The maximum power densities for the cell are 170, 215 and 302mW/cm$^2$ at 700-800$^oC$, comparable with the Ni-Fe cermet anode reported previously [256]. The impedance data in Figure 5.9(b) show that the ohmic losses for the cell are nearly the same as the cells with $CeO_2$ or $CeO_2$+Ni impregnated $LSCT_{A-}$ anode. The total resistances are mainly dominated by the polarization resistances, exhibiting a decreasing trend with the increasing temperature. Even Ni and Fe have a comparably high catalytic activity for methane decomposition, the incorporation of Ni-Fe bimetal into the anode shows a apparently larger polarization resistance than the Ni impregnated cell with the ceria as a supporting layer on the anode backbone. It is presumable that the state of Fe is oxide rather than metal, as described in the Ni-Fe impregnated $LSCT_{A-}$ anode.

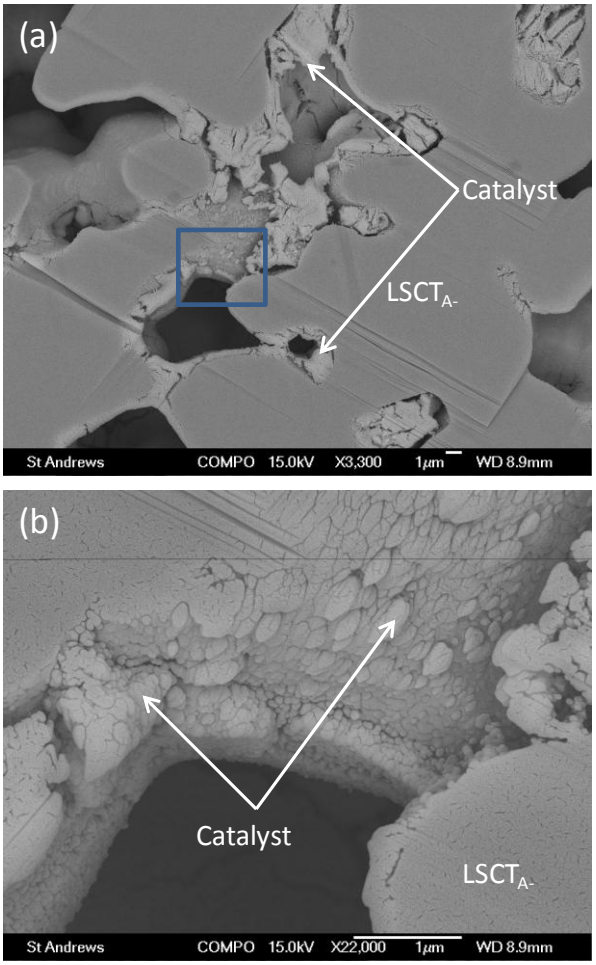


Figure 5.10 Back-scattered electron (BSE) images of $CeO_2$ and Ni-Fe co-impregnated $LSCT_{A-}$ anode after testing in humidified $CH_4$ at 700-800$^oC$. (b) the enlarged image of the rectangular area in (a).

Although the agglomeration of catalyst particles on the $LSCT_{A-}$ backbone are apparent after the operation in humidified methane at 700-800$^oC$ for the $CeO_2$ and Ni-Fe co-impregnated $LSCT_{A-}$ anode, as shown in Figure 5.10, no trace of carbon deposition is observed on the sample. From the results, the carbon deposition is obviously prohibited by the use of Ni-Fe bimetal where likely the iron oxides are not fully reduce into Fe.

### 5.3.3 Stability in hydrogen

#### 5.3.3.1 $CeO_2$ impregnated $LSCT_{A-}$ cell

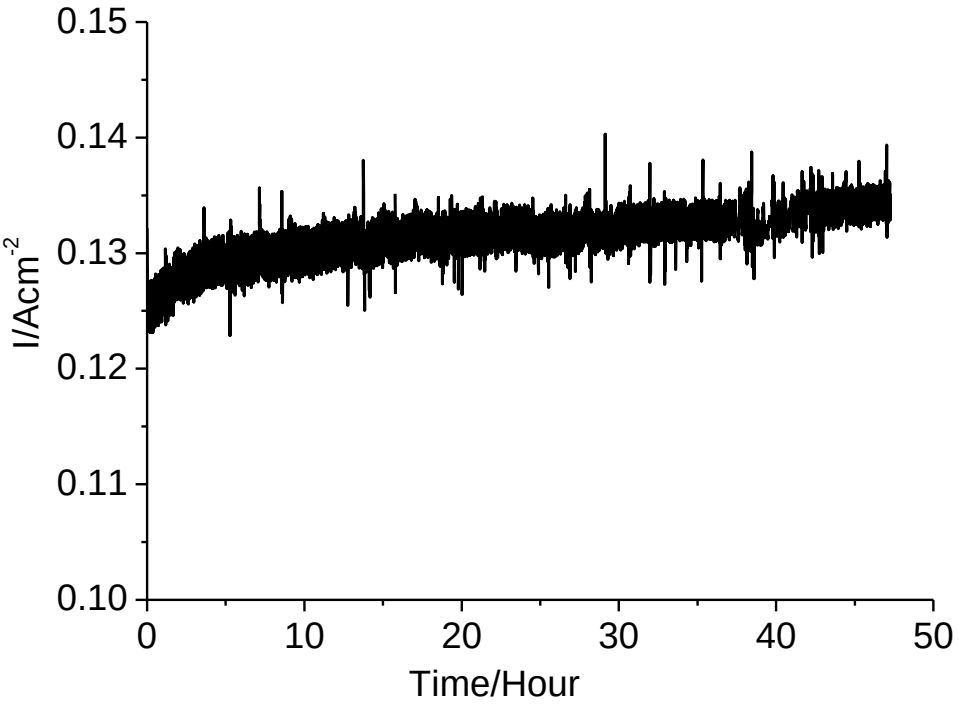


Figure 5.11 Stability testing of the 6wt.% $CeO_2$-impregnated $LSCT_{A-}$ anode at 700°C in humidified hydrogen (3% $H_2O$) under the applied voltage of 0.7V

The stability of ceria-impregnated $LSCT_{A-}$ cell in hydrogen at 700°C is shown in Figure 5.11. The current density under the applied constant voltage of 0.7V increases slightly in the early stage of operation, and remains considerably stable for 50h. The addition of ceria into the anode significantly improved the cell stability, in particular, compared with the bare $LSCT_{A-}$ cell, as demonstrated in section 4.3.4 of chapter 4. In the $CeO_2$-impregnated anode, the transport of oxygen ions is mainly achieved by the connecting ceria particles rather than the $LSCT_{A-}$ backbone, so the partial oxidation of titanate surface upon operation leading to the increase of ohmic and polarization losses is alleviated.

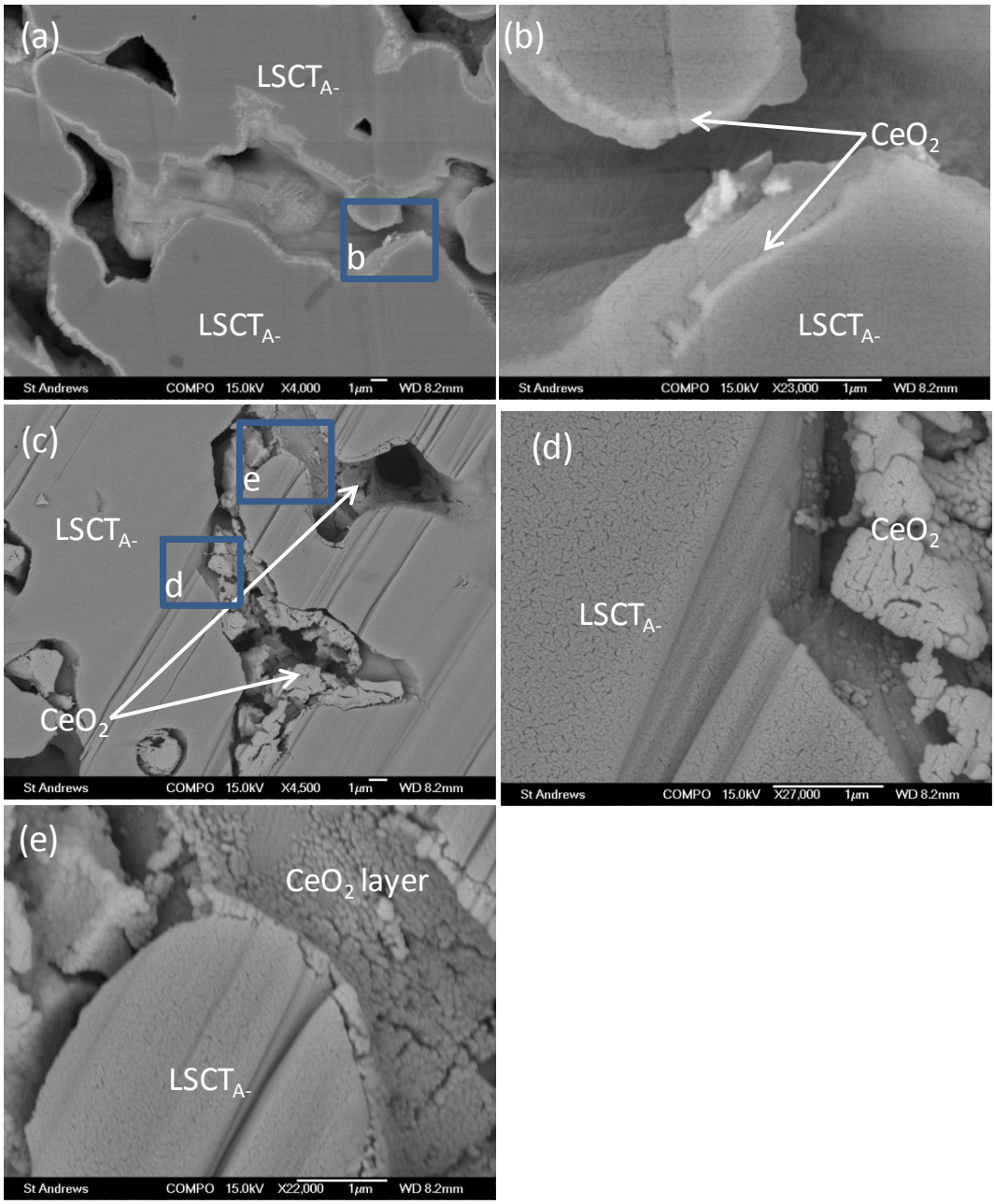


Figure 5.12 Back-scattered electron (BSE) images of $CeO_2$-impregnated $LSCT_{A-}$ (a, b) before testing and (c, d and e) after testing for 50 h at 700$^oC$. (b), (d) and (e) the enlarged images of the rectangular areas in the general images (a) and (c), respectively.

Figure 5.12(a) and (b) are the BSE images of the cross section of the ceria-impregnated $LSCT_{A-}$ anode after calcination at 450$^oC$ for 30min prior to the cell testing. The catalyst layer evenly covers the surface of the anode perovskite, as shown

in Figure 5.12(a). In Figure 5.12(b), a layer brighter than the backbone emerging in the $LSCT_{A-}$ margin can be identified as ceria in terms of the brightness contrast. A firing temperature of 450$^{o}$C was used in our study, which is too low to cause the interaction between the underlying perovskite and infiltrated ceria. The formation of ceria layer within the titanate particle envelop could be perhaps due to the partial dissolution of the perovskite edge in the acid atmosphere originating from the nitrate solution and the re-nucleation upon infiltration-firing cycles. It has been known that YSZ scaffold structure could be modified by treatment in hydrofluoric acid [276], therefore titanate might topographically react in nitrate solution during impregnation and the subsequent firing process, which will affect the subsequent interaction between titanate and catalytic metal during the working condition of anode as an alternative explanation for the degradation. After the testing in wet hydrogen for 50h, a completely different microstructure is displayed in Figure 5.12(c), where the agglomeration of ceria in the open pores is observed. Fortunately, there are ceria nano-particles adhering to the anode surface (Figure 5.12(d)) and/or the ceria layer covering over the perovskite particles (Figure 5.12(e)). They play an important role for the cell in maintaining a constant performance. Combining both the microstructure and the stability testing result, we believe that a dense ceria was formed before the cell was exposed to humidified $H_2$ and the short-term exposure in $H_2$ afterwards causes the break apart of the fine particles that increases the triple phase boundary for the oxidation of $H_2$.

### 5.3.3.2 $CeO_2$+Ni impregnated $LSCT_{A-}$ cell

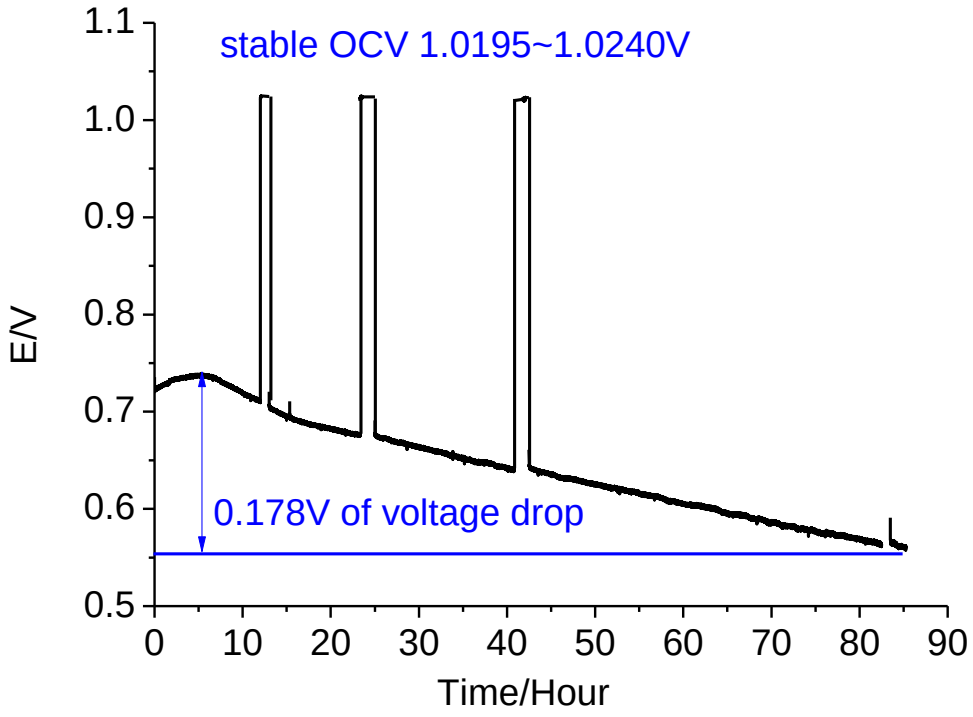


Figure 5.13 Stability testing of the 6wt.% $CeO_2$+3wt.% Ni-impregnated $LSCT_{A-}$ anode at 700°C in humidified hydrogen (3% $H_2O$) under the applied current density of 430mA/$cm^2$

Figure 5.13 presents the evolution of voltage as a function of time for SOFC with $CeO_2$ and Ni co-impregnated $LSCT_{A-}$ anode, operated under a current density of 430mA/$cm^2$ at 700°C in humidified hydrogen (3% $H_2O$). The OCVs were tested on the intervals during the stability testing, being ~1.02V, indicating that there were no cracks formed on the cell. The cell voltage steadily increases by 0.015V in the first 5h, and then decreases significantly in the following 80h from the initial voltage of 0.723V to 0.56V. The slow increase at the beginning can be due to the reduction of $Ce^{4+}$ to $Ce^{3+}$, which increases the ionic conductivity and creates more reaction sites. The same phenomenon has been seen in the $CeO_2$-impregnated $LSCT_{A-}$ cell. The degradation rate observed after 5-h operation is relatively low in comparison with that of the cell with bare $LSCT_{A-}$ and Ni-impregnated $LSCT_{A-}$ as anode, depicted in last chapter. This can be explained by the ceria layer underneath the nickel catalyst. The presence of ceria layer can conduct the oxygen ions from the electrolyte; therefore,

the partial oxidation of $LSCT_{A-}$ leading to the decrease of conductivity can be prevented. Besides, ceria appears to have an influence on the inhibition of nickel coarsening. However, a steady degradation reveals that the growth of catalyst and the interaction of both catalyst and backbone may happen to deviate from the desired performance.

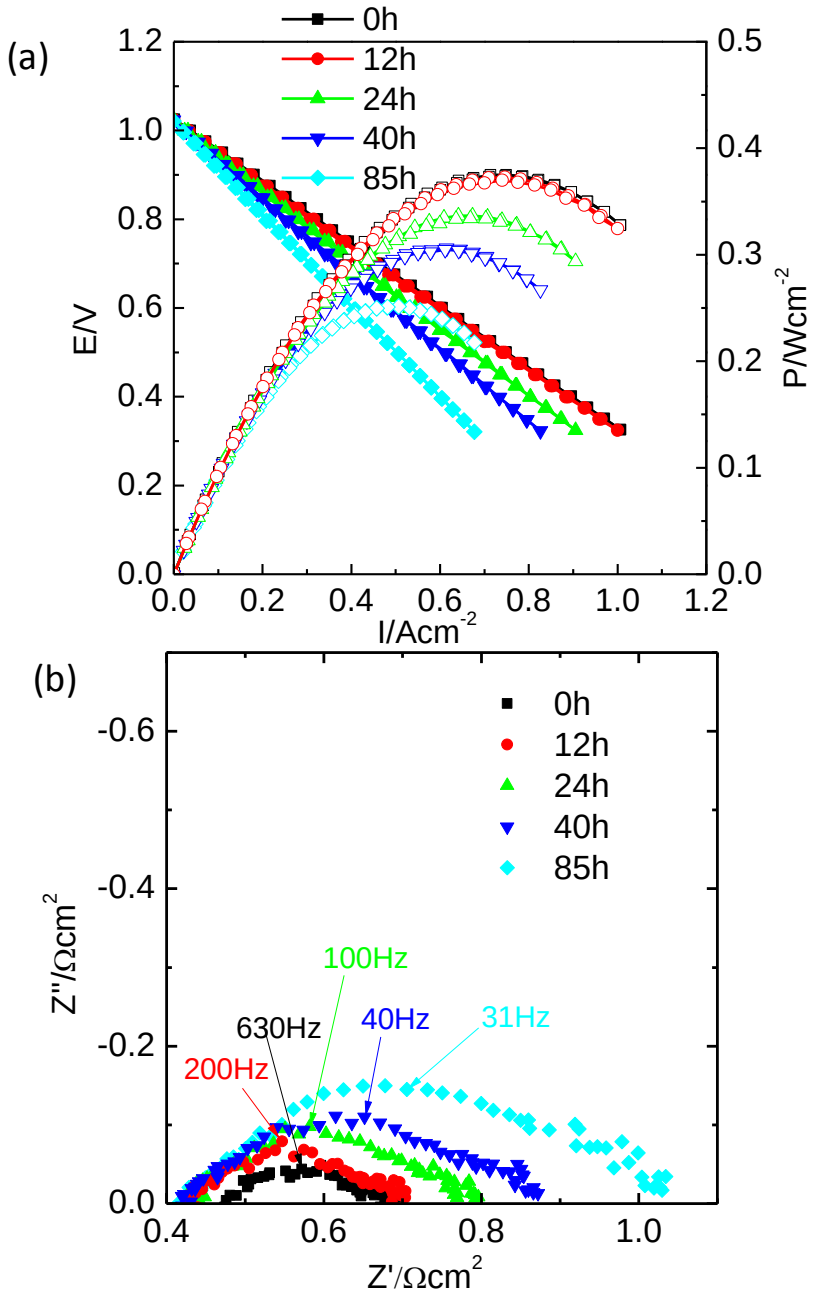

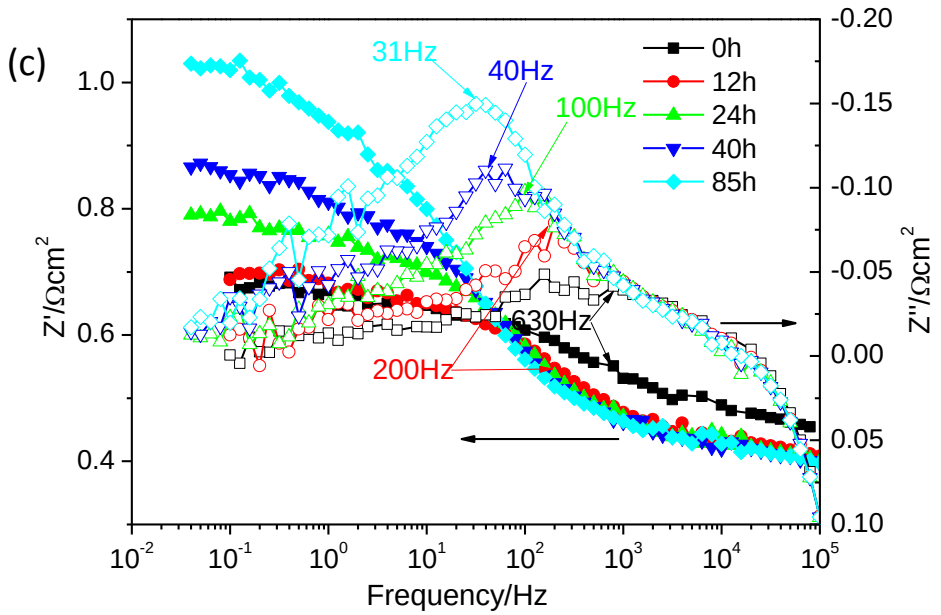


Figure 5.14 (a) I-V and I-P curves and (b) Nyquist plot and (c) Bode plot of EIS curves of the 6wt.% $CeO_2$ and 3wt.% nickel co-impregnated $LSCT_{A-}$ anode at different time upon stability testing at 700°C in humidified hydrogen (3% $H_2O$). I-V and I-P curves in (a) are signified by solid and open symbols, respectively. The impedance data were recorded under OCV.

The performances of the cell at the different time during the stability operation were measures and shown above in Figure 5.14(a). The maximum power density of the cell after 12-h testing is almost the same as that at the initial time, but degrades by ~50% from 380 to 250mW/cm$^2$ during the test. In order to examine the effects causing the degradation of the cell performance, the impedance spectra recorded at OCV with the testing time are presented in Figure 5.14(b) and (c). The ohmic resistance obtained from the intercept between the high-frequency arc and the real axis drops from 0.48 to 0.42Ωcm$^2$ after being operated for 12h and maintains stable at the following time in Figure 5.14(b). The ohmic resistances decrease because of the reduction of $Ce^{4+}$ to $Ce^{3+}$ in the reducing atmosphere and the sintering process of catalysts leading to the enhancement of electronic conductivity of the whole anode and current collector. While the total resistance of the cell after 12-h operation is almost the same as that in the beginning, the difference of the two impedances is characterized by a broader

polarization resistance with the time, especially the medium-frequency arc (~100Hz), as shown in Figure 5.14(c). With time the impedance in the medium-frequency region constantly increases and the frequency corresponding to the peak of the medium-frequency semicircle has shifted towards the lower value. This means that the relaxation time for this process is becoming longer with the operation time, which might relate with the adsorption of reactant species. The degradation of medium-frequency impedance under current loading could be explained by the fact that the originally available reaction sites decreases because of the coarsening process of the catalysts under operation at 700$^{o}$C. The low-frequency arcs are temperature independent, as shown in Figure 5.2, suggesting that the associated process is fuel delivery and gas diffusion at the anode. The resistance values across the low frequency remain stable with the operation time, because the open porosity for the gas diffusion at the anode is practically the same.

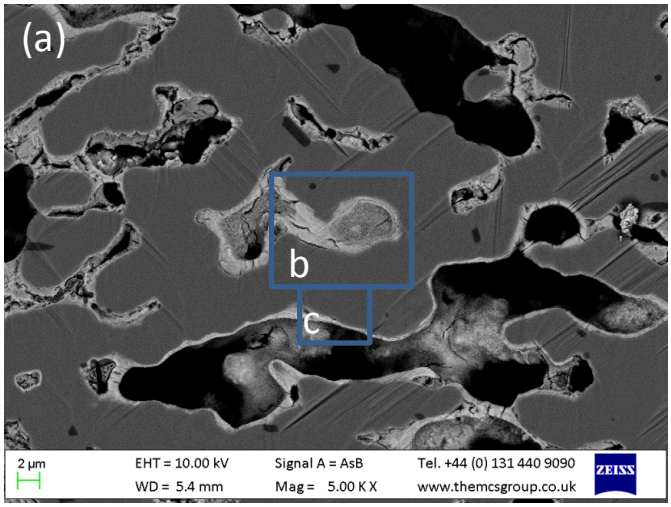


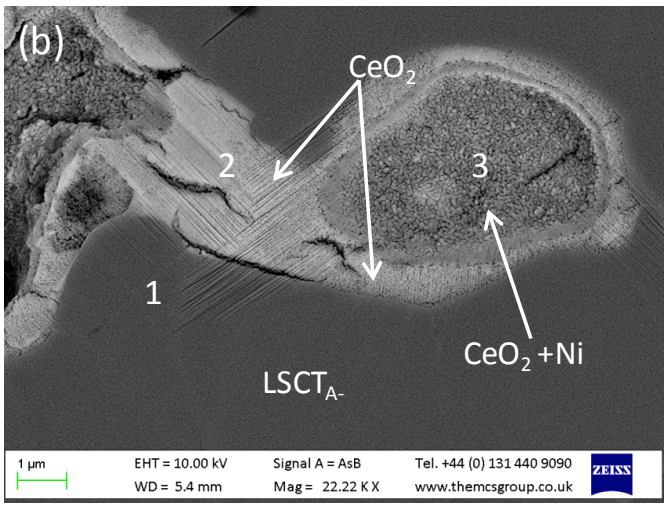


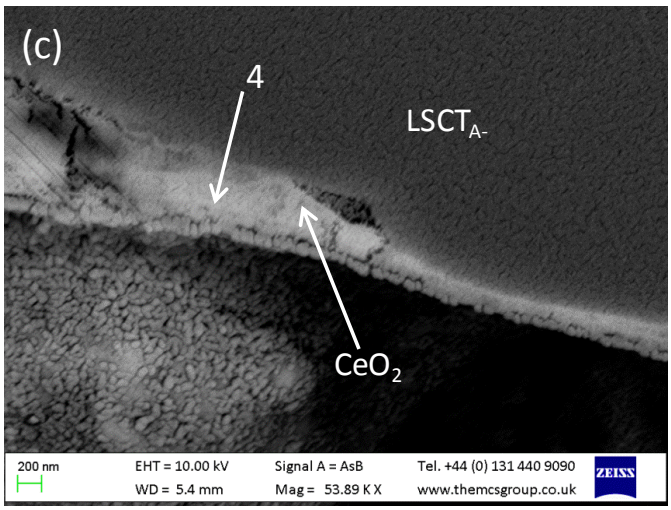


(Continued on the next page)

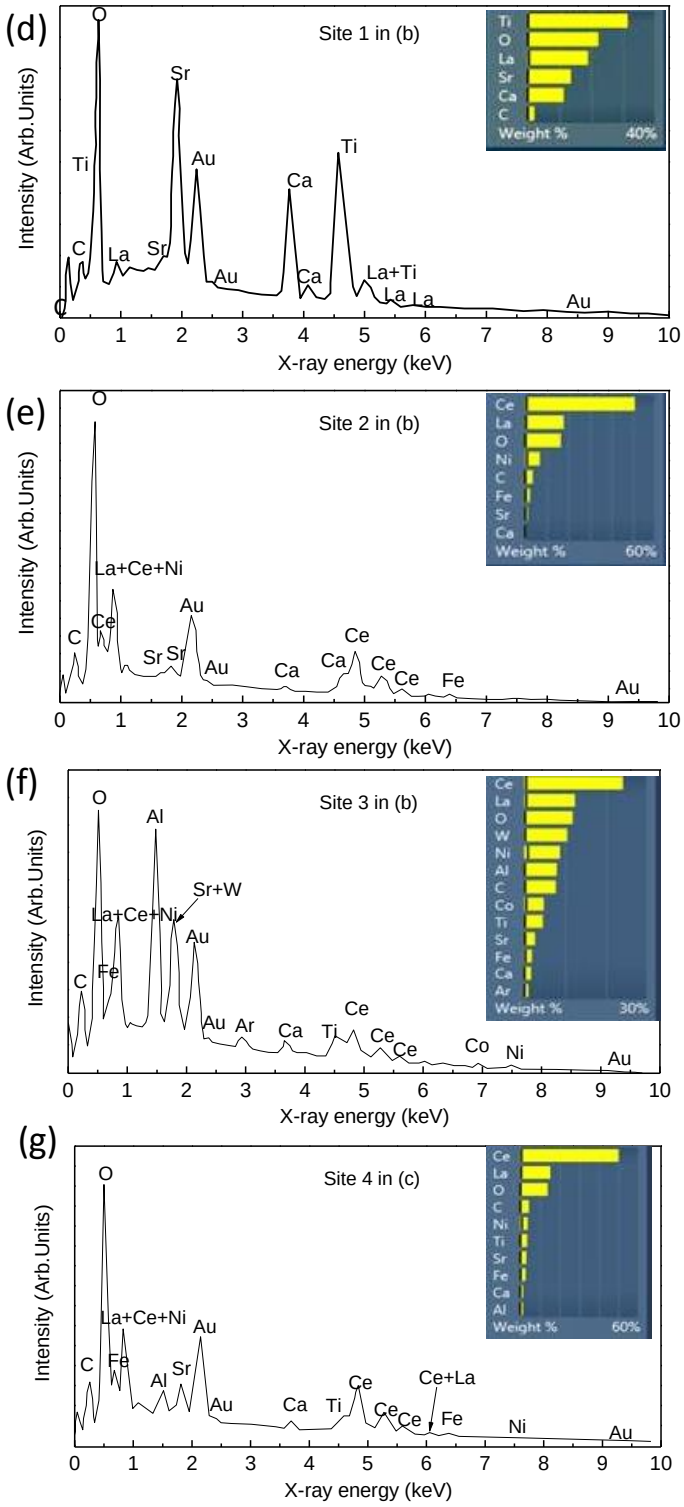


Figure 5.15 (a, b and c) Back-scattered electron (BSE) images of $CeO_2$ and Ni-impregnated $LSCT_{A-}$ after firing at 450$^{o}$C in air for 30 min and (d, e, f and g) energy dispersive X-ray analysis (EDX) spectra of the areas marked by the sites 1, 2, 3 and 4 in (b) and (c), respectively. (b) and (c) are the enlarged images of the rectangular areas in the general image (a).

Figure 5.15 presents the BSE images of the $LSCT_{A-}$ anode after the sequential infiltration of nitrate solution precursors containing $CeO_2$ and Ni and firing at 450$^oC$ in air for 30min. As shown in Figure 5.15(a), the catalysts are distributed in the open pores. Combining the EDX and BSE results in Figure 5.15(b) and (c), a bright layer mainly comprised of ceria is formed on the $LSCT_{A-}$ surface. This wetting layer can ensure a good connectivity for the ionic conductive phase and hence minimise the polarization losses in the anode due to the insufficient ionic conductivity of titanate. The NiO particles of approximately 100nm supported by the ceria layer form a porous network after annealing at 450$^oC$, which is supposed to provide the catalytic activity for fuel oxidation when being exposed in the reducing atmosphere (Figure 5.15(c)). The appearance of Au shown in the EDX spectra is from the coated gold layer. The Fe and Al elements detected by the EDX technique may come from the specimen holder, which is used to place the sample.

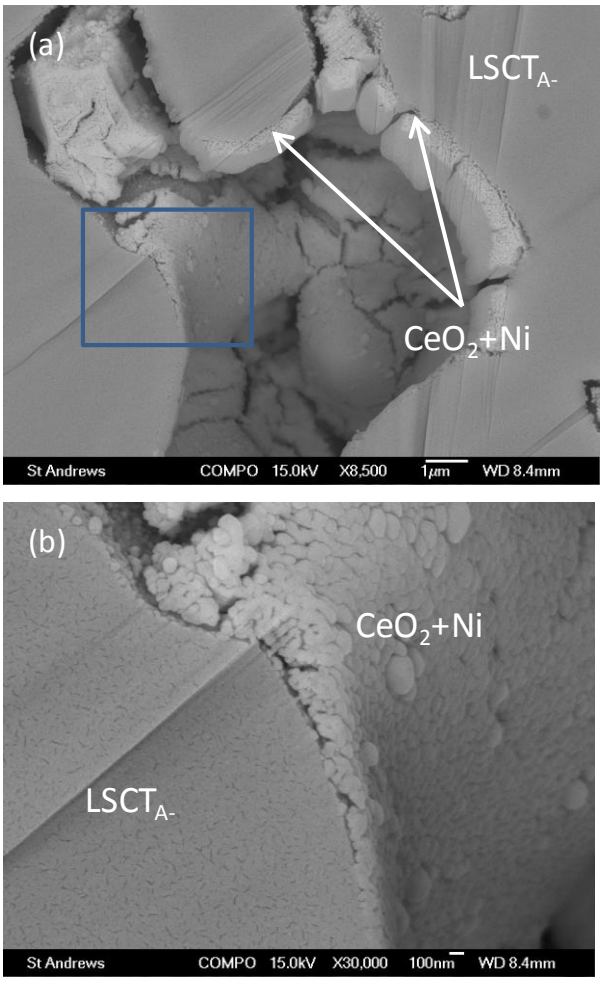


Figure 5.16 Back-scattered electron (BSE) images of $CeO_2$ and Ni-impregnated $LSCT_{A-}$ anode after operation in humidified hydrogen (3% $H_2O$) at 700°C for 24h. (b) the enlarged image of the rectangular area in the general image (a).

After 24-h exposure in 3% $H_2O$+97% $H_2$ at 700°C under a constant current density of 430mA/cm$^2$, the catalyst nanoparticles seem to have undergone coalescence, where the large bulk of agglomerates has been peeled off from the $LSCT_{A-}$ backbone, as displayed in Figure 5.16(a). It also has been noted that a large amount of cracking on the catalyst layer could cause the decrease of the ionic conductivity and the efficient triple phase boundary length for electrochemical reaction within the anode. Even so, nano-sized catalyst attaching against the backbone shown in the top left corner of Figure 5.16(b) can to some extent provide an extra triple phase boundary length for anode operation. While the coverage of catalyst on the anode scaffold is optimum initially, the microstructure change of catalyst including ceria and nickel would

restrict the efficient reaction sites at the operation condition. The distribution of ceria and nickel on the $LSCT_{A-}$ particles makes the connectivity of ionic conductive phase impossible, which would expect an increase in the polarization resistance.

The microstructure of the ceria and nickel co-impregnated $LSCT_{A-}$ anode after being operated at 700$^{o}$C for 85h is presented in Figure 5.17. The crystal particles on the $LSCT_{A-}$ surface are much more apparent than those tested for 24h, fully emerging in the open pores with the biggest particle reaching 1μm in diameter, as shown in Figure 5.17(a). Some of the bright catalyst particles are located inside the dark backbone particle. This unique structure means that the interaction between the perovskite backbone and the catalyst is happening as a function of time, at the cost of the required triple phase boundary length for anode reaction. Compared with the anode prior to the testing, the evolution of morphology can be observed with time: the catalyst particles appear to become more distinct and isolated, and meanwhile it is more difficult to separate nickel particles from the ceria particles. The availability of the gaps between the impregnates could be responsible for a decrease of the ionic conductivity provided by the interconnected ceria layer at the initial stage. However, the incorporation of impregnates into the backbone explains the improvement of the electronic conductivity, presented by the decrease in the ohmic losses. The comparison of BSE images at different times clearly demonstrates that the cell performance is strongly dependent on the microstructure evolution.

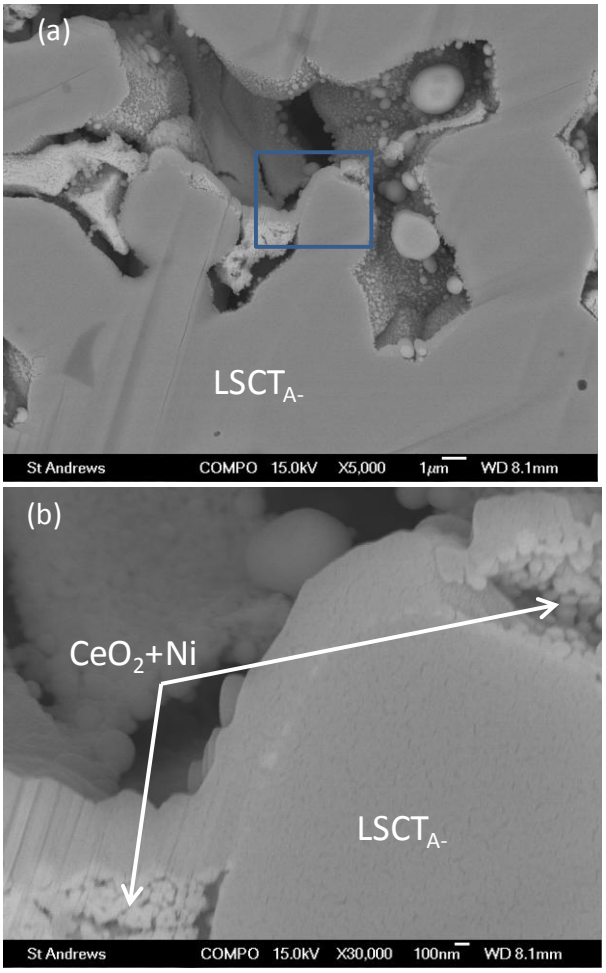


Figure 5.17 Back-scattered electron (BSE) images of $CeO_2$ and Ni-impregnated $LSCT_{A-}$ anode after operation in humidified hydrogen (3% $H_2O$) at 700$^oC$ for 85h. (b) the enlarged image of the rectangular area in the general image (a).

#### 5.3.3.3 $CeO_2$+$Ni_{0.75}Fe_{0.25}$ impregnated $LSCT_{A-}$ cell

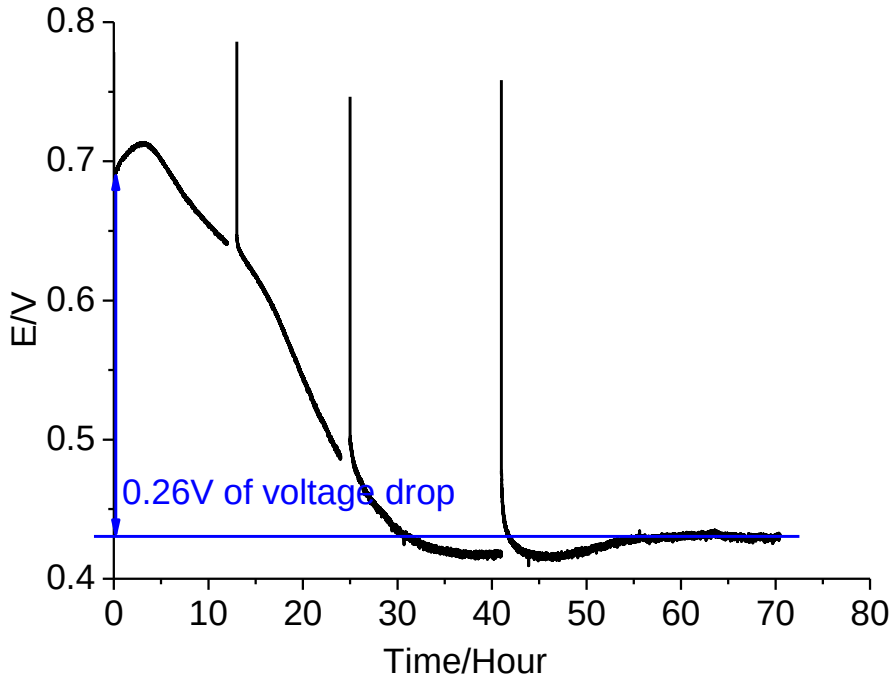


Figure 5.18 Stability testing of the 6wt.% $CeO_2$+3wt.% $Ni_{0.75}Fe_{0.25}$ impregnated $LSCT_{A-}$ anode at 700°C in humidified hydrogen (3% $H_2O$) under the applied current density of 360mA/cm$^2$

Figure 5.18 shows the time dependence of voltage under the current density of 360mA/cm$^2$ for the 6wt.% $CeO_2$ and 3wt.% Ni-Fe co-impregnated $LSCT_{A-}$ cell at 700°C in humidified hydrogen (3% $H_2O$). The voltage has shown a slightly increasing tendency in the first 3h. After that, the cell demonstrates a significant degradation until the voltage is stable at 0.43V.

The I-V curves measured before and after the stability testing for 72h are shown in Figure 5.19. The OCV values are approximately 1.0V, suggesting that the stability process did not harm the integrity of the cell. The maximum power density after 72-h operation has been decreased by around 50% from 290 to 150mW/cm$^2$. From the impedance spectra presented in Figure 5.19(b), the cell degradation can be attributed to the deteriorative ohmic and polarization resistance, in particular, the non-ohmic losses. The growth and agglomeration of catalyst particles could cause the crack on the initially interconnected electronic conductive phase on the $LSCT_{A-}$ surface,

leading to an increased ohmic resistance. In addition, the sintering catalyst could decrease the number of reaction sites for fuel oxidation, resulting in a worse non-ohmic resistance.

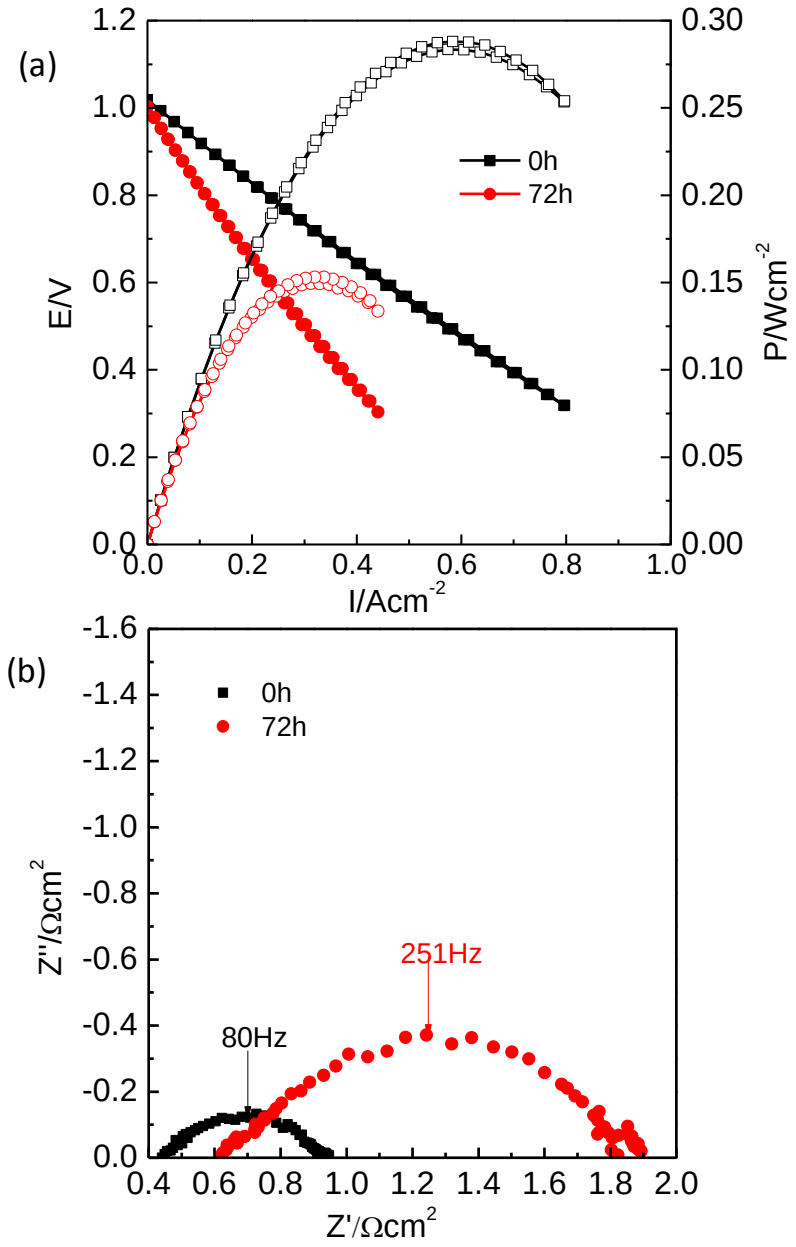


Figure 5.19 (a) I-V and I-P curves and EIS curves (b) of the 6wt.% $CeO_2$ and 3wt.% $Ni_{0.75}Fe_{0.25}$ co-impregnated $LSCT_{A-}$ anode at different time upon stability testing at 700°C in humidified hydrogen (3% $H_2O$). I-V and I-P curves in (a) are signified by solid and open symbols, respectively. The impedance data were recorded under OCV.

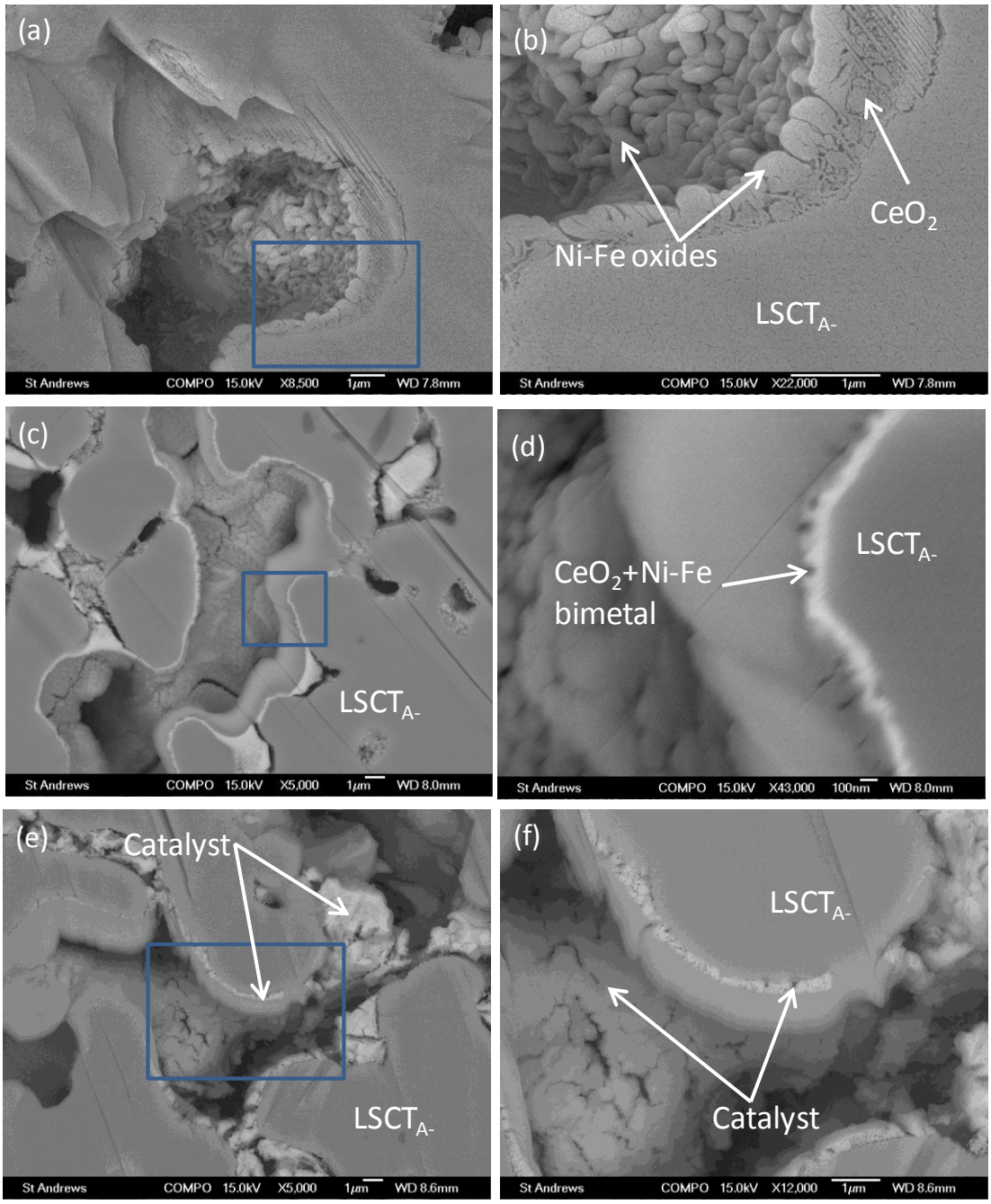


Figure 5.20 Back-scattered electron (BSE) images of $CeO_2$ and Ni-Fe impregnated $LSCT_{A-}$ (a, b) before testing, (c, d) and (e, f) after testing for 24 and 72h, respectively, at 700$^{o}$C. (b), (d) and (f) the enlarged images of the rectangular areas in the general images (a), (c) and (e), respectively.

Figure 5.20 shows the microstructure of the $LSCT_{A-}$ anode coated with $CeO_2$ and Ni-Fe catalyst at the different time during the stability testing. Two different layers containing $CeO_2$ and Ni-Fe oxides are located on the perovskite surface after firing at $450^oC$, as shown in Figure 5.20(a) and (b): the Ni-Fe oxides with the particle size of 200nm are supported by the underlying ceria layer of nano-particles. After being operated in hydrogen for 24h, the catalyst particles visible on the open pores become coarsening in Figure 5.20(c). Interestingly, a bright catalyst layer with a width of 100nm is visible inside the darker $LSCT_{A-}$ particles in Figure 5.20(d). The formation of this strange structure is likely to be associated with the re-nucleation and outward diffusion of the $LSCT_{A-}$ particles, the edge of which are dissolved on the highly acid condition originating from the nitrate solution upon the impregnation-firing cycle. This explanation can be confirmed by the coalescing catalysts beside the bright layer in the open pores. On the other hand, the ceria layer is typically used for the anti-diffusion layer, therefore the diffusion between the backbone and Ni-Fe catalyst though ceria at $700^oC$ is impossible. After the 72-h operation, the images in Figure 5.20 (e) and (f) exhibits a very similar structure as those after 24-h testing, except that more cracks are observed on the catalyst layer.

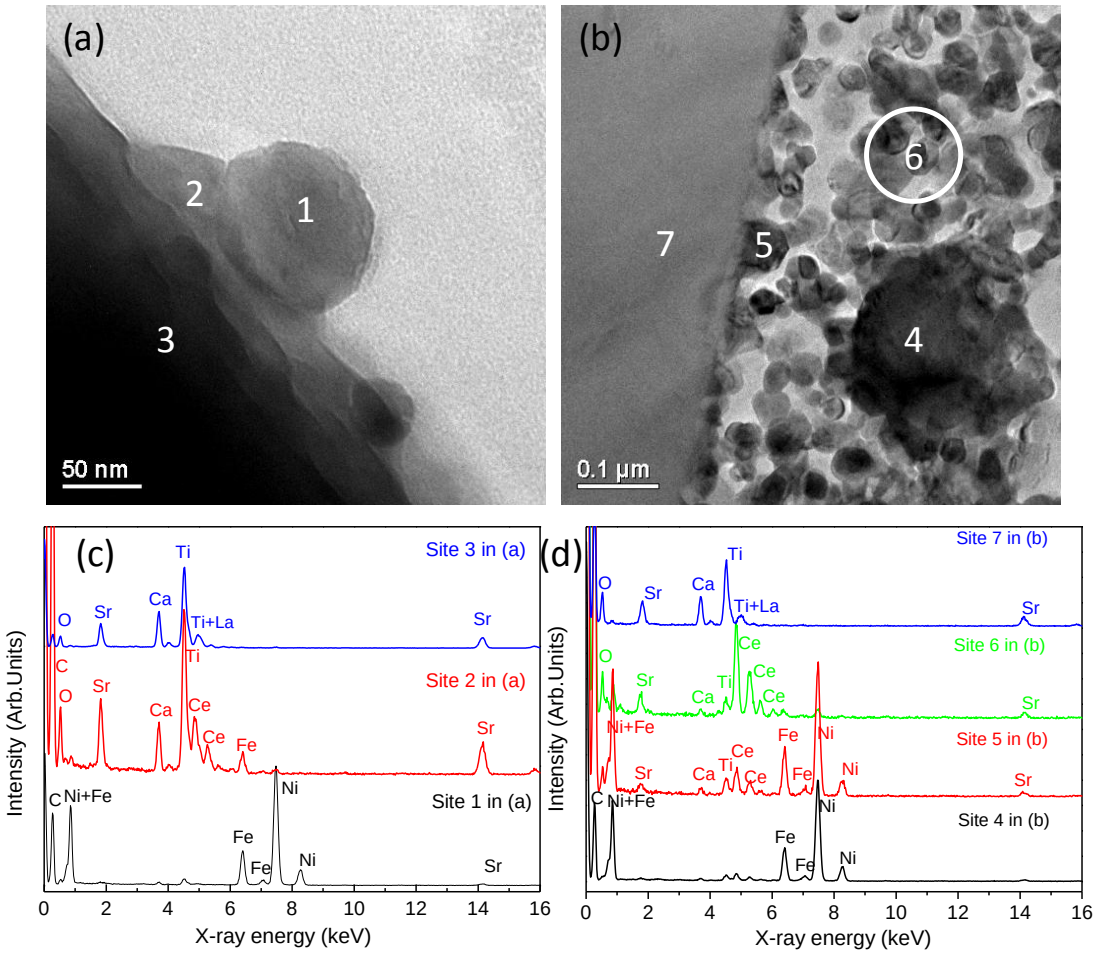


Figure 5.21 (a, b) Transmission electron microscopy (TEM) images of $CeO_2$ and Ni-Fe impregnated $LSCT_{A-}$ anode after stability testing for 72h at 700°C in humidified hydrogen and (c, d) the corresponding EDX spectra of the marked areas by numbers 1-3 in (a) and 4-7 in (b), respectively

In order to further understand the catalyst distribution on the backbone surface, TEM images were taken with the corresponding EDX spectra of the different regions for the sample tested after 72h, as displayed in Figure 5.21. By the analysis of the TEM images of two regions, it can be noted that the nature and thickness of the catalyst particles varies. Figure 5.21(a) shows that a nano-sized Ni-Fe particle has grown on the thin ceria layer on the top of the $LSCT_{A-}$ grain. It appears that the top layer whether it is a Ni particle or ceria layer has embedded into the adjacent and underlying layer indicating that the interaction of the neighbouring phases happens. Figure 5.21(b) shows the Ni particles either residing on the $LSCT_{A-}$ surface or

surrounded by the nano-sized ceria particles. The EDX spectra in Figure 5.21(d) reveal that the elements from the perovskite are detected in the catalyst layer, also suggesting that the possibility of the dissolution and subsequent re-nucleation of titanate.

### 5.3.4 Redox stability and microstructure of $CeO_2$+Ni impregnated cell

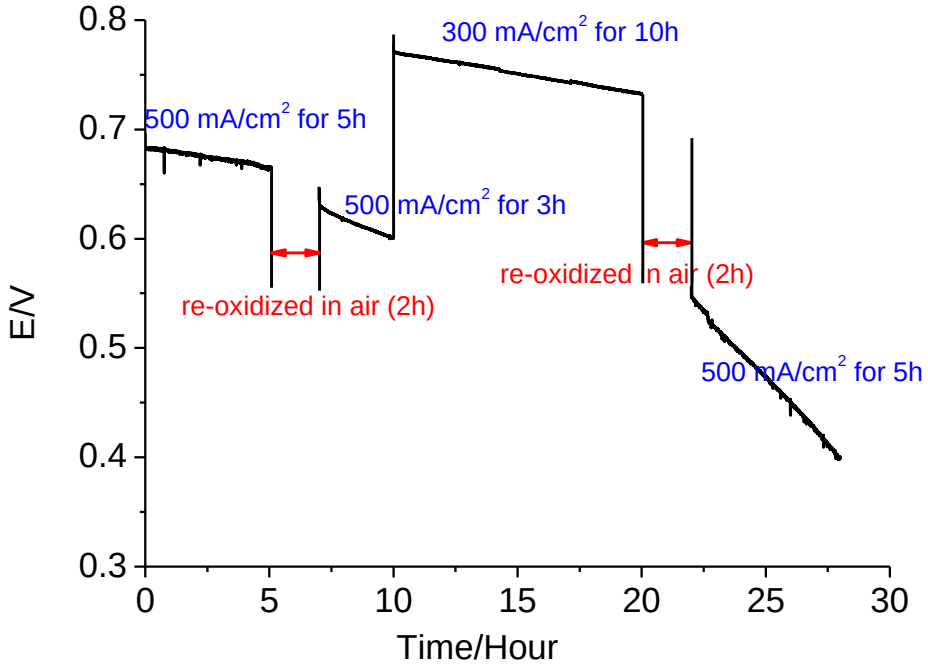


Figure 5.22 Time dependence of voltage for the $CeO_2$ and Ni co-impregnated $LSCT_{A-}$ anode in humidified hydrogen (3% $H_2O$) at 700°C under the redox cycles

In order to see the influence of the oxidizing atmosphere on the stability of the cell with $CeO_2$+Ni impregnated $LSCT_{A-}$ anode in reducing atmosphere, the redox experiments were performed, as shown in Figure 5.22. First, the cell was thermally treated at 750°C for 12h in humidified hydrogen in order to ensure the reduction of $Ce^{4+}$ to $Ce^{3+}$ and then it was cooled down to 700°C for the measurement of the redox stability. After testing the anode in humidified hydrogen at 700°C for 5h, the anode compartment was first flushed with nitrogen, and then exposed to the flowing air for 2h. Before switching back to hydrogen, the anode compartment was flushed by nitrogen again. Figure 5.22 shows the voltage change with time upon every redox cycle. The applied current densities during redox cycling are presented in the graph.

At the initial stage, in 5-h operation, the voltage has degraded by 0.004V/h from 0.68V to 0.66V under a bias of 500mA/cm$^2$. After the oxidation in air for 2h, the voltage degradation rate is much faster than that observed initially, being 0.013V/h. The second oxidation step increases the degradation rate for the cell performance even further, which can be calculated by the slope of the graph about 0.03 V/h.

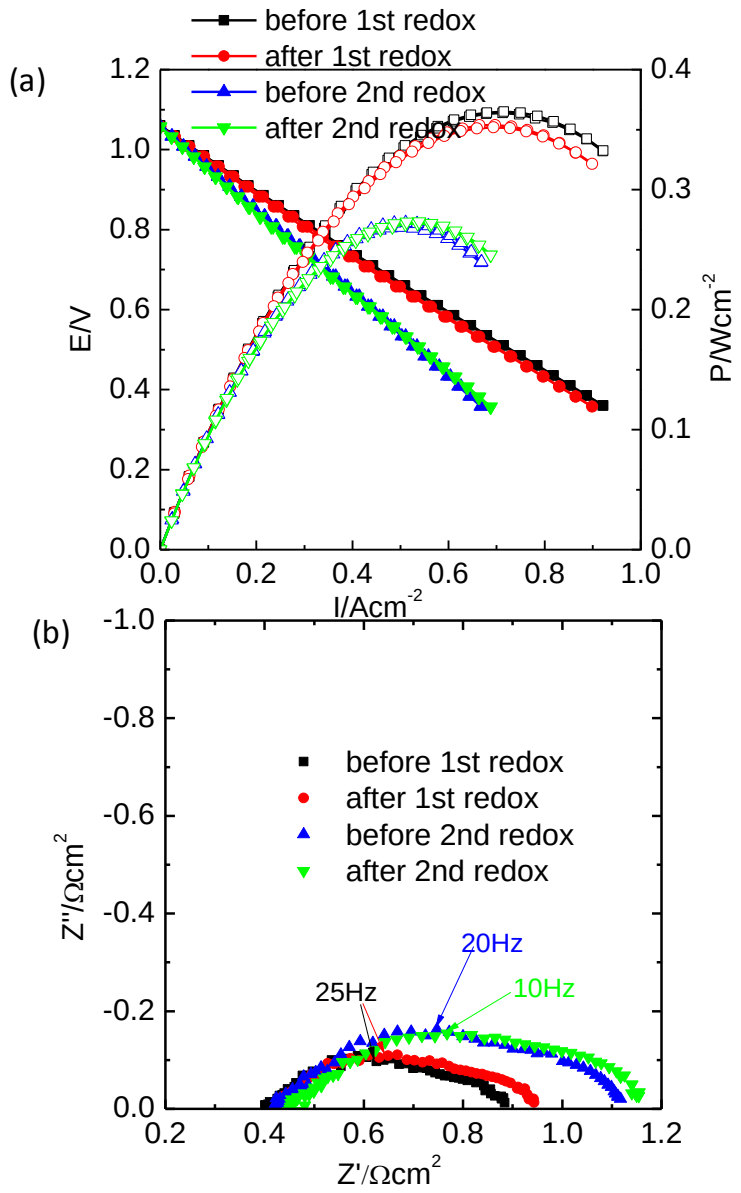


Figure 5.23 (a) I-V and I-P curves and (b) Nyquist plot of EIS curves of the 6wt.% $CeO_2$ and 3wt.% nickel co-impregnated $LSCT_{A-}$ anode at 700$^o$C in humidified hydrogen (3% $H_2O$) before and after the first and second redox cycle. I-V and I-P curves in (a) are signified by solid and open symbols, respectively. The impedance data were recorded under OCV.

Figure 5.23 show V-I curves and impedance spectra for the same cell used in the redox stability testing, before and after the treatment in air. The OCVs are 1.05V for all the graphs, suggesting that the oxidation process in air for 2h did no harm for the cell integrity of electrolyte. Before the oxidation treatment, the maximum power density is 363mW/cm$^2$, and the impedance spectrum reveals that the ohmic losses contribute approximately 0.41Ωcm$^2$ to the total resistance of 0.88Ωcm$^2$, The ohmic resistance in this cell is slightly lower than that observed in the cells for initial performance and stability testing, and this could be attributed to the thermal treatment at 700$^o$C before the test, leading to a interconnected electronic conductive layer on the $LSCT_{A-}$ surface consisting of ceria and nickel. The same phenomenon has been observed in $CeO_2$+Ru co-infiltrated YST-YSZ anode after the pre-treatment at 800$^o$C for 12h [158]. After the first oxidation treatment, the maximum power density is 353mW/cm$^2$, and the total cell resistance increases to 0.95Ωcm$^2$ without changing the ohmic resistance of the cell. The cell performances before and after the second redox cycle are also similar. However, the impedance spectrum after the oxidation treatment shows a rightward shift compared with the one before without changing the shape and magnitude of the polarization resistance. Combining the redox stability and the cell performance before and after the oxidation process shown in Figure 5.22 and 5.23, respectively, it can be concluded that the degradation rate for the voltage after the individual re-oxidation process in air is much faster that that during the previous stage under the same current density, while no significant deterioration of electrochemical performance occurred upon each redox cycle. So far, the reason has been attributed to the catalyst microstructure change in the reducing and oxidizing atmosphere. In particular, the ceria layer would undergo a contraction and expansion process due to the valence transition between $Ce^{4+}$ and $Ce^{3+}$ under the oxidizing/reducing atmosphere on the $LSCT_{A-}$ backbone. The reduction of $Ce^{4+}$ to $Ce^{3+}$ may produce a large amount of microcracks on the ceria layer leading to a decrease in the number of the electrochemical reaction sites for hydrogen oxidation.

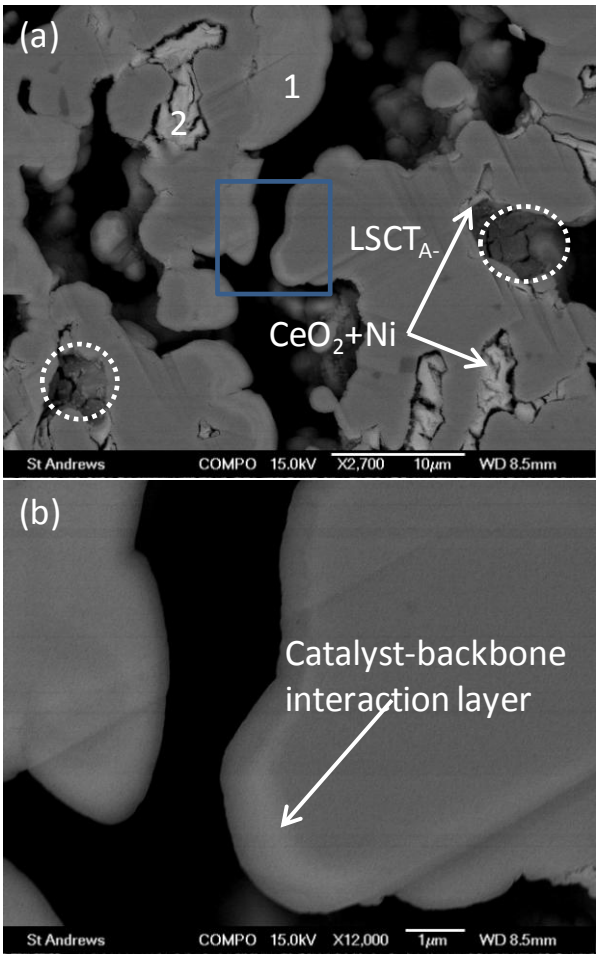
(a)
1
2
LSCT$_{A-}$
CeO$_2$+Ni
St Andrews COMPO 15.0kV X2,700 10μm WD 8.5mm
(b)
Catalyst-backbone
interaction layer
St Andrews COMPO 15.0kV X12,000 1μm WD 8.5mm

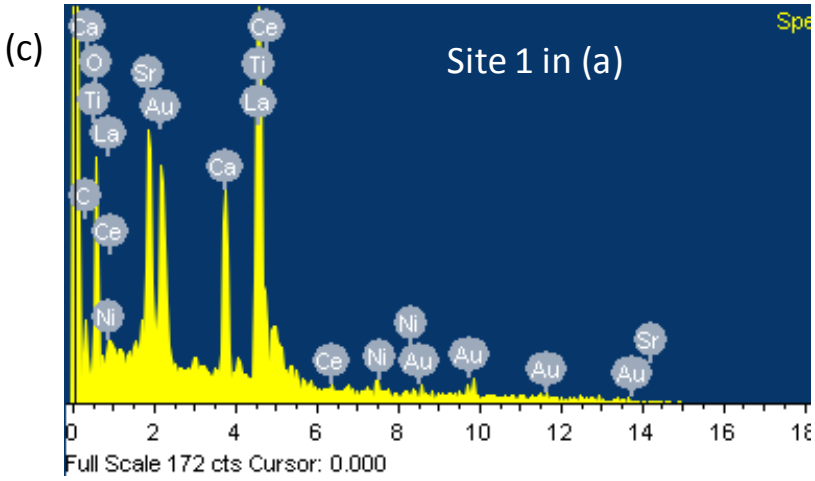
(c)
Site 1 in (a)
Ca
O
Sr
Ti
Au
La
C
Ce
Ni
Ti
La
Ca
Ce
Ni
Au
Au
Au
Sr
Au
0 2 4 6 8 10 12 14 16
Full Scale 172 cts Cursor: 0.000

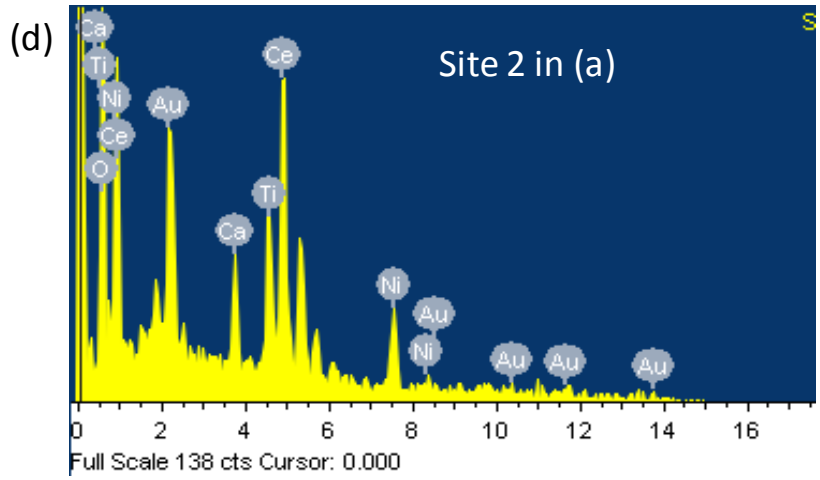


Figure 5.24 Back-scattered electron (BSE) images of $CeO_2$ and Ni-impregnated $LSCT_{A-}$ anode after two the redox cycles operated between humidified hydrogen and air. (b) the enlarged image of the rectangular area in the general image (a) and (c, d) the EDX results of site 1 and 2 in (a).

The anode experiencing the two redox cycles has been polished by FIB and characterized by BSE, as shown in Figure 5.24. As expected, the catalyst particles on the $LSCT_{A-}$ surface agglomerate together and a lot of gaps are visible among the catalysts, which has been clearly denoted by the dotted circle in Figure 5.24(a). The size of catalyst particles are much larger than those undergoing the stability testing under the same condition. By comparing the EDX results of site 1 and 2 in Figure 5.24(a), it can be seen that the interaction of $LSCT_{A-}$ backbone and ceria happens along the edge of the perovskite particle. The region for the catalyst-backbone interaction is brighter than the backbone itself and darker than the coarsening catalyst. From the enlarged BSE image shown in Figure 5.24(b), it also can be found that the catalyst layer mixing with the perovskite edge is quite smooth, different from the microstructure observed initially.

By contrasting the microstructure after redox cycles and stability testing, more cracks are visible on the catalyst layer after the redox cycles. This could explain the gradually increasing degradation rate after the oxidation treatment. More importantly, the interaction between the perovskite backbone and the catalysts can be clearly seen after the redox experiments without the catalyst nanoparticles attaching against the $LSCT_{A-}$ surface, like the sample experiencing the stability testing as shown in Figure

5.16 and 5.17. The interaction surface is quite smooth, consisting of the catalyst and backbone material. The formation of this dense layer possibly associated with the oxidation treatment could decrease the ionic conductivity offered by the initial ceria layer and block the inter-diffusion of hydrogen, therefore causing a significant decrease of the available triple phase boundary length for the anode reaction.

## 5.4 Conclusion

The sequential infiltration of ceria and nickel into the porous $LSCT_{A-}$ anode support improves the cell performance in hydrogen; however, the addition of nickel induces the carbon deposition in methane leading to the cell delamination and cracking. The bi-metal Ni-Fe along with the underneath ceria is able to inhibit the carbon coking problem but the cell performance is not comparable with the $CeO_2$-Ni impregnated $LSCT_{A-}$ cell. The performance degradation can be attributed to the growth and agglomeration of catalyst particles and the interaction between the $LSCT_{A-}$ edge and adjacent catalysts.

# Chapter 6. Effects of YSZ/$LSCT_{A-}$ ratio and ball-milling process on sintering processes and electrical properties

## 6.1 Introduction

Electrochemical Impedance Spectroscopy (EIS) has been extensively used to study the electrochemical behaviour of materials and interfaces. Besides the fact that it can be used to analyze the different processes that occur in the whole fuel cell, it also can be used to describe the electrical properties of a bulk material for understanding the conduction mechanism by separating the bulk and grain boundary resistance. The electrical properties of a bulk material are generally governed by its microstructure.

Yttria-stabilized zirconia, YSZ is known as a state-of-the-art electrolyte material due to high ionic conductivity, low electronic conductivity, good mechanical strength and chemical stability under oxidizing and reducing atmospheres. A-site deficient lanthunum and calcium co-doped $SrTiO_3$ ($LSCT_{A-}$) is an electronic conductor in reducing atmosphere. When the YSZ-$LSCT_{A-}$ composite is used for the anode scaffold with a sufficient percolation of electronic and ionic conductive phases, more electrochemical reaction sites are expected on the $LSCT_{A-}$-YSZ-gas triple phase boundaries, leading to a more promising performance. It is necessary to study the effect of varied $LSCT_{A-}$/YSZ composition on the electrical properties of a bulk composite, along with the microstructure and the sintering process. Impedance spectra were collected over a wide frequency range allow to determine the bulk and grain boundary resistance over a wide range of compositions in order to discuss the influence of the composition on the ionic conduction mechanism. Since the conduction mechanisms for $LSCT_{A-}$ and YSZ in air are dependent of holes and oxygen ion vacancies respectively, the electrical properties measured in air are capable of representing the conduction behaviours in reducing atmosphere in which anode is exposed.

The microstructure and impurity content of the ceramic can have a strong impact on its ion conduction behaviour [277].YSZ electrolytes undergoing varied sintering processes have been studied by AC impedance spectroscopy [278,279]. It has been

reported that the grain boundary resistance is predominately correlated with the relative density and grain size. In addition, trace of impurities along the grain boundary can significantly deteriorate the ionic conductivity of the grain boundary on the YSZ electrolyte.

The ball milling technique is a useful method to mix two ceramic materials evenly and break the agglomerates of both. The use of this technique may have an effect on the electrical properties and shrinkage processes of the studied composite, which is also demonstrated in this chapter. Ball milling is a commonly used technique in manufacture of slurries for both tape casting and screen printing, with the initial step in both being an agglomeration milling step. Therefore this technique can be used to mix the two phases without introducing an additional step into the process.

## 6.2 Experimental

YSZ powder with mean particle size of 1μm mixed with $LSCT_{A-}$ powder calcined at 1100$^{o}$C for 5h (mean particle size is 2.198μm in section 3.1.2) with and without ball milling procedure were prepared and pressed into a pellet of 1.3mm in diameter and 2mm in thickness under a uniaxial pressure of 110Mpa. The ratio of YSZ powder is at the range of 5-80wt.% to the total weight of mixed powders. Pure $LSCT_{A-}$ and YSZ pellets were also prepared for comparison. The pellets were set up in the dilatometer for the sinterability measurement. The testing was performed in air at a heating rate of 3$^{o}$Cmin$^{-1}$ to 1350$^{o}$C and a cooling rate of 3$^{o}$Cmin$^{-1}$ after a dwelling time of 3h at 1350$^{o}$C.

The theoretical densities of pure $LSCT_{A-}$ and YSZ are taken as 4.97 and 5.9g/cm$^3$, respectively, according to their lattice parameters. The theoretical densities of the $LSCT_{A-}$-YSZ composites were calculated by the mixing rule in terms of the following equation:

$$\rho_t = v_1\rho_1 + v_2\rho_2 \qquad \text{(Equation 6.1)}$$

Where $v_1$ and $v_2$ are volume fractions of each component with the corresponding theoretical densities of $\rho_1$ and $\rho_2$ respectively. The experimental densities of the

mixed composites, $\rho_e$, are obtained by the geometry of the sintered pellets. The relative densities, $\rho_r$, can be calculated by the equation below:

$$\rho_r = \frac{\rho_e}{\rho_t} \qquad \text{(Equation 6.2)}$$

In this study, the relative densities of the composite specimens are in the order of 92-96%.

The microstructures of the samples sintered at 1350$^o$C for 3h in air were characterized by Back-scattered Electron (BSE) images. The sintered samples were mounted in epoxy resin and polished using a diamond polishing paste (1μm) after being ground by 1200-grit emery sandpaper. A thin layer of gold was sputtered on the cross surface of the samples to get better BSE images. The cross section of the samples were taken by BSE to study the distribution of YSZ grains in the composite bulk.

Platinum paste was applied on both the flat surfaces of the sintered pellets and then fired at 900$^o$C for 30min in air. The AC impedance measurements were carried out in the frequency range of 10MHz to 1Hz and the temperature range of 290-675$^o$C in air. The impedance data were analyzed by the Zview software to segregate the contribution of grain and grain boundary.

## 6.3 Results and discussion

### 6.3.1 Microstructure

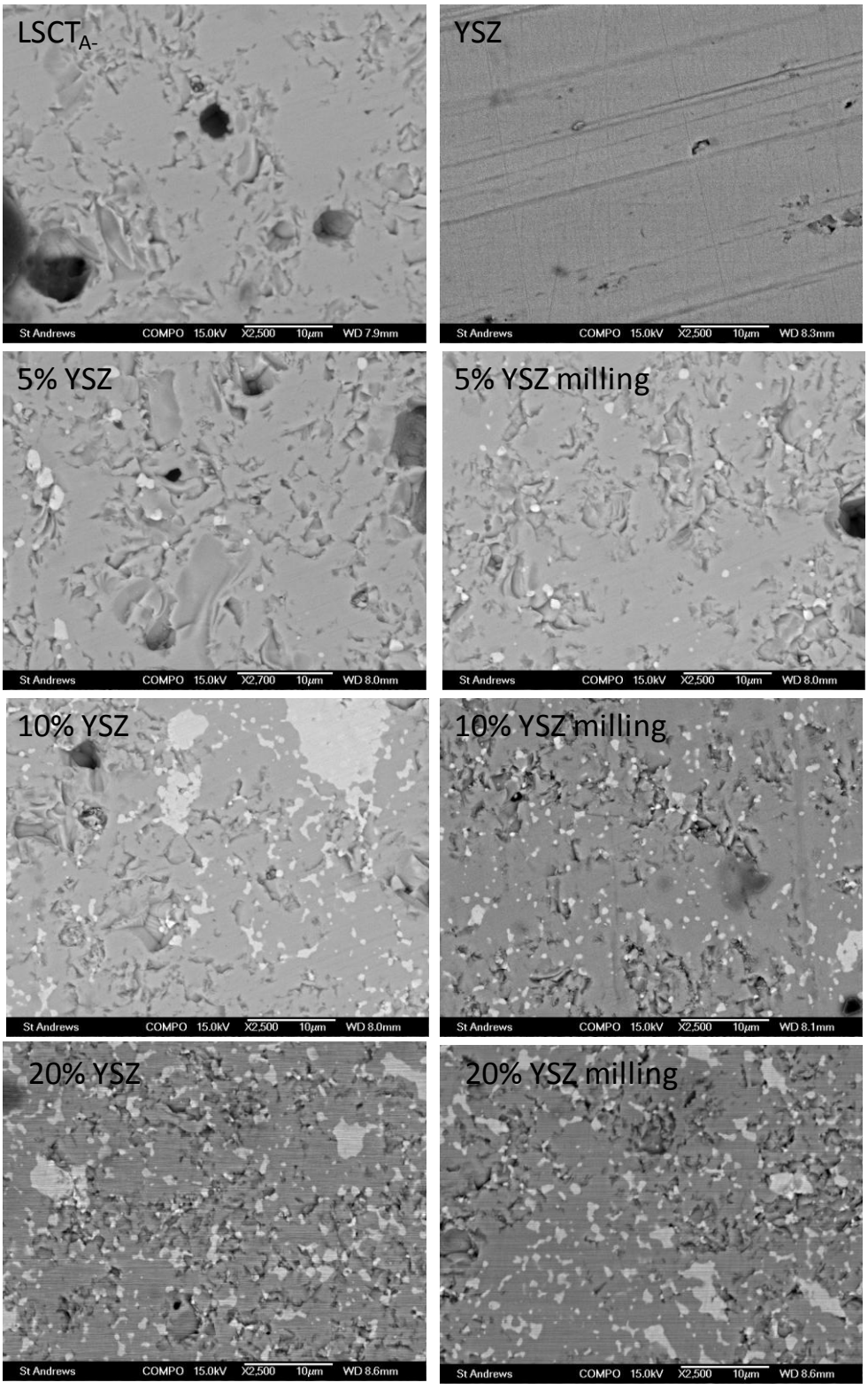

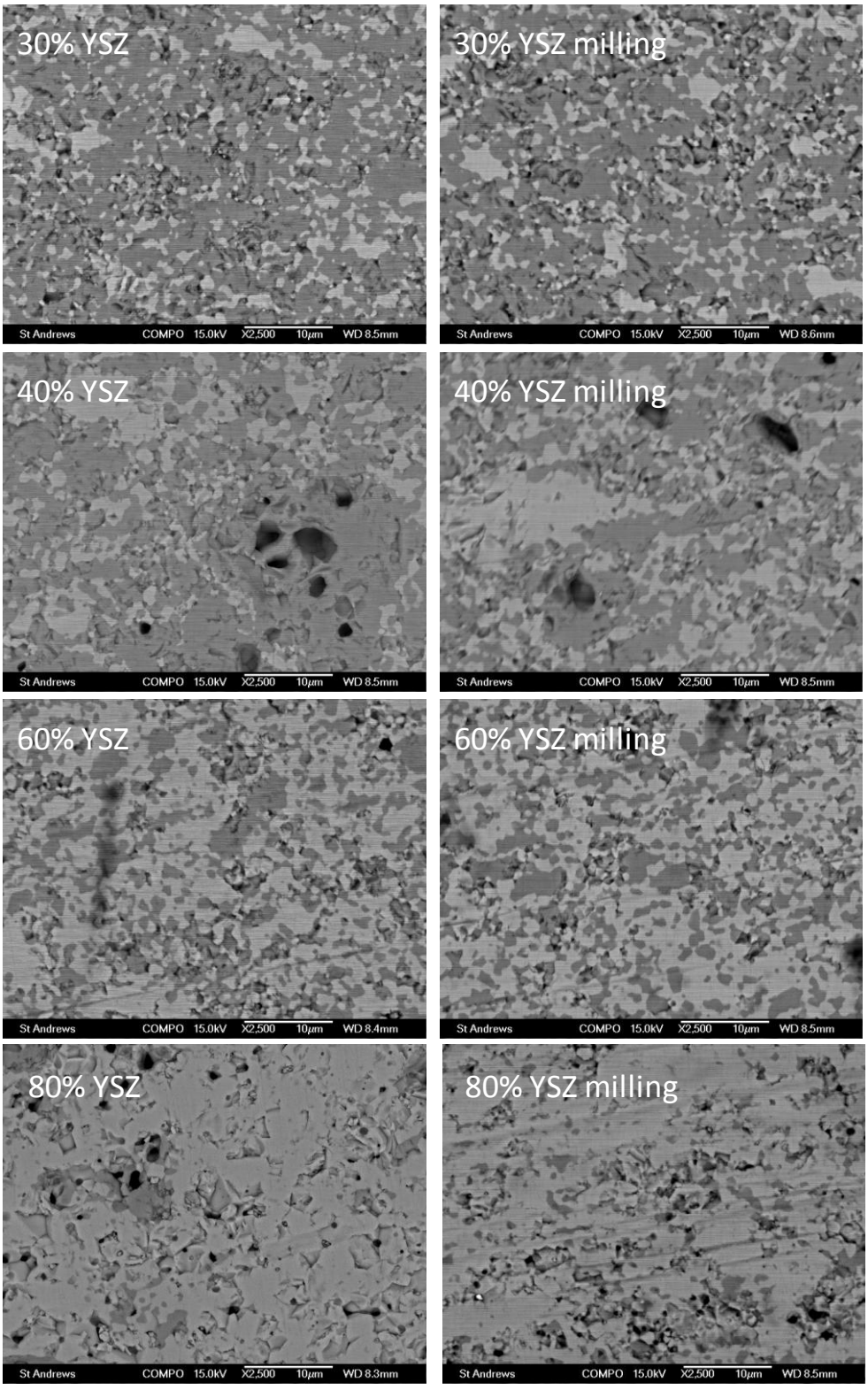


Figure 6.1 Back-scattered electron (BSE) images of the sintered samples at 1350°C without and with ball milling technique: white colour is YSZ, gray $LSCT_{A-}$ and dark pores. The compositions of the bulk composites were denoted in the graphs.

Figure 6.1 presents the BSE images of all the YSZ-$LSCT_{A-}$ composites sintered at 1350$^{o}$C for 3h. The dark pores, bright-looking YSZ grains and gray $LSCT_{A-}$ grains are easily distinguished from each other. It has be seen that sub-micrometer pores are formed in the pure $LSCT_{A-}$ sample, while the pores are seldom found in the YSZ cross section. The densification of YSZ can be completed below 1270$^{o}$C, and the grain will grow above this temperature without further densification [280], leading to a very low porosity of the order of 2%. The relative density of YSZ is reported to be ~97% when sintered above 1270$^{o}$C. However, the relative density of $LSCT_{A-}$ calculated by the ratio of the geometric density to the theoretical density is around 92%, indicating that the densification process of $LSCT_{A-}$ is not completely achieved by 1350$^{o}$C. The bright YSZ particles with grain size of 1-2μm are observed in 5% YSZ+$LSCT_{A-}$ sample. However, after ball milling, the much smaller YSZ particles are observed and distributed more evenly. The formation of larger YSZ particles without ball milling suggests that the crystallization and grain growth behaviours of YSZ occur during heating due to the agglomeration of YSZ particles. The ball milling technique can lead to the more even distribution of YSZ grains in the large amount of $LSCT_{A-}$ grains, and hence reduce the YSZ grain growth by decreasing the touch of the adjacent YSZ grains. When 10% YSZ was added to the $LSCT_{A-}$ powder without ball milling, the accumulative behaviour of the YSZ grains is more obvious. Likewise, the ball milling technique improves the distribution of YSZ grains. For the mixtures with 20% YSZ with and without ball milling process, the microstructures are similar: a small amount of YSZ agglomerates are seen, along with the well distributed YSZ grains inside the $LSCT_{A-}$ bulk. With addition of 30% YSZ into the $LSCT_{A-}$ powder, YSZ grains start to connect together by the diffusion of the neighbouring YSZ particles at the high temperature. When the percentage of YSZ in the mixture is 40%, two separately interconnected phases can be obtained from the white YSZ and the gray $LSCT_{A-}$. With the addition of more YSZ in the $LSCT_{A-}$ powder over 60 %, YSZ grains grow into a bulk with the gray $LSCT_{A-}$ spread. Large agglomerates of $LSCT_{A-}$ grains are observed in the 80% YSZ+20% $LSCT_{A-}$ sample without ball milling. The pores are mainly formed in the $LSCT_{A-}$ region, which also suggests that the sintering temperature is not high enough to complete the densification of $LSCT_{A-}$.

### 6.3.2 Dilatometry

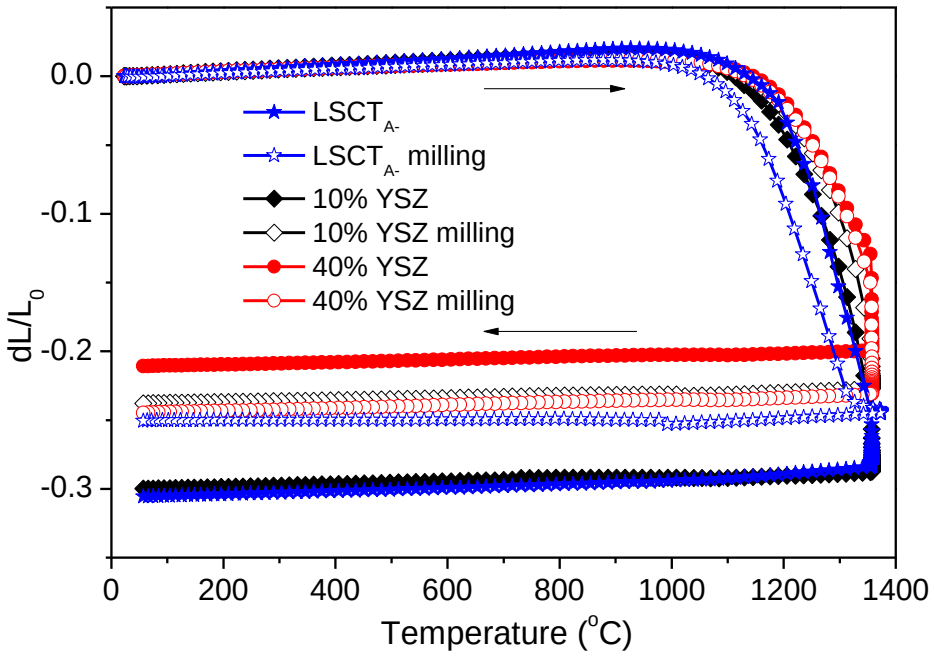


Figure 6.2 Sintering processes of the typical samples: $LSCT_{A-}$, 10% and 40% YSZ additive mixture with and without ball milling in air

The sintering processes of a few typical samples as a function of temperature carried out in air are presented in Figure 6.2. The initial temperature of densification for the pure $LSCT_{A-}$ pellet without ball milling is around 1100°C, and the total shrinkage can reach 25.06%. However, the ball milled $LSCT_{A-}$ pellet shows a lower temperature for the starting densification and a lower shrinkage at the end of the temperature program. It is indicative that the large agglomerates of $LSCT_{A-}$ particles have been broken down, allowing to be prepared as a packing green pellet. It also can be found that the sinterability behaviour of the milled $LSCT_{A-}$ sample has been completed below the sintering temperature 1350°C, anticipating a higher relative density of 95% vs 92% for the unmilled sample.

For the composite with 10% YSZ content, the temperatures corresponding to the initial densification for both samples are the same, but the sample with ball milling shows a lower shrinkage than the same composite without. This can be attributed to

the blocking effect of the YSZ grains along the grain boundary of $LSCT_{A-}$ grains due to the better distribution of YSZ resulting from the ball milling process.

When the YSZ content is 40%, the shrinkage patterns are different: the final shrinkage of ball milled sample is obviously higher than that of the sample without. The YSZ content is sufficiently high to form a continuous layer within the $LSCT_{A-}$ bulk, and the non-ball milled sample could have to some extent agglomerates of YSZ grains, becoming a blocking effect for the percolation of $LSCT_{A-}$ grains. In this way, the individual growth of the well-distributed YSZ and $LSCT_{A-}$ grains can ensure a higher relative density.

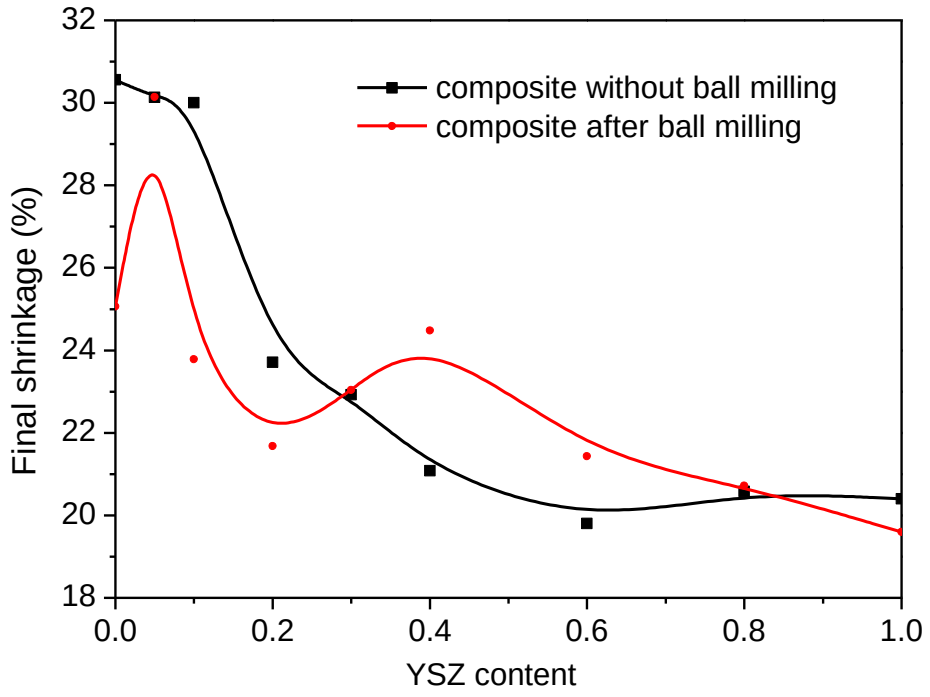


Figure 6.3 Summary of the final shrinkage of YSZ-$LSCT_{A-}$ composites with and without ball milling process as a function of the YSZ content

Figure 6.3 shows the tendency of the final shrinkage for the pure $LSCT_{A-}$, YSZ and YSZ-$LSCT_{A-}$ composites with the increasing YSZ concentrations. With the addition of YSZ, the total shrinkage decreases for the unmilled composites. The same trend also applies to the milled composites except the composites with the YSZ contents at the range of 20-40%. For 5% YSZ –added $LSCT_{A-}$, the sintering behaviours of both samples with and without ball milling treatment are very similar up to a same final shrinkage. This means that a YSZ addition below 5% is not able to block the diffusion and growth of $LSCT_{A-}$ grains during heating to high temperature. When the YSZ concentration increased over 5% and below 30%, the ball milled composites show a lower shrinkage than those without. The ball milling treatment may facilitate the uniform dispersion of YSZ grains within the $LSCT_{A-}$ grains, which will have a blocking effect for the bulk densification and grain growth. 30% YSZ composites exhibit a similar shrinkage value, where the YSZ concentration dispersed in the $LSCT_{A-}$ is sufficiently high to form a continuous bulk by diffusion and touching the neighbouring grains rather than the blocking grains along the $LSCT_{A-}$ grain boundary. The percolation of two phases at the high temperature ensures a lower shrinkage at the end. When the YSZ content is over 30%, a higher shrinkage value can be observed on the milled samples. The lower shrinkage for the unmilled composites can be attributed to the existence of the YSZ grain agglomerates, blocking the densification of $LSCT_{A-}$ grains.

### 6.3.3 Impedance analysis

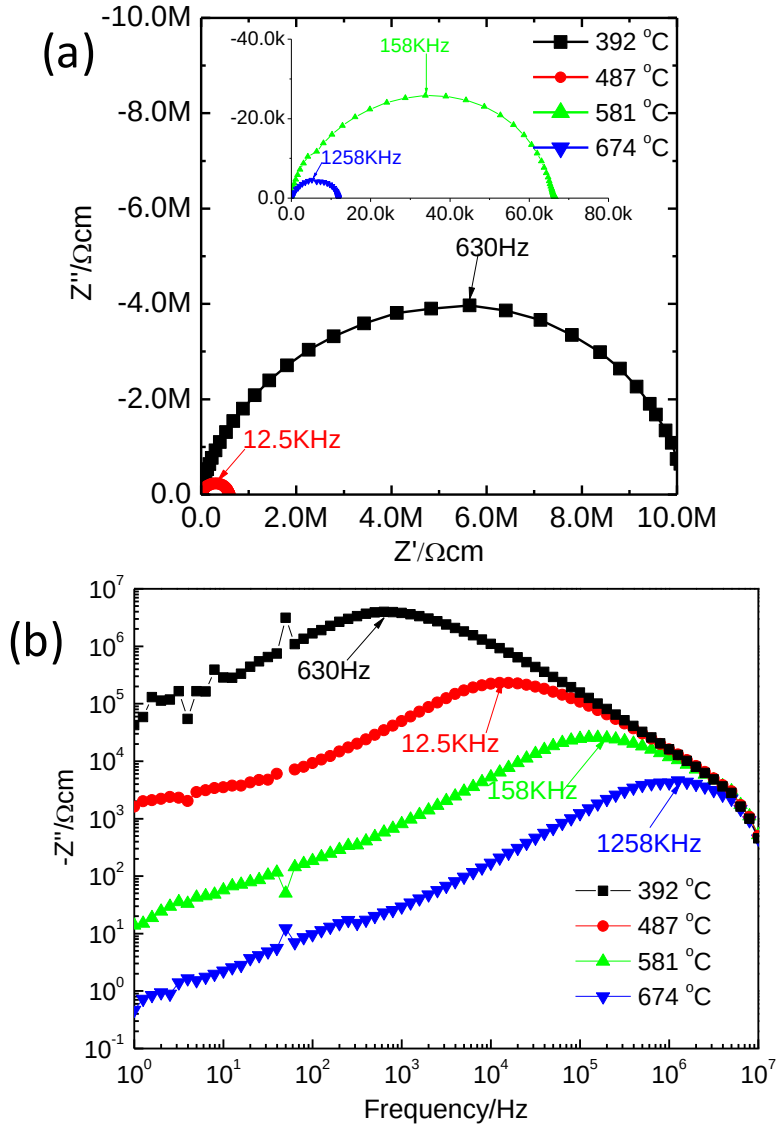


Figure 6.4 (a) Nyquist plot and (b) Bode plot of the complex impedance of pure $LSCT_{A-}$ pellet measured in air at 392-674°C

The Nyquist and Bode plots in Figure 6.4 exhibit that the impedance plots for $LSCT_{A-}$ consist of two overlapping arcs in the range of 392-674°C, which could be modelled by an equivalent circuit based on two parallel RC elements connected in series. It is also noted that the resistance deceases with the increasing temperatures, as expected for an electronic semiconductor. R values can be extracted from the diameters of the arcs and the associated C for each element can be estimated using the following relationship $\omega RC = 1$ at the arc maxima, where $\omega = 2\pi f$ and $f$ is the frequency at the

arc maximum. The associated capacitance values for the impedance spectra at lower frequency and higher frequency are estimated in the range of ~$10^{-9}$ and $10^{-11}$ F/cm respectively. Therefore, the lower frequency arc is consistent with a grain boundary response and the higher frequency arc is associated with a bulk (grain) response. The total resistivity is dominated by a large bulk arc, suggesting that the $LSCT_{A-}$ pellets are well sintered at 1350$^{o}$C leading to a narrow grain boundary.

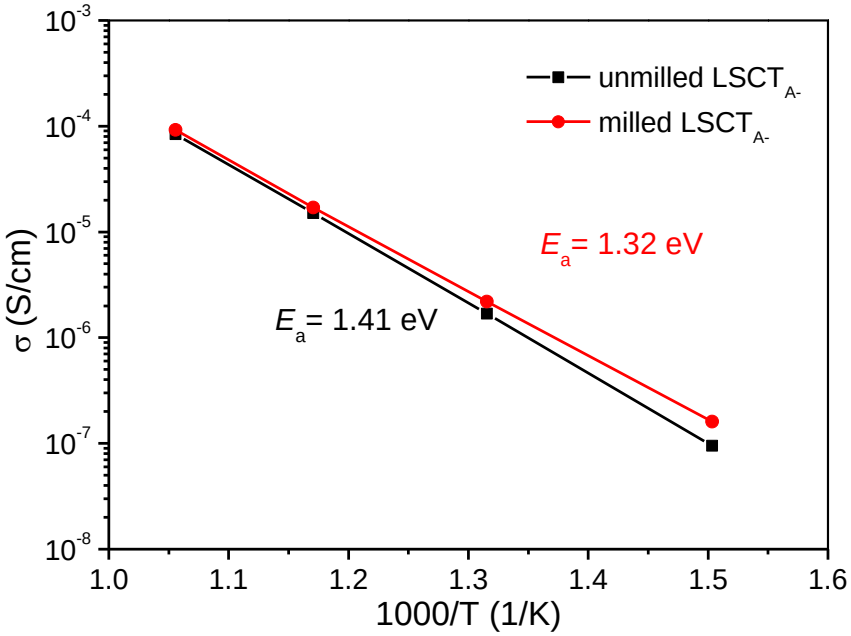


Figure 6.5 Arrhenius plot for the pure $LSCT_{A-}$ specimens without and with ball milling process as a function of temperature

The variations in total conductivity as a function of temperature for both the $LSCT_{A-}$ samples are shown in Figure 6.5. The conductivity for the milled sample is consistently higher than the sample without ball milling throughout the studied temperature range, which can be attributed to the higher relative density. The conductivity shows a linear increase with temperature, implying Arrhenius type behaviour. The straight lines of the Arrhenius conductivity plots enable us to calculate the activation energy values, presented in Figure 6.5, 1.41eV for the unmilled sample and 1.32eV for the milled sample.

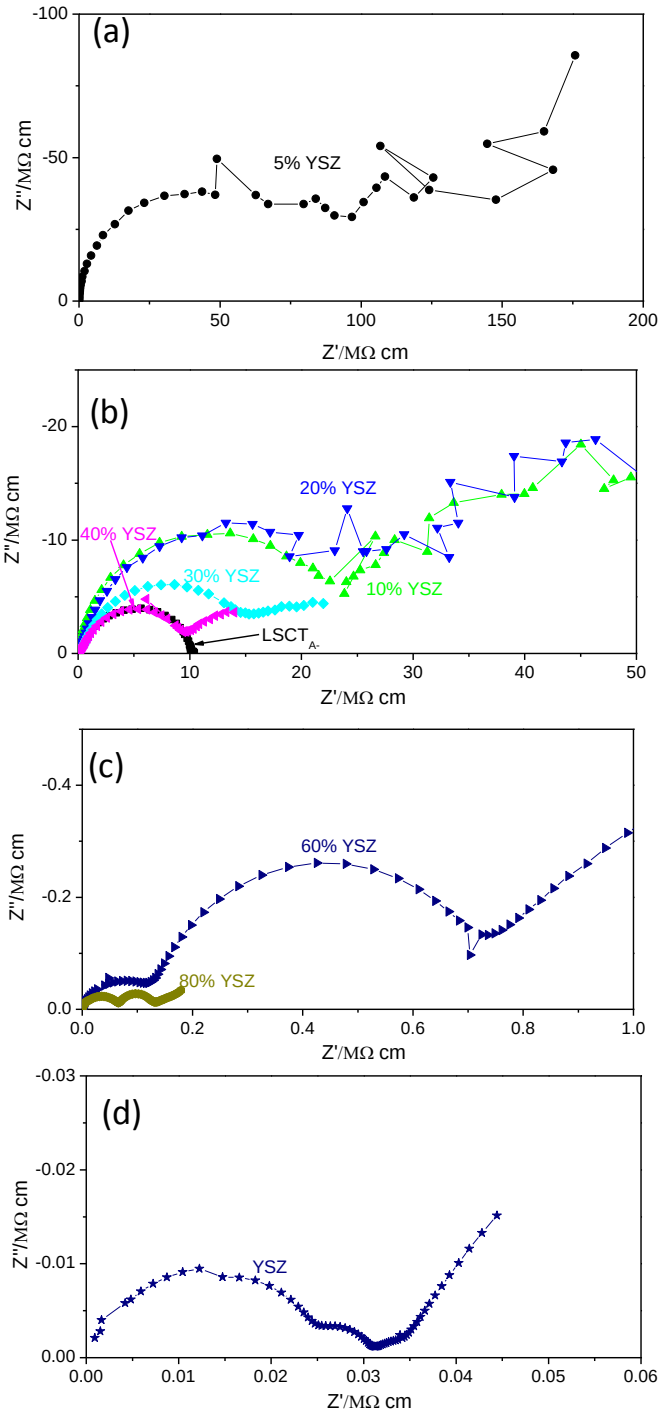


Figure 6.6 Impedance spectra of composite samples without ball milling obtained at 392°C. (a) 5% YSZ, (b) 10-40% YSZ and pure $LSCT_{A-}$, (c) 60-80% YSZ, (d) pure YSZ

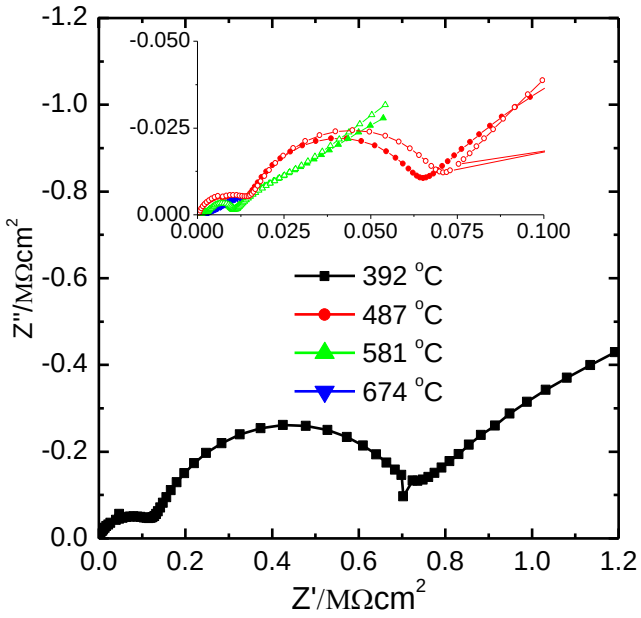


Figure 6.7 Impedance spectra of the 60% YSZ-40% $LSCT_{A-}$ composite sample without ball milling obtained at 392-674$^{o}$C in air

Figure 6.6 shows the impedance spectra of YSZ-$LSCT_{A-}$ composites measured at 392$^{o}$C in air. In general, the spectra show two clearly distinguished semicircles on the high, medium frequency domain, and a tail at the low frequency for YSZ rich composites, while for the YSZ deficient samples, one single semicircle at high frequency and a tail at low frequency are observed. The low-frequency tail is ascribed to the electrode response [281]. No electrode response is observed at the low frequency for $LSCT_{A-}$ sample. This means that the resistance corresponding to the electrode process occurring on the $LSCT_{A-}$/Pt interface can be negligible because the conducting species are electrons. With the YSZ contents between 5 to 40 %, the spectra in Figure 6.6 (a) and (b) show a tail at low frequency, suggesting that the electrode processes change from the $LSCT_{A-}$/Pt interface to YSZ/Pt interface. The charge carriers become the oxygen vacancies of YSZ [281] and the conducting species are oxygen ions. The bulk resistances represented by the semicircle diameter decreases with the increasing YSZ contents.

For the 100% YSZ composition, the capacitances calculated at the two semicircles at the high and medium frequency side are about $5\times10^{-12}$F/cm and $8\times10^{-10}$F/cm, as

expected for the bulk and grain boundary responses. For YSZ-rich samples, shown in Figure 6.6 (c) and (d), the impedance spectra contain two well defined semicircles representing the bulk and grain boundary response at the high and medium frequency range, respectively, and a low-frequency tail corresponding to the electrode process. Because the diameter of one semicircle represents the resistance value, it is clearly shown that the resistivity of the grain is much larger than that of the grain boundary for YSZ sample. Since the resistance of $LSCT_{A-}$ is larger than that of YSZ, the leakage of electrons can be neglected. In addition, the lower sintering temperature for completion of the YSZ densification could lead to a relatively clean boundary without many pores. With the addition of $LSCT_{A-}$ into YSZ (20 and 40% $LSCT_{A-}$) in Figure 6.6 (c), the bulk resistance ($R_b$) and the grain boundary resistance ($R_{gb}$) increases and the ratio of $R_b/R_{gb}$ decreases, judging from the diameter of arcs. At 20% $LSCT_{A-}$, $R_b/R_{gb}$ is about 1. When the $LSCT_{A-}$ content is 40%, $R_{gb}$ is significantly larger than $R_b$. The total resistance ($R_b+R_{gb}$) of 60% YSZ composite is much smaller than that of the 40% YSZ composite, indicating the formation of an interconnected YSZ phase. At high temperature, the high-frequency arc starts to disappear for the 60% YSZ+40% $LSCT_{A-}$ composite, as shown in Figure 6.7. Therefore, 60% YSZ-$LSCT_{A-}$ composite is expected to be the threshold concentration for the percolation.

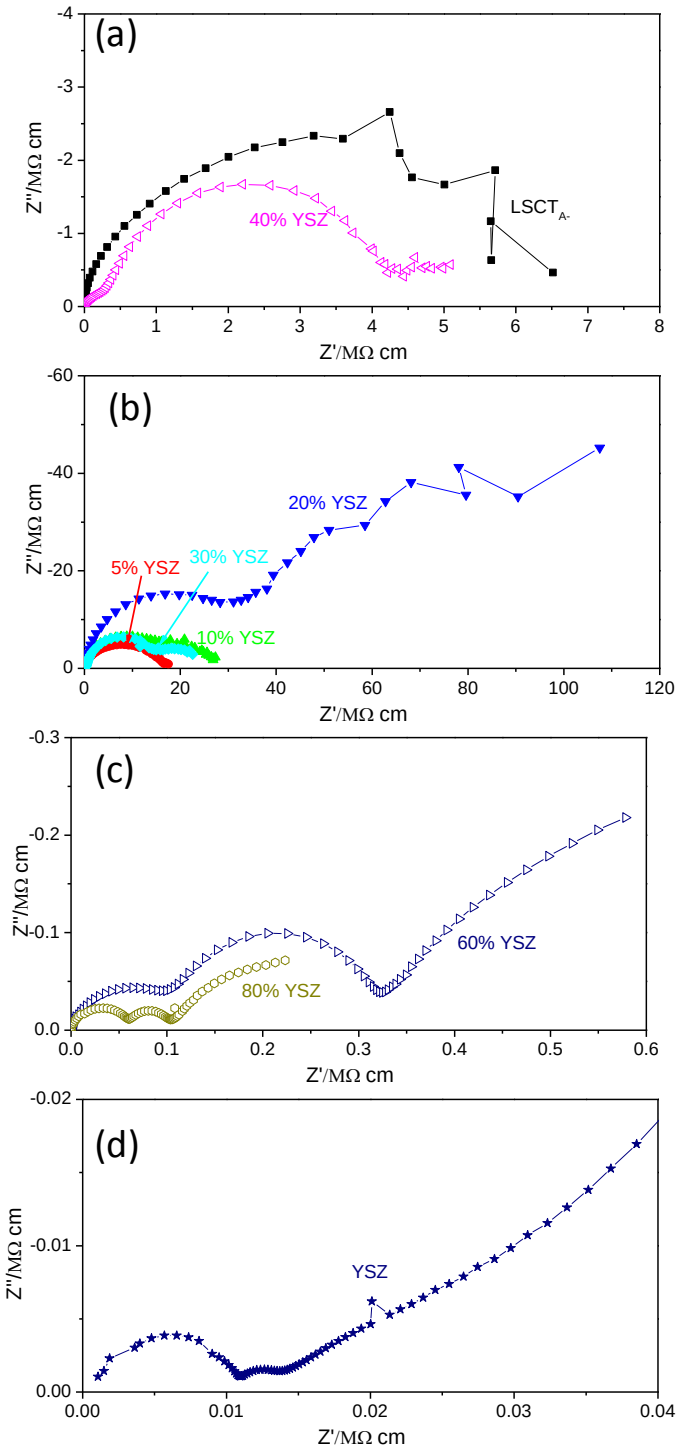


Figure 6.8 Impedance spectra of composite samples with ball milling obtained at 392°C. (a) $LSCT_{A-}$ and 40% YSZ, (b) 5-30% YSZ, (c) 60-80% YSZ, (d) YSZ

Figure 6.8 shows the impedance data for the milled composite specimens measured at 392$^{o}$C in air. Two closely overlapping semicircles at high and low frequency are observed for the composite with YSZ contents between 5-30%, as shown in Figure 6.8(b). The corresponding capacitances are of the order of ~$10^{-11}$ and $10^{-8}$F/cm, and therefore, the resistances can be attributed to the bulk and grain boundary process, respectively. The electrode process is invisible for the 5-30% YSZ added composites, suggesting that the main charge transport is electron in the semiconductor $LSCT_{A-}$. The different behaviour between the same composites but with and without ball milling process can be explained by the fact that the differently distributed YSZ grains within the $LSCT_{A-}$ matrix are not able to form a percolation network for the ionic conduction, but rather form a conduction barrier along the grain boundary of electronic conducting phase. Up to 20% of YSZ addition, the total resistance $R_b$+$R_{gb}$ decreases with the increasing YSZ contents. At 40% YSZ, the grain boundary resistance $R_{gb}$ is significantly larger than the bulk resistance $R_b$, and an electrode process at the low frequency is seen. This indicates that the conduction mechanism starts to change from the pure electronic conduction within the $LSCT_{A-}$ phase to the ionic conduction in the YSZ phase. Compared with the same composite without ball milling technique, the total resistance has been decreased by a factor of 2, pointing out that the ball milling process could help the dispersion of the dual-phase composite and the formation of the individual phase percolation. Moreover, the ball milling process has changed the shape of EIS data: only one semicircle for 40% YSZ composite without ball milling and two semicircles for the same composite after ball milling. When the concentration of YSZ increases above 40%, the total resistance decreases and the ratio of $R_b/R_{gb}$ increases with increasing YSZ content. By contrast, the percolation threshold concentration is not only dependant on the actual concentration but also related to the local arrangement of two phases.

## 6.4 Conclusion

The microstructure, sintering process and electrical properties of YSZ-$LSCT_{A-}$ mixtures over the entire concentration of composites (5-80wt.% YSZ) were studied. The ball milling technique could affect the local arrangement of YSZ particles within the $LSCT_{A-}$ bulk, and result in a different densification for the same composites. The

contribution from bulk and grain boundary resistance varies for the same composites with and without ball milling process, suggesting that the threshold concentration for the percolation of electronic and ionic conducting phase is also dependent on the distribution of YSZ and $LSCT_{A-}$ grains.

# Chapter 7. Ni-YSZ coating prepared by electroless co-deposition process for an SOFC anode

## 7.1 Introduction

Electroless plating, also known as chemical or autocatalytic method, is a non-galvanic plating process involving several chemical reactions simultaneously occurring in an aqueous solution without the use of external electric current [ 282 ]. The film deposition can be accomplished when hydrogen is released from the oxidation of a reducing agent in the solution, such as sodium hypophosphite, which produces an internal current on the substrate surface. A typical electroless plating bath includes a source of metal ions, reducing agents, complexants, accelerators, buffering agent and pH adjustment [283]. Their roles have been summarized in Table 7.1.

Table 7.1 Components and their roles included in the electroless plating bath [283]

| Components | Functions |
|---|---|
| Metal ions | Source of metal ready for deposition |
| Reducing agents | Supply electrons to reduce the metal ions |
| Complexants | Prevent excess of free metal ions concentration |
| Accelerators | Accelerate the reducing agent and increase the deposition |
| Stabilizers | Stabilize the bath from decomposition |
| Buffers | Sustain the pH |
| pH regulators | Adjust pH |

The electroless nickel plating (EN) is the most mature and common electroless plating method. It is capable of producing a uniform surface layer of nickel-phosphorus on a solid substrate by an auto-catalytic electrochemical reaction. Recently, electroless co-

deposition of nickel and ceramic, such as YSZ, has been proposed to manufacture the nickel-YSZ cermet coating on the dense electrolyte for use as an SOFC anode. Compared with other manufacturing techniques used to fabricate effective Ni-YSZ anodes, such as screen printing, vacuum plating spraying, chemical vapour deposition (CVD) etc. [284], electroless co-deposition is a single fabrication method without the requirement for further sintering processes. It can be achieved by an in-situ incorporation of inert ceramic particles in the conventional Ni matrix [285]. Not only does this technique saving energy and time, but also reduces the negative effects of the high-temperature sintering on the cell performance, which could cause the growth of nickel particles and reduce the active surface areas, therefore leading to a lower electrochemical reaction rate.

In 1994, Murphy et al. [286] used electroless deposition for depositing anode and cathode electrocatalysts, demonstrating that a continuous metal film can be deposited at ambient temperature onto a non-conducting surface such as YSZ and that the produced films showed good catalytic activity for SOFC anodic and cathodic reactions. However, operation in a $H_2$-$H_2O$ atmosphere at 700-800$^oC$ causes nickel particles to agglomerate and segregation leading to the loss of electrical conductivity of the anode film and deterioration of the electrode-electrolyte contact. The incorporation of YSZ into the thin Ni matrix may reduce the agglomeration of Ni particles and improve the match of TEC values of anode and electrolyte. More work involving electroless plating has been reported [287~289], demonstrating that Ni coatings was successfully deposited on fine YSZ powder particles. However, Ni-coated YSZ powders require a further fabrication process, such as screen printing, followed by a sintering step to form a complete cell. In this circumstance, the direct incorporation of Ni-YSZ as the effective anode is much more attractive due to the reduced processing required.

In previous work, the electroless Ni-YSZ co-deposition technique has been developed to fabricate a Ni-YSZ cermet coating directly onto a YSZ electrolyte for SOFCs without the final sintering process [290,291]. A uniform but dense Ni-YSZ cermet layer can be observed on an alumina substrate. In order to optimize the

microstructure of the formed Ni-YSZ layer, rice starch as pore former is used to create the porosity for hydrogen diffusion.

Cetyltrimethyl ammonium bromide (CTAB) is known as a cationic surfactant, which has been used to accelerate the Ni-P plating [292,293]. The thickness of the deposited coating is strongly dependant on the concentration of the CTAB. At the concentration of 1.2g/L, the maximum thickness of the film - around 15μm - can be seen. However, the presence of surfactants could reduce the pore size of the Ni-P film because the addition of surfactant could result in finer nickel grains in the deposited layer than the bath without surfactant [293]. There is possible that the combination of pore formers and surfactants could improve the plating of the Ni-YSZ anode and introduce an efficient porosity of sub-micron size. In this chapter such a fabrication technique and the effect of pore formers and surfactants in the plating solution on the microstructure and performance of Ni-YSZ anodes is investigated and discussed.

## 7.2 Experimental

### 7.2.1 Preparation of the half cells

Dense YSZ pellets for use as electrolytes were fabricated by an aqueous tape casting technique that has been described in section 3.2. The dried YSZ tapes were laminated by passing through a hot laminator and cut into an appropriate size. After sintering at 1350$^{o}$C in air for 2h, a dense YSZ pellet of 20mm diameter and 240μm thickness was obtained. The cathode of LSM-YSZ (50:50wt.%) was prepared by screen printing, followed by firing at 1100$^{o}$C to form a 60μm thick layer. The detail related with screen printing has been described in section 2.1.2.

### 7.2.2 Ni-YSZ co-deposition onto half cells

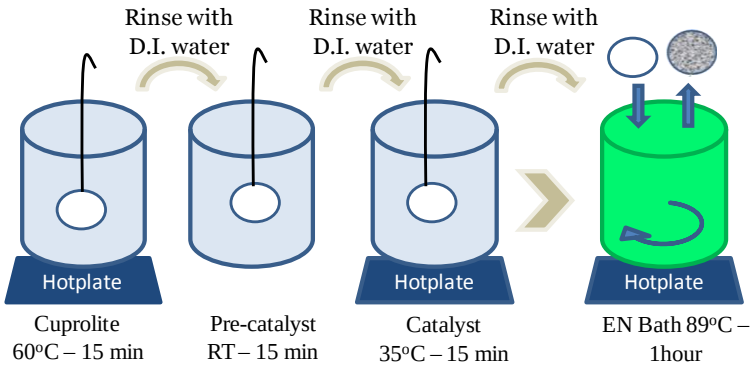


Figure 7.1 Schematic illustration of electroless Ni-YSZ deposition

The produced cathode was protected by high temperature masking tape to avoid the deposition of Ni and YSZ during the plating process. In order to activate the ceramic surfaces, a series of pre-treatment processes was carried out, as shown in Figure 7.1:

1) Cuprolite X-96 DP (2-Aminoe-thanols (1-4%)) (Alfachimici, Italy), was employed on the clean YSZ surface at 60°C for 15 minutes to degrease the surface of the substrate;

2) A stannous chloride solution was used at room temperature (RT) for 15 minutes to sensitise the surface;

3) The substrate was immersed into a solution containing palladium chloride at 35°C for 15 minutes to active the surface.

50g/L of 8mol.% yttria doped zirconia (8YSZ) powder with the nominal particle size of 5μm (Unitec Ceramics Limited, Stanford, England) was added to the electroless nickel solution and kept in suspension through mechanical stirring. The plating operation was carried out by immersing the substrate into the solution heated to a temperature range of 89-92°C for 1 hour using a Jenway hotplate with stirrer. To achieve a porous structure of Ni-YSZ coating as a comparison, 10g/L of rice starch with the particle size range of 1-4μm (Sigma Aldrich, UK) was added to the nickel solution with YSZ powders so that they would co-deposit along with the Ni and the YSZ. The rice starch was chosen because of its low burnout temperature in air. Thermal gravimetric analysis (TGA) of the rice starch was carried out on a Netzsch TG 209 instrument in flowing air to determine its combustion temperature. 1.2g/L

CTAB was also added to the electroless nickel solution to investigate the effects on the microstructure and performance of the produced Ni-YSZ anode.

The plating process is governed by the electrochemical reactions as detailed below [294]:

$$(H_2PO_2)^- + H_2O \xrightarrow{\text{Catalyst\&Heat}} (H_2PO_3)^- + H_2 \quad \text{(Equation 7.1)}$$

$$Ni^{2+} + (H_2PO_2)^- + H_2O \rightarrow Ni + (H_2PO_3)^- + 2H^+ \quad \text{(Equation 7.2)}$$

The overall reaction is

$$Ni^{2+} + 2(H_2PO_2)^- + 2H_2O \rightarrow Ni + 2(H_2PO_3)^- + 2H^+ + H_2 \quad \text{(Equation 7.3)}$$

The reduction of nickel ions yields nickel metal and phosphorus, with the release of hydrogen. Thereafter the nickel metal entraps YSZ particles while being absorbed onto the activated zirconia substrates to form Ni-YSZ film.

### 7.2.3 Characterization of Ni-YSZ coatings

The obtained sample was characterized using a PANalytical X-ray diffractometer with $CuK_{\alpha 1}$ radiation in the range $2\theta$ = 20-100$^o$. The X-ray diffraction (XRD) pattern was analysed using X'pert highscore plus software to determine the crystal structures. The morphology of the cross section of the samples was analyzed by scanning electron microscopy (SEM) using a JEOL 6700 microscope with energy dispersive X-ray analysis (EDX) before and after the electrochemical testing at 700-800$^o$C in humidified hydrogen (3% $H_2O$).

### 7.2.4 Cell performance testing

Silver paste (ESL Europe) was used for the current collection on the anode and cathode side and silver wire (Advent) as the lead for the electrodes. A single cell was sealed onto an alumina tube using ceramic adhesive (Ceramabond 552, Aremco). Humidified hydrogen (3vol.% $H_2O$) was fed into the anode as the fuel at a flow rate of 20ml/min and ambient air was used as the oxidant. The current-voltage curves were measured using a Solartron 1287 Electrochemical Interface and CorrWare v3.2c

software (Scribner Associates) with 4-lead configuration at 700-800$^{o}$C upon heating. The electrochemical impedance test was carried out under a frequency of between 100kHz and 0.04Hz using a combination of Solartron 1255 Frequency Response Analyser, Solartron 1287 Electrochemical Interface and ZPlot v3.2c software (Scribner Associates).

## 7.3 Results and discussion

### 7.3.1 XRD pattern

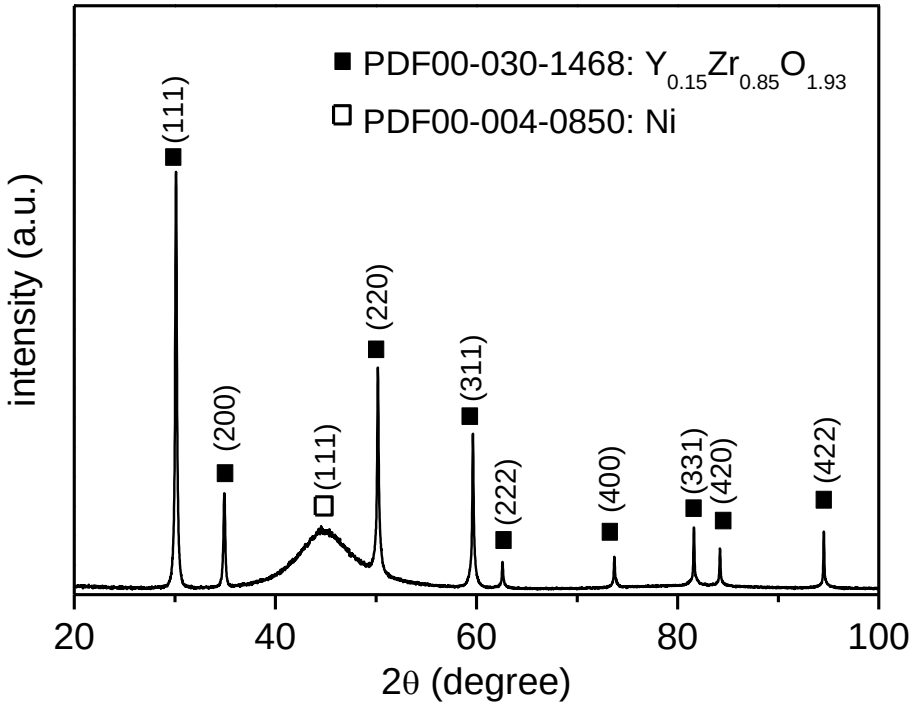


Figure 7.2 XRD pattern of the produced Ni-YSZ coating on the dense YSZ substrate

According to the XRD analysis in Figure 7.2, the obtained Ni-YSZ coating contains two phases: 8YSZ with a cubic crystalline structure and an amorphous Ni phase. It can be observed that a broad peak is located at 45$^{o}$, which is related to the amorphous profile of Ni-P deposits, in agreement with the cases in the Ni-P electroless plating bath [295,296].

### 7.3.2 Ni-YSZ anode without surfactant and pore formers

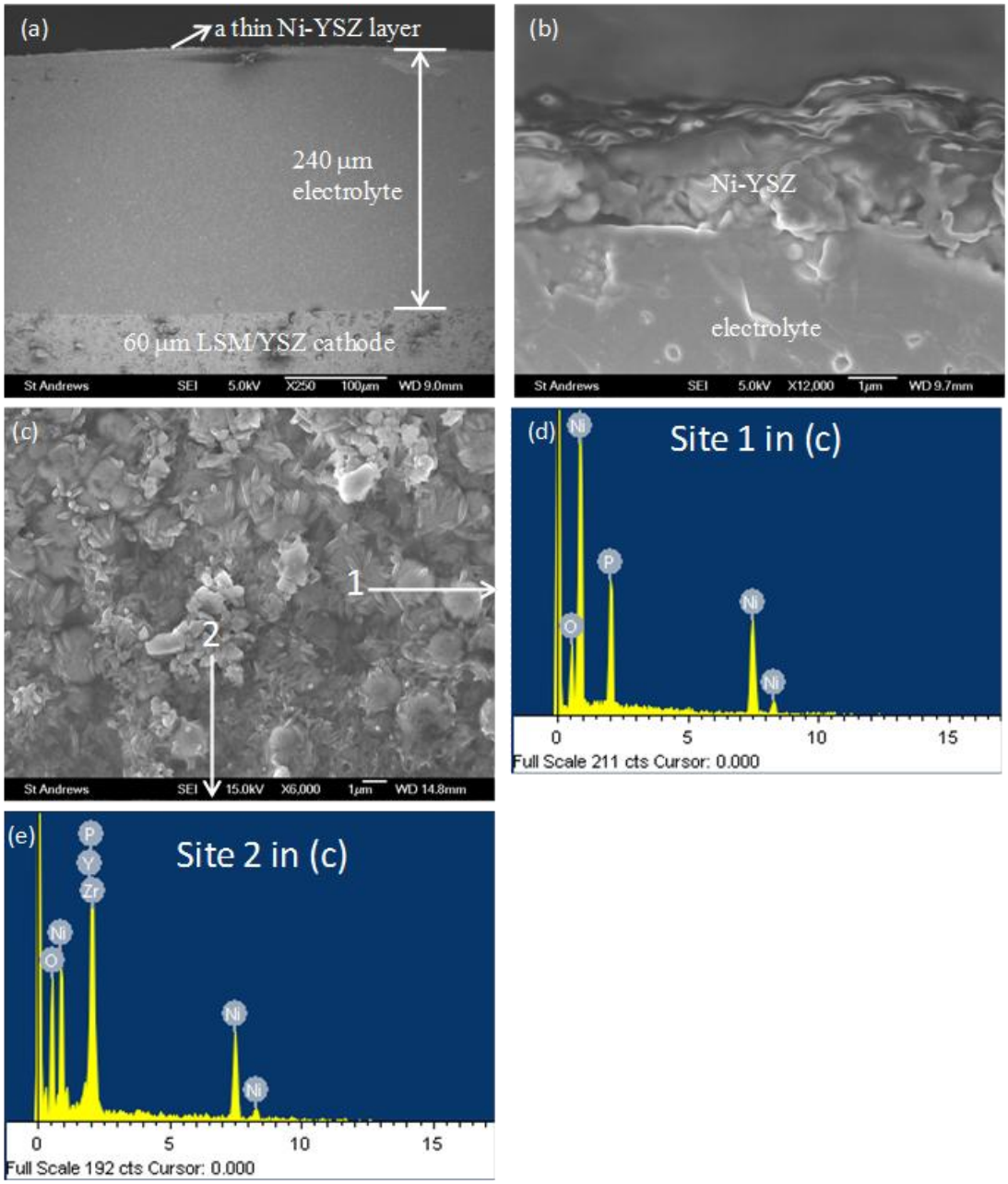


Figure 7.3 SEM images of the cross sections of (a) the produced cell, and (b) the Ni-YSZ coating on the YSZ electrolyte. (c) SEM image of the surface of Ni-YSZ coating. (d) and (e) the EDX results of sites 1 and 2 indicated in (c).

Figure 7.3(a) shows the cross-section of the cell after electroless Ni-YSZ deposition process. The thicknesses of the dense YSZ electrolyte and the porous LSM-YSZ cathode are 240 and 60µm, respectively. A continuous and thin layer of Ni-YSZ

coating has formed on the YSZ surface with an average thickness of 2μm, as shown in Figure 3(b). It also shows a good intimacy between the Ni-YSZ anode and the YSZ electrolyte, while the porosity in the anode seems to be insufficient for the access of the gaseous species. For this technique, the high nickel content is likely to be a concern, which could cause the delamination of the coating during testing as well as insufficient pathways for the ionic and gaseous transport, hence leading to reduced electrochemical performance. However, according to the surface of Ni-YSZ coating in Figure 7.3(c), the YSZ particles of 2μm in diameter are covered and surrounded by the nickel grains. The combination of EDX results (Figure 7.3(d) and (e)) and the SEM image in Figure 7.3(c) shows the formed nickel to have a columnar shape of around 1μm in length and nano-size in diameter.

The YSZ electrolyte-supported button fuel cells with an active area of $0.5cm^2$ were electrochemically characterized at 700-800$^oC$ using humidified $H_2$ (3vol.% $H_2O$) as fuel and ambient air as oxidant, shown in Figure 7.4. In Figure 7.4(a), the open circuit voltages (OCVs) recorded are 1.05, 1.06 and 1.07V at 700, 750 and 800$^oC$, respectively, which is close to the theoretical values calculated from the Nernst equation. The slopes at different current densities for all the I-V curves are varied: at high current densities, the high Area Specific Resistance (ASR) values calculated as the slope of the I-V curves suggests that the mass transport is the limiting factor of the performance, which is in good agreement with the Ni-YSZ anode microstructure before the electrochemical testing. The maximum power densities (Figure 7.4(a)) for the cell are 37, 38 and 43mW $cm^{-2}$ at 700, 750 and 800$^oC$, respectively. The electrochemical impedance spectra measured at OCV from 700 to 800$^oC$ are presented in Figure 7.4(b). The ohmic resistance of the cell ($R_s$), determined from the high-frequency intercepts with the abscissa, is in the range of 1-0.8Ω$cm^2$ at 700-800$^oC$, mainly from the electrolyte support. The cell losses are dominated by the polarization resistance of electrodes ($R_p$), which are represented by the distance between the high and low frequency intercepts of the curves with the abscissa. With the increase in the temperature, the $R_p$ decreases from 30Ω$cm^2$ at 700$^oC$ to 11.5Ω$cm^2$ at 800$^oC$.

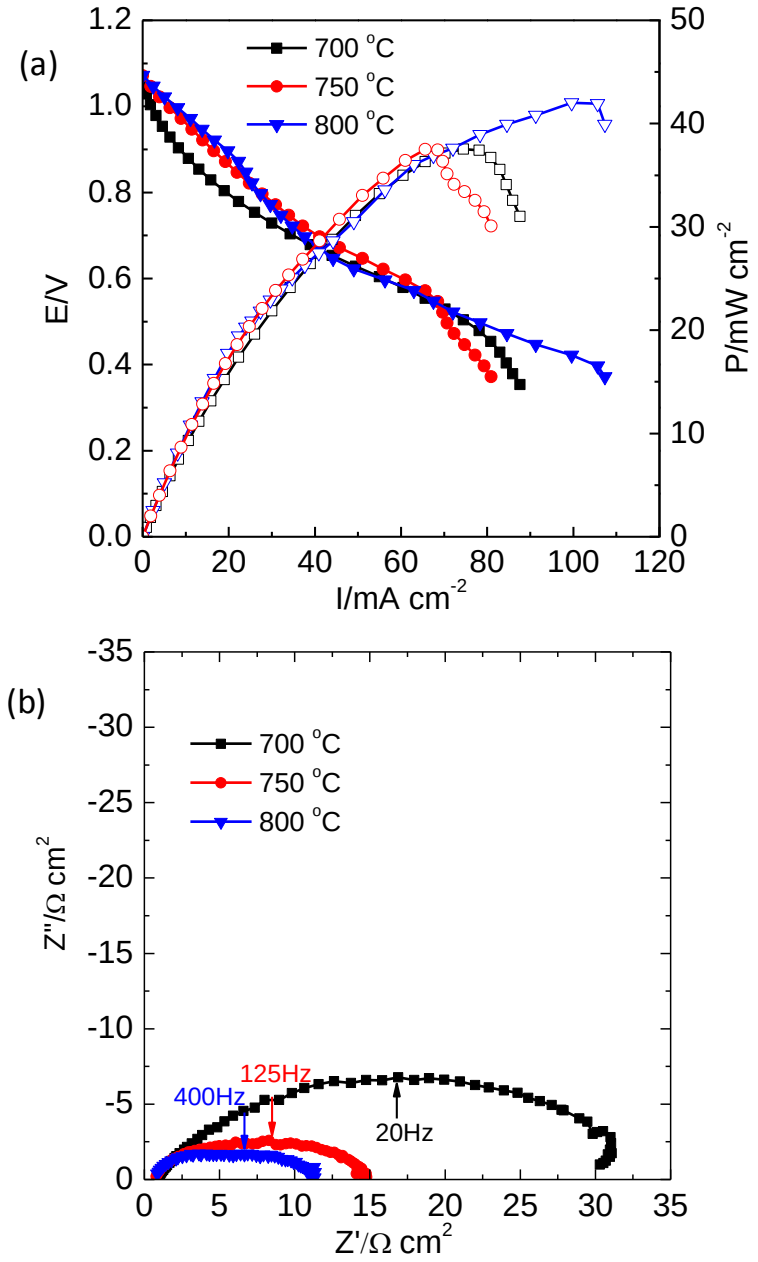


Figure 7.4 (a) I-V curves and (b) impedance curves with co-deposited Ni-YSZ anodes -without starch- tested at 700-800°C

Figure 7.5 shows the microstructure of the Ni-YSZ anodes without pore formers in the bath solution after the stability testing at 800°C. The sample still shows a good intimacy between the anode and the electrolyte, indicating that the TEC mismatch between electroless plated Ni-YSZ anode and YSZ electrolyte during operation is not a concern using this plating technique. The YSZ concentration in the produced coating is high enough to yield a matched TEC value with the YSZ electrolyte. As

confirmed by the I-V curves that the mass transport is the limiting step for the cell performance, a relatively dense microstructure of Ni-YSZ anode can be observed in Figure 7.5(b). The porosity in the anode could lower the gas permeation resulting in the observed performance limitations. Therefore, increasing the porosity in this layer would improve diffusion rate of hydrogen into and water out of the triple phase boundary and enhance the electrochemical performance.

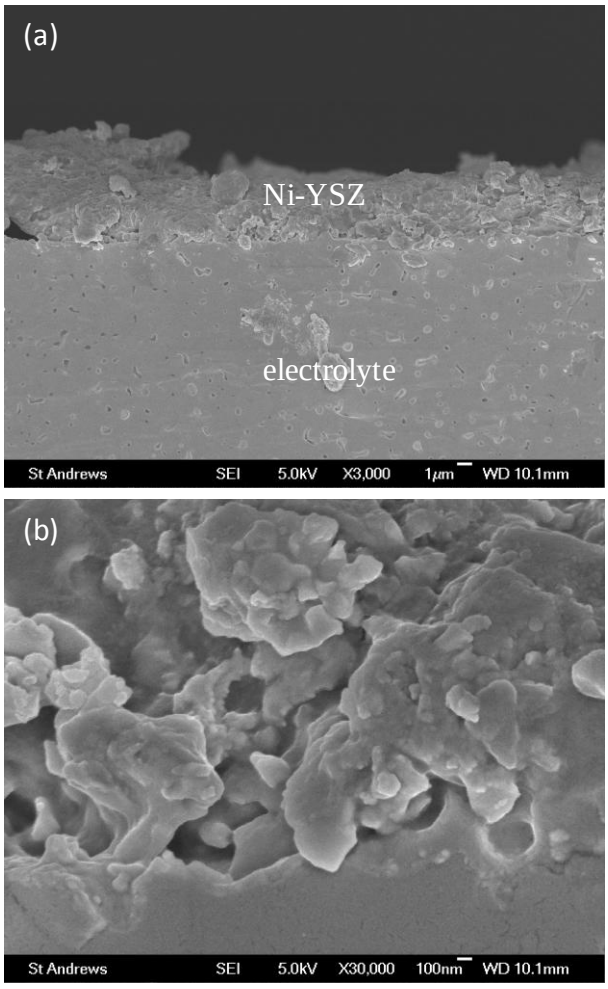


Figure 7.5 SEM images of the cross sections of the Ni-YSZ coating without starch after electrochemical testing at 800$^{o}$C in humidified hydrogen (3% $H_2O$)

### 7.3.3 Effect of pore formers on the Ni-YSZ anode

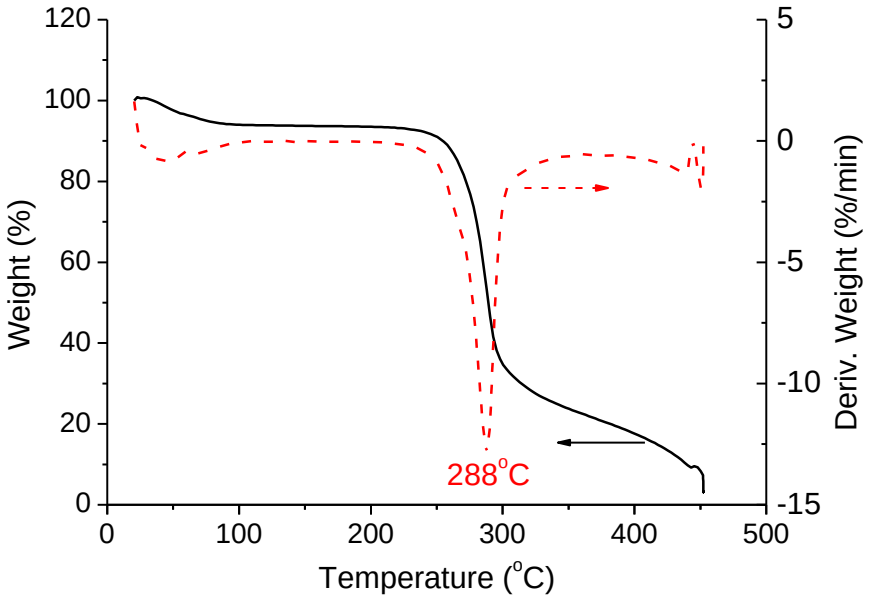


Figure 7.6 TGA and DTG curves of rice starch in air

The Thermal Gravimetric Analysis (TGA) and Derivative Thermogravimetric Analysis (DTG) of rice starch, the pore former in this study, are shown in Figure 7.6. After firing at 450°C in flowing air for 3 hours, only 3.0% residue remains. The combustion process occurs mainly at 250-300°C, when 70% of rice starch has been fired. The combustion temperature corresponding to the maximum rate for mass decrease is 288°C. It is well known that the high-temperature combustion process could accelerate the growth and oxidation of nickel [297], possibly causing the exfoliation of the produced coating through the volumetric change of the Ni/NiO redox cycle. To minimize these effects of the volumetric change, the rice starch was chosen due to the low burnout temperature.

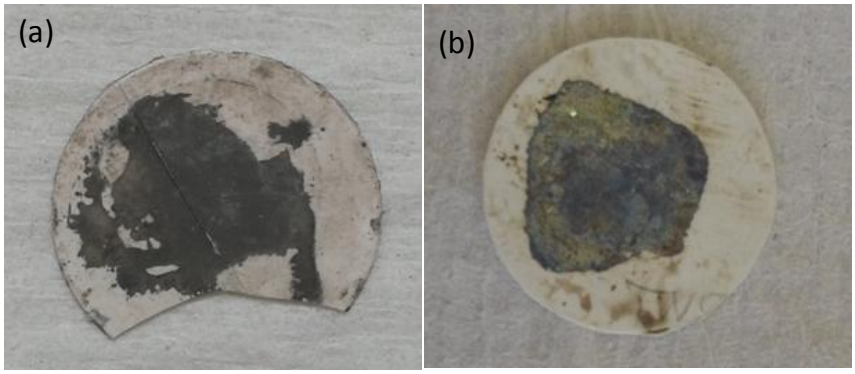


Figure 7.7 Pictures of the electroless plated Ni-YSZ-(starch) coating before and after firing at 450$^{o}$C in air

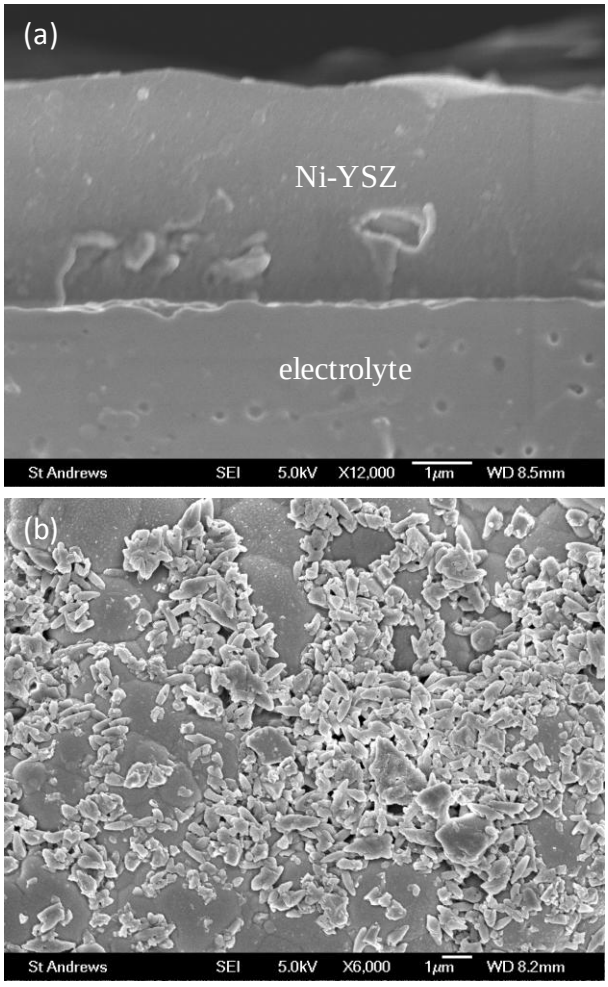


Figure 7.8 SEM images of (a) the cross section and (b) the surface of the Ni-YSZ coating on the YSZ electrolyte after firing at 450$^{o}$C in air for 3h

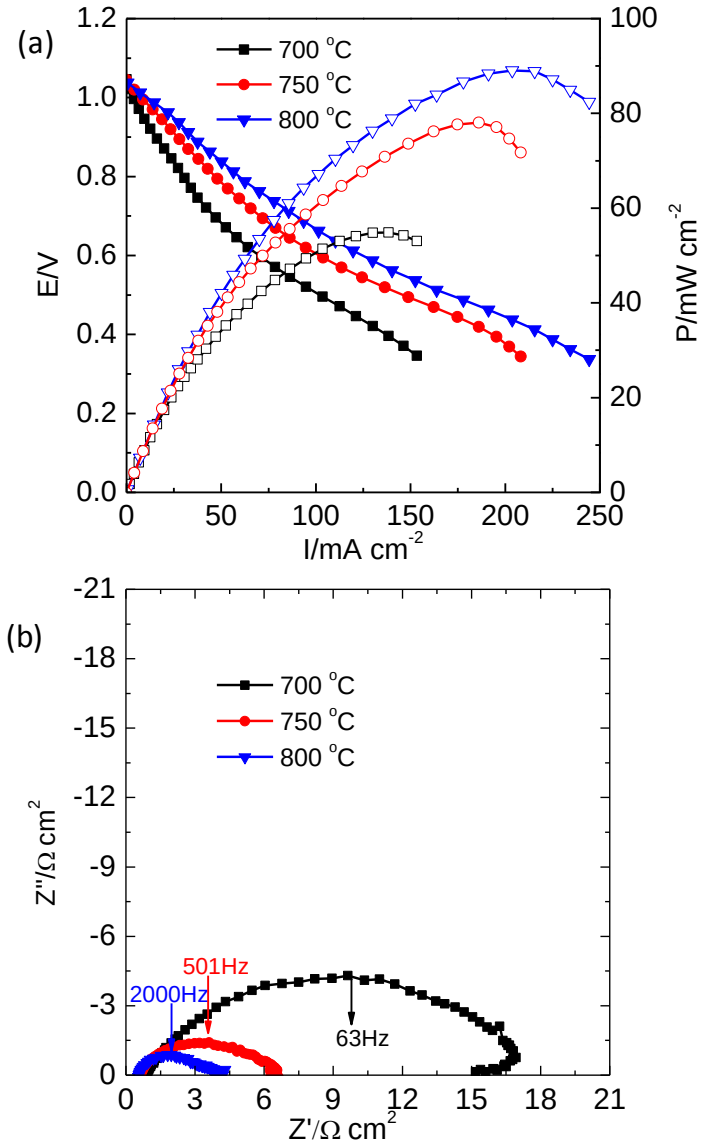


Figure 7.9 (a) I-V curves and (b) impedance curves with plated Ni-YSZ anodes -after burnout of starch- tested at 700-800°C

After the firing at 450°C, the colour of electroless plated Ni-YSZ coating has changed from black to green in Figure 7.7, which is indicative that the metallic nickel is oxidized to during starch combustion step. A relatively dense structure of Ni-YSZ anode with a good adherence on the YSZ electrolyte can be observed, as shown in Figure 7.8(a), which can be attributed to the connectivity and oxidation of nickel at oxidizing atmosphere [298]. This also can be verified from the surface of Ni-YSZ coating in Figure 7.8(b), which shows much larger nickel particles covering the surface compared to the one without this combustion process, as shown in Figure

7.3(c). During the electroless plating, when starch was added to the nickel solution, it started to absorb water leading to gelatinization. Therefore, the starch loading is expected to be very low when considering nickel ions to drag the starch particles.

After the combustion of rice starch in air at 450$^{o}$C, the cell shows an improved performance, around twice the power density of the one without pore formers. As shown in Figure 7.9(a), the peak power densities reach 50, 80 and 90 mWcm$^{-2}$ at 700, 750 and 800$^{o}$C, respectively. In addition, a significant decrease in $R_p$ values can be observed for the Ni-YSZ anode plated with rice starch of between 15 Ωcm$^2$ at 700$^{o}$C and 4.5Ωcm$^2$ at 800$^{o}$C (Figure 7.9(b)). Considering that the polarization resistance of LSM-YSZ on a symmetric cell is likely to be around 9Ωcm$^2$ at 700$^{o}$C [299], the porosity introduced by the combustion of rice starch plays an important role in decreasing the polarization resistance of the anode. The SEM image shows a dense structure on the Ni-YSZ coating, which can be attributed to the formation of NiO during the combination process of pore formers in air. Under the electrochemical testing the reduction of NiO to Ni can create some porosity in the reducing atmosphere, which improves facilitation of the transport of hydrogen into the TPBs.

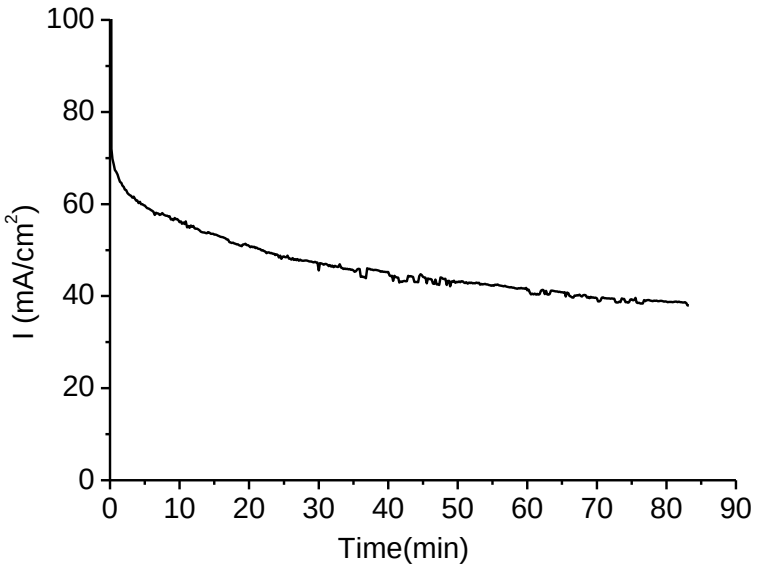


Figure 7.10 Stability testing of plated Ni-YSZ anodes -after the burnout of starch- tested under 0.7V at 800$^{o}$C

The stability testing of the plated Ni-YSZ anode under 0.7 V was tested to examine the adherence between the YSZ electrolyte and Ni-YSZ anode at 800$^{o}$C and is shown in Figure 7.10. During the 90-minute test, the current density drops from 70 to 40mA/cm$^2$, but no sudden decrease of performance can be found, suggesting that no delamination or spalling of the plated Ni-YSZ anode occurs upon the operation.

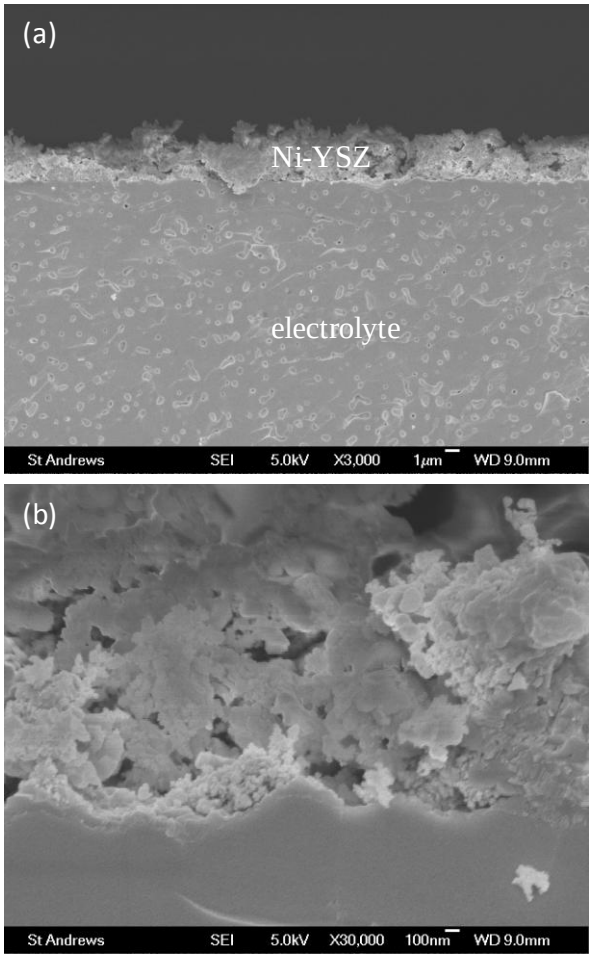


Figure 7.11 SEM images of the cross sections of the Ni-YSZ coating with starch after electrochemical testing at 800$^{o}$C in humidified hydrogen (3% $H_2O$)

Figure 7.11 shows the SEM images of the Ni-YSZ anode after the combustion of starch at 450$^{o}$C in air and electrochemical performance testing at 800$^{o}$C in humidified hydrogen with 3% $H_2O$. No evident delamination is observed between the plated anode and electrolyte. This means that a matched TEC value can be expected with that of YSZ electrolyte. However, the low combustion temperature might be the key factor in keeping the integrity of the fuel cell, as oxidation and sintering of Ni/NiO

would be limited at this low temperature in air. It can be seen that the anode with pore former is much thinner than the one without in Figure 7.5, which can be attributed to the gelatinization of starch in hot water, retarding the deposition rate by increasing the difficulty for Ni ions to get through the ceramic/starch mixture. From the enlarged images of Ni-YSZ without and with starch in the plating bath (Figure 7.5(b) and 7.11(b)), the formation of a more porous structure can be observed for the two cells after testing. However, a significant difference can be distinguished, showing much smaller nickel particles and pores in the anode layer for the cell with pore formers. The connectivity of the fine pores in the anode could be the contributing reason for the improvement of the cell performance.

### 7.3.4 Effect of pore formers and surfactant on the Ni-YSZ anode

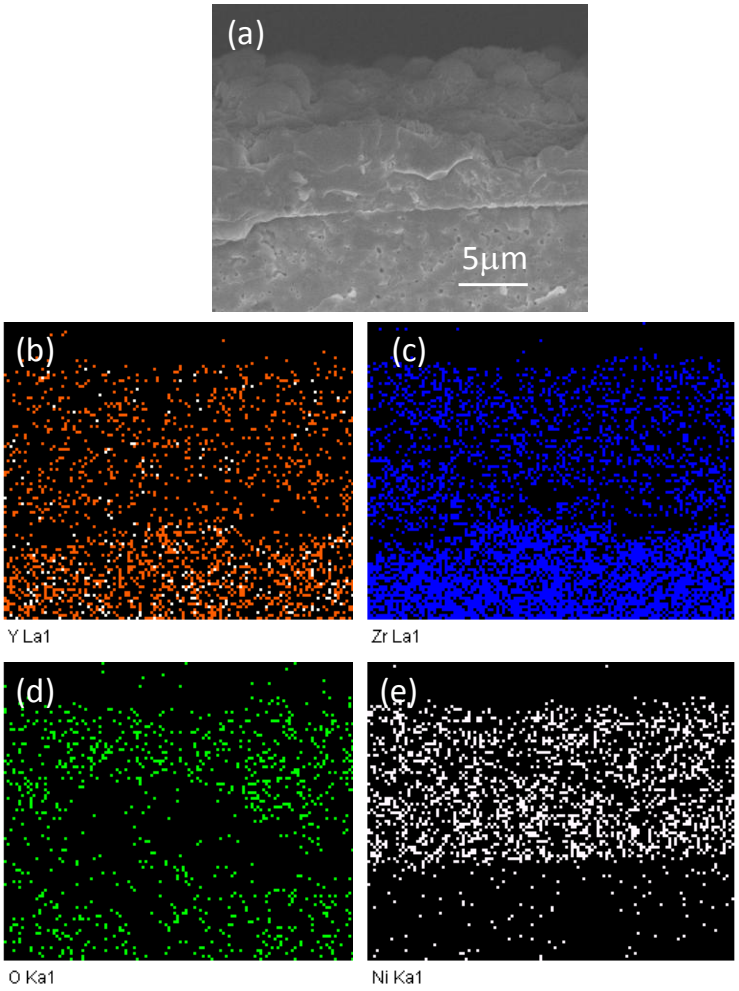


Figure 7.12 SEM image of the cross section of the Ni-YSZ coating on the YSZ electrolyte after firing at 450$^{o}$C in air for 3h

The surfactant (CTAB) and pore former (rice starch) are added into the electroless nickel solution with YSZ to investigate the effect of both on the microstructure and performance of the Ni-YSZ anode. After firing at 450$^{o}$C to burn off the starch, an SEM image is shown in Figure 7.12(a) with the corresponding EDX mapping. The Ni-YSZ coating is around 10μm in thickness and coherent with the YSZ electrolyte. Compared with the cell without CTAB in the solution bath, the addition of CTAB improves the deposition rate of nickel-ceramic film. The reason is possibly due to the formation of nano crystalline structure of nickel grains in the deposited layer with addition of CTAB, which has been reported by Elansezhian et al. [292]. The EDX mapping graphs show that a nickel-rich layer is possibly formed on the electrolyte/anode interface. It could result in a much higher TEC value upon operation than the outer Ni-YSZ layer and YSZ electrolyte, leading to the spalling of the anode and hence the failure of the cell itself.

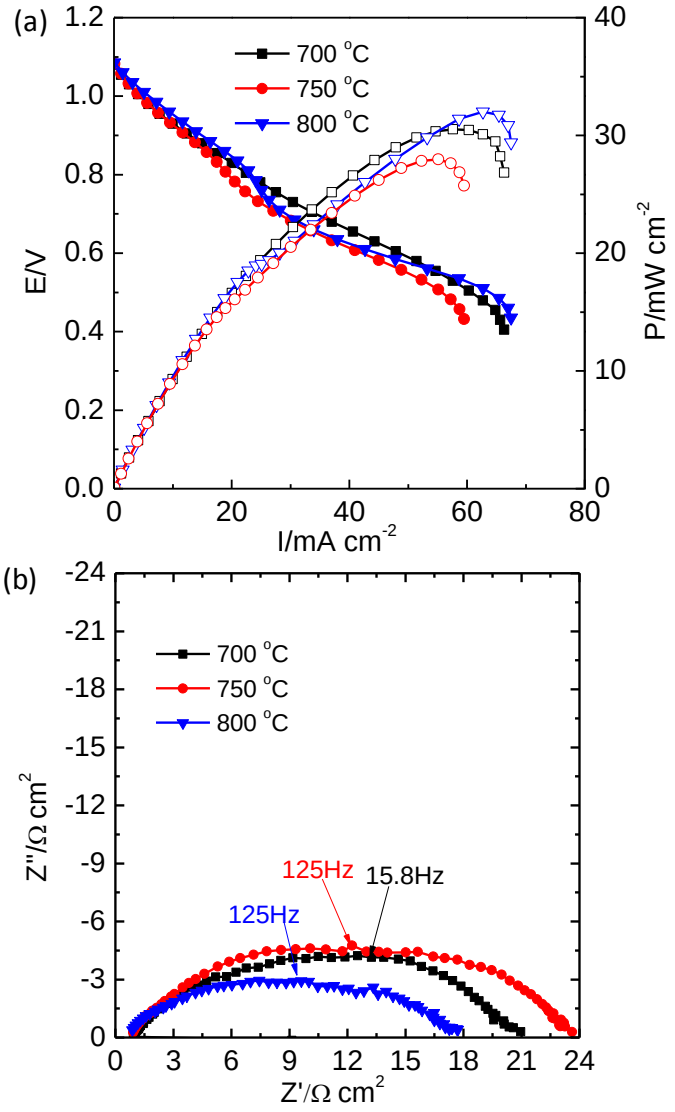


Figure 7.13 (a) I-V curves and (b) impedance curves with plated Ni-YSZ anodes - after burnout of starch- tested at 700-800°C

After the combustion process in air, cell testing was carried out in humidified hydrogen with 3% $H_2O$ at 700-800°C, as shown in Figure 7.13. It shows a reasonable OCV value under the operation condition, implying an airtight YSZ electrolyte. The maximum power densities can be read as 30, 27 and 32mW/cm$^2$ at 700-800°C, lower than those without and with starch only, meaning that CTAB as cationic surfactant could retard the incorporation of starch and ceramic in the Ni-YSZ coating. The anode is not able to provide the sufficient diffusion pathways for hydrogen transport, which is signified by the significant V/I slope at relatively high current densities. Compared

with the Ni-YSZ anode incorporated with starch only, the cell plated with CTAB and starch shows higher polarization resistances at the all testing temperatures, as shown in Figure 7.13(b). After cooling from 800$^{o}$C, the Ni-YSZ anode was observed to have peeled off from the YSZ electrolyte most likely due to the mismatched thermal expansion between Ni-rich layer on the electrolyte/anode interface and YSZ electrolyte.

## 7.4 Conclusion

This study has shown the possibility using an electroless Ni-YSZ co-deposition process with pore formers in the bath solution as a manufacturing technique for the anodes of planar solid oxide fuel cells (SOFCs). Nickel-yttria stabilized zirconia (Ni-YSZ) anodes prepared by this technique show a good intimacy with YSZ electrolyte before and after testing at 800$^{o}$C in humidified hydrogen. The addition of pore formers enhance the peak power density by a factor of two, and can be attributed to the connectivity of the fine pores after the combustion of the rice starch at a low burning-out temperature. When the surfactant CTAB was added to the bath solution, a Ni-rich layer located between on the YSZ electrolyte/Ni-YSZ anode interface is observed. Although CTAB addition improves the Ni-YSZ co-deposition on the YSZ electrolyte, the Ni-rich layer could cause a mismatched thermal expansion with both the outer Ni-YSZ layer and the underneath YSZ electrolyte, therefore leading to the spalling of the entire anode. Additional research will be undertaken to manufacture the anode and the cathode using this technique directly onto the dense YSZ substrate for SOFCs without high-temperature sintering.

# General conclusions

Traditional Ni-YSZ anodes suffer from the problems such as poor redox stability and low tolerance to sulphur poisoning and carbon deposition. A-site deficient $LSCT_{A-}$ ($La_{0.2}Sr_{0.25}Ca_{0.45}TiO_3$), exhibited many characteristics that make it suitable to be used as an anode support for SOFCs operated at intermediate temperature, such as a high electronic conductivity in reducing atmosphere, an excellent chemical stability with the commonly used electrolyte materials (YSZ and GDC) and a good redox stability.

The thermal and electrical properties of the $LSCT_{A-}$ powder was examined, showing a matched thermal expansion value with the commonly used electrolyte materials (YSZ and GDC), and a high conductivity of 5.9S/cm in 5% $H_2$-Ar at 700$^o$C for porous $LSCT_{A-}$ support after high-temperature reduction. The flat and crack-free ceramic cells with anode support were fabricated using both aqueous and organic tape casting techniques by the optimization of particle size distribution of $LSCT_{A-}$ in this study.

The addition of metal catalysts into the anode support was able to improve the cell electrochemical performance in humidified hydrogen (3% $H_2O$) at 700$^o$C. Compared with the $LSCT_{A-}$ bare cell, the maximum power density had been increased at least by a factor of 2 for the Ni-impregnated cell. The substitution of 25mol.% Fe for Ni as catalyst greatly enhanced the electrochemical performance of the cell, achieving a maximum power density of 272mW/cm$^2$. The combined impregnation of ceria and metal could offer more electrochemical reaction sites for hydrogen oxidation and increase the cell performance because the interconnected ceria layer improved the ionic conducting pathways.

Introducing the bimetallic catalysts into the $LSCT_{A-}$ scaffold was able to improve the cell stability under operation, compared to the cells without impregnation and with impregnation of nickel only. The combined addition of ceria and metal could further decrease the degradation rate. The microstructures of the impregnated anodes before and after stability testing show that the agglomeration/growth of catalyst and the chemical interaction between catalysts and backbone are the factors responsible for the performance degradation.

The ball milling process could help the agglomeration breakdown and even distribution of dual-phase composite, YSZ-$LSCT_{A-}$, resulting in a lower shrinkage when YSZ content is below 30% and a higher shrinkage when YSZ content is above 30%, compared with those of the same composite without ball-milling treatment. 60% YSZ-$LSCT_{A-}$ composite without ball milling shows a significantly larger grain boundary resistance than the bulk resistance, which was expected to be the threshold concentration for the individual phase percolation. The ball milling process was able to alter the local arrangement of two phases and decrease the threshold concentration to 40%YSZ-$LSCT_{A-}$ composite.

The electroless co-deposited Ni-YSZ anode showed a low performance in humidified hydrogen (3% $H_2O$) at 700-800$^oC$ due to the low porosity in the anode. The addition of starch in the bath solution could improve the cell performance and optimize the anode microstructure after the electrochemical testing. However, the performance of the electroless plated Ni-YSZ anode was far lower than that of the traditional Ni-YSZ anode made by tape casting or screen printing. More research need to be carried out with respect to increasing the YSZ content and the formation of open pores.

# Suggestions for future work

In this work, anode-supported SOFCs using single phase $LSCT_{A-}$ backbone have show a promising performance after impregnation of ionic conducting ceria and electrocatalytic nickel. This significant improvement suggests that $LSCT_{A-}$ undergoing a high-temperature reduction has sufficient electronic conductivity as anode support, but lacks ionic conductivity and catalytic activity. New experiments using YSZ-$LSCT_{A-}$ composite as anode support would be of interest, where YSZ and $LSCT_{A-}$ provide sufficient oxygen ionic conductivity and electronic conductivity respectively required for SOFC anode. The $LSCT_{A-}$/YSZ ratio in the composite is crucial for the cell performance.

The infiltration of ionic conducting phases and catalytic metals into porous $LSCT_{A-}$ anode scaffolds has been proved to be an effective way to promote the electrode performance for button cells. This method has been employed in the electrolyte-supported fuel cells ($10\times10cm^2$) operating at $900^oC$ [144]. In order to decrease the operating temperature for SOFC and meanwhile retain a low ohmic loss, anode-supported fuel cell is preferred. It would be more practical to apply the infiltration method to the large-scale anode-supported fuel cells from a perspective of industrial application. More studies are needed to optimize the fabrication and infiltration methods for high-performance large-scale cells.

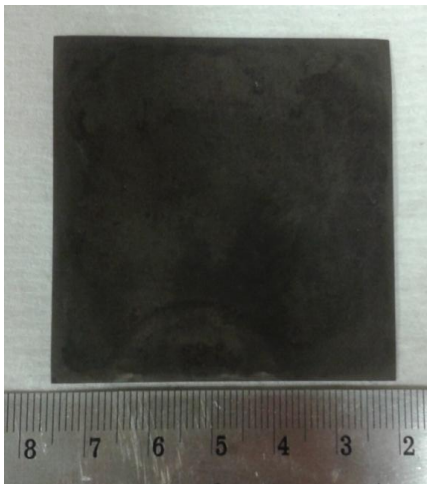


The size of the cell is $5.5\times5.5cm$.

On the top is the ceria and nickel-infiltrated $LSCT_{A-}$ anode support with thickness of 600μm.

Underneath the support is 80μm thick YSZ electrolyte and 60μm thick LSCF-YSZ cathode.

The Chapter 7 has shown that the electroless plating process could be used in manufacturing anodes for planar SOFCs. However, the existing method need to be optimized in order to achieve a fully functional SOFC anode: First, pore former insoluble in hot water with low combustion temperature, such as Poly(methyl methacrylate) (PMMA), is required to create sufficient porosity in the manufactured anode. Second, effective surfactants should be explored to help co-deposition process and increase the YSZ loading. Moreover, coating with a range of YSZ particle size should be investigated to determine if there is a synergistic effect using different sized ceramic.

# References

[1] http://www.fuelcelltoday.com/about-fuel-cells/history 2014 [cited 2014 February]

[2] M. L. Cooper, and V. M. D. Hall, William Robert Grove and the London Institution, 1841-1845, *Ann. Sci.*, **39** (3) : 229-254 (1982)

[3] W. R. Groves, On voltaic series and the combination of gases by platinum, *Philos. Mag.*, **14** (86): 127-130 (1839)

[4] O. Yamamoto, Solid oxide fuel cells: fundamental aspects and prospects, *Electrochim. Acta*, **45**: 2423-2435 (2000)

[5] A. Psoma, and G. Sattler, Fuel cell systems for submarines: from the first idea to serial production, *J. Power Sources*, **106** (1-2): 381-383 (2002)

[6] S. M. Haile, Materials for fuel cells, *Mater. Today*, **6** (3): 24-29 (2003)

[7] http://www1.eere.energy.gov/hydrogenandfuelcells/fuelcells/fc_types.html. 2011 [cited 2014 February]

[8] S. B. Adle, Factors governing oxygen reduction in solid oxide fuel cell cathodes, *Chem. Rev.*, **104** (10): 4791-4844 (2004)

[9] M. K. Stodolny, Cr-tolerance of the IT-SOFC La(Ni,Fe)$O_3$ material, PhD thesis, 2012

[10] http://www.doitpoms.ac.uk/tlplib/fuel-cells/printall.php. [cited 2014 February]

[11] S. C. Singhal, Solid oxide fuel cells: an overview, *Prepr. Pap.-Am. Chem. Soc., Div. Fuel Chem.*, **49** (2): 478-479 (2004)

[12] http://www.aki.che.tohoku.ac.jp/~koyama/html/research/SOFC.html. [cited 2014 February]

[13] N. Laosiripojana, W. Wiyaratn, W. kiatkittipong, A. Soottitantawat, and S. Assaburmrungrat, Reviews on solid oxide fuel cell technology, *Eng. J.-Canada*, **13** (1): 1-19 (2009)

[14] EG&G technical Services, Inc., Fuel cell handbook (seventh edition), U.S. department of Energy, 2004

[15] E. D. Wachsman, and K. T. Lee, Lowering the temperature of solid oxide fuel cells, *Science*, **334** (6058): 935-939 (2011)

[16] J. C. Ruiz-Morales, D. Marrero-Lopez, M. G. Sanchez, J. C. Vazquez, C. Savaniu, and S. N. Savvin, Engineering of materials for solid oxide fuel cells and other energy and environmental applications, *Energy Environ. Sci.*, **3** (11): 1670-1681 (2010)

[17] W. D. He, K. J. Yoon, R. S. Eriksen, S. Gopalan, S. N. Basu, and U. B. Pal, Out-of-cell measurements of $H_2$-$H_2O$ effective binary diffusivity in the porous anode of solid oxide fuel cells (SOFCs), *J. Power Sources*, **195** (2): 532-535 (2010)

[18] F. Zhao, T. J. Armstrong, and A. V. Virkar, Measurement of $O_2$-$N_2$ effective diffusivity in porous media at high temperatures using an electrochemical cell, *J. Electrochem. Soc.*, **150** (3): A249-A256 (2003)

[19] M. C. Tucker, Progress in metal-supported solid oxide fuel cells: a review, *J. Power Sources*, **195**: 4570-4582 (2010)

[20] N. P. Bradon, A. Blake, D. Cumming, A. Duckett, K. EI-Koury, D. Haigh, C. kidd, R. Leah, G. Lewis, C. Matthews, N. Maynard, N. Oishi, T. Mccolm, R. Trezona, A. Selcuk, M. Schmidt, and L. Verdugo, Development of metal supported solid oxide fuel cells for operation at 500-600$^o$C, *J. Fuel Cell Sci. Tech.*, **1**: 61-65 (2004)

[21] B. J. McKenna, N. Christiansen, R. Schauperl, P. Prenninger, J. Nielsen, P. Blennow, T. Klemensϕ, S. Ramousse, A. Kromp, and A. Weber, Advances in metal supported cells in the METSOFC EU consortium, *Fuel cells*, **13** (4): 592-597 (2013)

[22] R. T. Leah, N. P. Brandon, and P. Aguiar, Modelling of cells, stacks and systems based around metal-supported planar IT-SOFC cells with CGO electrolytes operating at 500-600$^o$C, *J. Power Sources*, **145** (2): 336-352 (2005)

[23] S. C. Singhal, Advances in solid oxide fuel cell technology, *Solid State Ionics*, **135**: 305-313 (2000)

[24] V. V. Kharton, F. M. B. Marques, and A. Atkinson, Transport properties of solid oxide electrolyte ceramics: a brief review, *Solid State Ionics*, **174**: 135-149 (2004)

[25] J. W. Fergus, Electrolytes for solid oxide fuel cells, *J. Power Sources*, **162**: 30-40 (2006)

[26] C. Clausen, C. Bagger, J. B. Bilde-Sørensen, and A. Horsewell, Microstructural and microchemical characterization of the interface between $La_{0.85}Sr_{0.15}MnO_3$ and $Y_2O_3$-stabilized $ZrO_2$, *Solid State Ionics*, **70-71** (1): 59-64 (1994)

[27] J. A. M. van Roosmalen, and E. H. P. Cordfunke, Chemical reactivity and interdiffusion of (La, Sr)$MnO_3$ and (Zr, Y)$O_2$ solid oxide fuel cell cathode and electrolyte materials, *Solid State Ionics*, **52** (4): 303-312 (1992)

[28] K. Kleveland, M. A. Einarsrud, C. R. Schmidt, S. Shamsili, S. Faaland, K. Wiik, and T. Grande, Reactions between strontium-substituted lanthanum manganite and yttria-stabilized zirconia: II, diffusion couples, *J. Am. Ceram. Soc.*, **82** (3): 729-734 (1999)

[29] C. Levy, Y. Zhong, C. Morel, and S. Marlin, Thermodynamic stabilities of $La_2Zr_2O_7$ and $SrZrO_3$ in SOFC and their relationship with LSM synthesis processes, *J. Electrochem. Soc.*, **157** (11): B1597-B1601 (2010)

[30] C. Levy, Y. Zhong, C. Morel, and S. Marlin, Fused LSM: a novel powder limiting the formation of $La_2Zr_2O_7$ and $SrZrO_3$ resistive phases at the interface with YSZ in SOFC cathodes, *ECS Trans.*, **25** (2): 2815-2823 (2009)

[31] M. Chen, Y. L. Liu, A. Hagen, P. V. Hendriksen, and F. W. Poulsen, LSM-YSZ reactions in different atmospheres, *Fuel cells*, **9** (6): 833-840 (2009)

[32] M. J. Heneka, and E. Ivers-Tiffée, Influence of high current cycling on the performance of SOFC single cells, *J. Fuel Cell Sci. Tech.*, **9** (1): 0110011-0110016 (2011)

[33] B. C. H. Steele, Appraisal of $Ce_{1-y}Gd_yO_{2-y/2}$ electrolytes for IT-SOFC operation at 500°C, *Solid State Ionics*, **129**: 95-110 (2000)

[34] T. Ishihara, H. Matsuda, and Y. Takita, Doped $LaGaO_3$ perovskite type oxide as a new oxide ionic conductor, *J. Am. Chem. Soc.*, **116**: 3801-3803 (1994)

[35] H. Uchida, S. Arisaka, and M. Watanabe, High performance electrode for medium-temperature solid oxide fuel cells $La(Sr)CoO_3$ cathode with ceria interlayer on zirconia electrolyte, *Electrochem. Solid-State Lett.*, **2** (9): 428-430 (1999)

[36] Y. Tao, J. Shao, W. G. Wang, and J. Wang, Optimisation and evaluation of $La_{0.6}Sr_{0.4}CoO_{3-\delta}$ cathodes for intermediate temperature solid oxide fuel cells, *Fuel cells*, **9** (5): 679-683 (2009)

[37] M. Shiono, K. Kobayashi, T. L. Nguyen, K. Hosoda, T. Kato, K. Ota, and M. Dokiya, Effect of $CeO_2$ interlayer on $ZrO_2$ electrolyte/$La(Sr)CoO_3$ cathode for low-temperature SOFCs, *Solid State Ionics*, **170**: 1-7 (2004)

[38] B. Dalslet, P. Blennow, P. V. Hendriksen, N. Bonanos, D. Lybye, and M. Mogensen, Assessment of doped ceria as electrolyte, *J. Solid-State Electrochem.*, **10**: 547-561 (2006)

[39] J. M. Ralph, A. C. Schoeler, and M. Krumpelt, Materials for lower temperature solid oxide fuel cells, *J. Mater. Sci.*, **36**: 1161-1172 (2001)

[40] T. N. Lin, M. C. Lee, R. J. Yang, J. C. Chang, W. X. Kao, and L. S. Lee, Chemical state identification of $Ce^{3+}/Ce^{4+}$ in the $Sm_{0.2}Ce_{0.8}O_{2-\delta}$ electrolyte for an anode-supported solid oxide fuel cell after long-term operation, *Mater. Lett.*, **81**: 185-188 (2012)

[41] I. R. Gibson, and J. T. S. Irvine, Study of the order-disorder transition in yttria-stabilised zirconia by neutron diffraction, *J. Mater. Chem.*, **6** (5): 895-898 (1996)

[42] B. C. H. Steele, Oxygen ion conductors, pp.402-446, in High conductivity solid ionic conductors, Edited by T. Takahashi, World Scientific Publishing, 1989

[43] P. Huang, and A. Petric, Superior oxygen ion conductivity of lanthanum gallate doped with strontium and magnesium, *J. Electrochem. Soc.*, **143** (5): 1644-1648 (1996)

[44] M. L. Faro, D. L. Rosa, V. Antonucci, and A. S. Aricó, Intermediate temperature solid oxide fuel cell electrolytes, *J. Indian Inst. Sci.*, **89** (4): 363-380 (2009)

[45] C. Sun, R. Hu, and J. Roller, Cathode materials for solid oxide fuel cells: a review. J. *Solid-State Electrochem.*, **14**: 1125-1144 (2010)

[46] T. Tsai, and S. A. Barnett, Effect of LSM-YSZ cathode on thin-electrolyte solid oxide fuel cell performance, *Solid State Ionics*, **93**: 207-217 (1997)

[47] E. P. Murray, and S. A. Barnett, $(La,Sr)MnO_3$-$(Ce,Gd)O_{2-x}$ composite cathodes for solid oxide fuel cells, *Solid State Ionics*, **143**: 265-273 (2001)

[48] M. J. L. Østergård, C. Clausen, C. Bagger, and M. Mogensen, Manganite-zirconia composite cathodes for SOFC: influence of structure and composition, *Electrochim. Acta*, **40** (12): 1971-1981 (1995)

[49] J. Piao, K. Sun, N. Zhang, and S. Xu, A study of process parameters of LSM and LSM-YSZ composite cathode films prepared by screen printing, *J. Power Sources*, **175**: 288-295 (2008)

[50] Y. Huang, J. M. Vohs, and R. J. Gorte, SOFC cathodes prepared by infiltration with various LSM precursors, *Electrochem. Solid-State Lett.*, **9** (5): A237-A240 (2006)

[51] J. S. Cronin, K. Muangnapoh, Z. Patterson, K. Yakal-Kremski, and S. A. Barnett, Firing temperature effect on 3D microstructure and performance of LSM-YSZ composite SOFC cathodes, *ECS Trans.*, **35** (1): 2369-2378 (2011)

[52] J. H. Choi, J. H. Jang, and S. M. Oh, Microstructure and cathodic performance of $La_{0.9}Sr_{0.1}MnO_3$/yttria-stabilized zirconia composite electrodes, *Electrochim. Acta*, **46**: 867-874 (2001)

[53] T. Z. Sholklapper, C. Lu, C. P. Jacobson, S. J. Visco, and L. C. De Jonghe, LSM-infiltrated solid oxide fuel cell cathodes, *Electrochem. Solid-State Lett.*, **9** (8): A376-A378 (2008)

[54] H. He, Y. Huang, J. Regal, M. Boaro, J. M. Vohs, and R. J. Gorte, Low-temperature fabrication of oxide composites for solid-oxide fuel cells, *J. Am. Ceram. Soc.*, **87** (3): 331-336 (2004)

[55] T. Z. Sholklapper, H. Kurokawa, C. P. Jacobson, S. J. Visco, and L. C. De Jonghe, Nanostructured solid oxide fuel cell electrodes, *Nano Lett.*, **7** (7): 2136-2141 (2007)

[56] Z. Jiang, Z. Lei, B. Ding, C. Xia, F. Zhao, and F. Chen, Electrochemical characterization of solid oxide fuel cell cathodes prepared by infiltrating $(La,Sr)MnO_3$ nanoparticles into yttria-stabilized bismuth oxide backbone, *Int. J. Hydrogen Energy*, **35**: 8322-8330 (2010)

[57] F. Zhao, R. Peng, and C. Xia, LSC-based electrode with high duarability for IT-SOFCs, *Fuel Cell Bull.*, **2**: 12-16 (2008)

[58] A. Egger, E. Bucher, M. Yang, and W. Sitte, Comparison of oxygen exchange kinetics of the IT-SOFC cathode materials $La_{0.5}Sr_{0.5}CoO_{3-\delta}$ and $La_{0.6}Sr_{0.4}CoO_{3-\delta}$, *Solid State Ionics*, **225**: 55-60 (2012)

[59] W. Wang, M. D. Gross, J. M. Vohs, and R. J. Gorte, The stability of LSF-YSZ electrodes prepared by infiltration, *J. Electrochem. Soc.*, **154** (5): B439-B445 (2007)

[60] S. P. Simner, J. F. Bonnett, N. L. Canfield, K. D. Meinhardt, J. P. Shelton, V. L. Sprenkle, and J. W. Stevenson, Development of lanthanum ferrite SOFC cathodes, *J. Power Sources*, **113**: 1-10 (2003)

[61] S. P. Simner, J. F. Bonnett, N. L. Canfield, K. D. Meinhardt, V. L. Sprenkle, and J. W. Stevenson, Optimized lanthanum ferrite-based cathodes for anode-supported SOFCs, *Electrochem. Solid-State Lett.*, **5** (7): A173-A175 (2002)

[62] B. C. H. Steele, Materials for IT-SOFC stacks 35 years R&D: the inevitability of gradualness, *Solid State Ionics*, **134**: 3-20 (2000)

[63] A. Mai, V. A. C. Haanappel, S. Uhlenbruck, F. Tietz, and D. Stöver, Ferrite-based perovskites as cathode materials for anode-supported solid oxide fuel cells Part I. Variation of composition, *Solid State Ionics*, **176**: 1341-1350 (2005)

[64] A. Mai, V. A. C. Haanappel, F. Tietz, and D. Stöver, Ferrite-based perovskites as cathode materials for anode-supported solid oxide fuel cells Part II. Influence of the CGO interlayer, *Solid State Ionics*, **177**: 2103-2107 (2006)

[65] J. Mizusaki, J. Tabuchi, T. Matsuura, S. Yamauchi, and K. Fueki, Electrical conductivity and seebeck coefficient of nonstoichiometric $La_{1-x}Sr_xCoO_{3-\delta}$, *J. Electrochem. Soc.*, **136** (7): 2082-2088 (1989)

[66] N. Teraoka, H. M. Zhang, K. Okanoto, and N. Yamazoe, Mixed ionic-electronic conductivity of $La_{1-x}Sr_xCo_{1-y}FeyO_{3-\delta}$ perovskite-type oxides, *Mater. Res. Bull.*, **23** (1): 51-58 (1988)

[67] H. Ullmann, N. Trofimenko, F. Tietz, D. Stöver, and A. Ahmad-Khanlou, Correlation between thermal expansion and oxide ion transport in mixed conducting perovskite-type oxides for SOFC cathodes, *Solid State Ionics*, **138**: 79-90 (2000)

[68] A. Fossdal, M. Menon, I. Wernhus, K. Wiik, M. A. Einarsrud, and T. Grande, Crystal structure and thermal expansion of $La_{1-x}Sr_xFeO_{3-\delta}$ materials, *J. Am. Ceram. Soc.*, **87** (10): 1952-1958 (2004)

[69] L. Lu, Y. Guo, H. Zhang, and J. Jin, Electrochemical performance of $La_2NiO_{4+\delta}$-$La_{0.6}Sr_{0.4}Co_{0.2}Fe_{0.8}O_{3-\delta}$ composite cathodes for intermediate temperature solid oxide fuel cells, *Mater. Res. Bull.*, **45**: 1135-1140 (2010)

[70] S. Hashimoto, Y. Fukuda, M. Kuhn, K. Sato, K. Yashiro, and J. Mizusaki, Thermal and chemical lattice expansibility of $La_{0.6}Sr_{0.4}Co_{1-y}Fe_yO_{3-\delta}$ (y=0.2, 0.4, 0.6 and 0.8), *Solid State Ionics*, **186**: 37-43 (2011)

[71] F. Zhao, R. Peng, and C. Xia, A $La_{0.6}Sr_{0.4}CoO_{3-\delta}$-based electrode with high durability for intermediate temperature solid oxide fuel cells, *Mater. Res. Bull.*, **43**: 370-376 (2008)

[72] N. Q. Minh, and T. Takahashi, Science and Technology of Ceramic Fuel Cell, Elsevier, Amsterdam, 117-118 (1995)

[73] F. M. Figueiredo, J. A. Labrincha, J. R. Frade, and F. M. B. Marques, Reactions between a zirconia-based electrolyte and $LaCoO_3$-based electrode materials, *Solid State Ionics*, **101-103**: 343-349 (1997)

[74] F. Zhao, L. Zhang, Z. Jiang, C. Xia, and F. Chen, A high performance intermediate-temperature solid oxide fuel cell using impregnated $La_{0.6}Sr_{0.4}CoO_{3-\delta}$ cathode, *J. Alloys compd.*, **487**: 781-785 (2009)

[75] S. P. Simner, J. P. Shelton, M. D. Anderson, and J. W. Stevenson, Interaction between La(Sr)$FeO_3$ SOFC cathode and YSZ electrolyte, *Solid State Ionics*, **161**: 11-18 (2003)

[76] L. W. Tai, M. M. Nasrallah, H. U. Anderson, D. M. Sparlin, and S. R. Sehlin, Structure and electrical properties of $La_{1-x}Sr_xCo_{1-y}Fe_yO_3$. Part 1. The system $La_{0.8}Sr_{0.2}Co_{1-y}Fe_yO_3$, *Solid State Ionics*, **76** (3-4): 259-271 (1995)

[77] L. W. Tai, M. M. Nasrallah, H. U. Anderson, D. M. Sparlin, and S. R. Sehlin, Structure and electrical properties of $La_{1-x}Sr_xCo_{1-y}Fe_yO_3$. Part 2. The system $La_{1-x}Sr_xCo_{0.2}Fe_{0.8}O_3$, *Solid State Ionics*, **76** (3-4): 273-283 (1995)

[78] A. Petric, P. Huang, and F. Tietz, Evaluation of La-Sr-Co-Fe-O perovskites for solid oxide fuel cells and gas separation membranes, *Solid State Ionics*, **135**: 719-725 (2000)

[79] J. W. Stevenson, T. R. Armstrong, R. D. Carneim, L. R. Pederson, and W. J. Weber, Electrochemical properties of mixed conducting perovskites $La_{1-x}M_xCo_{1-y}Fe_yO_{3-\delta}$ (M=Sr, Ba, Ca), *J. Electrochem. Soc.*, **143** (9): 2722-2729 (1996)

[80] J. Chen, F. Liang, L. Liu, S. Jiang, B. Chi, J. Pu, and J. Li, Nano-structured $(La,Sr)(Co,Fe)O_3$ + YSZ composite cathodes for intermediate temperature solid oxide fuel cells, *J. Power Sources*, **183**: 586-589 (2008)

[81] L. Wu, L. Zhao, Z. Zhan, and C. Xia, Cathode supported tubular solid oxide fuel cells with nanostructured $La_{0.6}Sr_{0.4}Co_{0.2}Fe_{0.8}O_3$ electrocatalysts, *J. Power Sources*, **266**: 268-274 (2014)

[82] P. I. Cowin, C. T. G. petit, R. Lan, J. T. S. Irvine, and S. Tao, Recent progress in the development of anode materials for solid oxide fuel Cells, *Andv. Energy Mater.*, **1**: 314-332 (2011)

[83] J. B. Goodenough, and Y. H. Huang, Alternative anode materials for solid oxide fuel cells, *J. Power Sources*, **173**: 1-10 (2007)

[84] S. K. Pratihar, A. Das Sharma, R. N. Basu, and H. S. Maiti, Preparation of nickel coated powder for application as an anode for solid oxide fuel cells, *J. Power Sources*, **129**: 138-142 (2004)

[85] Z. Cheng, J. H. Wang, Y. Choi, L. Yang, M. C. Lin, and M. Liu, From Ni-YSZ to sulphur-tolerant anode materials for SOFCs: electrochemical behaviour, in situ characterization, modelling, and future perspectives, *Energy Environ. Sci.*, **4**: 4380-4409 (2011)

[86] S. T. Aruna, M. Muthuraman, and K. C. Patil, Synthesis and properties of Ni-YSZ cermet: anode material for solid oxide fuel cells, *Solid State Ionics*, **111**: 45-51 (1998)

[87] M. Mori, T. Yamanoto, H. Itoh, H. Inaba, and H. Tagawa, Thermal expansion of nickel-zirconia anodes in solid oxide fuel cells during fabrication and operation, *J. Electrochem. Soc.*, **145** (4): 1374-1381 (1998)

[88] F. Tietz, Thermal expansion of SOFC materials, *Ionics*, **5**: 129-139 (1999)

[89] D. W. Dees, T. D. Claar, T. E. Easler, D. C. Fee, and F. C. Mrazek, Conductivity of porous $Ni/ZrO_2$-$Y_2O_3$ cermets, *J. Electrochem. Soc.*, **134** (9): 2141-2146 (1987)

[90] H. Koide, Y. Someya, T. Yoshida, and T. Maruyama, Properties of Ni/YSZ cermet as anode for SOFC, *Solid State Ionics*, **132**: 253-260 (2000)

[91] T. Klemensø, and M. Mogensen, Ni-YSZ solid oxide fuel cell anode behaviour upon redox cycling based on electrical characterization, *J. Am. Ceram. Soc.*, **90** (11): 3582-3588 (2007)

[92] D. M. Bastidas, S. Tao, and J. T. S. Irvine, A symmetrical solid oxide fuel cell demonstrating redox stable perovskite electrodes, *J. Mater. Chem.*, **16**: 1603-1605 (2006)

[93] M. Cassidy, G. Lindsay, and K. Kendall, The reduction of nickel-zirconia cermet anodes and effects on supported thin electrolytes, *J. Power Sources*, **61**: 189-192 (1996)

[94] D. Simwonis, F. Tietz, and D. Stöver, Nickel coarsening in annealed Ni/8YSZ anode substrates for solid oxide fuel cells, *Solid State Ionics*, **132**: 241-251 (2000)

[95] S. P. Jiang, and W. Wang, Sintering and grain growth of (La,Sr)MnO3 electrodes of solid oxide fuel cells under polarization, *Solid State Ionics*, **176**: 1185-1191 (2005)

[96] P. Tanasini, M. Cannarozzo, P. Costamagna, A. Faes, J. Van Herle, A. Hessler-Wyser, and C. Comninellis, Experimental and theoretical investigation of degradation mechanisms by particle coarsening in SOFC electrodes, *Fuel cells*, **9** (5): 740-752 (2009)

[97] Y. Matsuzaki, and I. Yasuda, The poisoning effect of sulphur-containing impurity gas on a SOFC anode: part 1. Dependence on temperature, time, and impurity concentration, *Solid State Ionics*, **132**: 261-269 (2000)

[98] M. L. Toebes, J. H. Bitter, A. J. Dillen, and K. P. de Jong, Impact of the structure and reactivity of nickel particles on the catalytic growth of carbon nanofibers, *Catal. Today*, **76**: 33-42 (2002)

[99] J.-H. Koh, Y.-S. Yoo, J.-W. Park, and H. C. Lim, Carbon deposition and cell performance of Ni-YSZ anode support SOFC with methane fuel, *Solid State Ionics*, **149**: 157-166 (2002)

[100] L. Yang, Z. Cheng, M. Liu, and L. Wilson, New insights into sulphur poisoning behaviour of Ni-YSZ anode from long-term operation of anode-supported SOFCs, *Energy Environ. Sci.*, **3**: 1804-1809 (2010)

[101] J. Dong, Z. Cheng, S. Zha, and M. Liu, Identification of nickel sulphides on Ni-YSZ cermet exposed to $H_2$ fuel containing $H_2S$ using Raman spectroscopy, *J. Power Sources*, **156**: 461-465 (2006)

[102] Y. M. Choi, C. Compson, M. C. Lin, and M. Liu, A mechanistic study of $H_2S$ decomposition on Ni- and Cu-based anode surfaces in a solid oxide fuel cell, *Chem. Phys. Lett.*, **421**: 179-183 (2006)

[103] S. Zha, Z. Cheng, and M. Liu, Sulfur poisoning and regeneration of Ni-bsed anodes in solid oxide fuel cells, *J. Electrochem. Soc.*, **154** (2): B201-B206 (2007)

[104] G. J. Offer, J. Mermelstein, E. Brightman, and N. P. Brandon, Thermodynamics and kinetics of the interaction of carbon and sulphur with solid oxide fuel cell anode, *J. Am. Ceram. Soc.*, **92** (4): 763-780 (2009)

[105] X.-M. Ge, S.-H. Chan, Q.-L. Liu, and Q. Sun, Solid oxide fuel cell anode materials for direct hydrocarbon utilization, *Adv. Energy Mater.*, **2**: 1156-1181 (2012)

[106] M. A. Buccheri, A. Singh, and J. M. Hill, Anode- versus electrolyte-supported Ni-YSZ/YSZ/Pt SOFCs: Effect of cell design on OCV, performance and carbon formation for the direct utilization of dry methane, *J. Power Sources*, **196**: 968-976 (2011)

[107] M. A. Buccheri, and J. M. Hill, Evaluation of a Cu/YSZ and Ni/YSZ bilayer anode for the direct utilization of methane in a solid-oxide fuel cell, *Fuel Cells*, **14** (2): 162-170 (2014)

[108] L. Yang, Development of alternative anode based on doped $SrTiO_3$ for solid oxide fuel cells, PhD theis, 2007

[109] R. J. Gorte, S. Park, J. M. Vohs, and C. Wang, Anodes for direct oxidation of dry hydrocarbons in a solid-oxide fuel cell, *Adv. Mater.*, **12** (9): 1465-1469 (2000)

[110] R. J. Gorte, H. Kim, and J. M. Vohs, Novel SOFC anodes for the direct electrochemical oxidation of hydrocarbon, *J. Power Sources*, **106**: 10-15 (2002)

[111] S. McIntosh, J. M. Vohs, and R. J. Gorte, An examination of lanthanide additives on the performance of Cu-YSZ cermet anodes, *Electrochim. Acta*, **47**: 3815-3821 (2002)

[112] S. Jung, C. Lu, H. He, K. Ahn, R. J. Gorte, and J. M. Vohs, Influence of composition and Cu impregnation method on the performance of $Cu/CeO_2/YSZ$ SOFC anodes, *J. Power Sources*, **154**: 42-50 (2006)

[113] A. Ringuedé, J. A. Labrincha, and J. R. Frade, A combustion synthesis method to obtain alternative cermet materials for SOFC anodes, *Solid State Ionics*, **141-142**: 549-557 (2001)

[114] A. Ringuedé, D. Bronine, and J. R. Frade, $Ni_{1-x}Co_x/YSZ$ cermet anodes for solid oxide fuel cells, *Electrochim. Acta*, **48**: 437-442 (2002)

[115] A. Ringuedé, D. P. Fagg, and J. R. Frade, Electrochemical behaviour and degradation of (Ni,M)/YSZ cermet electrodes (M=Co, Cu, Fe) for high temperature application of solid electrolytes, *J. Eur. Ceram. Soc.*, **24**: 1355-1358 (2004)

[116] S.-I. Lee, J. M. Vohs, and R. J. Gorte, A study of SOFC anodes based on Cu-Ni and Cu-Co bimetallics in $CeO_2$-YSZ, *J. Electrochem. Soc.*, **151** (9): A1319-A1323 (2004)

[117] H. Kim, C. Lu, W. L. Worrell, J. M. Vohs, and R. J. Gorte, Cu-Ni cermet anodes for direct oxidation of methane in solid-oxide fuel cells, *J. Electrochem. Soc.*, **149** (3): A247-A250 (2002)

[ 118 ] E. W. Park, H. Moon, M.-S. Park, and S. H. Hyun, Fabrication and characterization of Cu-Ni-YSZ SOFC anodes for direct use of methane via Cu-electroplating, *Int. J. Hydrogen Energy*, **34**: 5537-5545 (2009)

[ 119 ] Z. Xie, W. Zhu, B. Zhu, and C. Xia, $Fe_xCo_{0.5-x}Ni_{0.5}$-SDC anodes for low-temperature solid oxide fuel cells, *Electrochim. Acta*, **51**: 3052-3057 (2006)

[120] J. W. Yun, S. P. Yoon, J. Han, S. Park, H. S. Kim, and S. W. Nam, Ceria coatings effect on $H_2S$ poisoning of Ni/YSZ anodes for solid oxide fuel cells, *J. Electrochem. Soc.*, **157** (12): B1825-B1830 (2010)

[121] S. Choi, J. Wang, Z. Cheng, and M. Liu, Surface modification of Ni-YSZ using Niobium oxide for sulphur-tolerant anodes in solid oxide fuel cells, *J. Electrochem. Soc.*, **155** (5): B449-B454 (2008)

[122] J. W. Yun, H. C. Ham, H. S. Kim, S. A. Song, S. W. Nam, and S. P. Yoon, Effects of $Sm_{0.2}Ce_{0.8}O_{2-\delta}$ modification of a Ni-based anode on the $H_2S$ torelance for intermediate temperature solid oxide fuel cells, *J. Electrochem. Soc.*, **160** (2): F153-F161 (2013)

[123] S. Sengodam, M. Liu, T.-H. Lim, J. Shin, M. Liu, and G. Kim, Enhancing sulphur tolerance of a Ni-YSZ anode through $BaZr_{0.1}Ce_{0.7}Y_{0.1}Yb_{0.1}O_{3-\delta}$ (BZCYYb) infiltration, *J. Electrochem. Soc.*, **161** (5): F668-F673 (2014)

[124] E. K. Weise, and I. A. Lesk, On the electrical conductivity of some alkaline earth titanates, *J. Chem. Phys.*, **21** (5): 801-806 (1953)

[125] U. Balachandran, and N. G. Eror, Electrical conductivity in lanthanum-doped strontium titanate, *J. Electrochem. Soc.*, **129** (5): 1021-1026 (1982)

[126] R. Moos, and K. H. Hardtl, Electronic transport properties of $Sr_{1-x}La_xTiO_3$ ceramic, *J. Appl. Phys.*, **80** (1): 393-400 (1996)

[ 127 ] S. Hui, and A. Petric, Electrical conductivity of yttrium-doped $SrTiO_3$: influence of transition metal additives, *Mater. Res. Bull.*, **37**: 1215-1231 (2002)

[128] D. Neagu, and J. T. S. Irvine, Perovskite defect chemistry as exemplified by strontium titanate, pp. 397-415, in Comprehensive inorganic chemistry II, Edited by J. Reedijk, and K. Poeppelmeier, Elsevier, 2013

[129] J. T. S. Irvine, Perovskite oxide anodes for SOFCs, pp.167-182, in Perovskite oxide for solid oxide fuel cells, Edited by T. Ishihara, Springer, 2009

[130]S. Hui, and A. Petric, Electrical properties of yttrium-doped strontium titanate under reducing conditions, *J. Electrochem. Soc.*, **149** (1): J1-J10 (2002)

[131] H. S. Kim, S. P. Yoon, J. W. Yun, S. A. Song, S.-C. Jang, S. W. Nam, and Y.-G. Shul, $Sr_{0.92}Y_{0.08}TiO_{3-\delta}/Sm_{0.2}Ce_{0.8}O_{2-\delta}$ anode for solid oxide fuel cells running on methane, *Int. J. hydrogen Energy*, **37**: 16130-16139 (2012)

[132] G. Tsekouras, and J. T. S. Irvine, The role of defect chemistry in strontium titanates utilised for high temperature steam electrolysis, *J. Mater. Chem.*, **21** (25): 9367-9376 (2011)

[133] Q. Ma, and F. Tietz, Comparison of Y and La-substituted $SrTiO_3$ as the anode materials for SOFCs, *Solid State Ionics*, **225**: 108-112 (2012)

[134] O. A. Marina, N. L. Canfield, and J. W. Stevenson, Thermal, electrical, and electrocatalytical properties of lanthanum-doped strontium titanate, *Solid State Ionics*, **149**: 21-28 (2002)

[ 135 ] P. R. Slater, D. P. Fagg, and J. T. S. Irvine, Synthesis and electrical characterisation of doped perovskite titanates as potential anode materials for solid oxide fuel cells, *J. Mater. Chem.*, **7** (12): 2495–2498 (1997)

[136] X. Sun, S. Wang, Z. Wang, X Ye, T. Wen, and F. Huang, Anode performance of LST-x$CeO_2$ for solid oxide fuel cells, *J. Power Sources*, **183**: 114-117 (2008)

[137] Z. Du, H. Zhao, X. Zhou, Z. Xie, and G. Zhang, Electrical conductivity and cell performance of $La_{0.3}Sr_{0.7}Ti_{1-x}Cr_xO_{3-\delta}$ perovskite oxides used as anode and interconnect materials for SOFCs, *Int. J. Hydrogen Energy*, **38**: 1068-1073 (2013)

[138] S. Roudeau, J. C. Grenier, and J. M. Bassat, $La_{0.5}Sr_{0.2}TiO_{3-\delta}$ perovskite as anode material for solid oxide fuel cells, *J. Fuel Cell Sci. Tech.*, **11**: 041006(1)-041006(6) (2014)

[139] X. Huang, H. Zhao, W. Qiu, W. Wu, and X. Li, Performances of planar solid oxide fuel cells with doped strontium titanate as anode materials, Energy Conversion and Management, **48**: 1678-1682 (2007)

[140] S. Lee, G. Kim, J. M. Vohs, and R. J. Gorte, SOFC anodes based on infiltration of $La_{0.3}Sr_{0.7}TiO_3$, *J. Electrochem. Soc.*, **155** (11): B1179-B1183 (2008)

[141] S.-L. Zhang, C.-X. Li, and C.-J. Li, Chemical compatibility and properties of suspension plasma-sprayed $SrTiO_3$-based anodes for intermediate-temperature solid oxide fuel cells, *J. Power Sources*, **264**: 195-205 (2014)

[142] K. B. Yoo, and G. M. Choi, Performance of La-doped strontium titanate (LST) anode on $LaGaO_3$-based SOFC, *Solid State Ionics*, **180** (11-13): 867–871 (2009)

[143] M. C. Verbraeken, B. Iwanschitz, A. Mai, and J. T. S. Irvine, Evaluation of Ca doped $La_{0.2}Sr_{0.7}TiO_3$ as an alternative material for use in SOFC anodes, *J. Electrochem. Soc.*, **159** (11): F757-F762 (2012)

[144] P. Holtappels, J.T.S. Irvine, B. Iwanschitz, L. T. Kuhn, L. Y. Lu, Q. Ma, J. Malzbender, A. Mai, T. Ramos, J. Rass-Hansen, B. R. Sudireddy, F. Tietz, V. Vasechko, S. Veltzé, and M.C. Verbraeken, Full ceramic fuel cells based on strontium titanate anodes, an approach towards more robust SOFCs, *ECS Trans.*, **57** (1): 1175-1184 (2013)

[145] T. Ikebe, H. Muroyama, T. Matsui, and K. Eguchi, Fabrication of redox tolerant anode with an electronic conductive oxide of Y-doped $SrTiO_3$, *J. Electrochem. Soc.*, **157** (6): B970-B974 (2010)

[146] L. Fan, Y. Xiong, L. Liu, Y. Wang, H. Kishimoto, K. Yamaji, and T. Horita, Performance of $Gd_{0.2}Ce_{0.8}O_{1.9}$ infiltrated $La_{0.2}Sr_{0.8}TiO_3$ nanofiber scaffolds as anodes for solid oxide fuel cells, *J. Power Sources*, **265**: 125-131 (2014)

[147] Q. Ma, F. Tietz, A. Leonide, and E. Ivers-Tiffee, Electrochemical performances of solid oxide fuel cells based on Y-substituted $SrTiO_3$ ceramic anode materials, *J. Power Sources*, **196**: 7308– 7312 (2011)

[148] W Zhou, N. Yan, T. Chuang, and J. Luo, Progress in La-doped SrTiO3 (LST)-based anode materials for solid oxide fuel cells, *RSC Adv.*, **4**: 118-131 (2014)

[149] C. Arrivé, T. Delahave, O. Joubert, and G. Guathier, Exsolution of nickel nanoparticles at the surface of a conducting titanate as potential hydrogen electrode material for solid oxide electrochemical cells, *J. Power Sources*, **223**: 341-348 (2013)

[150] G. Tsekouras, D. Neagu, and J. T. S. Irvine, Step-change in high temperature steam electrolysis performance of perovskite oxide cathodes with exsolution of B-site dopants, *Energy Environ. Sci.*, **6**: 256-266 (2013)

[151] D. Neagu, G. Tsekouras, D. N. Miller, H. Ménard, and J. T. S. Irvine, In situ growth of nanoparticles through control of non-stoichiometry, *Nat. Chem.*, **5** (11): 916-923 (2013)

[152] C. Perillat-Merceroz, G. Gauthier, P. Roussel, M. Huve, P. Gelin, and R. N. Vannier, Synthesis and study of a Ce-doped La/Sr titanate for solid oxide fuel cell anode operating directly on methane, *Chem. Mater.*, **23** (6): 1539-1550 (2011)

[153] S. H. Cui, J. H. Li, X. W. Zhou, G. Y. Wang, J. L. Luo, K. T. Chuang, Y. Bai, and L. J. Qiao, Cobalt doped $LaSrTiO_{3-\delta}$ as an anode catalyst: effect of Co nanoparticle precipitation on SOFCs operating on $H_2S$-containing hydrogen, *J. Mater. Chem. A*, **1**: 9689-9696 (2013)

[154] C. D. Savaniu, and J. T. S. Irvine, Reduction studies and evaluation of surface modified A-site deficient La-doped $SrTiO_3$ as anode material for IT-SOFCs, *J. Mater. Chem.*, **19**: 8119–8128 (2009)

[155] C. D. Savaniu, and J. T. S. Irvine, La-doped $SrTiO_3$ as anode material for IT-SOFC, *Solid State Ionics*, **192**: 491–493 (2011)

[156] C. D. Savaniu, D. N. Miller, J. T. S. Irvine, Scale up and anode development for La-doped $SrTiO_3$ anode-supported SOFCs, *J. Am. Ceram. Soc.*, **96** (6):1718-1723 (2013)

[157] C. D. Savaniu, and J. T. S. Irvine, Intermediate temperature SOFC anode component based on A-site deficient La-doped $SrTiO_3$, *ECS Trans.*, **25** (2): 2213-2222 (2009)

[158] H. Kurokawa, L. Yang, C. P. Jacobson, L. C. De Jonghe, and S. J. Visco, Y-doped $SrTiO_3$ based sulfur tolerant anode for solid oxide fuel cells, *J. Power Sources*, **164**: 510–518 (2007)

[159] J. H. Kim, H. Schlegl, and J. T. S. Irvine, The catalytic effect of impregnated (La, Sr)(Ti, Mn)$O_{3\pm\delta}$ with $CeO_2$ and Pd as potential anode materials in high temperature solid oxide fuel cells, *Int. J. Hydrogen Energy*, **37**: 14511-14517 (2012)

[160] J. H. Kim, D. Miller, H. Schlegl, D. McGrouther, and J. T. S. Irvine, Investigation of microstructural and electrochemical properties of impregnated (La,

Sr)(Ti, Mn)$O_{3\pm\delta}$ as a potential anode material in high-temperature solid oxide fuel cells, *Chem. Mater.*, **23**: 3841-3847 (2011)

[161] G. Kim, M. D. Gross, W. Wang, J. M. Vohs, and R. J. Gorte, SOFC anode based on LST-YSZ composites and on $Y_{0.04}Ce_{0.48}Zr_{0.48}O_2$, *J. Electrochem. Soc.*, **155** (4): B360-B366 (2008)

[162] P. Puengjinda, H. Muroyama, T. Matsui, and K. Eguchi, Optimization of anode material composed of Y-doped $SrTiO_3$ and metal and/or oxide additives for solid oxide fuel cells, *J. Power Sources*, **204**: 67–73 (2012)

[163] P. Blennow, A. Hagen, K. K. Hansen, L. R. Wallenberg, and M. Mogensen, Defect and electrical transport properties of Nb-doped $SrTiO_3$, *Solid State Ionics*, **179**: 2047-2058 (2008)

[164] J. Karczewski, B. Riegel, M. Gazda, P. Jasinski, and B. Kusz, Electrical and structural properties of Nb-doped $SrTiO_3$ ceramics, *J. Electroceram.*, **24**: 326-330 (2010)

[ 165 ] P. Blennow, K. K. Hansen, L. R. Wallenberg, and M. Mogensen, Electrochemical characterization and redox behaviour of Nb-Doped $SrTiO_3$, *Solid State Ionics*, **180**: 63-70 (2009)

[166] A. M. Hussain, J. V. T. Høgh, T. Jacobsen, and N. Bonanos, Nickel-ceria infiltrated Nb-doped $SrTiO_3$ for low temperature SOFC anodes and analysis on gas diffusion impedance, *Int. J. Hydrogen Energy*, **37** (5): 4309-4318 (2012)

[167] P. Blennow, B. R. Sudireddy, Å H. Persson, T. Klemensø, J. Nielsen, and K. Thydén, Infiltrated $SrTiO_3$:FeCr-based anodes for metal-supported SOFC, *Fuel Cells*, **13** (4): 494-505 (2013)

[168] T. Ramos, S. Veltzé, B. R. Sudireddy, and P. Holtapplels, Impedance and stability of M/CGO (M; Ni, Pd, Ru) Co-infiltrated Nb-doped $SrTiO_3$ SOFC anodes, *ECS Electrochem. Lett.*, **3** (2): F5-F6 (2014)

[169] S. Cho, D. E. Fowler, E. C. Miller, J. S. Cronin, K. R. Poeppelmeier, and S. A. Barnett, Fe-substituted $SrTiO_{3-\delta}$-$Ce_{0.9}Gd_{0.1}O_2$ composite anodes for solid oxide fuel cells, *Energy Environ. Sci.*, **6**: 1850-1857 (2013)

[170] A. Rothschild, W. Menesklou, H. L. Tuller, and E. Ivers-Tiffée, Electronic structure, defect chemistry, and transport properties of $SrTi_{1-x}Fe_xO_{3-y}$ solid solutions, *Chem. Mater.*, **18**: 3651-3659 (2006)

[171] N. Danilovic, A. Vincent, J. L. Luo, K. T. Chuang, R. Hui, and A. R. Sanger, Correlation of Fuel cell anode electrocatalytic and ex situ catalytic activity of perovskites $La_{0.75}Sr_{0.25}Cr_{0.5}X_{0.5}O_{3-\delta}$ (X=Ti, Mn, Fe, Co), *Chem. Mater.*, **22** (3): 957-965 (2010)

[172] K. B. Yoo, and G. M. Choi, Co-doped $La_{0.2}Sr_{0.8}TiO_3$ as a potential anode for the $LaGaO_3$-based solid oxide fuel cell, *ECS Trans.*, **25** (2): 2259-2266 (2009)

[173] X. Li, H. Zhao, F. Gao, Z. Zhu, Ni. Chen, and W. Shen, Synthesis and electrical properties of Co-doped $Y_{0.08}Sr_{0.92}TiO_{3-\delta}$ as a potential SOFC anode, *Solid State Ionics*, **179**: 1588-1592 (2008)

[174] A. Ovalle, J. C. Ruiz-Morales, J. Canales-Vázquez, D. Marrero-López, and J. T. S. Irvine, Mn-substituted tinanates as efficient anodes for direct methane SOFCs, *Solid State Ionics*, **177**: 1997-2003 (2006)

[175] Q. X. Fu, F. Tietz, and D. Stöver, $La_{0.4}Sr_{0.6}Ti_{1-x}Mn_xO_{3-\delta}$ perovskite as anode materials for solid oxide fuel cells, *J. Electrochem. Soc.*, **153** (4): D74-D83 (2006)

[176] M. J. Escudero, J. T. S. Irvine, and L. Daza, Development of anode materials based on La-substituted $SrTiO_3$ perovskites doped with manganese and/or gallium for SOFC, *J. Power Sources*, **192**: 43-50 (2009)

[177] R. J. Gorte,and J. M. Vohs, Nanostructured anodes for solid oxide fuel cells, *Curr. Opin. Colloid Interface Sci.*, **14**: 236-244 (2009)

[178] F. Yi, H. Li, H. Chen, R. Zhao, and X. Jiang, Preparation and haracterization of La and Cr co-doped $SrTiO_3$ materials for SOFC anode, *Ceram. Int.*, **39** (1): 347-352 (2013)

[179] S. McIntosh, and R. J. Gorte, Direct hydrocarbon solid oxide fuel cells, *Chem. Rev.*, **104**: 4845-4865 (2004)

[180] Y. Lin, Direct methane solid oxide fuel cells and their related applications, PhD thesis, 2006

[181] C. Ni, Optimization and testing of large ceramic-impregnated solid oxide fuel cells (SOFCs), PhD thesis, 2014

[182] M. J. Jørgensen, S. Primdahl, C. Bagger, and M. Mogensen, Effect of sintering temperature on microstructure and performance of LSM-YSZ composite cathodes, *Solid State Ionics*, **139** (1-2): 1-11 (2001)

[183] Q. Zhu, and B. Fan, Low temperature sintering of 8YSZ electrolyte film for intermediate temperature solid oxide fuel cells, *Solid State Ionics*, **176** (9-10): 889-894 (2005)

[184] O. Yamamoto, Y. Takeda, R. Kanno, and M. Noda, perovskite-type oxides as oxygen electrodes for high temperature oxide fuel cells, *Solid State Ionics*, **22** (2-3): 241-246 (1987)

[185] D. Mori, H. Oka, Y. Suzuki, N. Sonoyama, A. Yamada, R. Kanno, Y. Sumiya, N. Imanishi, and Y. Takeda, Synthesis, structure, and electrochemical properties of epitaxial perovskite $La_{0.8}Sr_{0.2}CoO_3$ film on YSZ substrate, *Solid State Ionics*, **177** (5-6): 535-540 (2006)

[186] D. Ding, X. Li, S. Y. Lai, K. Gerdes, M. Liu, Enhancing SOFC cathode performance by surface modification through infiltration, *Energy Environ. Sci.*, **7**: 552-575 (2014)

[187] M. Kishimoto, M. Lomberg, E. Ruiz-Trejo, and N. P. Brandon, Enhanced triple-phase boundary density in infiltrated electrodes for solid oxide fuel cells demonstrated by hing-resolution tomography, *J. Power Sources*, **266**: 291-295 (2006)

[188] S. P. Jiang, A review of wet impregnation-an alternative method for the fabrication of high performance and nano-structured electrodes of solid oxide fuel cells, *Mater. Sci. Eng. A*, **418**: 199-210 (2006)

[189] A. D. Aljaberi, and J. T. S. Irvine. Ca-substituted, A-site deficient perovskite $La_{0.2}Sr_{0.7}TiO_3$ as a potential anode material for SOFCs, *J. Mater. Chem. A*, **1** (19): 5868-5874 (2013)

[190] C. Setevich, F. Prado, D. Z. de Florio, and A. Caneiro, Stabilization of the cubic perovskite in the system $La_{1-x}Ba_xCo_{1-y}Fe_yO_{3-\delta}$ ($0.7 \leq x \leq 0.9$) and its electrochemical performance as cathode materials for intermediate-temperature solid oxide fuel cells, *J. Power Sources*, **247**: 264-272 (2014)

[191] Y. Liu, F. Wang, B. Chi, J. Pu, L. Jian, and S. P. Jiang, A stability study of impregnated LSCF–GDC composite cathodes of solid oxide fuel cells. *J. Alloys Compd.*, **578**: 37-43 (2013)

[192] Q. Ma, B. Iwanschitz, E. Dashjav, A. Mai, F. Tietz, H.-P. Buchkremer, Electrochemical performance and stability of electrolyte-supported solid oxide fuel cells based on Y-substituted $SrTiO_3$ ceramic anodes, *Solid State Ionics*, **262**: 465-468, (2014)

[193] Q. Ma, B. Iwanschitz, E. Dashjav, S. Baumann, D. Sebold, I. A. Raj, A. Mai, F. Tietz, Microstructural variations and their influence on the performance of solid oxide fuel cells based on yttrium-substituted strontium titanate ceramic anodes, *J. Power Sources*, **27**: 678-685 (2015)

[194] D. Hotza, and P. Greil, Review: aqueous tape casting of ceramic powders, *Mater. Sci. Eng.*, **A202**: 206-217 (1995)

[195] J.-H. Myung, H. J. Ko, C. H. Im, J. Moon, and S.-H. Hyun, Development of solid oxide fuel cells (SOFCs) by tape-casting and single-step co-firing of monolithic laminates, *Int. J. Hydrogen Energy*, **39**: 2313-2319 (2014)

[196] C. Zhao, R. Liu, S. Wang, and T. Wen, Fabrication of a large area cathode-supported thin electrolyte film for solid oxide fuel cells via tape casting and co-sintering techniques, *Electrochem. Commun.*, **11**: 842-845 (2009)

[197] C. Fu, S. H. Chan, Q. Liu, X. Ge, and G. Pasciak, Fabrication and evaluation of Ni-GDC composite anode prepared by aqueous-based tape casting method for low-temperature solid oxide fuel cell, *Int. J. Hydrogen Energy*, **35**: 301-307 (2010)

[198] S. Zhang, L. Bi, L. Zhang, C. Yang, H. Wang, and W. Liu, Fabrication of cathode supported solid oxide fuel cell by multi-layer tape casting and co-firing method, *Int. J. Hydrogen Energy*, **34**: 7789-7794 (2009)

[199] X. Zhou, K. Sun, J. Gao, S. Le, N. Zhang, and P. Wang, Microstructure and electrochemical characterization of solid oxide fuel cells fabricated by co-tape casting, *J. Power Sources*, **191**: 528-533 (2009)

[200] N. H Menzler, J. Malzbender, P. Choderböck, R. Kauert, and H. P. Buchkremer, Sequential tape casting of anode-supported solid oxide fuel cells, *Fuel Cells*, **14** (1): 96-106 (2014)

[201] S. Le, K. N. Sun, N. Zhang, X. Zhu, H. Sun, Y. X. Yuan, and X. Zhou, Fabrication and evaluation of anode and thin $Y_2O_3$-stabilized $ZrO_2$ film by co-tape casting and co-firing technique, *J. Power Sources*, **195**: 2644-2648 (2010)

[202] S. Nayak, B. P. Singh, L. Besra, T. K. Chongdar, N. M. Gokhale, and S. Bhattacharjee, Aqueous tape casting using organic binder: a case study with YSZ, *J. Am. Ceram. Soc.*, **94** (11): 3742-3747 (2011)

[203] A. Akbari-Fakhrabadi, R. V. Mangalaraja, F. A. Sanhueza, R. E. Avila, S. Ananthakumar, and S. H. Chan, Nanostructured Gd-$CeO_2$ electrolyte for solid oxide fuel cell by aqueous tape casting, *J. Power Sources*, **218**: 307-312 (2012)

[204] http://www.gwent.org/gem_screen_printing.html. 2014 [cited July 2014]

[205]http://serc.carleton.edu/research_education/geochemsheets/techniques/XRD.html. 2013 [cited July 2014]

[206]http://www.greenwood.wa.edu.au/resources/Physics%203B%20WestOne/content/004_em_fields_force/page_12.htm. 2014 [cited July 2014]

[207] http://academic.udayton.edu/ShirleyWright/SEM/Principle/2_Imaging.htm. 2014 [cited July 2014]

[208] http://www.capcoat.be/auger-electron-spectroscopy-aes. 2014 [cited July 2014]

[209] http://en.wikipedia.org/wiki/Energy-dispersive_X-ray_spectroscopy. 2014 [cited July 2014]

[210] http://www.ammrf.org.au/myscope/analysis/eds/. 2013 [cited July 2014]

[211] http://www.hk-phy.org/atomic_world/tem/tem02_e.html. 2014 [cited July 2014]

[212] Oxford instruments, EDS in the TEM explained, Oxford instrument analytical Ltd, 2013

[213] L. A. Giannuzzi, and F. A. Stevie, A review of focused ion beam milling techniques for TEM specimen preparation, *Micron*, **30**: 197-204 (1999)

[214] C. A. Volkert, and A. M. Minor, Focused ion beam microscopy and micromachining, *Mrs Bull.*, **32**: 389-399 (2007)

[215] N. Yao, Focused ion beam systems: basic and application, Cambridage University Press, 2007

[216] http://en.wikipedia.org/wiki/Focused_ion_beam. 2014 [cited July 2014]

[217] http://www.leica-microsystems.com/news-media/news/news-details/article/leica-em-tic-3x-triple-ion-beam-techniques/. 2011 [cited April 2015]

[218] Leica Microsystems, Leica EM TIC020 triple ion-beam cutter for easy site specific sample preparation, 2011

[219] http://innopharmalabs.com/products/particle_sizing_and_characterization. 2012 [cited July 2014]

[220] http://particle.dk/methods-analytical-laboratory/surface-area-bet/surface-area-bet-theory/. 2014 [cited July 2014]

[ 221 ] NETZSCH Analyzing and Testing, Dilatometry: method, instruments, application-from -180 $^{o}$C to 2800 $^{o}$C, NETZSCH

[222] http://www.azom.com/article.aspx?ArticleID=5951. 2014 [cited July 2014]

[223] http://en.wikipedia.org/wiki/Thermogravimetric_analysis. 2014 [cited July 2014]

[224] R. Yeetsorn, M. W. Fowler, and C. Tzoganakis, A review of thermoplastic composite for bipolar plate materials in PEM fuel cells, pp. 317-344 in Nanocomposites with unique properties and applications in medicine and industry, Edited by J. Cuppoletti, InTech, 2011

[225] W. Lai, and S. M. Haile, Impedance spectroscopy as a tool for chemical and electrochemical analysis of mixed conductors: a case study of ceria, *J. Am. Ceram. Soc.*, **88** (11): 2979-2997 (2005)

[ 226 ] M.-G. Olivier, and M. Poelman, Use of electrochemical impedance spectroscopy (EIS) for the evaluation of electrocoatings performances, pp. 1-26, in Recent researches in corrosion and protection, Edited by R. S. Razavi, InTech, 2012

[ 227 ] Scribner Associates, Electrochemical impedance spectroscopy (EIS): a powerful and cost-effective tool for fuel cell diagnosis, Scibner Associates, Inc., 2008

[228] V. F. Lvovich, Impedance spectroscopy: application to electrochemical and dielectric phenomena, John Wiley & sons, Inc., 2012

[ 229 ] E. Barsoukov, and J. R. Macdonald, Impedance spectroscopy theory, experiment, and applications, Second edition, John Wiley & Sons, Inc., 2005

[230] Y. M. Park, and H. Kim, Composite cathodes based on $Sm_{0.5}Sr_{0.5}CoO_{3-\delta}$ with porous Gd-doped ceria barrier layers for solid oxide fuel cells, *Int. J. hydrogen Energy*, **37**: 15320-15333 (2012)

[231] J. T. S. Irvine, D. C. Sinclair, and A. R. West, Electroceramics: characterization by impedance spectroscopy, *Adv. Mater.*, **2** (3): 132-138 (1990)

[232] M. C. Verbraeken, Doped alkaline earth (nitride) hydrides, PhD thesis, 2009

[233] V. Vashook, L. Vasylechko, N. Trofimenko, M. Kuznecov, P. Otchik, J. Zosel, and U. Guth, A-site deficient perovskite-type compounds in the tenary CaTiO3-LaCro3-$La_{2/3}TiO_3$ system, *J. Alloys Compd.*, **419**: 271-280 (2006)

[234] A. Yaqub, C. Savaniu, N. K. Janjua, and J. T. S. Irvine, preparation via a solution method of $La_{0.2}Sr_{0.25}Ca_{0.45}TiO_3$ and its characterization for anode supported solid oxide fuel cells, *J. Mater. Chem. A*, **1** (45): 14189-14197 (2013)

[ 235 ] D. Neagu, and J. T. S. Irvine, Structure and properties of $La_{0.4}Sr_{0.4}TiO_3$ ceramics for use as anode materials in solid oxide fuel cells, *Chem. Mater.*, **22**: 5042-5053 (2010)

[236] D. Burnat, A. Heel, L. Holzer, D. Kata, J. Lis, and T. Graule, Synthesis and performance of A-site deficient lanthanum-doped strontium titanate by nanoparticle based spray pyrolysis, *J. Power Sources*, **201**: 26– 36 (2012)

[ 237 ] S. Boulfrad, M. Cassidy, and J. T. S. Irvine; Dimensional Pd–LSCM composites for SOFC anode current collection, *Adv. Func. Mater.*, **20**: 861–866 (2010)

[238] Z. M. Shen, X. D. Zhu, S. R. Le, W. Sun, and K. N. Sun, Co-sintering anode and $Y_2O_3$ stabilized $ZrO_2$ thin electrolyte film for solid oxide fuel cell fabricated by co-tape casting, *Inter. J. Hydrogen Energy*, **37** (13): 10337-10345 (2012).

[ 239 ] Q. Ma, F. Tietz, D. Sebold, and D. Stöver, Y-substituted $SrTiO_3$-YSZ composites as anode materials for solid oxide fuel cells: interaction between SYT and YSZ, *J. Power Sources*, **195**: 1920-1925 (2010)

[240] A. Atkinson, S. Barnett, R. J. Gorte, J. S. I. Irvine, A. J. Mcevoy, M. Mogensen, S. C. Singhal, and J. Vohs, Advanced anodes for high-temperature fuel cells, *Nat. Mater.*, **3** (1): 17-27 (2004)

[241] J.-D. Kim, G.-D. Kim, J.-W. Moon, Y. Park, W.-H. Lee, K. Kobayashi, M. Nagai, and C.-E. Kim, Characterization of LSM-YSZ composite electrode by ac impedance spectroscopy, *Solid State Ionics*, **143**: 379-389 (2001)

[242] J. S. Park, I. D. Hasson, M. D. Gross, C. Chen, J. M. Vohs, and R. J. Gorte, A high-performance solid oxide fuel cell anode based on lanthanum strontium vanadate, *J. Power Sources*, **196** (18): 7488-7494 (2011)

[243] J. S. Kim, V. V. Nair, J. M. Vohs, and R. J. Gorte, A study of the methane tolerance of LSCM-YSZ composite anodes with Pt, Ni, Pd and ceria catalysts, *Scripta Mater.*, **65** (2): 90-95 (2011)

[244] G. Kim, S. Lee, J. Y. Shin, G. Corre, J. T. S. Irvine, J. M. Vohs, and R. J. Gorte, Investigation of the structural and catalytic requirements for high-performance SOFC anodes formed by infiltration of LSCM, *Electrochem. Solid State Lett.*, **12** (3): B48-B52 (2009)

[245] G. Kim, G. Corre, J. T. S. Irvine, J. M. Vohs, and R. J. Gorte, Engineering composite oxide SOFC anodes for efficient oxidation of methane, *Electrochem. Solid State Lett.*, **11** (2): B16-B19 (2008)

[246] D. A. Osinkin, N. M. Bogdanovich, S. M. Beresnev, and V. D. Zhuravlev, High-temperature anode-supported solid oxide fuel cell with impregnated electrodes, *J. Power Sources*, **288**: 20-25 (2015)

[247] M. D. Gross, J. M. vohs, and R. J. Gorte, Recent progress in SOFC anodes for direct utilization of hydrocarbons, *J. Mater. Chem.*, **17** (30): 3071-3077 (2007)

[248] M. D. Gross, J. M. vohs, and R. J. Gorte, An examination of SOFC anode functional layers based on ceria in YSZ, *J. Electrochem. Soc.*, **154** (7): B694-B699 (2007)

[249] G. Corre, G. Kim,, M. Cassidy, J. M. Vohs, R. J. Gorte, and J. T. S. Irvine, Activation and ripening of impregnated manganese containing perovskite SOFC electrodes under redox cycling, *Chem. Mater.*, **21** (6): 1077-1084 (2009)

[250] K. Chen, and S. P. Jiang, degradation and durability of electrodes of solid oxide fuel cells, pp. 245-307, in Materials for high-temperature fuel cells, Edited by S. P.

Jiang and Y. Yan, Wiley-VCH Verlag GmbH & Co. KGaA, Weinheim, Germany, 2013

[251] S. P. Jiang, Sintering behaviour of Ni/$Y_2O_3$-$ZrO_2$ cermet electrodes of solid oxide fuel cells, *J. Mater. Sci.*, **38**: 3775-3782 (2003)

[252] A. Faes, A. Hessler-Wyser, D. Presvytes, C. G. Vayenas, and J. Van herle, Nickel-zirconia anode degradation and triple phase boundary quantification from microstructural analysis, *Fuel Cells*, **9** (6): 841-851 (2009)

[253] T. Ishihara, J. Yan, M. Shinagawa, and H. Matsumoto, Ni-Fe bimetallic anode as an active anode for intermediate temperature SOFC using $LaGaO_3$ based electrolyte film, *Electrochim. Acta*, **52**: 1645-1650 (2006)

[254] C. J. Fu, S. H. Chan, X. M. Ge, Q. L. Liu, and G. Pasciak, A promising Ni-Fe bimetallic anode for intermediate-temperature SOFC based on Gd-doped ceria electrolyte, *Int. J. Hydrogen Energy*, **36**: 13727-13734 (2011)

[255] H. Kan, and H. Lee, Enhanced stability of Ni-Fe/GDC solid oxide fuel cell anodes for dry methane fuel, *Catal. Commun.*, **12**: 36-39 (2010)

[256] H. Zhong, H. Matsumoto, and T. Ishihara, Development of Ni-Fe based cermet anode for direct CH4 fueled intermediate temperature SOFC using $LaGaO_3$ electrolyte, *Electrochem. Commun.*, **77** (2): 155-157 (2009)

[257] Y. Huang, and J. Yang, Gel-tape-casting of ceramic substrates, pp. 16-73, in Novel colloidal forming of ceramics, Edited by Y. Huang and J. Yang, Tsinghua University Press, Beijing and Springer-Verlag Berlin Heidelberg, 2010

[258] D. Marrocchelli, S. R. Bishop, H. L. Tuller, and B. Yildiz, Understanding chemical expansion in non-stoichiometric oxides: ceria and zirconia case studies, *Adv. Funct. Mater.*, **22**: 1958-65 (2012)

[259] R. Küngas, J. M. Vohs, and R. J. Gorte, Effect of the ionic conductivity of the electrolyte in composite SOFC cathodes, *J. Electrochem. Soc.*, **158** (6): B743-B748 (2011)

[260] M. Shah, G. Hughes, P. W. Voorhees, and S. A. Barnett, Stability and performance of LSCF-infiltrated SOFC cathodes: effect of nano-particle coarsening, *ECS Trans.*, **35** (1): 2045-2053 (2011)

[261] M. Shah, P. W. Voorhees, and S. A. Barnett, Time-dependent performance changes in LSCF-infiltrated SOFC cathodes: the role of nano-particle coarsening, *Solid State Ionics*, **187**: 64-67 (2011)

[262] R. M. Hazen, Wustite ($Fe_{1-x}O$): a review of its defect structure and physical properties, *Rev. Geophys. Space Phys.*, **22** (1): 37-46 (1984)

[263] T. Ishihara, and H. Zhong, Effects of Fe addition on the surface reaction of the anode of intermediate temperature solid oxide fuel cells, *Scripta Mater.*, **65**: 108-111 (2011)

[264] T. H. Shin, S. Ida, and T. Ishihara, Doped CeO2-LaFeO3 composite oxide as an active anode for direct hydrocarbon-type solid oxide fuel cells, *J. Am. Chem. Soc.*, **133** (48): 19399-19407 (2011)

[265] F. P. F. van Berkel, Y. Zhang-Steenwinkel, G. P. J. Schoemakers, M. M. A. van Tuel, and G. Rietveld, Enhanced ASC performance at 600 $^{o}$C by ceria barrier layer optimization, *ECS Trans.*, **25** (2): 2717-2726 (2009)

[266] P. Plonczak, M. Joost, J. Hjelm, M. Søgaard, M. Lundberg, and P. V. Hendriksen, A high performance ceria based interdiffusion barrier layer prepared spin-coating, *J. Power Sources*, **196**: 1156-1162 (2011)

[267] R. Küngas, F. Bidrawn, J. M. Vohs, and R. J. Gorte, Doped-ceria diffusion barriers prepared by infiltration for solid oxide fuel cells, *Electrochem. Solid-State Lett.*, **13** (8): B87-B90 (2010)

[268] J.-S. Kim, N. L. Wieder, A. J. Abraham, M. Cargnello, P. Fornasiero, R. J. Gorte, and J. M. Vohs, Highly active and thermally stable core-shell catalysts for solid oxide fuel cells, *J. Electrochem. Soc.*, **158** (6): B596-B600 (2011)

[269] X. J. Chen, K. A. Khor, and S. H. Chan, Suppression of carbon deposition at $CeO_2$-modified Ni/YSZ anodes in weakly humidified $CH_4$ at 850 $^{o}$C, *Electrochem. Solid-State Lett.*, **8** (2): A79-A82 (2005)

[270] L. Kundakovic, and M. Flytzani-Stephanopoulos, Cu- and Ag-modified cerium oxide catalysts for methane oxidation, *J. Catal.*, 179(1): 203-221 (1998)

[271] J. C. Ruiz-Morales, J. Canales-Vázquez, C. Savaniu, D. Marrero-López, W. Zhou, and J. T. S. Irvine, Disruption of extended defects in solid oxide fuel cell anodes for methane oxidation, *Nature*, **439** (7076): 568-571 (2006)

[272] S. Park, R. Craciun, J. M. Vohs, and R. J. Gorte, Direct oxidation of hydrocarbon in a solid oxide fuel cell I. methane oxidation, *J. Electrochem. Soc.*, **146** (10): 3603-3605 (1999)

[273] M. Liu, S.Wang, T. Chen, C. Yuan, Y. Zhou, S. Wang, and J. Huang, Perofrmance of the nano-structured Cu-Ni (alloy)-CeO2 anode for solid oxide fuel cells, *J. Power Sources*, **274**: 730-735 (2015)

[274] V. Sariboga, and F. Öksüzömer, The investigation of active Ni/YSZ interlayer for Cu-based direct-methane solid oxide fuel cells, *Appl. Energ.*, **93**: 707-721 (2012)

[275] Y. Lin, Z. Zhan, J. Liu, and S. A. Barnett, Direct operation of solid oxide fuel cells with methane fuel, *Solid State Ionics*, **176**: 1827-1835 (2005)

[276] R. Küngas, J.-S. Kim, J. M. Vohs, and R. J. Gorte, Restructuring porous YSZ by treatment in hydrofluoric acid for use in SOFC cathodes, *J. Am. Ceram. Soc.*,**94** (7): 2220-2224 (2011)

[277] R. K. Lenka, T. Mahata, A. K. Tyagi, and P. K. Sinha, Influence of grain size on the bulk and grain boundary ion conduction behaviour in gadolinia-doped ceria, *Solid State Ionics*, **181**: 262-267 (2010)

[278] M. Han, X. Tang, H. Yin, and S. Peng, Fabrication, microstructure and properties of a YSZ electrolyte for SOFCs, *J. Power Sources*, **165**: 757-763 (2007)

[279] X. J. Chen, K. A. Khor, S. H. Chan, and L. G. Yu, Influence of microstructure of the ionic conductivity of yttria-stabilized zirconia electrolyte, *Mater. Sci. Eng. A*, **335**: 462-252 (2002)

[280] M. C. Steil, F. Thevenot, and M. Kleitz, Densification of yttria-stabilized zirconia: impedance spectroscopy analysis, *J. Electrochem. Soc.*, **144** (1): 390-398 (1997)

[281] Y. M. Park, and G. M. Choi, Microstructure and electrical properties of YSZ-NiO composites, *Solid State Ionics*, **120**: 265-274 (1999)

[282] http://www.swicofil.com/textile_metallization.html. 2013 [cited September 2014]

[283] J. Sudagar, J. Lian, and W. Sha, Electroless nickel, alloy, composite and nano coatings – a critical review, *J. Alloys Compd.*, **571**: 183-204 (2013)

[284] N. H. Menzler, F. Tietz, S. Uhlenbruck, H. P. Buchkremer, and D. Stöver, Materials and manufacturing technologies for solid oxide fuel cells, *J. Mater. Sci.*, **45**: 3109-3135 (2010)

[285] N. B. Baba, YSZ reinforced Ni-P composite by electroless nickel co-deposition, pp. 457-482, in Composites and their properties, Edited by N. Hu, Intech, 2012

[286] M. M. Murphy, J. Vanherle, A. J. McEvoy, and K. R. Thampi, Electroless deposition of electrodes in solid-oxide fuel cells, *J. Electrochem. Soc.*, **141** (8): L94-L96 (1994)

[287] G. Wen, Z. X. Guo, and C. K. L. Davies, Microstructural characterisation of electroless-nickel coatings on zirconia powder, *Scripta Mater.*, **43**: 307-311 (2000)

[288] S. K. Pratihar, A. Dassharma, and H. S. Maiti, Properties of Ni/YSZ porous cermets prepared by electroless coating technique for SOFC anode application, *J. Mater. Sci.*, **42**: 7220-7226 (2007)

[289] L. Li, P. Zhang, R. Liu, and S. M. Guo, Preparation of fibrous Ni-coated-YSZ anodes for solid oxide fuel cells, *J. Power Sources*, **196**: 1242-1247 (2011)

[290] N. O. Nwosu, A. M. Davidson, and C. S. Hindle, Effect of sodium dodecyl sulphate on the composition of electroless nickel-yttria stabilized zirconia coatings, *Adv. Chem. Eng. Sci.*, **1**: 118-124 (2011)

[291] N. B. Baba, W. Waugh, and A. M. Davidson, Manufacture of electroless nickel/YSZ composite coatings, *World Academy of Science, Engineering and Technology*, **25**: 715-720 (2009)

[292] R. Elansezhian, B. Ramamoorthy, and P. K. Nair, Effect of surfactants on the mechanical properties of electrodes (Ni-P) coating, *Surf. Coat. Tech.*, **203**: 709-712 (2008)

[293] V. K. Bulasara, Ch. S. N. M. Babu, and R. Uppaluri, Effect of surfactants on performance of electroless plating baths for nickel-ceramic composite membrane fabrication, *Surface Eng.*, **28** (1): 44-48 (2012)

[294] G. O. Mallory, The fundamental aspects of electroless nickel plating, pp. 1-56, in Electroless plating – fundamentals and applications, Edited by G. O. Mallory, J. B. Hajdu, William Andrews Publishing/Noyes, 1990

[295] V. K. Bulasara, M. S. Abhimanyu, T. Pranav, R. Uppaluri, and M. K. Purkait, Performance characteristic of hydrothermal and sonication assisted electroless plating baths for nickel-ceramic composite membrane fabrication, *Desalination*, **284**: 77-85 (2012)

[296] I. R. Mafi, and C. Dehghanian, Comparison of the coating properties and corrosion rates in electroless Ni-P/PTFE composites prepared by different types of surfactants, *Appl. Surf. Sci.*, **257**: 8653-8658 (2011)

[297] R. Haugsrud, On the high-temperature oxidation of nickel, *Corros. Sci.*, **45**: 211-235 (2003)

[298] M. J. Graham, and M. Cohen, On the mechanism of low-temperature oxidation, *J. Electrochem. Soc.*, **119** (7): 879-882 (1972)

[299] S. McIntosh, S. B. Adler, J. M. Vohs, and R. J. Gorte, Effect of polarization on and implication for characterization of LSM-YSZ composite cathodes, *Electrochem. Solid-State Lett.*, **7** (5): A111-A114 (2004)